

UNIVERSITY OF BIRMINGHAM

BUCKLING ANALYSIS OF TUBULAR WIND TURBINE TOWERS BY MEANS OF THE APPLIED ENERGY METHOD

By
Yang Ma

A thesis submitted to the University of Birmingham

for the degree of DOCTOR OF PHILOSOPHY

Department of Civil Engineering,

School of Engineering

University of Birmingham

November 2020

UNIVERSITY OF
BIRMINGHAM

University of Birmingham Research Archive

e-theses repository

This unpublished thesis/dissertation is copyright of the author and/or third parties. The intellectual property rights of the author or third parties in respect of this work are as defined by The Copyright Designs and Patents Act 1988 or as modified by any successor legislation.

Any use made of information contained in this thesis/dissertation must be in accordance with that legislation and must be properly acknowledged. Further distribution or reproduction in any format is prohibited without the permission of the copyright holder.

ABSTRACT

Tubular steel towers are currently the most practical type of supporting structure for wind turbines used in wind energy harvesting. The surging demand for energy has necessitated an increase in the scale and capacity of wind power plants. However, higher towers result in greater threats from external loadings, as historical records of failure incidences reveal the severity of tower collapses due to various buckling modes of the shell structures. It seems, therefore, necessary to thoroughly investigate the collapse mechanisms of the respective structures in response to environmental actors.

The first part of this dissertation discusses a historical case study which indicates that buckling is a common type of tower failure. The buckling mode shown in this case study displays a range of thin-walled structure buckling patterns, in which the wavenumber on the compression side is between 1 and 9. A new approach to the buckling behaviour of cylindrical steel shells under combined axially asymmetric compressive loads and bending moment is presented, employing the energy method.

Within the proposed framework, in the second section, the classical buckling analysis was conducted to determine the governing equilibriums which express the displacement function of a shell's mid-surface in terms of stress–strain elementary expressions. The equations describing curvatures were obtained at the same time. The outcomes of classical buckling theory analysis provided a basis for the application of energy methods.

The governing partial differential equations have been rescaled using energy methods, in order to obtain dimensionless expressions which show stored energy taking place along the shell surface by surface displacement functions. For the perfect shell under axial compression (pure bending moment and combined load), equilibrium buckling paths close to bifurcation points

have been investigated by energy functions to establish the critical points. The analysis shows that bifurcation buckling is at the infimum of energy levels, whereas multiple longitudinal and circumferential wavenumbers may occur with the energy magnitude jumping over adjacent buckling eigenmodes.

The initial geometric imperfections have been introduced to the shell by trigonometric deformation functions, updating the previous governing functions for imperfection sensitivity analysis. The diverse final buckle point numbers verified according to the buckling types of historically observed incidents are determined by shell geometry and external load magnitude. The respective imperfection sensitivity analysis indicated lower energy bound levels and fewer diversities in circumferential wavenumbers.

The last section comprises numerical analysis, performed by modelling twenty shell sections, with five loading scenarios for each. Shell models were implemented with initial imperfections embedded using the finite element method via the Riks method for tracking buckling paths. The results show that buckling evolution paths are significantly affected by bending parts, which leads to section ovalisation that in turn changes the internal strain energy dissipation routine and section curvature. The cylinder's geometrical parameters, the length–radius ratio (L/R) and radius–thickness ratio (R/t), also show a strong influence on buckling behaviours, seemingly linked to a noticeable reduction in the shell buckling bearing capacity during the combined loading scenarios. The results of the numerical simulation are also interpreted and validated the derived theoretical equations under various conditions.

Keywords: Wind Turbine, Shell Structure, Buckling, Energy Method, Combined Load, Finite Element Method, Riks Method, Imperfection.

LIST OF PUBLICATIONS

The results of this research have been published or submitted for publication in journals and conferences relevant to the research field and are the authour's own work. Where the explicit reference is made in text necessarily.

1. Ma, Y.; Martínez-Vázquez, P.; Baniotopoulos, C. Wind Turbine Tower Collapse Cases: A Historical Overview. Proceedings of the Institution of Civil Engineers - Structures and Buildings. 2019, 172, 547–555, doi:10.1680/jstbu.17.00167.
2. Ma, Y.; Martínez-Vázquez, P.; Baniotopoulos, C. Buckling Analysis of a Tubular Wind turbine tower by Means of the Applied Energy Method. 12th HSTAM International Congress on Mechanics, 2019, Thessaloniki Greece.
3. Ma, Y.; Martinez-Vazquez, P.; Baniotopoulos, C. Buckling Analysis for Wind Turbine Tower Design: Thrust Load versus Compression Load Based on Energy Method. *Energies* 2020, *13*, 5302, doi: 10.3390/en13205302.
4. Ma, Y.; Martinez-Vazquez, P.; Baniotopoulos, C. Buckling Mode Jumpping Analysis for Wind Turbine Tower by Energy Method. (*in preparation*)

ACKNOWLEDGEMENTS

First and foremost, the author greatly to express his sincere gratitude to his supervisors, Professor Charalampos Baniotopoulos, Dr Pedro Martinez-Vazquez, for their generous guidance, advice, and constructive suggestions throughout this research. For their motivations, patience, enthusiasms, and immense knowledge, the author has benefited far beyond the academic area, into life philosophy.

The author's sincere thanks also go to the School of Engineering, University of Birmingham, who created the ideal research environment, with various assistances from other researchers as well as the research team. Loads of thanks for all the author's PhD colleagues in and out our everyday office for a supportive and delightful lifestyle.

Also, thanks to the projects that supported the academic activities during the author's research journey. The author would like to acknowledge the supports by the WINERCOST COST Action TU1304, the AEOLUS4FUTURE ITN Network, and the IGI Global Challenges Funding Scheme of the University of Birmingham.

The author extremely grateful to his parents for their love, caring, believe and sacrifices for educating and preparing for the author's future life. He is very much thankful to his love, Dan, for her love, understanding and continuing support to complete his research work in despite of their distance extended over mountains and seas.

Contents

LIST OF FIGURES I

LIST OF TABLES IX

NOMENCLATURE X

1 INTRODUCTION 1

1.1 Background and Research motivation 1

1.2 Aim and Objectives 2

1.3 Layout of thesis 3

2 LITERATURE REVIEW 5

2.1 Wind energy industry 5

2.2 Historical case study of wind turbine collapse 9

2.2.1 Overview 9

2.2.2 Wind turbine tower collapse case studies and buckling types 20

2.3 The development of buckling research 28

2.3.1 Overview 28

2.3.2 Buckling paths 32

2.3.3 Cylindrical shells under axial compressive load 36

2.3.4 Geometry Imperfections 38

2.3.5 Energy methods on buckling analysis 44

2.4 Concluding remarks 47

3 CLASSICAL SHELL BUCKLING ANALYSIS 48

3.1 Buckling problems in columns and plates 48

3.2 Geometries and curvatures of cylindrical shells 51

3.3 Stress and strain in axially compressed cylindrical shells 60
3.3.1 Basic relations for shells under axial compression 60
3.3.2 The eigenvalue calculation in linear buckling 62
3.4 Stress and strain in cylindrical shells under bending moment 65
3.5 Stress and strain in cylindrical shells under combined compression and bending 70
3.6 Geometry imperfections in buckling calculation 77
3.7 Concluding remarks 82
4 NON-CLASSICAL BUCKLING ANALYSIS AND ENERGY METHODS 84
4.1 Equations of shell structures 84
4.2 Strain energies on cylindrical shells 92
4.3 Combined bending moment and axial load on cylindrical shells using energy methods 98
4.4 Concluding remarks 102
5 NUMERICAL SIMULATIONS 103
5.1 Finite element method 103
5.1.1 The concept of finite element method 103
5.1.2 The original wind turbine structure 104
5.1.3 Shell elements 107
5.1.4 Eigenvalue buckling prediction, geometry imperfections and the Riks method 108
5.2 Applied external loads on shell section 114
5.3 Concluding remarks 120
6 NUMERICAL RESULTS 121

6.1 Modelling details 121
6.2 Buckling eigenmodes in linear analysis 125
6.3 Buckling under axial compressions 129
6.3.1 Validation of axial compression buckling analysis 129
6.3.2 Buckling behaviour according to different shell lengths 131
6.3.3 Buckling behaviour according to different shell thicknesses 136
6.4 Pure bending buckling analysis 137
6.4.1 Bending behaviour for different shell lengths 137
6.4.2 Bending behaviour for different shell thicknesses 142
6.5 Buckling analysis under combined loading conditions 145
6.5.1. The typical buckling induced failure under combined loading conditions 145
6.5.2 Buckling progression under different loading conditions 146
6.5.3. Buckling development for different shell lengths 149
6.5.4. Buckling behaviour analysis considering energy – curvature relations 151
6.5.6. Buckling development for different shell thickness 158
6.5.7. Bending – compression ratios and imperfections 159
6.6 Concluding remarks 163
7 CONCLUSIONS AND RECOMENDATIONS 164
APPENDIX A 171
MATLAB code relating to Section 6.2 171
The buckling load validation of equations in MATLAB 171
APPENDIX B 174

MATLAB code relating to Section 6.2 174

The solving approach by finite-difference method in MATLAB 174

REFERENCES 177

LIST OF FIGURES

Figure 2.1. Historic development of total installations (GWEC, 2020a). 7

Figure 2.2. The installation outlook 2020-2024 (GWEC, 2020a). 7

Figure 2.3. Market by country, 2019 (GWEC, 2020a). 8

Figure 2.4. European operational facilities by country and number of facilities by component (WindEurope, 2020). 9

Figure 2.5. Number of incidences of wind turbine failure from 1996 to 2019 (CWIF (2020a). 11

Figure 2.6. Percentages of accident reasons (Ma et al., 2019). 12

Figure 2.7. A Bathtub Curve of Failure Rate versus Time (Gintautas and Sørensen, 2014). 18

Figure 2.8. Representative structural failure of wind turbines caused by Usagi (Chen and Xu, 2016). 24

Figure 2.9. On-site photos of wind turbine collapse cases: (a), collapse photo and FEM simulation results in the case of Typhoon Maemi (Ishihara et al., 2005b); (b) (c), in Evia, Greece (thestructuralengineer.info, 2020); (d) in Saxony, Germany, 2017 (PEI, 2017); (e) in Montreal, Canada (NationalPost, 2016). 25

Figure 2.10. Typical buckling behaviours : (a) Buckled tanks at Wente Brothers, California, USA (Bushnell, 1981); (b) laminated composite cylindrical tube under axially compressive load, (Degenhardt et al., 2012); (c) buckled thin unstiffened cylindrical shell under axially compressive load, (Horton and Durham, 1963); (d) elliptical cross section tube under axial compression, (Chan et al., 2010); (e) aluminium shell with internal pressure under axial compression, (Harris et al., 1957); (f) spirally welded large tubes under bending load, (Reinke

et al., 2014); (g) cylindrical tank buckling due to internal vacuum (De Paor et al., 2012). 29

Figure 2.11. A typical load–end shortening curve of a thick-walled tube shell, which demonstrates a complex elastic–plastic buckling path under axial compressive load; the radius-thickness ratio is 10–20 (Edlund, 2007). 33

Figure 2.12. Multiple types of buckling behaviours for a thin-walled cylindrical shell under compressive load (Ma et al., 2020) 33

Figure 2.13. load–end shortening curves of perfect (a) and imperfect (b) cylinder (Edlund, 2007), in the axially-compressed buckling processes. Buckling-mode jumping can be observed in (b). 35

Figure 2.14. Experimental data based on cylindrical shell knock-down factor according to the radius-to-thickness ratio, R/t, under axial compressive loads, with a selected range of R/t from 0 to 1800 (Seide et al., 1960, Peterson et al., 1968). 37

Figure 2.15. The 'Koiter circle', where (a) represents three points of classical buckling modes, A, D1, and D2 (Calladine and Sanders, 1984), and (b) cylindrical shells under axial compression, Koiter circles in the ξ–η dimensionless wavelength space (Shakouri et al., 2014). 39

Figure 2.16 The influence of imperfection parameters on buckling capacities, where (a) $d = 3.2\sqrt{Rt}$ and (b) $d = 4.5\sqrt{Rt}$. d represents the side length of imperfection square, and a represents the imperfection amplitude in these figures (Edlund, 2007, Esslinger and Geier, 1977). 40

Figure 3.1. Buckling behaviours of pin-ended rods under axial concentrate loads: (a) initially straight rod; (b) buckled rod; (c) multiple buckling paths on a straight rod; (d) no bifurcation point along the buckling path on an initially crooked rod. 49

Figure 3.2. Angular displacements for a flat plate. (a) A rectangular plate element. (b) Shear distortion. (c) Tensile distortion. 52

Figure 3.3. Loads on a shell element 54

Figure 3.4. Assumed circumferential shell element deformation 55

Figure 3.5. A random shell element in Cartesian coordinate system. 57

Figure 3.6. (a) Section ovalisation of a bending cylindrical shell; (b) the resulting effect of combined loads; and (c) the strip of a highly stressed shell segment (Ma et al., 2020). 67

Figure 3.7. Loading conditions of undeformed and ovalised shell cross-sections, (a) tubular shell cross-section without ovalisation and (b) ovalised tubular shell cross-section (Ma et al., 2020) 69

Figure 3.8. (a) Forces applied on a turbine tower shell tube; (b) four stress resultants that may be applied to the cylinder shell; (c) coordinates and twisting moment if considered. 71

Figure 3.9. Assumed basic buckling shell deformation function under axial compressive load (Ma et al., 2020). 73

Figure 3.10. Experimental results of axially compressed cylindrical shells (after Harris et al. (1957) by Teng and Rotter (2006)). 77

Figure 3.11. (a) Load-end shortening curves; (b) postbuckling modes in different buckling progressions. Axial compression applied to cylinder shells, reproduced by Teng and Rotter (2006), based on the data from Yamaki (1984). 78

Figure 3.12. An illustration of displacements on a shell surface in the prebuckling stage, based on the assumption by sinusoidal functions. 79

Figure 3.13. The relationship between different imperfection amplitudes and bifurcation points in axially compressive cylinders (reproduced by Teng and Rotter (2006) based on data produced by Yamaki (1984)). 80

Figure 4.1. Energy state fields of stability analysis (Ma et al., 2020). 86

Figure 4.2. A differential element of a general shell section. 88

Figure 5.1. The illustration of conventional versus continuum shell elements by Abaqus (2014). 107

Figure 5.2. The 4-node element and the S4R element. 108

Figure 5.3. Modal imperfection shape combination of the cylindrical shell; the result is shown in a scale factor of 100 (Ma et al., 2020). 110

Figure 5.4. Relationship between buckling stress reduction and amplitude of axisymmetric imperfections. (Reproduced by Teng and Rotter (2006)). 110

Figure 5.5. The relation of imperfect amplitudes to the critical buckling modes. 111

Figure 5.6. The snap-through and snap-back phenomenon in the postbuckling stage for a cylinder. 112

Figure 5.7. The arc-length iteration in the postbuckling path for a cylinder. 113

Figure 5.8. The model of the NREL 5 MW wind turbine and wind grid in ASHES. 115

Figure 5.9. Results of NREL 5 MW wind turbine under 12 m/s wind. (a) Moment magnitude – end shortening curve. (b) Strain energy curve. (c) Maximum normal stress. (d) Moment magnitude. (e) Shear stress. 115

Figure 5.10. Results of the NREL 5 MW wind turbine under 30 m/s and 70 m/s wind. (a) Moment magnitude – end shortening curve in 30 m/s wind. (b) Moment magnitude – end shortening curve in 70 m/s wind. (c) Shear stresses

in 30 m/s and 70 m/s winds. (d) Moment magnitudes in 30 m/s and 70 m/s winds. (e) Strain energy curves; the magnitude of the 70 m/s curve is far above the 30 m/s curve, which is very close to the axis due to the unit of vertical coordinate is kJ. 117

Figure 6.1. An example of meshing for 20.0 m shell section. 124

Figure 6.2. Imperfection implement in ABAQUS via keyword editor, based on linear buckling modal calculations. 125

Figure 6.3. An illustration of the first three modals of the 20 m shell section at 30 mm thickness. The combination of modal shapes resulted in the asymmetric geometry imperfection. 126

Figure 6.4. (a) The feathering of deviations of surface displacement according to the initial perfect surface, ready for curve fittings. (b) The curve fitting example by Fourier function with eight terms. 127

Figure 6.5. The curve fitting example by the sum of sinusoidal functions with two terms. The displacement function f(x) shares the convertible form with Equation (3.82); coefficients ai, bi were shown by the right side. 127

Figure 6.6. Linear buckling load in ABAQUS vs. buckling load using linear theory, in accordance with cylinders of various wall thickness. 129

Figure 6.7. Imperfect shell knockdown factor of simulation results, compared to experimental results conducted by Peterson et al. (1968), over a selected range of R/t from 0 to 150 (Ma et al., 2020). 130

Figure 6.8. Shell (9 m at 24 mm) surface deformation and stress distribution under axial compressive load (Ma et al., 2020). 131

Figure 6.9. Shell (20 m at 24 mm) surface deformation and stress distribution under axial compressive load. 132

Figure 6.10. Shell (20 m at 24 mm) extreme fibre wavenumber change under axial compressive load. 134

Figure 6.11. Shell (20 m at 24 mm) circumferential fibre curvature change under axial compressive load. 134

Figure 6.12. Shell (20 m at 24 mm) circumferential fibre curvature change under axial compressive load. 135

Figure 6.13. Shell (20 m and 9 m at 24 mm) axial load–end shortening curves under axial compressive load. 136

Figure 6.14. Shell (20 m at 36 mm) surface deformation and stress distribution under axial compressive load. 137

Figure 6.15. Shell (20 m at 30 mm) surface deformation and stress distribution under the pure bending moment. 138

Figure 6.16. Shell (9 m at 30 mm) surface deformation and stress distribution under the pure bending moment. 138

Figure 6.17. Shell (20 m at 30 mm) extreme fibre wavenumber change under bending. 139

Figure 6.18. The curve fitting example by the sum of sinusoidal functions with (a) eight terms and (b) three terms. (a) Contains two points on boundaries while (b) omitted boundary conditions observed a better fit with less coefficient terms. The displacement function f(x) shares the convertible form as Equation (3.82), coefficients were shown as well. 140

Figure 6.19. The cut-out view of the circumferential curvature change on 20 m at 30 mm shell under a bending moment. 142

Figure 6.20. Shell (20 m at 24 mm) surface deformation and stress distribution under the pure bending moment. 143

Figure 6.21. The cut-out view of circumferential curvature change on the 20 m at 24 mm shell under a bending moment. 144

Figure 6.22. Shell (20 m at 24 mm) stress distributions and deformations on the compressive side of the cylindrical shell in 11 increment steps, and the view of tension side showing a flattening effect (Ma et al., 2020). 146

Figure 6.23. Shell (20 m at 24 mm) longitudinal surface displacement under axial compressive load, (scale factor = 5). 147

Figure 6.24. Shell (20 m at 24 mm) longitudinal surface displacement under the bending moment (scale factor = 5). 148

Figure 6.25. Shell (20 m at 24 mm) longitudinal surface displacement under combined loading, (scale factor = 5). 148

Figure 6.26. Shell (9 m at 24 mm) stress distributions and deformations on the compressive side of the cylindrical shell in 10 increment steps, and the view of the tension side showing a flattening effect. 150

Figure 6.27. Shell (9 m at 24 mm) surface deformation and stress distribution under the pure bending moment. 151

Figure 6.28. Shell (9 m at 24 mm) strain energy magnitudes along the normalised longitudinal length at typical increment steps, under combined loads. 152

Figure 6.29. Shell (24 m at 24 mm) strain energy magnitudes along the normalised longitudinal length at typical increment steps, under combined loads. 152

Figure 6.30. Shell (9 m at 24 mm) strain energy magnitudes along the normalised longitudinal length in typical increment steps, under the pure bending moment. 153

Figure 6.31. Shell (20 m at 24 mm) section curvature along the normalised longitudinal length in typical increment steps, under the pure bending moment. 154

Figure 6.32. Partially enlarged shell (20 m at 24 mm) section curvature along the normalised longitudinal length at early increment steps, under the pure bending moment. 155

Figure 6.33. Shell (20 m at 24 mm) section curvature along the normalised longitudinal length under combined loads, (a) at typical increment steps and (b) partially enlarged at early increment steps. 157

Figure 6.34. Shell strain energy magnitude along the normalised longitudinal length under combined loads, at typical increment steps: (a) 9 m at 24 mm shell and (b) 24 m at 24 mm shell. 159

Figure 6.35. Shell (9 m at 36 mm) stress distributions and deformations on the compressive side of the cylindrical shell in 10 incremental steps, and a view of the tension side showing a flattening effect. 159

Figure 6.36. The buckling types observed in collapsed wind turbine towers on-site. The wavenumbers can be identified as 3 and 4 (CWIF, 2020). 160

Figure 6.37. The curves of the bending/compression ratio to buckling load factor for shell structure, under combined loading conditions with different wall thickness. 160

Figure 6.38. Load–rotation curves of 4 shell models of 24 mm thickness in different lengths. 161

Figure 6.39. Load–rotation curves of 4 shell models of 36 mm thickness in different lengths. 162

Figure 6.40. Load–end shortening curves of 20 m 24 mm shells with and without initial geometry imperfection. 162

LIST OF TABLES

Table 1.1. Detailed typical failure incidence list from 2000 to 2019, filtered from the report by CWIF (2020b). 12

Table 1.2. Main causes of tower collapse, from 1996 to 2016, filtered from the report by CWIF (2020b). 16

Table 3.1 Shell geometrical tolerance in selected codes. 81

Table 5.1 Basic information on the NREL 5 MW tower. 105

Table 5.2 Basic information about the NREL 5 MW tower, secondary bottom section. 106

Table 5.3. Model geometry size in the FEM analysis. 106

Table 6.1. Mesh sensitivity analysis results. 123

NOMENCLATURE

$\boldsymbol{U_T}$	Mean wind speed
U_{10}	10-minute mean wind speed
S_U	Harris spectrum
f_f	Frequency of wind
Λ	Dimensionless buckling load
A	Shell surface area
B	Width of a flat plate
D	Bending stiffness of slabs
EI	Bending stiffness
L	Length of cylindrical shell; characteristic length for wind calculation; length of a flat plate
R	Radius of tubular shell
R_1, R_2	Equivalent radius of ovalised tubular shell
V	Vector of unknown nodal displacements
X, Y, Z	The Cartesian coordinate note
l	Longitudinal half-wavelength
m	Factor of the membrane part of the structural critical load, lateral wavenumber
n	Wavenumber in vertical direction
r	Radius of shell element
s	Arc length of shell element along the circumferential direction
t	Shell element thickness
$\bar{u}_x, \bar{v}_\theta$	the values of coordinate on the mid-surface of shell
θ	Angular of selected shell element, rad
a, a_n, b_n, c_n, d_n	Constants depend on loading conditions
b	Circumferential half-wavelength

$\overrightarrow{r_0}$, $\vec{b}$, $\overrightarrow{b_+}$, $\vec{r}$	Energy components, in the format of vector on energy field
Π	Total potential energy
ΔK_i	Changes of local Gaussian curvature
K	Local Gaussian curvature
K_T	Tangent stiffness matrix
K_e	Linear elastic stiffness matrix
K_{gl}	Initial geometrical stiffness matrix, linear
K_{vl}	Initial displacement matrix, linear
K_{gn}	Initial geometrical stiffness matrix, nonlinear, quadratic
K_{vn}	Initial displacement matrix, nonlinear, quadratic
K_x, K_y, K_{xy}	Curvature components
κ_1, κ_2	Curvature changes
x_x, x_y, x_{xy}	Curvature variations
$x_{x\theta}$	Distortion rate of the shell cross section
λ_b	Bending part of the structural critical load factor
λ_{cr}	Structural ideal critical load factor
λ_m	Membrane part of the structural critical load factor
λ^*	Lowest eigenvalue
M	Bending moment
M_θ	Bending moment according to longitudinal axis
M_x	Bending moment on the radial plane
M_μ^e	Maximum bending moment on the tubular shell
N_x, N_y, N_{xy}	Compression loads
N_{cr}	Critical buckling load
N_θ	Circumferential load
x	Length of shell element along the longitudinal direction
u, v, f	Displacements in the x, y, and z direction
f_x, f_y	Body forces in respective direction

P_r	Radical compression load
P_x	Longitudinal compression load
Q_x	Shear force on the plane perpendicular to x axis
ν	Poisson ratio
ε_x, ε_θ	Normal strains along x-axis and radial direction
ε_{x_2}, ε_{θ_2}	Mid-surface axial strains after buckling
ε_{x0}, ε_{y0}, γ_{xy0}	Initial strains in the x, y directions, initial shear strain
$\varepsilon_{x\theta}$, $\varepsilon_{y\theta}$, $\gamma_{xy\theta}$	Strains in the x, y directions at angle θ, shear strain at angle θ, rad
h_i	Roots of polynomial function
C_i	Constants of integration
α	Buckling knock down factor of imperfect shell
β	A parameter of the simplified polynomial function; ring displacement parameter on rotation
e	ring displacement parameter in radius direction
φ	The stress function
U, U_b , U_m, U_s	Stain energy, bending energy, membrane energy, strain energy of slab
δ_U, δ_{U_m}, δ_{U_b}	Internal virtual work, virtual work due to membrane strain energy, virtual work due to bending strain energy
σ	Stress, normal stress
δ_w	External virtual work
F_{Ci}	Equivalent concentrated compression force
F_t	Equivalent concentrated tension force
r_{Ci}, r_t	Length of equivalent compressive uniform load, length of equivalent tensile uniform load

1 INTRODUCTION

1.1 Background and Research motivation

Aeolus (Αίολος in Greek) is a symbolic hero in Greek mythology who keeps the winds, especially those of the storms, inside the cave on his floating island of Aeolia. Homer narrates the tale of Aeolus in his epic poem, *The Odyssey* (Homer, 2015), in which he alludes to the respect and desire human beings have for the natural resource of the wind. After harnessing the wind in various ways for thousands of years, and following the great leap in electromagnetism development, we have now found the best way to use wind, by harvesting it and transforming it into a convenient format for energy storage and consumption: electricity. Wind turbines using multidisciplinary modern technologies have become a tool for harvesting wind energy efficiently over the last four decades.

In the hunt for more wind energy, we have built higher towers. Stochastic winds, sometimes viewed as extreme winds, are given 'beautiful' names by humans, such as typhoon, hurricane, tornado. However, these beautiful forces can have negative consequences: when this kind of fierce power acts on the modern tower, the tower unfortunately sometimes collapses. The primary question of tower collapse is buckling, which is a major topic that we still do not thoroughly understand. Theories, tests and hypothesises have been developed for buckling, and as W. R. Hamilton said, 'we must gather and group appearances, until the scientific imagination discerns their hidden laws, and unity arises from variety; and then from unity we must rededuce variety, and force the discovered law to utter its revelations of the future'.

We are now closer to a scientific explanation that will reveal the hidden laws of buckling compressively, using powerful apparatus. One of these should not be ignored: the energy method. We are lucky to stand on shoulders of giants, who previously discovered one of the fundamental truths of nature, that energy is always in balance.

Therefore, using state-of-the-art methods, we are able to continue the research into piece of the hidden laws of buckling, in order to better understand the harvesting of wind energy; we must keep in mind an appreciation of buckling theories, and utilise powerful energy methods and computational numerical simulations. After many years of research, we can now present the 'Buckling Analysis of Tubular Wind Turbine Towers by means of the Applied Energy Method'.

1.2 Aim and Objectives

The aim of this study is to find a method of energy expression based on classical buckling theories for the buckling collapse analysis of wind turbine towers. Based on previous studies, this research focuses on a buckling path study of a cylindrical shell, which is the essential structure of towers for modern onshore wind power plants. In order to achieve this aim, the following objectives were defined:

1. To carry out the wind turbine tower collapse case study, to summarise the most severe tubular wind tower collapse types and reasons, and to conclude the typical shell buckling modes for the following study.
2. To explore the energy expression for tubular shells under a combined axially compressive load and bending moment; to deduce the classic and non-classic buckling equations containing geometric parameters.
3. To obtain the variational form of energy expressions, and to obtain the dimensionless equilibrium equations about the energy expression, seeking stationary solutions and buckling predictions to understand the buckling path from the perspective of the relations between strain energy–curvature.

4. To simulate a set of cylindrical shells modelled by the Riks method via ABAQUS, with step-by-step increment iterations, and to elaborate the prebuckling–transient–postbuckling processes, revealing the effects on buckling types by the interactions between external wind load and the initial gravity loads.

5. To estimate the effect of R/t ratios and L/R ratios on the buckling stability of towers in typical geometry configurations, and to summarise their buckling eigenvalues and modes.

1.3 Layout of thesis

This thesis is organised into seven chapters.

Chapter 1 presents the project background regarding wind turbine towers and introduces the aims, objectives, and the structure of the thesis.

Chapter 2 comprises a detailed literature review in the field of wind turbine towers, which includes two main parts: historical case studies examining wind turbine tower collapse, and the buckling theories for wind turbine tower buckling analysis. The typical buckling types have been concluded from historical case study, which provided the guide directions of buckling forms for the buckling analysis in the latter sections.

Chapter 3 discusses the classical buckling methodology used for buckling analysis under axial compression, bending moment, and combined loading conditions. The linear buckling analysis, geometry and curvature calculations, eigenvalue calculations and overall governing equations have been introduced and derived in this chapter.

Chapter 4 concerns the application of non-classical buckling theories and energy concepts to the shell buckling analysis. The nonlinearity of displacement has been introduced, and energy equilibriums and derivation forms have been deduced via the expressions of curvature and stress–strain relations.

Chapter 5 discusses the numerical simulation methods and settings for finite element analysis. The modelling settings in ABAQUS are explained in this chapter, and the Riks method is chosen as the calculation algorithm. The selected prototype of a wind turbine tower model is simulated in the software ASHES to provide reference data for later shell element analysis in ABAQUS.

Chapter 6 presents the full results of buckling analysis in ABAQUS and discusses the intended outcomes. The FEM results have been compared to theoretical analysis and ASHES solutions, and the effects of a combined load on buckling behaviour have been investigated.

Chapter 7 summarises the conclusions of the research and proposes relevant discussions based on previous studies.

2 LITERATURE REVIEW

2.1 Wind energy industry

Wind – a gift given to human beings by nature – is an energy source that may have been harvested since the first supposed windmills in Egypt, three thousand years ago (König, 1976). However, the first reliable record of windmills comes from the year 644 A.D., at the Persian-Afghan border (Hau, 2013). By constructing windmills and windwheels, humans from these ancient times were able to convert natural wind energy into the power needed for water pumping and grain milling. Finally, in the 20th century, wind power again emerged as the best choice for the production of necessary power, in the form of electricity (Burton et al., 2001). The story, of the evolution of windmills, windwheels and wind turbines, is a long one, moving from the vertical-axis windmill, through post and hollow-post windmills, to the tower windmill, the Dutch windmill, the Paltrock mill, and the typical American Halladay wind turbine (Hau, 2013). The materials used in the construction of wind turbines have also evolved, from bamboo, stone, wood, and bricks, to the steel, concrete and composite materials of recent decades. In 1882 in New York, a milestone in human history was reached when the world's first wind turbine for electricity was built; it had a power output of 500 kW, and was followed two years later by another wind power plant in Berlin (Golding and Harris, 1976).

Since that time, thousands of ideal and practical designs for wind turbines have been drawn, and the key parameters (power output, height, and rotor diameter) have multiplied tens of times. For example, the first large wind turbine in the US – the Smith-Putnam, in 1941 – had a power output of 1250 kW and a rotor diameter of 53.3m

(Putnam, 1974). By the year 1988, the prototype wind turbine LS-1, by Windenergy Group, had reached a power output of 3.0 MW, with a rotor diameter of 60m and two blades (Hau, 2013). The development of the relevant engineering technology is ongoing; this year, the largest onshore wind power plant achieved 5.6 MW; this was the model V162/5.6MW by Vestas, who produce a range of large-diameter steel towers (LDST) for their large turbines, with heights of 148, 155 and 166 metres (WindPower, 2020). Meanwhile, the largest offshore wind turbine – the Haliade-X by GE Renewable Energy – has attained the highest power efficiency, at 63%. This turbine is rated at 12 MW, with a 260m tower height and a 220m rotor diameter (GE-RenewableEnergy, 2020). The Haliade's combination of long rotor blades and a high supporting tower section means that up to 67 GWh of gross annual electric energy could be generated using just one turbine.

Wind energy plays a decisive role in global renewable energy development. The Global Wind Energy Council (GWEC) reported that in 2019, 60.4 GW of wind energy capacity was installed globally, which was a 19% increase from 2018; total capacity for wind energy globally is now over 651 GW (GWEC, 2020a). The booming trend of total global wind power installations can be seen in Figure 2.1. Offshore wind power plants have accounted for a higher percentage of the total since the year 2007, and achieved 29GW in 2019; meanwhile, onshore wind turbines continued to occupy the dominant position, reaching 621GW in the same year. In 2020, there were plans to install 71.3 GW of wind power, despite the impact of the COVID-19 crisis, providing an essential contribution to economic recovery and representing an astonishing 18% increase from 2019 (GWEC, 2020b). The new installation outlook reported by GWEC is shown in Figure 2.2; the slower annual capacity growth rate of 4.0% is mainly due to the large accumulated wind power capacity compared to previous years (GWEC, 2020a).

As shown in Figure 2.3, China had the leading percentages of new and total onshore installations, followed by the USA. European countries, who own abundant natural wind resources, progressed to a certain extent.

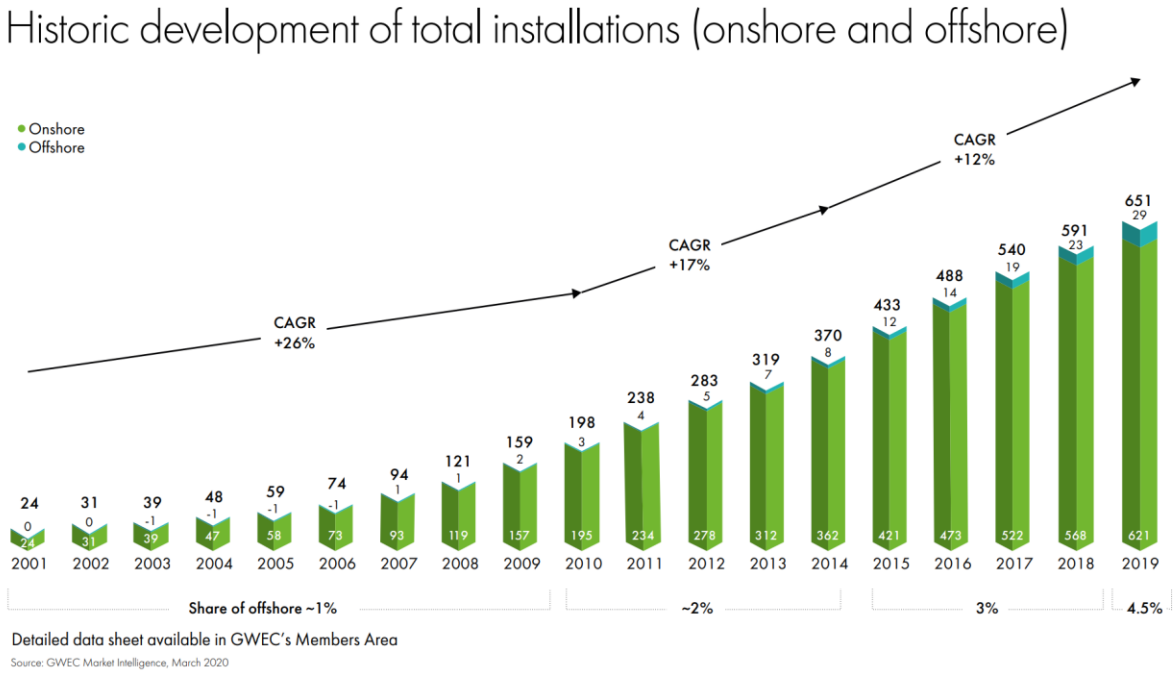


Figure 2.1. Historic development of total installations (GWEC, 2020a).

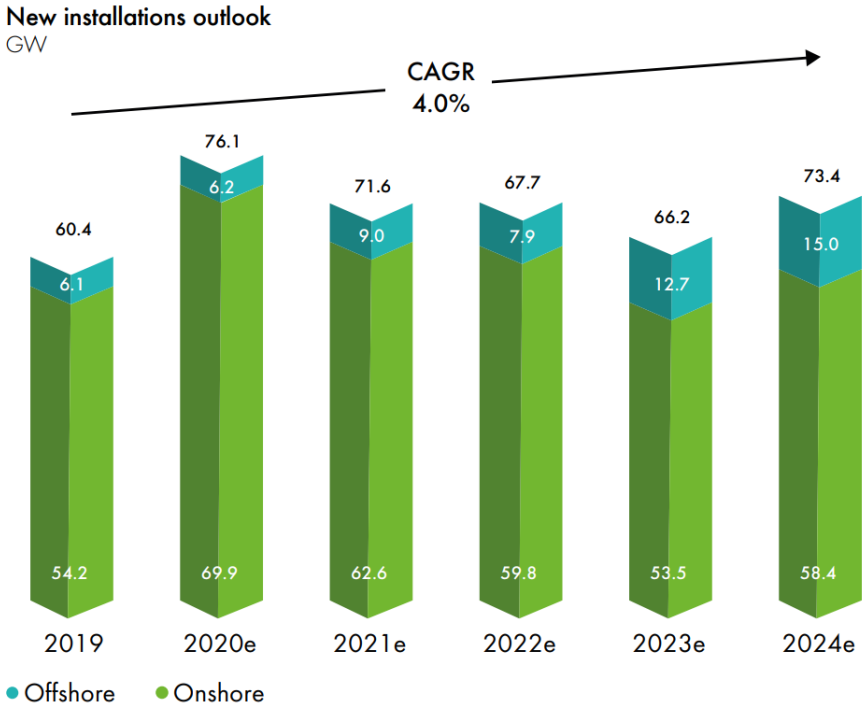


Figure 2.2. The installation outlook 2020-2024 (GWEC, 2020a).

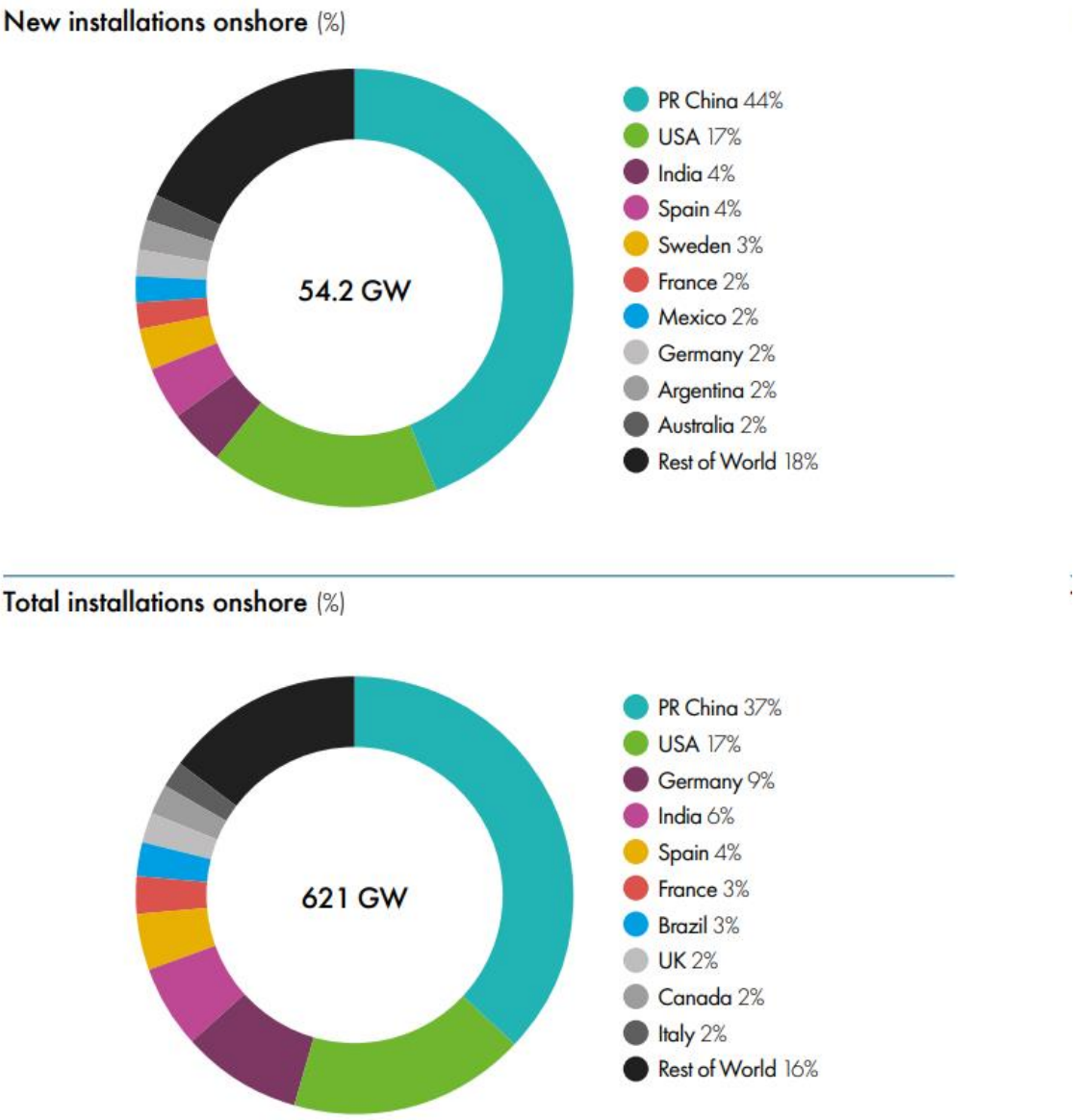


Figure 2.3. Market by country, 2019 (GWEC, 2020a).

In Europe, wind energy is now the cheapest form of new power generation, surpassing coal as the primary source, and accounting for 44% of all new power installations (WindEurope, 2020). Among European countries, Germany has the highest number of operational facilities, at 82, followed by Spain at 41; the UK is in 8th position, with 8 facilities, as shown in Figure 2.4 (WindEurope, 2020). Figure 2.4 also shows that on the component side, turbine towers occupy the first position, reflecting their fundamental role in the wind turbine industry.

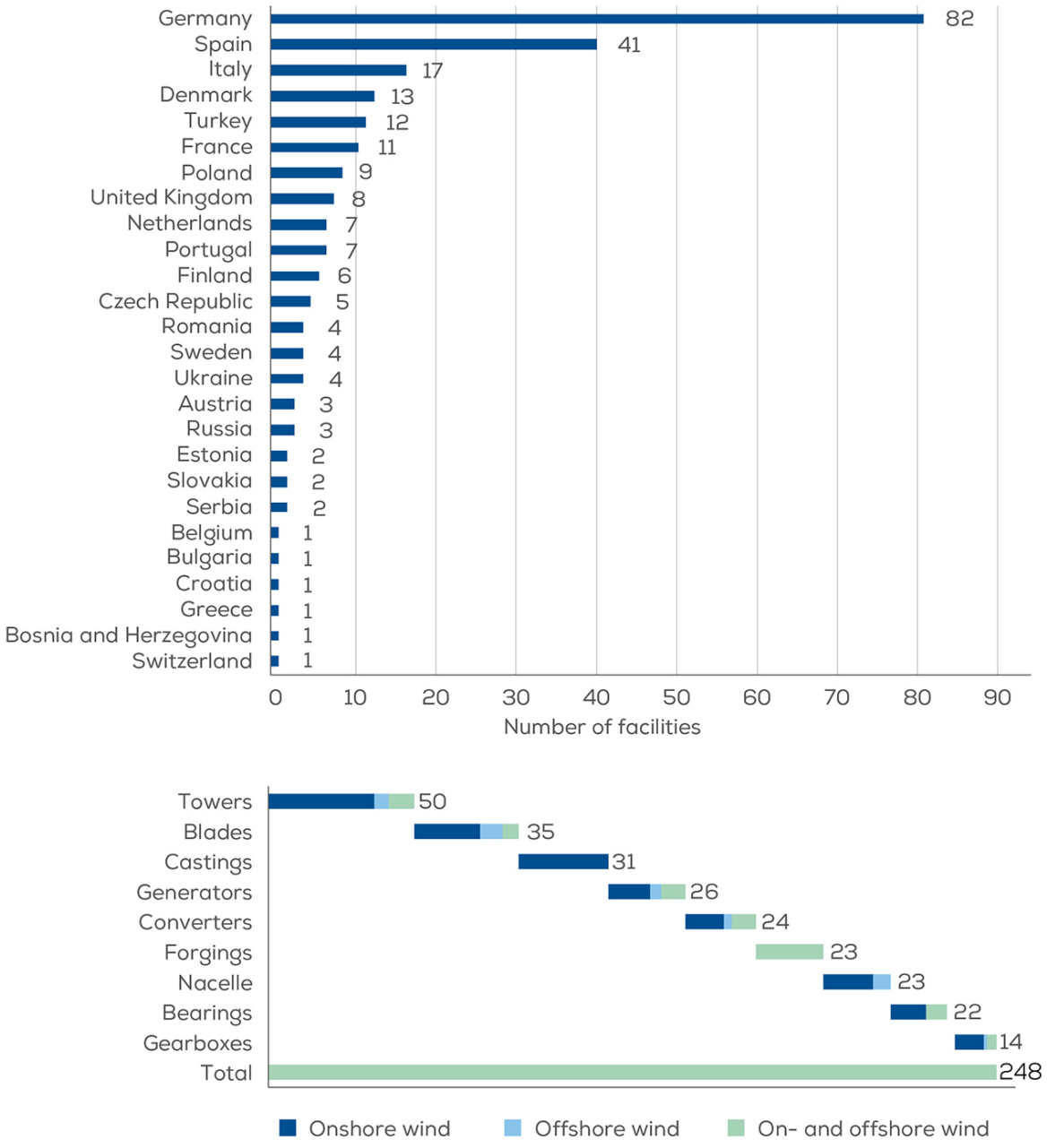


Figure 2.4. European operational facilities by country and number of facilities by component (WindEurope, 2020).

2.2 Historical case study of wind turbine collapse

2.2.1 Overview

The high demand for wind energy requires higher productivity from wind power plants, as well as accelerated development within the engineering industry. The

leading concept for increasing the size of the wind energy harvest is the design of the aerodynamic characteristics of rotors and blades. Previously, the main method of increasing rotor performance, despite the improvements in pitch/yaw optimisation technology, was to lift the altitude of the axis of the rotor; in other words, to build a taller tower to allow the blades to be propelled by a higher and steadier wind. The hunt for better wind resource has meant that these towers are now up to 200 m high, and are in the capacity class of multi-megawatt. The efficiency of power conversion increases significantly both with the enlargement of the rotor coverage area and with the availability of more advanced optimisation, design and construction techniques. The supporting structures, however – towers – still face various challenges; these range from promoting buckling and fatigue resistance, to the application of practical mitigation measures against multiple hazards such as fire, lightning, earthquakes, and extreme winds. The pursuit of higher wind power generation percentages in turn increases the potential hazard of turbine collapse, and this is reflected in the damage statistics (Ma et al., 2019, CWIF, 2020a).

The current study involved investigating historical cases to identify common causes of wind turbine tower failure, and was based on a detailed scrutiny of recorded cases in the past decades. This is expected to enhance our understanding of collapse mechanisms, and to enlighten the research path to address potential mitigation approaches. Owing to the dominance of onshore wind turbines, this investigation concentrated strictly on cases of tower collapse in modern, onshore, mega-watt-class wind turbines, which are built up with cylindrical steel shell sections.

A non-negligible number of wind turbine failure cases is still being recorded each month, with an accumulation of incidence occurrence over the past decades. The Caithness Windfarm Information Forum (CWIF) reported that from October 1980 to September 2020, 2744 accidents were recorded, among which there were 154 fatal incidences (CWIF, 2020a). In Figure 2.5, an overall increasing trend can be observed in line with the progress of the turbine industry, although there are year-on-year

fluctuations. It is to be expected that the more turbines that are built, the more cases there are recorded; however, the average of 49 cases per year during the period 2000-2004 increased to 109 in 2005-2009, to 163 in 2010-2014, and eventually, in the 2015-2019 period, to 210 cases per year (CWIF, 2020b).

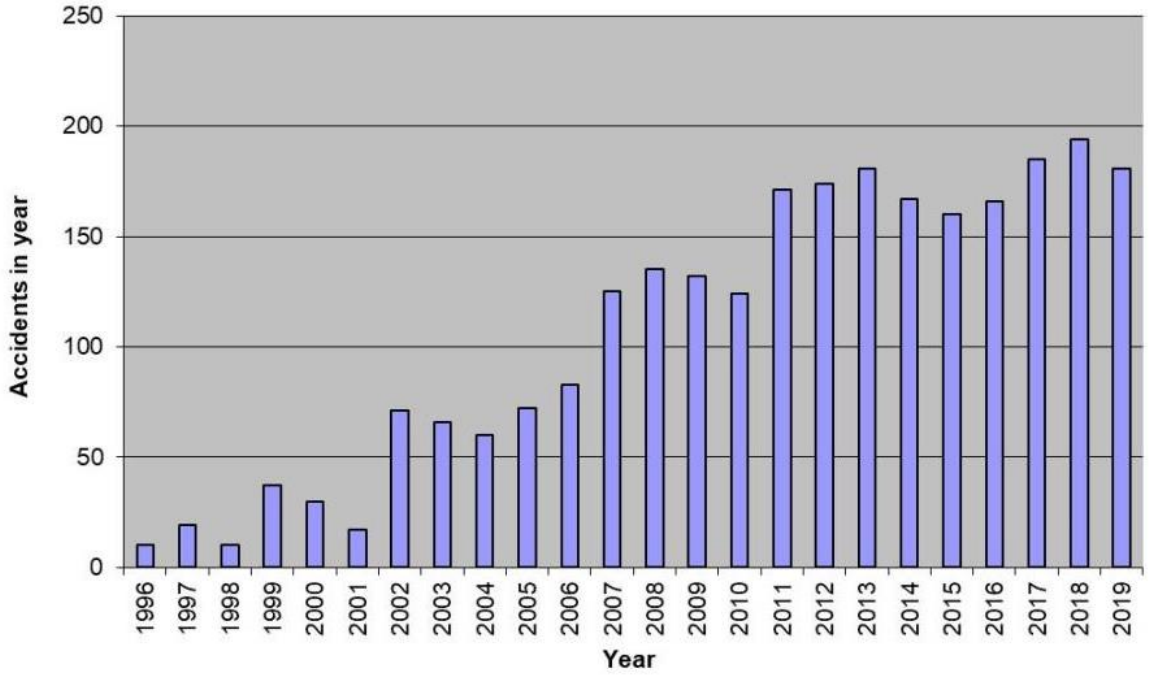


Figure 2.5. Number of incidences of wind turbine failure from 1996 to 2019 (CWIF (2020a).

Based on the 1999 cases from 1996-2016, Figure 2.6 shows that structure failure accounts for 9.2% of the total wind power plant accidents, while blade failure accounts for the largest number of incidences, with 17.9%. Fire, mostly associated with lighting and mechanical failures, comes in second at 14.5%. Tower collapse falls into the category of structure failure; in most such cases, the resultant turbine damage means that it is impossible to maintain power generation without costly repairs (Ma et al., 2019).

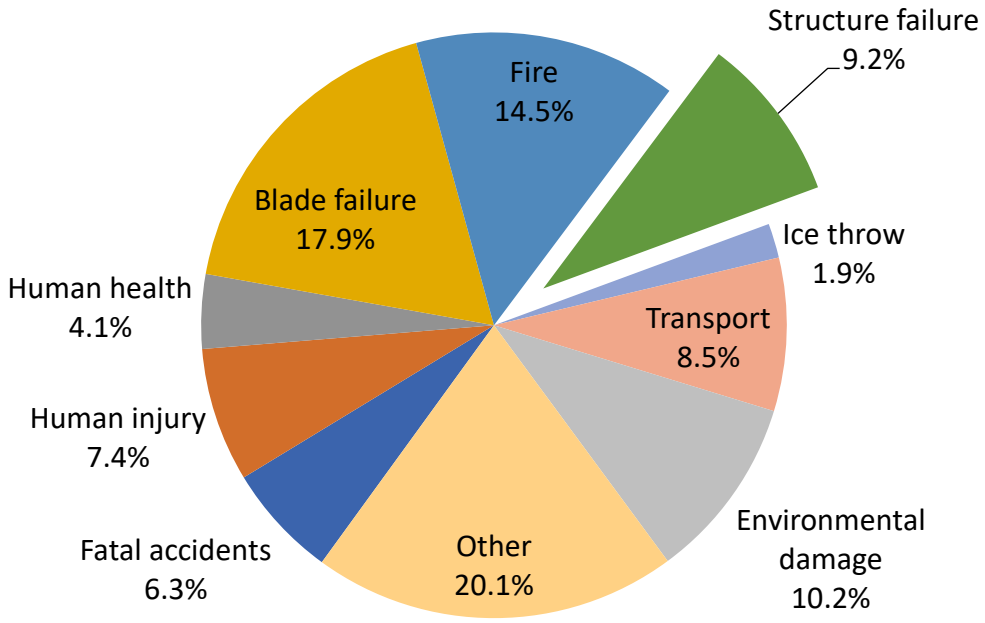


Figure 2.6. Percentages of accident reasons (Ma et al., 2019).

The detailed list of accident cases shown in Table 1.1, filtered from the full 2020 list from CWIF (2020b), contains 75 entries for the period 2000-2019. Most of the wind turbines from before the year 2000 are not in the multi-megawatt class. Turbines with power capacity less than 300 kW, and non-steel-tubular towers, have also been omitted.

No.	Date	Country	Turbine Character	Cause
1	20/01/2000	Germany	Sudwind S 46/600 kw	Lightning strike
2	10/02/2000	Germany	Enercon E32	Concrete damage
3	15/02/2000	Holland	Lagerwey	Storm
4	11/03/2000	Holland	Newinco in Rhenen,30m tower	Storm
5	09/12/2000	Spain	GamesaEólica G-47 660KW	Blade struck
6	15/01/2001	Spain	GamesaEólica G-47 660KW	Unidentified
7	28/01/2002	Germany	Windrad HSW 250 28m tower	Storm
8	15/05/2002	USA	WTC	Blade struck
9	27/10/2002	Germany	GET 41a 600kW Hub height 70m, rotor diameter 41m	Storm
10	19/11/2002	USA	Anemometer	Ice storm

11	18/12/2002	Germany	Vestas V80 2.0MW	Faulty Welding
12	28/12/2002	France	600kW, 75m total height	Storm
13	02/02/2003	Germany	Enercon	Fire
14	20/03/2004	France	Lagerwey 300kw 30m high turbine	Storm
15	11/09/2003	Japan	Micon M750/400kW and Enercon E40/500kW	Typhoon
16	01/01/2004	France	Lagerwey 750kw	Storm
17	28/12/2004	USA	1MW wind turbine	Bolts failure
18	06/05/2005	USA	GE Wind 1.5 MW	Unidentified
19	31/10/2005	Holland	Nedwind 500kw, 41m diameter, 40m tower	Unidentified
20	10/01/2006	Holland	Nedwind, 1MW, 55m diameter, 63m tower	Unidentified
21	06/07/2006	Holland	Nedwind	Lightning
22	15/08/2006	China	Hub height 50m, rotor diameter 50m	Typhoon
23	31/10/2006	Holland	Vestas NM 48/750	Fire
24	04/12/2006	France	30m high turbine tower	Strong Wind
25	09/01/2007	Germany	N/A	Fire
26	13/01/2007	Germany	HSW 100	Storm
27	25/08/2007	USA	Siemens 2.3MW	Unidentified
28	22/02/2008	Denmark	Vestas (Nordtank NKT600 - 180/43)	Braking failure
29	24/02/2008	Denmark	Vestas V47 660kW	Bolts failure
30	28/09/2008	China	Tower 62m high, blade length 34m	Typhoon
31	16/10/2008	USA	Zond Z-40-FS	Blade struck
32	23/10/2010	China	Z72-2000	Typhoon
33	16/03/2011	USA	Suzlon S88-2.1 MW	Braking failure
34	07/07/2011	USA	N/A	Storm
35	31/10/2011	Norway	Bonus 2MW	Cracking
36	01/12/2011	UK	N/A	Storm
37	15/03/2013	Japan	38 tonne, 50m tower	Fatigue
38	09/10/2013	China	Total tower height 45m, blade length 22.9m	Typhoon
39	18/07/2014	China	TW1500/77, tower height 75m	Typhoon
40	06/12/2014	Nicaragua	Suzlon S88 2.1 MW	Fire

41	10/12/2014	Germany	60m tower	Bolts failure
42	17/12/2014	USA	GE 1.85MW	Unidentified
43	17/12/2014	Germany	600kW, 70m hub height, 48m rotor diameter	Faulty construction
44	22/12/2015	Brazil	Suzlon S95 2.1MW	Unidentified
45	21/11/2016	USA	152m height	Design defect
46	28/12/2016	Germany	Tacke TW 600, 95m height	Blade imbalance
47	03/01/2017	Germany	1.5MW, 130m height	Blade failure
48	04/01/2017	Germany	Vestas 660kW	Blade failure
49	05/01/2017	Germany	100 metre tall	Structural failure
50	06/01/2017	UK	Repower Systems, 2MW	Fire
51	20/01/2017	UK	Gamesa, 146m height, 160 tonne	Structural failure
52	02/02/2017	UK	Nordex N80 2.5MW, 100m height	Structural failure
53	25/04/2017	Canada	GE 1.6MW, 100m tall	Blade failure
54	03/06/2017	USA	GE 1.7MW XLE	Blade failure
55	13/06/2017	USA	GE 1.7MW, 103m height	Structural failure
56	07/08/2017	Denmark	Vestas V164 9.5MW, 140m height	Fire
57	09/10/2017	Croatia	Vestas 850kW	Storm
58	03/01/2018	Germany	Vestas V39 0.5MW	Storm
59	10/03/2018	Germany	Enercon E115	Blade failure
60	04/05/2018	Canada	Vestas V80 1.8MW	Storm
61	22/05/2018	USA	Gamesa G83 2MW	Fire
62	18/07/2018	Germany	Repower MM 92	Blade failure
63	24/08/2018	Japan	60m tower	Structural failure
64	30/10/2018	Thailand	Vestas 157m high, 3MW V136 turbine	Structural failure
65	10/12/2018	Germany	Kenersys K110, 2.4MW	Blade failure
66	16/12/2018	UK	Gamesa G80-2MW	Blade failure
67	21/02/2019	USA	GE 2.5 - 127	Structural failure
68	18/03/2019	Germany	Prokon P3000/ Amperax A3000	Blade failure
69	22/05/2019	USA	GE 2.4 - 107	Structural failure
70	19/06/2019	Germany	Vestas V80-2MW	Lightning strike
71	05/07/2019	USA	GE 2.5 - 116	Structural failure
72	23/07/2019	Brazil	GE 1.7 - 103	Structural failure
73	16/09/2019	Australia	V136 - 3.6MW	Blade failure

74	18/09/2019	Germany	DeWind D4 48	Structural failure
75	09/10/2019	Germany	NEG Micon NM82/1500	Blade failure

Table 1.1. Detailed typical failure incidence list from 2000 to 2019, filtered from the report by CWIF (2020b).

The detailed list provides a full range of turbine types; the failure causes are varied, and often refer to more than one wind power plant within a wind farm. Tower collapse, within the category of structural failure, is the main concern of the current study. Multiple tower collapses within one event occurred frequently in the historical record (Ma et al., 2019). For example, six turbines were damaged by Typhoon Maemi on Miyakoji Island in 2003; of these, three turbine towers were fully collapsed down to the ground (Ishihara et al., 2005b). Another typhoon event, 'Dujuan', happened in the same year in Guangdong, China; this caused a loss of $1.6 million by damaging the large wind farm there (Chen et al., 2015). Typhoon Saomai landed in Zhejiang province, China and caused a loss of $70 million. In this extreme event, 15 wind turbine blades were broken, and two towers were overturned (Li et al. (2013). An accident in which two towers were struck and ruptured by fractured blades occurred in Denmark in 2008, and a thorough investigation was conducted by Riso (2008). In the years 1999, 2000 and 2003, 'blade struck' incidents occurred in Germany (CWIF (2020a). Tower buckling cases occurred in Taiwan, caused by Typhoon Jangmi; the direct cause was torrential rainfall, which resulted in bolt failure in multiple tower sections simultaneously (Chou and Tu, 2011). Typhoon Megi caused a tower collapse in Fujian, China, in 2010; Typhoon Usagi toppled eight towers and fractured eleven blades in Guangdong, China, resulting in a loss of $16 million (Chen et al., 2015, Chen and Xu, 2016, Chen et al., 2016).

In 2014, when Typhoon Rammasun attacked the South China Sea, one wind tower in Hainan and another thirteen towers in Guangdong collapsed; this is the most tragic case in the record list (Chen et al., 2016). An abrupt tower collapse in Sweden was investigated by Bäckstrand and Hurtig (2017); they found that insufficient pre-tensioning force had been applied during construction, and that this led to bolt fatigue

failure. In Germany in 2017 (PEI, 2017), one of three blades fell from a tower; this resulted in an imbalanced rotation force, and caused tower shell buckling at fifteen metres above ground level.

By summarising the full list for the period 1996-2016, we find that the most commonly identified reason for wind turbine tower collapse is the extreme wind event; this can be caused by typhoons or hurricanes, and accounts for 42% of all reports. The full summary is shown in Table 1.2.

Cause of failure	Tower(s)	Occurrence(%)
Typhoon	29	42
Storm	10	14.5
Blade failure	4	5.8
Fire	4	5.8
Bolts Failure / Fatigue	4	5.8
Brake Failure	2	2.9
Lightning	2	2.9
Faulty construction	2	2.9

Table 1.2. Main causes of tower collapse, from 1996 to 2016, filtered from the report by CWIF (2020b).

The main causes of extreme wind events in east and southeast Asia are tropical cyclones and typhoons generated in the Pacific Ocean; north American and European countries are more vulnerable to hurricanes and strong winds or storms. Irrespective of location, however, tower collapse is the most severe form of damage to a wind turbine. Compared to component failure, which can be repaired as necessary before recommencing the harvesting of wind energy, tower collapse is generally considered to lead to irreparable damage. This is largely because blades and nacelles containing electrical components will be cracked down onto the ground after the supporting tower topples over. Tower collapse is regarded as catastrophic failure in a wind turbine, and will cost between £500,000 and £5,000,000 depending on the particular wind turbine configuration; on the other hand, the construction cost of a tower accounts for less than 10% of the overall investment.

The first step in analysing such failures is to categorise the external loads acting on wind power plants. In general, it is usually assumed that external excitation loads are categorised in terms of their time history (Robert Gasch, 2012). This approach gives four categories: constant, cyclic, stochastic and short-time. Constant load includes gravity load from the mass of the components, centrifugal force from rotor revolution, and mean thrust force from the mean wind. Cyclic load comes from unbalanced blade mass rotation, oblique flow and blade passage. Stochastic load includes aerodynamic load and seismic load. Finally, short-time load includes frictional and braking loads during turbine shutdown or the yawing of a nacelle, as well as abnormal impact forces (Hau, 2013). Most of the collapse cases recorded today reveal that stochastic load – the most difficult type to quantify – should be regarded as the essential consideration (Ma et al., 2019).

In terms of tower reliability analysis, it can be observed that tower reliability is in line with the overall reliability of the wind turbine, and is shown by the 'bathtub curve' in Figure 2.7 (Gintautas and Sørensen, 2014). That is, the failure rate of the wind turbine tower will stay at a high level during both the early and the later stages of its typical twenty years of designed service life; meanwhile, the failure rate during the middle period, or 'useful life', will remain at a relatively low level. In the early life of a wind tower, collapses may be caused by design defects, construction errors or poor quality control. In the middle stage, fatigue, unexpected wind load and mechanical system failures will be the dominant reasons. In the later period of the designed service life, wear-out failures can occur; this may be due to improper maintenance, or as a result of corrosion. Figure 2.7 also shows that random failures may occur at any time during the life span of a wind turbine.

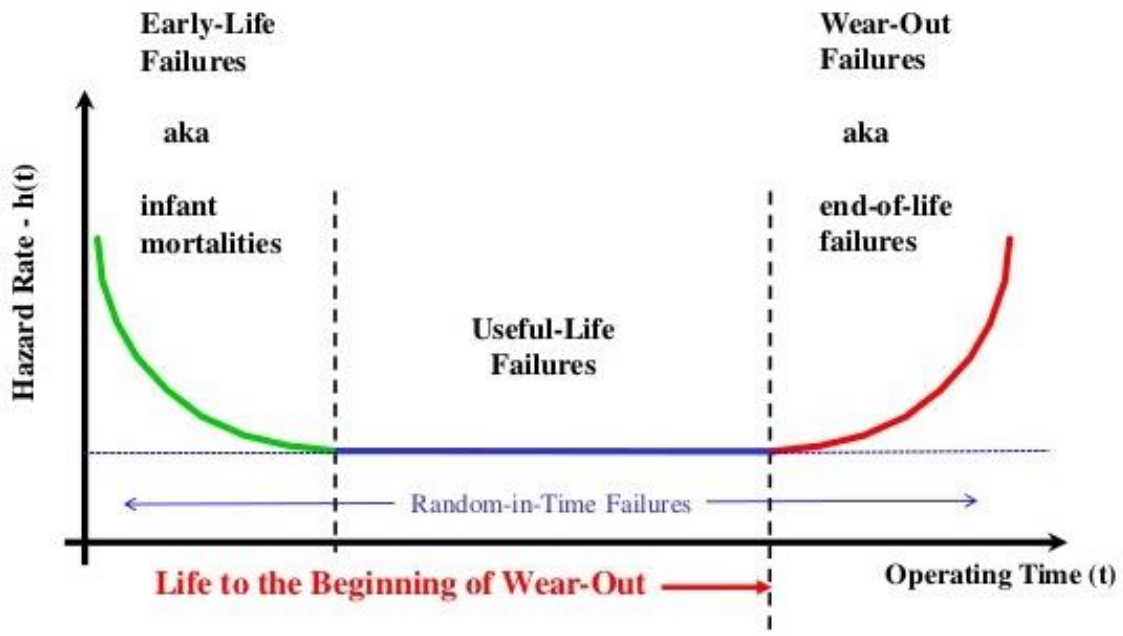


Figure 2.7. A Bathtub Curve of Failure Rate versus Time (Gintautas and Sørensen, 2014).

Carlstedt (2004) enhanced this concept of the service life of wind turbines, based on the annual failure rate in Sweden, after fourteen years of operations. Carlstedt concluded that the two major reasons for the bathtub curve throughout the operating time are (Ma et al., 2019): a) extreme load conditions, and b) human or mechanical errors.

Under extreme wind effects, stress and strain could exceed the designed ultimate bearing capacity of the tower steel tube, then result in local buckling on the shell surface, or overall buckling in a particular shell section. When a tower suffers the imbalance force generated by damaged blades, or an impact load produced by a blade strike, the tower structure also faces snapping hazards. Further, human error may result in bolt failure, fatigue collapse, or unfavourable pitch angle, which may give rise to eventual tower collapse. Those reasons could trigger chain effects and increase the entire failure risk to an unacceptable level.

Buckling failure may be caused by extreme load conditions; more specifically, extreme wind loads acting on the rotor and tower. There are also two subordinate root causes

for wind turbine tower collapse under extreme wind load. These are a) insufficient bearing strength, and b) inadequate buckling strength.

The design strengths may be surpassed by extreme wind load at any time throughout the lifespan of a wind turbine; on the other hand, the design objectives could be guaranteed by wind turbine design guidelines (EN1993, 2007, IEC International Electrotechnical Commission, 2005, DNV, 2013, Veritas, 2002). The tower dimensions are determined by a series of structural requirements. One typical factor is survival wind speed, the so-called 'reference wind speed average' over 10 minutes (Hau, 2013). In particular, the buckling strength becomes the most demanding requirement; this is due to the promotion of steel tube technologies, which constantly attenuate wall thickness. The demands of wind energy harvesting exaggerate the effects of higher towers and put pressure on the efficiency of material usage, which all renders the turbine tower more vulnerable to buckling collapse. According to the guidelines, survival wind speed is calculated on the premise that the entire wind turbine is regarded as a stationary structure, with different wind direction and stop positions omitted. However, the accurate wind loads on turbine structures are difficult to define, due to the complex geometry of wind power plants, especially the blades. Historically, tower collapse cases have revealed that towers fractured, not only when wind speeds exceeded design limits, but also at speeds under the reference wind speed. An approximate formula to transform mean wind speed U_T in the period T (in minutes) to the 10-minute mean wind speed U_{10} is shown (Veritas, 2002) as:

$$U_{10} \approx \frac{U_T}{1 - 0.047 \ln \frac{T}{10}} \tag{2.1}$$

A stochastic turbulence model widely used for spectral density, called the Harris spectrum (S_U) is shown (Veritas, 2002) as:

$$S_U(f_f) = \sigma_U^2 \frac{3.66\frac{L}{U_{10}}}{\left(1+\frac{3}{2}\left(\frac{2\pi f_f L}{U_{10}}\right)^2\right)^{5/6}} \quad (2.2)$$

In this formula, f_f represents the frequency of the wind, L is the characteristic length, and σ_U is the wind standard deviation. Another popular spectrum, the Kaimal spectrum (IEC61400-1) is shown (IEC International Electrotechnical Commission, 2005) as:

$$S_U(f) = \sigma_U^2 \frac{4\frac{L_k}{U_{10}}}{\left(1+6\frac{fL_k}{U_{10}}\right)^{5/3}} \quad (2.3)$$

In this formula, L_k is related to the integral length scale based on a turbulence scale parameter. These spectrums provided designers and researchers with the insight that energies generated by multiple-frequency wind forces could be distributed in varied ways compared to static wind speed, and revealed the possibility that wind turbine towers may be subjected to transient loading conditions to an extent beyond the strength design category. At this point, buckling may occur.

2.2.2 Wind turbine tower collapse case studies and buckling types

Because of insufficient bearing strength, tower structures can be unable to withstand the stresses and strains generated by the forces propagated down from rotors under the effects of strong winds. Typhoon Saomai, with maximum wind speeds exceeding 60 m/s, and extreme gusts over 80 m/s, landed in the Zhejiang province of China in the year 2006 (Li et al., 2013). The result was a five-tower collapse. Two of the five towers were buckled in the middle of the base steel tower tube; this was due to the extreme wind turbulence, with a recorded turbulent intensity reference factor (I_{ref}) of over 0.2, in the context of a design factor determined at 0.12. Unexpectedly, the high turbulence intensity was experienced at the same time as high wind speed, which resulted in a dangerously intense vibration in the wind turbine structures. Another

two towers collapsed because of foundations failure, and the final fallen tower fractured at the welded joint between two tower sections. The investigation concluded that the wind farm in question was located in an area affected by tropical cyclones, and that the towers had been designed on the premise of insufficient bearing strength. This underestimated design strategy led the tower structures to lack the bearing capacity required to carry such drastic wind loads. Moreover, fixed-pitch wind turbines all survived in this accident, indicating that under extreme wind conditions a stationary structure might be more reliable than one with variable shape coefficients. In design terms, the possibility of wind turbine loss should be accepted if the weather event is so extreme that the conditions far exceed the normal design requirements, or if the site is located in an area where the probability of extreme events is small; moreover, sacrificing one or more blades to reduce the thrust load on the tower top, to avoid the collapse of the entire tower, is a practical strategy that could be considered in these cases.

The use of a pitching system is the most common method of alleviating wind load when wind speed surpasses cut-out speed (Hau, 2013, DNV, 2013). Practically, if the rotor rotates slowly with a proper blade pitch angle, or with an effective aerodynamic brake, the thrust loads are less than in the locked situation. Some turbines will come to a locking state when wind speed is very high, in order to prevent rotor over-speed revolution. In the worst case, a crosswind acting on the pitched or locked aerofoils will create higher wind loads than favourable fore-aft winds, and the windward surface area of the blades may be larger than that of the tower structure. The influence of an extreme crosswind is a high probability when wind turbines are built in tropical cyclone activity zones, where the wind direction may change drastically in a short period. Extreme crosswinds are usually regarded as ±15° deviation to the direction of a 10-minute mean wind; for comparison, the record of Typhoon Saomai indicated that the wind direction changed around 100° in a time interval of only 20 minutes (Li et al., 2013, Chen et al., 2015). Similar data can also be found in the record of Typhoon Maemi;

the change of wind direction was 120° in a very short time period (Ishihara et al., 2005b). Lack of synchronisation between yawing azimuth adjustment and rapid wind direction change produces large crosswind loads, as well as torsional vibration, in tower shells. The tower section is subjected to a considerable magnitude of combined loading conditions in extreme winds, including axial compressive load, thrust load, bending moment, and torsional forces (Ma et al., 2020).

The investigation of a tower collapse incident that occurred in Japan revealed the importance of blade position (Ishihara et al., 2005a). Typhoon Maemi landed on Miyakojima Island in 2003, with a recorded maximum wind speed of 38.4 m/s, and gust speeds of 74.1 m/s. Three towers collapsed; one because of foundation failure and the other two through buckling near the entrance door. It is interesting to note the outcomes for three identical wind turbines at the same site; these were numbered 3, 4 and 5. Numbers 3 and 5 were damaged, while Number 4 survived intact. The authors concluded, and proved by means of the Finite Element Method (FEM), that the survival of Number 4 turbine was due to a different yawing angle compared to the other two; this resulted in a lower bending moment throughout the tower. A more favourable nacelle direction against the wind would mean that less thrust force was transferred to the tower cylinder, enabling the maximum bending moment to be kept within the designed range.

In parallel to the Typhoon Maemi accident, another catastrophic tower failure incident happened in 2013 in China (Chen et al., 2015, Chen and Xu, 2016). Typhoon Usagi, whose maximum wind speed reached 69.4 m/s, made landfall in Shanwei City and blew down 8 of the 25 steel tube towers at the Shanwei wind farm. A forensic study of the turbine collapse was conducted and it was observed that the directions in which all 8 collapsed towers fell were similar, i.e. toward SSW of SW (Chen and Xu, 2016). The investigators came to the conclusion that strong winds from NNW and NW should be held responsible for the failure. However, according to the meteorological records and the re-computed Computational Fluid Dynamics (CFD) results, the

research group found that the direction of the maximum wind at hub height, with the wind speed at 75.8 m/s, was SSW instead of NNE or NE, and that the 3s average speeds were 59.8 and 62.8 m/s respectively. The turbines were designed as class S at a survival wind speed of 70 m/s, and the investigators deduced that the 75.8 m/s SSW wind would have allowed for an advantageous turbine stop position against the wind. By contrast, the unfavourable stop positions against NNE and NE, under the extreme wind, went beyond the safety zone of the tower structures. The stop positions of the faulty blades, under a low wind speed, could generate a considerably higher force than a favourable locking position against a higher wind speed. Monitoring research was carried out into the relationship between tower strain and yawing angle (Bas et al., 2012). This study showed that the nacelle orientation could affect the strain distribution in the tower shell substantially, even at low wind speeds. The interactions between yawing angle, pitch angle and tower stress/strain should be thoroughly considered in the design procedure, even for scenarios where wind speed may not be at a high level.

Inadequate buckling strength is another major cause of tower failure under extreme winds. Buckling is a well-known issue with steel tubular structures; it may occur not only in weak areas, or near defect points along the tower shells, but also unexpectedly in some perfect areas. As for a turbine steel tube, the weak point or trigger point of a chain buckling process usually emerges in zones of changing wall thickness; door opening areas, welding seams, jointing parts etc. Historical cases have proved that local buckling of tower shells can be the initial stimulus for a domino-like total loss of wind turbines (Ma et al., 2019). In the aforementioned case of typhoon Usagi, investors found that the buckle points of all of these 8 collapsed towers appeared at about 9 or 10 metres of tower height from the ground, where the tube shell thickness changed drastically, as shown in Figure 2.8 (Chen et al., 2015). In photographs (a) and (e) of Figure 2.8 it is noticeable that the final buckling type of the tower shell has dents and bulges along the circumferential direction on the compressive side, and flattening on

the tensile side. Compared to another on-site case in Typhoon Maemi in Japan, Ishihara et al. (2005b) provided similar buckling analysis via FEM simulations, proving the wave-like displacements happened on the compressive side of the shell surface. More records showing the final buckling types of wind turbine towers are to be found in Evia, Greece, 2020 (thestructuralengineer.info, 2020); in Saxony, Germany, 2017 (PEI, 2017); and in Montreal, Canada (NationalPost, 2016). Forensic studies of wind turbine tower collapse cases have revealed wave-shaped buckling patterns, both circumferential and longitudinal; wave numbers fall within particular ranges, as shown in Figure 2.8-2.9. The circumferential and longitudinal wave-shapes have been discussed, both in theoretical analysis and experimental tests, in the past decades (Wang et al., 2018, Karam and Gibson, 1995, Benedettini, 1999, Almroth, 1963, Weingarten et al., 1965, Almroth, 1965).

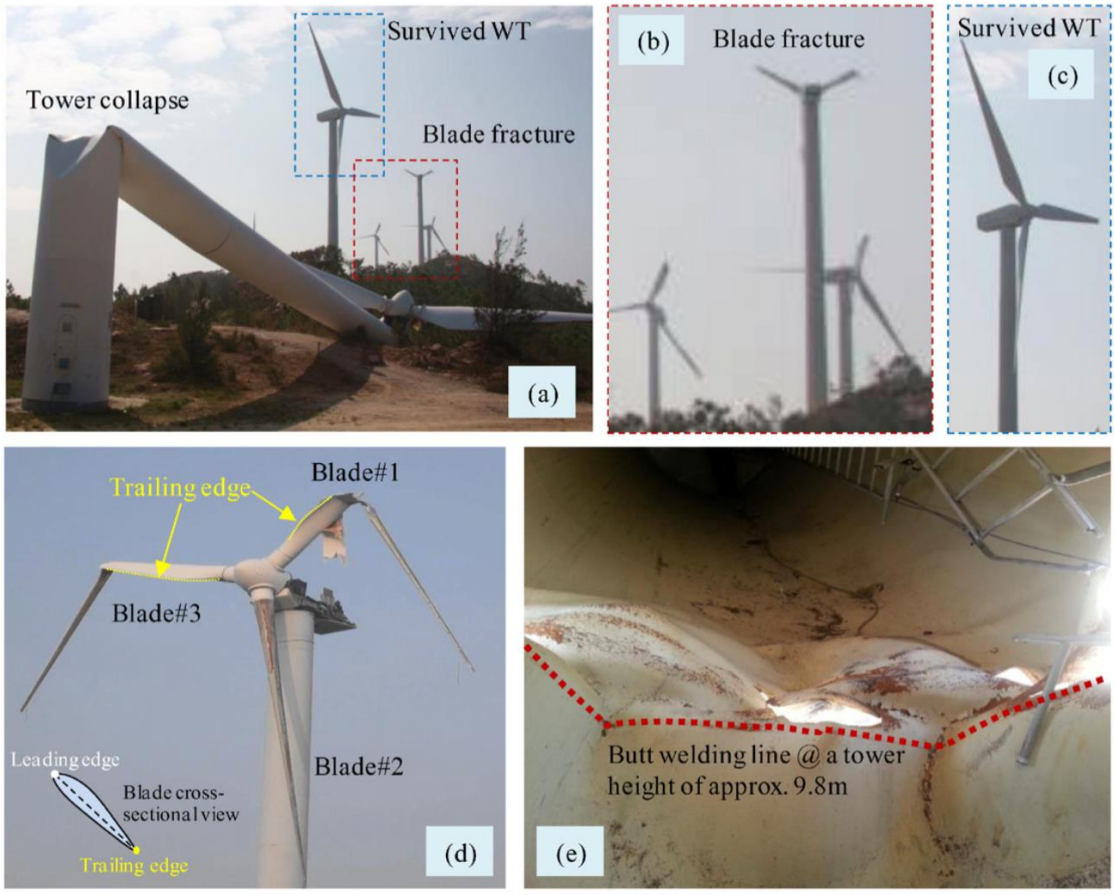
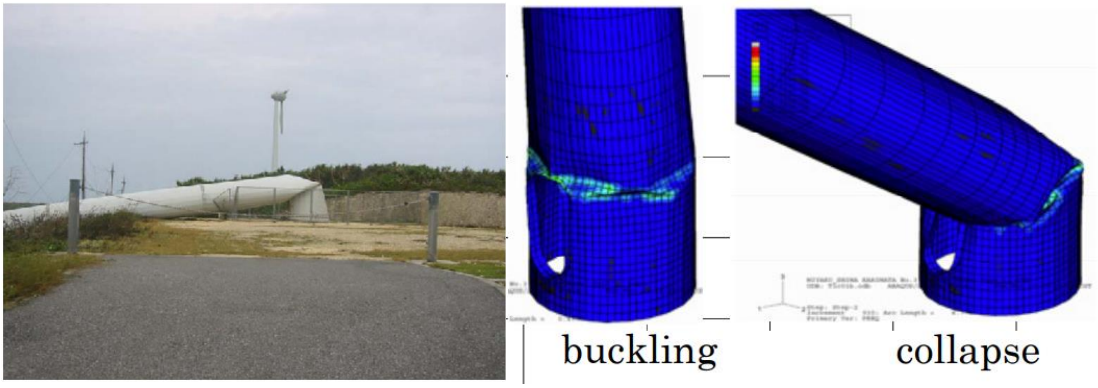


Figure 2.8. Representative structural failure of wind turbines caused by Usagi (Chen and Xu, 2016).



(a)



(b) (c)



(d) (e)

Figure 2.9. On-site photos of wind turbine collapse cases: (a), collapse photo and FEM simulation results in the case of Typhoon Maemi (Ishihara et al., 2005b); (b) (c), in Evia, Greece (thestructuralengineer.info, 2020); (d) in Saxony, Germany, 2017 (PEI, 2017); (e) in Montreal, Canada (NationalPost, 2016).

The buckling patterns of wind turbine towers informed the research to reveal the mechanism of the buckling process, through the prebuckling and postbuckling stages, and to provide an explanation for this kind of final buckling wave-shape. Buckling types are considerably dominated by specific parameters of the tower section, such as tower diameter, steel shell thickness, shell section length, stiffening rings, connections, door-openings, and welding (Hau, 2013, Manwell et al., 2006, LEE, 1962, Chou et al., 2013, Arabian-Hoseynabadi et al., 2010, Lee and Bang, 2012, Dimopoulos and Gantes, 2012). Those parameters could be normalised for running parametrical analyses, and further clarify the nature of the buckling-related cases of wind turbine collapse recorded in the forensic studies. The current study concentrates on the buckling behaviour of an unstiffened cylindrical steel shell section of a wind turbine tower, subject to compression and bending, with an intended focus on the progression of buckling that leads to the failure of structural towers.

Wall thickness change results in bending stiffness change; this is an inherent danger of local yield, due to the compressive stress accumulation. The modelling calculation by Chen et al. (2015) revealed that large compressive stress was prone to occur in the region between 8.2 m and 11.4 m tower height, which covered the turbine buckle points. As long as stress or strain beyond the tolerant limit of the tower shell exists, local buckling may appear, followed by a catastrophic collapse; a buckled shell structure is unable to sustain any increasing eccentric loads, when these are combined with the bending moments acting on it. This incident can be attributed to a design defect which disregarded a dramatic stiffness change in the tower shell. The trial-and-error approach had been conducted, in an analysis of a 1 MW wind turbine tower, in order to get to the best wall thickness dimension (Lavassas et al., 2003). The researchers applied the plastic limit state as a criterion for the lower part of tower shell; this precludes the emergence of a buckling limit state. At the same time, they adopted a buckling limit state as a criterion for the upper tower shells.

The door-opening area has been known for some time as a hotspot of buckling failure in wind turbine tower structures; therefore, door-opening areas are usually enhanced and reinforced, by means of multiple approaches. The buckle points of the collapsed towers in the Typhoon Maemi accident emerged at the door opening region, which should be regarded as the vulnerable failure part (Ishihara et al., 2005b). Also, an FEM post-mortem simulation showed that the towers were prone to collapse at the opening region under compression load, as shown in Figure 2.9. Researchers further found that buckling possibility increased markedly if the angle between the horizontal wind direction and the door opening direction was no more than 40°. The ultimate bearing moment of the entrance door region is the threshold of the entire tower, which was 2.98% superior to the design value; i.e., already beyond the sufficient structural redundancy range. Because of the door opening direction, Nuta et al. (2011) applied pushover analysis on a 1.65 MW wind turbine model, and claimed that the lowest base resistance moment occurred when the angle of resultant force direction to door opening was 22.5°. The typical cut-out of a wind turbine is approximate 25°, therefore shell stiffness tends to vary considerably around the thickened edge of the cut-out region. However, an experimental and modelling study indicated that the effect of this angle variation can be negligible if stiffeners are set appropriately (Dimopoulos and Gantes, 2012). A number of turbine tower stiffener studies have been carried out, with different perspectives (Dimopoulos and Gantes, 2012, Hao et al., 2015, Hu et al., 2014, Lagaros and Karlaftis, 2016); the design theory is still immature, and we have not yet come to a consensus. Comprehensive buckling analysis is recommended for Megawatt-class wind turbines, as the modern shell structures show remarkable material usage efficiency; this can result in uncontrolled geometrical failure – in other words, buckling.

2.3 The development of buckling research

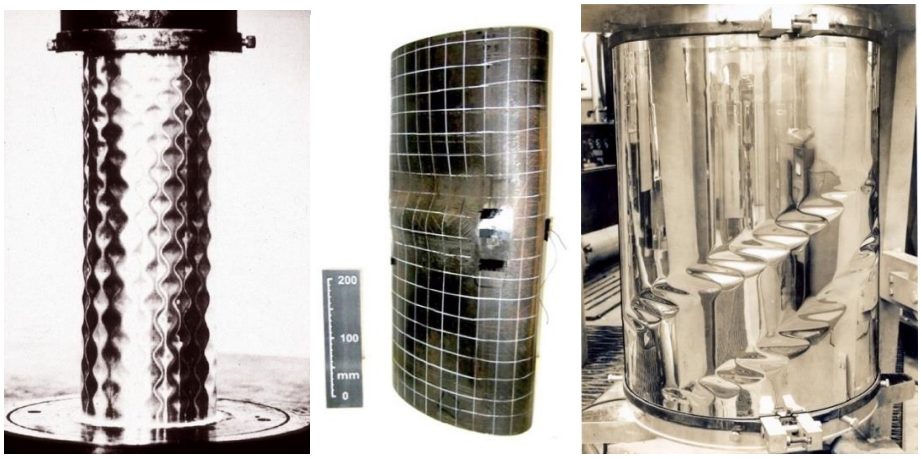
2.3.1 Overview

The study of the phenomenon of buckling – a kind of sudden failure – began with Leonhard Euler in 1757 (EncyclopaediaBritannica, 2009). After centuries of development, modern shell buckling theory is very complex, containing aspects of mathematics (pure and applied), applied mechanics, and even statistics. Famed scientists in applied mechanics history – such as von Karmen, Tsien, Novozhilov, Koiter, Donnell, Timoshenko, Love, Rayleigh, Reissner, Mindlin and Hutchinson (Teng and Rotter, 2006) – promoted buckling theory to a very well-developed stage. The boom period or 'classical era' of theory development, from the beginning of the 20th century to the 1970s, brought great improvements through the use of novel numerical methods and high-performance computers; and these developments continue. Still, knowledge gaps remain, with discrepancies between theoretical solutions and the results of experiments undertaken on physical structures. Buckling and yielding (geometric and material softening, respectively) still cause failures under ultimate load conditions, even though modern Mega-watt wind turbine tower design specifies material strengths that are certainly above the safe domain for regular supporting structures.

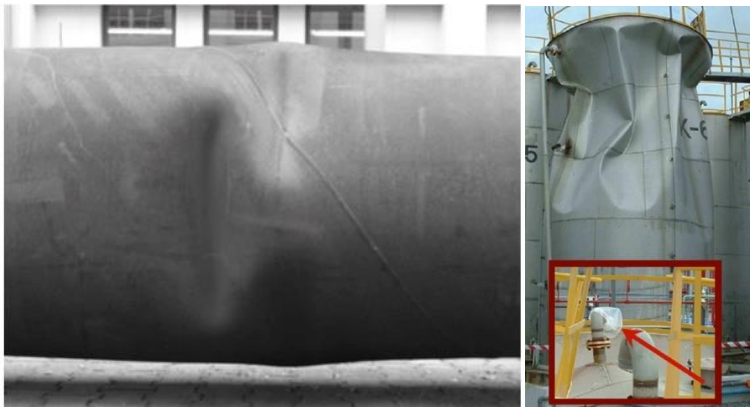
Buckling behaviour can be widely observed in multiple engineering subjects, including columns, beams, rods, water tanks, silos, tower shells, tubes, rockets, aeroplane wing surfaces and spherical constructions (Peterson et al., 1968, Teng and Rotter, 2006, Calladine and Sanders, 1984, Bardi and Kyriakides, 2006). Various typical buckling phenomena, especially cylindrical shell buckling, are shown in Figure 2.10.



(a) (b)



(c) (d) (e)



(f) (g)

Figure 2.10. Typical buckling behaviours : (a) Buckled tanks at Wente Brothers, California, USA (Bushnell, 1981); (b) laminated composite cylindrical tube under axially compressive load, (Degenhardt et al., 2012); (c) buckled thin unstiffened cylindrical shell under axially compressive load, (Horton and

Durham, 1963); (d) elliptical cross section tube under axial compression, (Chan et al., 2010); (e) aluminium shell with internal pressure under axial compression, (Harris et al., 1957); (f) spirally welded large tubes under bending load, (Reinke et al., 2014); (g) cylindrical tank buckling due to internal vacuum (De Paor et al., 2012).

In order to address buckling problems properly, and to explain the mechanisms of buckling processes, some basic features have been identified. The variety of buckling behaviours is evident in Figure 2.10; buckling types and shapes can differ greatly in different geometric configurations, using different materials and under different loading conditions, and this variety led the relevant research into increasingly complex areas. There have been numerous studies of cylindrical shell buckling. Teng (1996) and Arbocz and Starnes Jr (2002) discussed the imperfections of shell structures, using shell stability analysis and nonlinear finite element methods. Rotter (1998) compared cylindrical shell structures in engineering to the Eurocode 3 standards, mainly focusing on silos and tanks. A general report by Schmidt (2000) considered the state of the art of stability issues in steel structure design, and compared aspects of this to the European Prestandard ENV 1993-1-6. Juan et al. (2006) also compared the same standard to finite element results in an account of cylindrical silos. The topic of uncertainty buckling, based on initial configuration aspects such as material imperfections, elasticity, applied loads and thicknesses, has been reviewed by Elishakoff and Structures (2000). Edlund (2007) provided a review of buckling questions about metallic cylinders, with especial reference to imperfection effects. The most recent reviews on buckling issues were focused on vibration problems (Sofiyev, 2019), thin-walled structures manufactured using composite materials (Mittelstedt, 2020), buckling under specific loading conditions such as lateral distortion (Rossi et al., 2020), and on novel sandwich structures in both plates and cylindrical shells (Kumar and Srinivasa, 2020).

There is a large body of codes and guidelines for buckling design and calculation, based on experimental evidence. These include Eurocode 3 part 6, the aforementioned ENV 1993 and EN 1993-1-6 (EN1993-1-6, 2003, Rotter, 2005). The concept of two

strengths for design reference was introduced by Eurocode: elastic critical resistance, based on linear bifurcation analysis (LBA); and plastic reference resistance, based on material nonlinear analysis (MNA). Geometrically and materially nonlinear imperfection analysis (GMNIA) has also been introduced in the guidelines; this requires higher levels of calculation resource, and explicit methods.

Calladine and Sanders (1984) published a book on the topic of theories of shell structures, providing two concepts of shell buckling: classical buckling analysis and non-classical buckling analysis. The former concept presents basic approaches and equations to express strain/stress relationships, although full solutions to these high-order partial differential equations (PDE) are extremely difficult to obtain. The latter concept introduced nonlinearity and energy to buckling analysis, and greatly informed the current study. A book providing systematic knowledge of thin metal shell buckling was published by Teng and Rotter (2006); buckling issues were studied in the contexts of different loading conditions and configurations, and the book includes details of the efforts and understandings of a group of authors on buckling. The issue of the stability of elastic structures under static loads was discussed in a book written by Alfutov (2013). In his book, elastic stability issues were investigated from the perspectives of bifurcation point, limit load, linear equations, energy determinations for stability, and the stability boundary. Buckling behaviour is actually a problem of structural stability. The stability problem for composite structures has been explained in the book 'Stability loss and Buckling delamination' by Akbarov (2012). The asymptotical numerical techniques used to achieve solutions for thin-walled structures have been discussed in books by Andrianov et al. (2013); similarly, for the buckling problems of elastic shells, by Tovstik et al. (2001). Asymptotic methods contribute largely to the derivation of solutions for buckling processes, both theoretically and numerically.

The use of cylindrical steel shells is a popular construction method for modern high-res wind turbine towers. In operation, these towers, and therefore the associated shells,

are under a combined axial compressive load and bending moment, derived from the gravity loads of the power plant components and the thrust load of the wind. The torsional loads and shear forces are negligible compared to the axial compression and bending (Lavassas et al., 2003, van Es et al., 2016, Vasilikis et al., 2016, Karamanos, 2002, Ma et al., 2020). Therefore, the literature on buckling research primarily focuses on cylindrical steel shells, under the loading conditions of axial compressive load, pure bending, and combined axial compression and bending moments; the axial compressive loading condition is the foundation for further combined loading analysis. In real-world wind turbine constructions and installations, a perfect shell section is rarely available; certain imperfections will usually be found on the surface of steel shells. The influence of this initial imperfection on the buckling process is central to the current study; a number of authors have mentioned the high sensitivity of initial imperfections (Vasilikis et al., 2016, Schneider, 1996, Castro et al., 2013, Dimopoulos and Gantes, 2012, Wang and Sadowski, 2020, Degenhardt et al., 2012, Hornung and Saal, 2002). The following sections review the literature on buckling analysis, related to linear and nonlinear buckling, prebuckling and postbuckling, imperfections, and energy methods.

2.3.2 Buckling paths

The load-displacement curve that measures the thin-walled cylindrical shell is an effective approach to showing clearly buckling behaviour throughout the entire process. The choice of axial end-shortening of the shell section is the most widely used way to track buckling paths. Figure 2.11 shows a typical load-end shortening curve of a thick-walled cylinder under axial compression, while Figure 2.12 illustrates the types of buckling behaviour of a thin-walled tube shell.

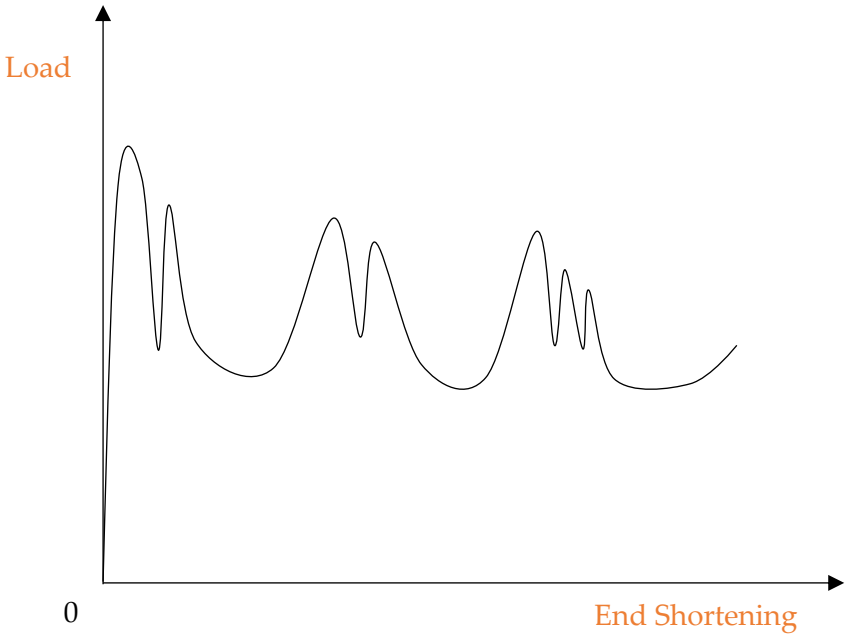


Figure 2.11. A typical load–end shortening curve of a thick-walled tube shell, which demonstrates a complex elastic–plastic buckling path under axial compressive load; the radius-thickness ratio is 10–20 (Edlund, 2007).

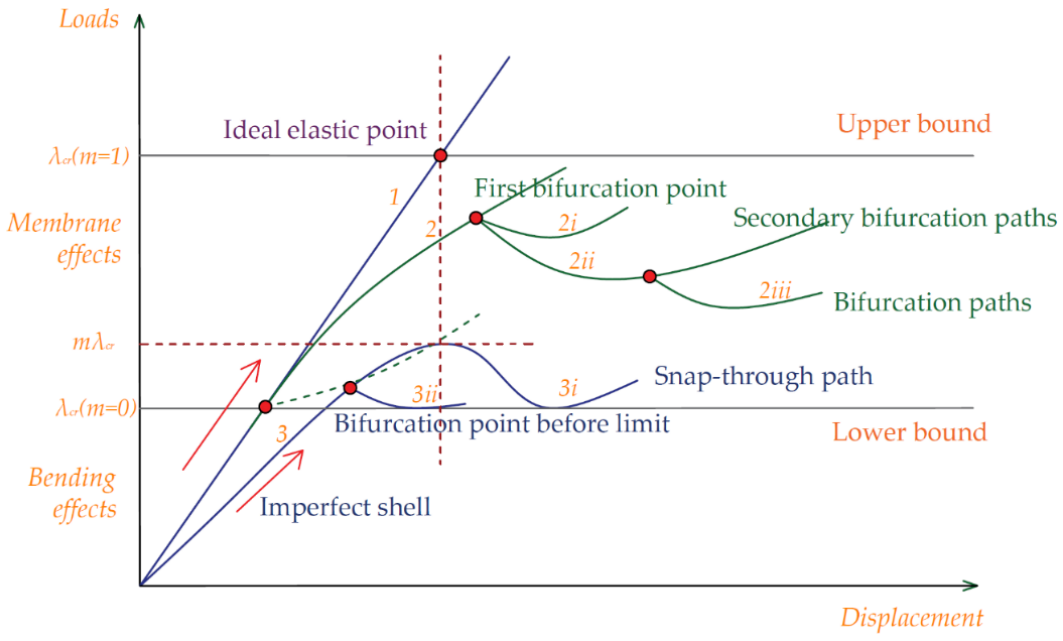


Figure 2.12. Multiple types of buckling behaviours for a thin-walled cylindrical shell under compressive load (Ma et al., 2020).

The buckling behaviour of cylindrical shells is distinguished between bifurcation point and limit-point buckling, and, particularly with increasing loads, axial

compression load. As shown in Figure 2.12 (Ma et al., 2020), bifurcation buckling occurs in ideal elasticity shells (curves 1 and 2), with both linear and nonlinear pre-buckling paths. The vertical axis represents axial compression while λ_{cr} is the ideal critical load factor of the structure. The horizontal axis represents displacement, typically the end-shortening of the shell section. The bifurcation-point buckling path might be asymmetric or symmetric. It might also be stable or unstable, as is revealed in the secondary bifurcation buckling path, after the first bifurcation point has passed; for instance, this can be seen in curves 2i, 2ii, 3ii, though there are probably more possible bifurcation paths afterwards. Another buckling phenomenon is limit-point buckling, with or without a snap-through behaviour, as shown in curve 3. Shells with imperfections due to factory construction or on-site installation are prone to experiencing this typical phenomenon, in which a dynamic jump happens after having achieved the limit point. This leads to a new equilibrium and, for the most part, a stable path. The bifurcation path may emerge in the limit-point buckling category where the interaction between load and deformation passes a bifurcation point before it has reached the limit point, as depicted by the curves 3i and 3ii. This is a problem in the buckling equilibrium path, and is based on buckling control equations in light of markable initial imperfection.

Before buckling, the structure stays in a stable situation, and the theoretical linear critical load (the ideal elastic point) does not exist in reality. When the critical buckling load is achieved, an unstable equilibrium path descends dramatically to a certain distance below the critical buckling load. The question in need of attention lies in the description of this unstable equilibrium path, by means of analytical or numerical solutions. Energy-method-based buckling control equations contain items beyond 3 orders, and these items reveal the nonlinear equations' multiple equilibrium paths (Langhaar, 2016). Initial imperfection is a directional derivative introduced into these equations; afterwards, the solutions degenerate into fewer equilibrium paths, or perhaps even a single option. To obtain the minimum point along this equilibrium

path, the lower bound must be obtained; this is closer to a realistic critical buckling load.

The full buckling process has been categorised into several stages by Edlund (2007): pre-buckling, bifurcation buckling, initial postbuckling, early postbuckling, intermediate postbuckling and advanced postbuckling. More specifically, the typical buckling paths of perfect and imperfect cylinders have been illustrated as shown in Figure 2.13 (Edlund, 2007). The mode-jumping process is fundamentally a dynamic procedure.

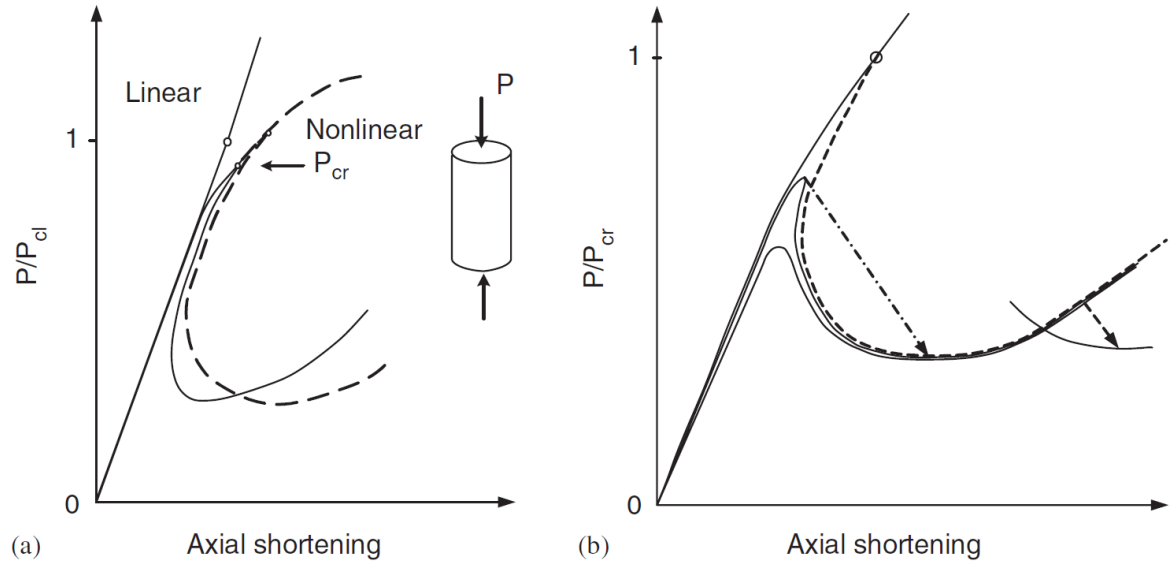


Figure 2.13. load–end shortening curves of perfect (a) and imperfect (b) cylinder (Edlund, 2007), in the axially-compressed buckling processes. Buckling-mode jumping can be observed in (b).

Kroplin et al. (1986) claimed that in order to fully investigate the mechanism and behaviour of buckling procedures, dynamic analysis must be employed. For Kröplin et al. (1985) and Schneider and Thiele (1999), meanwhile, a compatible quasi-static analysis is sufficient to in order to obtain the necessary results for a buckling analysis of specific structures. Some research on transient stage analysis was conducted in the 1990s by Riks et al. (1996), using a classical path-following and a transient integration method but in relation to the problem of plates and composite thin-walled cylinders. Hilburger et al. (1997) then carried out a series of perturbations to a cylindrical shell

structure, involving cut-out under an axially compressive load; in this manner, they identified the unstable buckling characteristics in the transient stage, based on the established postbuckling equations. Riks (1997) then enhanced his method, adopting a computational approach in his work on elastic structures by means of energy criterion. Recent transient analyses were mainly done by FEM. These involved various loading conditions with structural configurations, including stiffened metallic cylinders by Rudd et al. (2018), liquid-filled tanks by Johnson (2019), and composite cylinders underwater (Matos et al., 2020).

2.3.3 Cylindrical shells under axial compressive load

A perfect cylindrical shell under axial compression is the most straightforward objective in cylindrical shell-buckling analysis, and has provided the foundations of theory centred on complex loading conditions and geometrical variations. Buckling theories here have not advanced for a significant period, as numerical simulations have focused exclusively on narrowing the gaps between analytical solutions and engineering applications (Teng, 1996, Weingarten et al., 1965, Almroth, 1965). The classic 'two-surface' model was delivered by Donnell (1934), Donnell and Wan (1950), and Koiter (1970); eigenvalue problems have since been connected to geometric imperfections, and four-order partial differential equations have been identified despite the fact that general solutions were very difficult to obtain during this era.

Experimental results have provided reliable solutions for cylindrical shell structure design in the past a few decades, following a comprehensive shell-buckling experiment carried out by NASA in the 1960s (Peterson et al., 1968, Seide et al., 1960). The scattered test results and regression formula of the lower bound are shown in Figure 2.14. Here, α represents the knock-down factor based on the theoretical ideal buckling capacity, while the recommended uniaxial comprehension expression is given as (Seide et al., 1960):

$$\alpha = 1 - 0.901(1 - e^{-\sqrt{(R/t)}/16}) \quad (2.4)$$

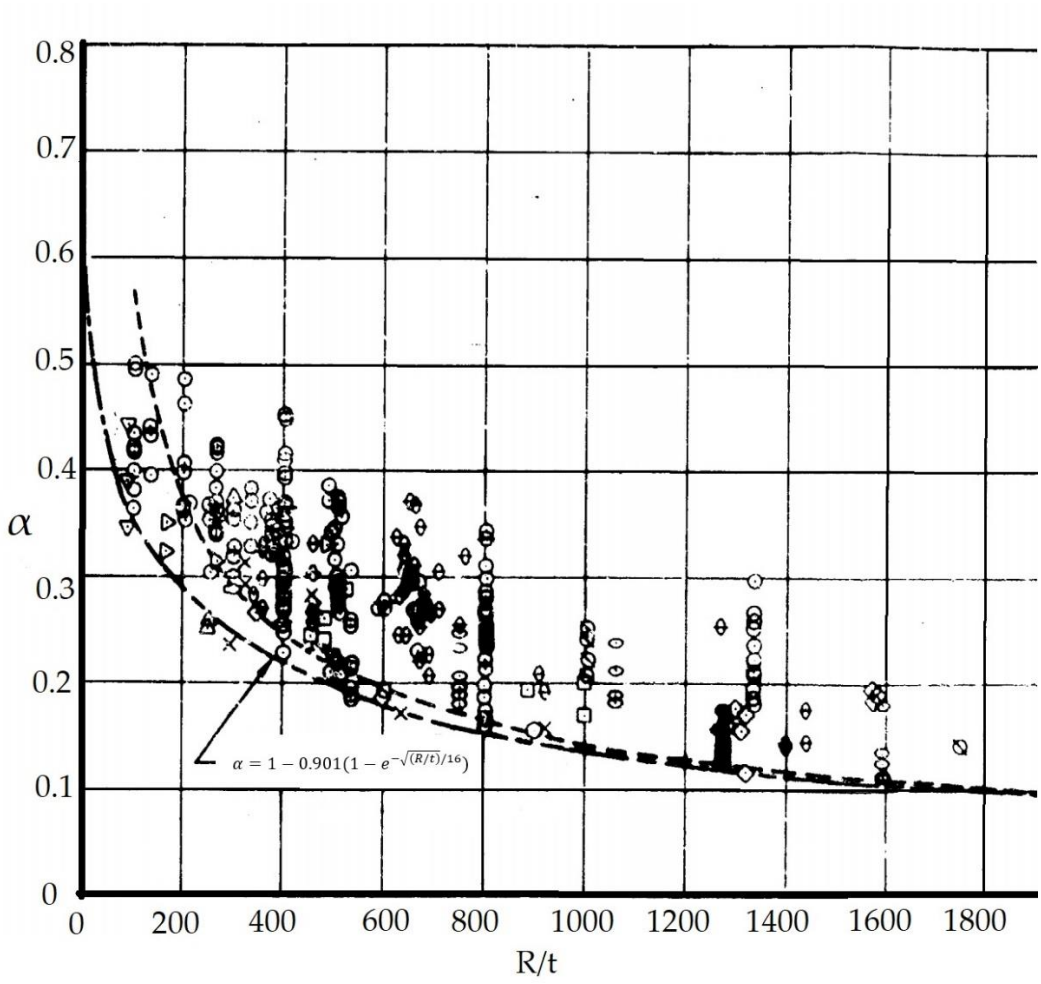


Figure 2.14. Experimental data based on cylindrical shell knock-down factor according to the radius-to-thickness ratio, R/t, under axial compressive loads, with a selected range of R/t from 0 to 1800 (Seide et al., 1960, Peterson et al., 1968).

Two outcomes can be observed in Figure 2.14: the actual buckling bearing capacity is lower than the analytical results; and the knock-down factor is closely related to the R/t ratio, which is the diameter (R) versus the thickness (t) of the shell. The former phenomenon was identified by designers and researchers some time ago, as in practice long, thin-walled tubes weren't able to achieve the requisite bearing load intended by designers, and the Euler-beam theory could not describe actual test results. Beginning with work by Von Karman et al. (1940), the curvature issue was

introduced to shell buckling problems, in relation to one-dimensional and two-dimensional structures. This work focussed on the discrepancy between laboratory tests and classical buckling theory. Following this, Koiter (1945) (English version available from 1967) connected the buckling load to dependency on equilibrium stability, going on to discuss shell imperfection (Koiter, 1967). Subsequently, the best explanation for the difference between test results and theoretical values is accepted as being imperfection on cylindrical shells (Donnell and Wan, 1950, Hutchinson, 1968). Other explanations for this discrepancy address the influence of boundary conditions, including load and supporting boundary conditions, and the nonlinearity of material behaviour (Ma et al., 2003, Hu et al., 2006, Fallah and Aghdam, 2011). The latter R/t ratio relates to the geometry of cylinder shells, which are well-represented by curvature expressions. Curvature expressions distinguish between plates, cylinders, arcs, and spherical shells with clarity. The R/t ratio of a wind turbine tower falls into a region of approximately 50 – 150, and therefore determined the research objective of the shell section chosen in this range.

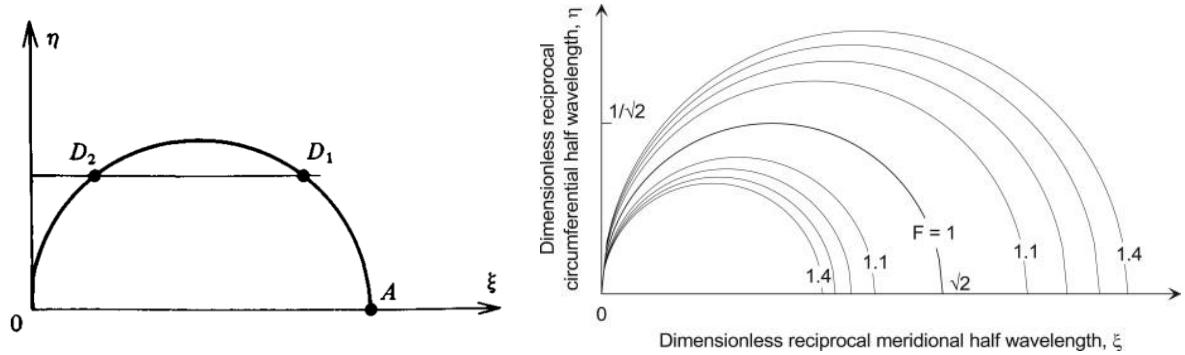
2.3.4 Geometry Imperfections

Geometry imperfections in shell buckling terms include shell-shape imperfection, load boundary condition, and shell thickness variation. In addition, these imperfections may include material imperfection, which includes initial internal stress or material change throughout the shell. Shape imperfection is the primary consideration in buckling research, and for the present study. Donnell (1950) identified a calculation to indicate that these imperfections might affect results around the bifurcation point in particular. A comparison offered by Koiter (1963) suggested that this behaviour is more noticeable in the immediate vicinity of bifurcation points. He expanded his focus from small initial imperfections considered in his initial work were to moderate and larger imperfections subsequently. Thus a shell with a finite initial imperfection under axial compression load might show a typical axisymmetric

buckling mode, which is then expressed well by an asymptotic analysis result, Koiter's previous formula (Koiter, 1963):

$$(1-\Lambda)^2 = \frac{3}{2}(3)^{\frac{1}{2}}\Lambda w_0/h \tag{2.5}$$

Here, Λ is the classical buckling load in dimensionless format; w_0 is the amplitude of initial geometric imperfection (equal to 1), and h is the effective thickness of the shell. Koiter (1945) addressed the famous 'Koiter circle', establishing that nonlinear buckling interaction is a possibility in three classical buckling modes; say, three points on the 'Koiter circle', shown in Figure 2.15 (a). His theory has been extended to multiple wavelengths under axial compression on cylindrical shells; the results are shown in wavelength space as Figure 2.15 (b) (Koiter, 1970, Shakouri et al., 2014).



(a) (b)

Figure 2.15. The 'Koiter circle', where (a) represents three points of classical buckling modes, A, D1, and D2 (Calladine and Sanders, 1984), and (b) cylindrical shells under axial compression, Koiter circles in the ξ–η dimensionless wavelength space (Shakouri et al., 2014).

As we have seen, the most common method of measuring initial shell-shape imperfection is to establish the radial deviations from the original perfect circle, and to define the ratio of deviation amplitudes, using w_0/h. Further research and experimentation have revealed a significant reduction in cylindrical shells under axial compression caused by initial shape imperfection, as shown in Figure 2.16, which shows the typical influence of imperfection parameters on elastic long cylinders: one

square dent on the shell surface. These figures reveal that the reduction magnitude of buckling capacity drops in line with the increasing of imperfection size.

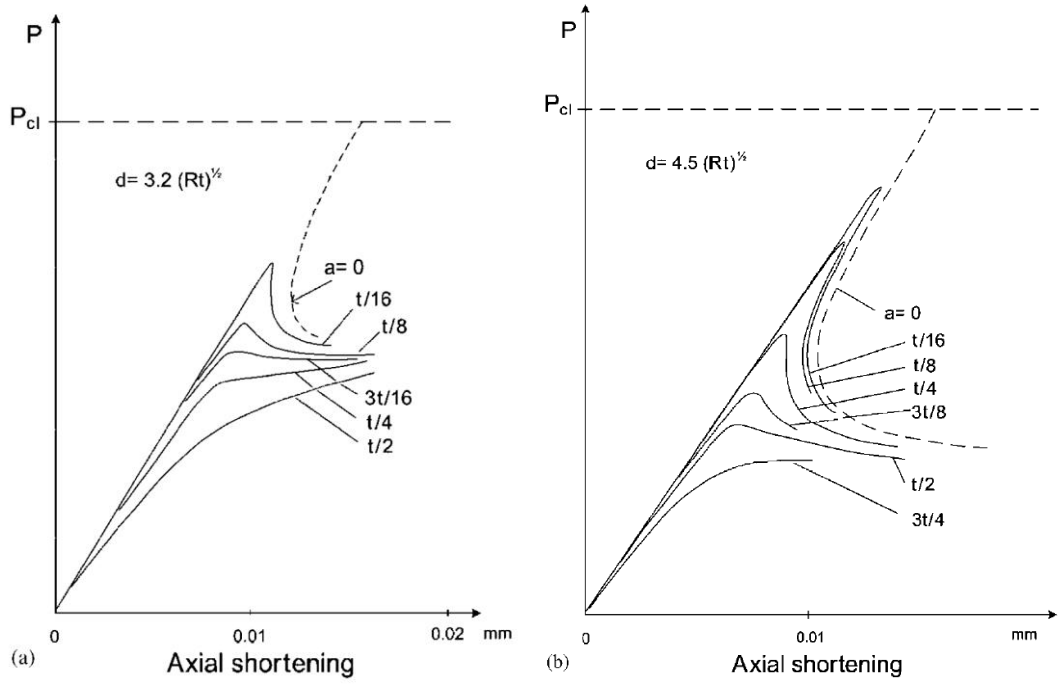


Figure 2.16. The influence of imperfection parameters on buckling capacities, where (a) $d = 3.2\sqrt{Rt}$ and (b) $d = 4.5\sqrt{Rt}$. d represents the side length of imperfection square, and a represents the imperfection amplitude in these figures (Edlund, 2007, Esslinger and Geier, 1977).

Gaussian curvature, K, is a practical expression of the imperfection parameter in buckling analysis. If K is positive, the shell shape is typically a spherical shell or arced-plate, which is very sensitive to imperfection under loads, especially external pressures (Hutchinson, 2016, Fitch and James, 1968, Wunderlich and Albertin, 2002, Von Karman and Tsien, 1939, Huang, 1964). When K is negative, the shell surface has an inward shape, which is very small, or at least not sensitive to the initial imperfections on the shell surface (Edlund, 2007). Negative Gaussian curvature in steel and hyperbolic cooling towers has been investigated by Wu et al. (2020), who focused on imperfection sensitivity within a framework of nonlinear stability. If K is equal to zero, the shell shape is cylindrical, located in the interval between the sensitive spherical shell and the insensitive inward shell, and shows a complex but highly sensitive behaviour in relation to imperfections (Hutchinson, 1968, Wang et al.,

2018, Degenhardt et al., 2012, Koiter, 1963, Wang and Sadowski, 2020, Hao et al., 2015, Schneider, 1996, Tomás et al., 2012).

During the 1950s and 70s, theoretical studies on various imperfection issues in shell structures began to grow in number. Pearson (1956) offered information on the background of stability problems in relation to imperfection. Thompson (1962), meanwhile, studied a spherical shell under external pressure and the resulting buckling paths, before Singer (1967) investigated cylindrical and conical shells strengthened by stiffeners. A general imperfection buckling criterion was arrived at by Arbocz and Babcock Jr (1969), who measured the initial geometrical imperfection applied to cylindrical structures. These stability issues were studied by the same research group in the 1970s (Arbocz, 1974), and were updated during the 1990s (Arbocz, 1992). Over time, an extensive literature on composite cylinders has been developed by Tennyson (1969), exploring both static and dynamic buckling behaviours, although a more comprehensive description can be found Thompson and Hunt (1973). The torsion effect on imperfect postbuckling of cylindrical shells has also been explored in studies by Yamaki (1976), and in a further study involving perturbation analyses (Yamki and Kodama, 1979).

If the steel shell of a wind turbine tower is made by revolution manufacture, the axisymmetric imperfection type is found regularly, although another type of imperfection, asymmetric shape, is more frequently observed on-site. Axisymmetric imperfection is a kind of ring dimple along the circumferential direction, being either convex or concave according to the original perfect cylindrical surface (Edlund, 2007, Teng and Rotter, 2006). To a certain extent, axisymmetric imperfection can be deduced from perfect shell-buckling problems, and the scatter characteristics of buckling capacity reduction is small. More specifically, axisymmetric imperfection due to welding has been studied by Rotter and Teng (1989), who concluded that plate-rolling cylinders with circumferential welded joints are highly sensitive to geometric imperfections. Local axisymmetric imperfections have been the focus of further study

by the same research group (Berry et al., 2000), and particularly in relation to steel silos and tanks, with similar outcomes seen by Pircher et al. (2001). Berry et al. (2000) claimed the ultimate buckling load loss is 79-83%, according to classical buckling loads. Khamlichi et al. (2004) investigated localised axisymmetric imperfection, basing their work on the analytical solutions of the Von karman-Donnell shell equations, and concluded that the buckling load could be up to twofold lower than that indicated by the general defects. Hutchinson (2016) introduced axisymmetric imperfections to spherical shells with different geometrical configurations to cylinders; however, some useful insights were still to be introduced to cylindrical shell-buckling problems. Symmetric breaking dimples were applied to spherical shells under external pressure, and the bifurcation buckling behaviour has been analyzed by Hutchinson and Thompson (2017).

In terms of asymmetric imperfections, the using of flattened panel strips to represent this parameter offers a general approach applicable to simpler configurations. The meridional curvature and flattened strip were introduced by Edlund (1974), and were a feature of his later works (Edlund, 2002, Edlund, 1977). Asymmetric imperfections are consistent with the asymmetric type of buckling seen on spherical caps, and have been identified in three differential equations (Kao and Perrone, 1971). Wullschleger (2006) carried out a series of numerical simulations in his thesis, proving that localised bulges are worse than localised dents. Further, he claimed that the worst non-axisymmetric dent is between two and three times the width of the deviation height of its height, while the bulge-like imperfection is normally axisymmetric. There are key questions and notions (full asymmetric material plasticities, for example) that have yet to be discussed in the literature that introduced an axisymmetric wrinkling to the NiTi tube under axial compression, and showed a relative large difference to steel tubes (Jiang et al., 2016). A series of recent studies based on FEM analysis has focussed on different shell geometries, such as cone-cylinder transition sections (Ismail et al., 2020), cylindrical steel panels (Martins and Silvestre, 2020), hyperbolic-

shaped cooling towers (Wu et al., 2020), and grid shells (Manuello, 2020). This tendency is mainly due to slow progression in theoretical analysis and the promotion of numerical simulation methods.

It is worth noting that the marked reduction that happened on shells with initial imperfection was mainly attributed to the loss of membrane part, as the bearing capacity of the shell structure is composed of the bending and the membrane part. The shape change (namely the curvature change) brought about by imperfection in a perfect shell reduces the membrane action significantly, while the membrane part plays a dominant role in shell-stress carryings. Imperfection sensitivity relates to membrane effect on initial postbuckling behaviour for cylindrical shells, as curvature changes affect the pre-buckling path that principally determines postbuckling behaviour (Hutchinson, 1968, Kempner and Chen, 1972, Aliabadi et al., 2008, Karam and Gibson, 1995, Yamaki et al., 1975).

Membrane effect on imperfect shells was the focus of a detailed study by Calladine (1995), addressing the alteration of the distribution of membrane stress along the progression of imperfections. The boundary condition, which was highlighted in his study, has a considerable effect on buckling performance. This concept was further refined in his subsequent research (Lancaster et al., 2000), and the 'locked-in' original stress was then addressed in his group's papers (Mandal and Calladine, 2000, Zhu et al., 2002). Zhu et al. (2002) claimed buckling stress in relation to thickness proportion is $t^{1.5}$ rather than the previously accepted direct proportion. However, there are many variations of theoretical representations of buckling performance in relation to thickness in the existing research (Hutchinson, 1965, Edlund, 2002). A further question exists as to whether boundary condition has a significant influence on imperfection sensitivity, in opposition to the experimental research carried out by Mandal and Calladine (2000) and Pinna and Ronalds (2004), who claimed boundary conditions showed insensitivity to imperfections, and that overall flexibility was most affected by the magnitude of axial flexibility.

Eurocode EN1993 (2007) suggests selecting the first eigenmode as the pattern for imperfection shapes, or the results of nonlinear buckling analysis. This pattern choice is widely held to be sufficient and convenient for addressing imperfection buckling analysis, while Schneider (2006) identified a 'consistent equivalent geometric imperfection' for buckling analysis based on the GMNIA scheme. The concept of quasi-collapse-affine imperfections has been mentioned in research by Schneider et al. (2005), where outcomes proved that multiple postbuckling paths determining the amplitude-depending imperfection pattern is uncertain. In this research, the first eigenmode of a linear buckling analysis (LBA) was chosen to express the initial imperfection on the shell surface. This is because the overall imperfection is better able to obtain a lower buckling result for wind turbine towers, which are easily affected by overall imperfection in the manufacturing process or installation procedure, or indeed in both. The LBA result is more convenient to apply to FEM models, especially if using the Riks method (Riks, 1997, Riks, 1979).

2.3.5 Energy methods on buckling analysis

Rather than the classical mechanics based on Newton's law, which contains the foundation of vector mechanics, energy methods formed a novel approach (Langhaar, 2016). In the original Greek work, undertaken virtually by two different formulations, one approach is found in the virtual velocities proposed by Aristotle's school, while another is the virtual displacement identified in the Hellenistic period. Energy methods built upon the substance of Bernoulli's principle for virtual work, and this could be derived from the stationary potential energy principle (Capecchi, 2012). After Legendre deduced and applied his own transformation approach to the virtual work, the principle of complementary energy became amenable to expression. Complementary energy is an ordinary expression of Castigliano's theorem (Tulczyjew, 1977). Hamilton (1834) introduced the essential Hamilton's principle in Lagrange's equations to express the motion directly, and he enhanced his method on dynamic

mechanics, especially in relation to vibration problems of structural systems (Hamilton, 1835). The concept of energy methods in applied mechanics has since been expanded to the category of algebra, and especially its variational methods; many mathematicians and mechanicians have improved and enhanced this method, such as Galerkin, Ritz, Rayleigh, Fourier, and Von Karman (Langhaar, 2016). The virtual work method is as comprehensively accurate as the vectorial methods, and offers an easier way to obtain solutions at an acceptable precision than classical mechanics containing numerous equations with no analytical solution.

Energy methods applied to buckling issues can be traced to Von Karman and Tsien (1941), who dealt with equations of nonlinear buckling proposed by Donnell (1934). They argued that the best approach to obtaining a solution is to calculate by means of energy concept. A simple pin-ended column was studied as the basis of shell buckling (Von Karman et al., 1940), and the equilibriums were able to explain the buckling-mode jumping behaviour, as well as the much lower buckling load than had been indicated by experimental results.

Energy-based analysis has been proposed as a solution to initial geometry imperfection problems by Donnell and Wan (1950), via modified energy calculation that lifts the results of Von Karman and Tsien (1941) to greater precision. Koiter (1945) found a form of equilibrium by taking the first derivative of the potential energy function, which indicated the equivalent buckling path in the vicinity of the bifurcation point. The meaning of the second order derivative in relation to stability issues has also been discussed Koiter's research. By applying the 'airy stress function' to potential energy expressions, a series of general total potential energy functions could be obtained, combined with the Euler equations that are equivalent to the general form of functions derived by Flügge (2013).

The cylindrical shell can be regarded as a conservative system along a relative not-too-long shell section; therefore, a series of simultaneous equations can be created with the concept of energy balance, and the external work is equal to the internal work.

When buckling happens, the expression of virtual work changes the character from positive to negative definiteness, sometimes to negative semi-definiteness, or even indefiniteness. This approach allows us to measure whether buckling has been triggered or not, based on the interactions between virtual works and displacements in the conservative system (Langhaar, 2016). Thompson and Hunt (1973) solved some buckling problems by introducing equilibrium between the increments of internal potential energy and work performed by external forces.

Energy methods explain multiple equivalent buckling paths near the bifurcation point, through a series of unstable equations in various forms. Previous studies have emphasised buckling behaviour under axial compression via energy concepts. Kidane et al. (2003) studied several grid-stiffened composite cylinders via the Ritz energy method for buckling load analysis, and the results were compared with experimental outcomes. Fok (2002) applied the energy method combined with the Rayleigh-Ritz trial function in an analysis featuring a long cylinder shell embedded in an elastic material. He concluded that the buckling load has a close relationship to the Poisson's ratio of the surrounding materials. This research reveals the influence of external pressure applied to shell structures; this external boundary condition had also been explored in prior studies by Forrestal and Herrmann (1965). The Ritz energy method has been discussed in a nonlinear elastic buckling analysis of cylindrical shells under compression loads, because of Donnell's assumptions, with mode-jumping behaviour observed in postbuckling stages (Huang and Han, 2009). A different cylinder configuration, with an elastic core, has also been investigated by Arani et al. (2007), who compared results with that of a hollow cylinder with equal mass. Recently, the author of this research published a simplified framework of energy methods for buckling analysis of wind turbine towers under combined loads (Ma et al., 2020), and this thesis lays out extended work in the same area.

2.4 Concluding remarks

This chapter presented a detailed literature review from two main perspectives: historical case studies examining wind turbine tower collapse, and the introduction of buckling theories for wind turbine tower analysis.

The most common reasons for wind turbine tower collapses were identified in the updated historical case study. It emerged that these were unexpected extreme wind load levels, combined with human errors such as poor quality-control, faulty construction, erroneous operation and improper maintenance. The extreme wind is identified as the most common major cause, and hence combined loads must be considered when analysing shell structure buckling. The typical buckling types have been concluded, which enlightened us the guide directions of buckling types for the buckling analysis in the latter sections. More specifically, the practical ranges of wind turbine tower collapse demonstrated a phenomenon in which the wavenumber in the circumferential direction was between 1 and 9, and usually in the range from 3 to 6; meanwhile, the longitudinal wavenumber had a narrower variation, between 1 and 4.

The brief review of basic buckling theories provided us with the fundamental concept of the framework for buckling analysis of wind turbine towers under combined loading conditions, via step-by-step development of equations from classical buckling analysis to the nonlinear novel energy method.

3 CLASSICAL SHELL BUCKLING ANALYSIS

3.1 Buckling problems in columns and plates

Analytical buckling analysis research into structure can be traced to the eighteenth century, where we find Euler's theory in relation to buckling in simple structures such as columns. Euler investigated an initially straight pin-ended rod and applied a concentrated load (P) along the axis of the rod. He then expressed the local curvature (K) of the rod curve $y(x)$ in the coordinate as:

$$\kappa = \frac{\mathrm{d}^2 y}{\mathrm{d}x^2} \Big/ \left[1 + \left(\frac{\mathrm{d}y}{\mathrm{d}x}\right)^2\right]^{\frac{3}{2}} \tag{3.1}$$

If the lateral displacement is very small, Equation (3.1) could be simplified to:

$$\kappa = \frac{\mathrm{d}^2 y}{\mathrm{d}x^2} \tag{3.2}$$

The buckling of a rod-shown buckling path contains a primary and secondary path, of the relation between axial load P and the central lateral deflection ω, depicted in Figure 3.1. The (a) in Figure 3.1 represents a perfect straight rod under axial loads, while (b) describes the buckled shape, and (c) illustrates the multiple potential buckling paths to the straight rod, divided by the bifurcation point and including the primary and secondary path. (d), a rod with an initial bend, shows no bifurcation point throughout the buckling process.

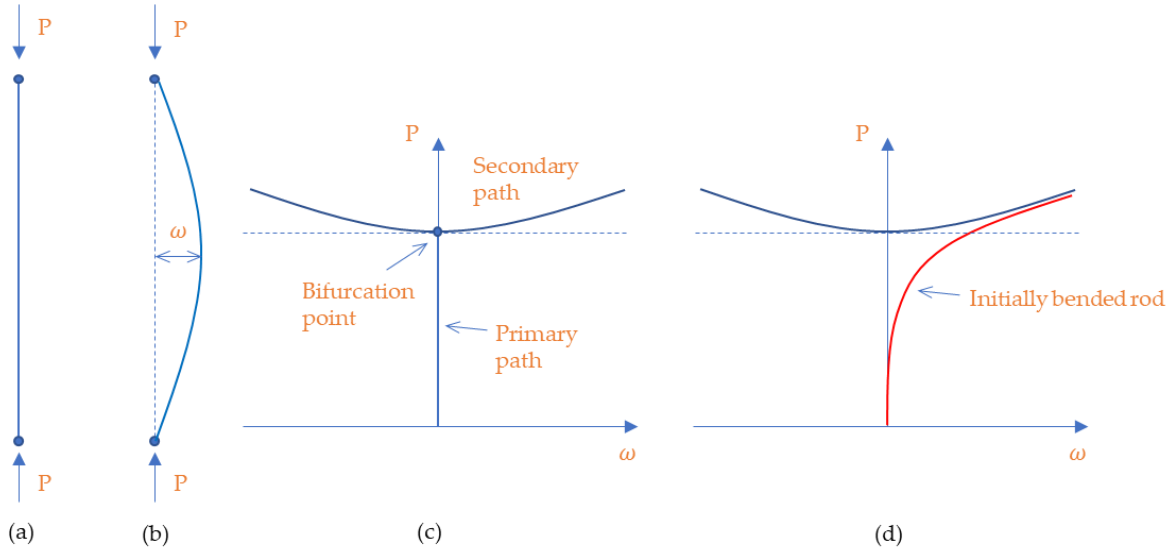


Figure 3.1. Buckling behaviours of pin-ended rods under axial concentrate loads: (a) initially straight rod; (b) buckled rod; (c) multiple buckling paths on a straight rod; (d) no bifurcation point along the buckling path on an initially crooked rod.

Euler then concluded the famous formula of the curved path as:

$$P = P_{\mathrm{E}} = \pi^2 EI/l^2 \tag{3.3}$$

Here, P_{E} represents the Euler buckling load, while EI is the flexural rigidity of the rod.

However, simple Euler buckling equations are inadequate for advanced buckling problems such as cylindrical-shell buckling, and nonlinear buckling. As aforementioned, nonlinear buckling theory developed largely in the 1940s through the 'two-surface' model (Donnell and Wan, 1950, Donnell, 1934). By regarding the rod as a tube with two surfaces, distorted configuration can be represented by a funicular curve connected to the inner lateral force f_1. The equivalent lateral force f_1 can be expressed in the form of a sinusoidal function as:

$$f_1 = (-P\pi^2\omega_0/l^2)\sin(\pi x/l) \tag{3.4}$$

Here, ω_0 is the small amplitude of a curved rod. The expression for the tube on another surface is beam-like, then:

$$f_2 = EI\frac{\mathrm{d}^4\omega}{\mathrm{d}x^4} \tag{3.5}$$

EI represents the flexural stiffness for the rod, and Equation (3.5) is expressed in sinusoidal form (Calladine and Sanders, 1984):

$$f_2 = (EI\pi^4/I^4)\omega_0 \sin(\pi x/l) \tag{3.6}$$

Also, ω_0 can be expressed in terms of f_2, if the small amplitude is unknown:

$$w_0 = \frac{I^3 f_2}{\pi^4 E \sin\left(\frac{\pi x}{l}\right)} \tag{3.7}$$

By allowing $f_1 + f_2 = 0$, which means externally lateral force equals zero, the eigenvalue of the buckling amenable to the form shown in Equation (3.3). The remarkable sinusoidal function in previous steps introduced the best way to represent lateral deviation from the original position, using the function format as:

$$\omega = \omega_n \sin(n\pi x/l) \tag{3.8}$$

This is available longitudinally for cylindrical shells, despite their circumferential geometrical difference when compared with a simple rod.

Euler's theory was then expanded to flat plates, considering the unit forces on the edge of each element, and on the entire rectangular plate. The in-plane stress is maintained with a relatively steady magnitude, and the curvature and twist happening to a plate can be written as:

$$\kappa_x = \frac{-\partial^2 w}{\partial x^2}, \kappa_y = \frac{-\partial^2 w}{\partial y^2}, \kappa_{xy} = \frac{-\partial^2 w}{\partial x\, \partial y} \tag{3.9}$$

Then we have the equilibrium of uniform forces N_x, N_y and lateral force p_{S}, the pressure on the plate:

$$(-N_x)\frac{\partial^2 \omega}{\partial x^2} + (-N_y)\frac{\partial^2 \omega}{\partial y^2} = p_{\mathrm{S}} \tag{3.10}$$

This explains the stretching surface, while the bending surface can be derived as:

$$D\nabla^4 w = p_{\mathrm{B}} \tag{3.11}$$

Here, D is the flexural rigidity of the plate and ∇ is Laplace calculation (Calladine and Sanders, 1984).

Applying the similar concept of the aforementioned rod to the plate, let the lateral forces on the bending surface be equal to the lateral force generated on the stretching surface; namely, $p_S + p_B = 0$, the well-known formula derived by Timoshenko et al. (1951):

$$(-N_x)\frac{\partial^2 w}{\partial x^2} + (-N_y)\frac{\partial^2 w}{\partial y^2} = -D\nabla^4 w \tag{3.12}$$

This is the governing equation for a rectangular plate when it is buckled. Moreover, we can apply the promoted sinusoidal function to describe the flat plate's deviation amplitude based on Equation (3.8):

$$\omega = \omega_{mn}\sin(m\pi x/L)\sin(n\pi y/B) \tag{3.13}$$

Here, L represents the length of the plate, and B represents the width. The simplified form of the equation (3.12) has been addressed by Calladine and Sanders (1984):

$$(-N_x)(m\pi/L)^2 + (-N_y)(n\pi/B)^2 = D[(m\pi/L)^2 + (n\pi/B)^2]^2 \tag{3.14}$$

Here, m represents the wavenumber along its length and n is the wavenumber in width direction. This expression provides us with a trial approach with which to find the minimum buckling load of a plate, as well as offering insight into cylindrical shells.

3.2 Geometries and curvatures of cylindrical shells

Before we address classical buckling analysis, the geometry of cylinders and its curvature should be investigated. We can represent the buckling type seen in wind turbine towers by a series of curvature equations, which are connected equivalently to stretch strains happening in-plane (Calladine and Sanders, 1984). The strain-curvature relationships can be derived through Figure 3.2.

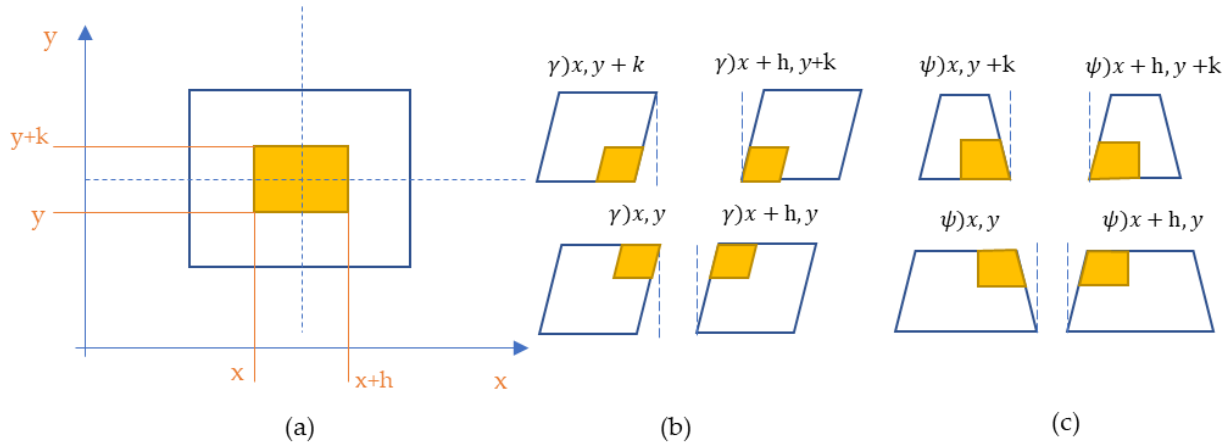


Figure 3.2. Angular displacements for a flat plate. (a) A rectangular plate element. (b) Shear distortion. (c) Tensile distortion.

In Figure 3.2 (a), we assume a perfect undeformed rectangle in x-y plane with four vertices *(x,y), (x, y+k), (x+h, y), and (x+h, y+k)* at original positions respectively, shown as yellow-shaded. Under the condition of the limits as h→0 and k→0, when the strains happened to the shaded element, the local Gaussian curvature could be calculated by the angular displacement divided by the respective area related to each vertex. When the shear-strain applied, as shown in Figure 3.2 (b), with the shear-strain component γ_{xy}, and the strain component along x-direction ϵ_x, we have the Gaussian curvature K (Calladine and Sanders, 1984), in terms of γ_{xy}:

$$K = \frac{\partial^2 \gamma_{xy}}{\partial x \, \partial y} \tag{3.15}$$

If we do the reassemble to the deformed shapes, the width of each rectangle will change slightly to a trapezoidal shape as shown in Figure 3.2(c). Then the angular displacement of the shaded area at the joint is:

$$\frac{1}{2}h\left\{\left(\frac{\partial \epsilon_x}{\partial y}\right)_{x,y} + \left(\frac{\partial \epsilon_x}{\partial y}\right)_{x+h,y} - \left(\frac{\partial \epsilon_x}{\partial y}\right)_{x,y+k} - \left(\frac{\partial \epsilon_x}{\partial y}\right)_{x+h,y+k}\right\} \tag{3.16}$$

Using Equation (3.16) divided by the area hk, and getting the limit when hk approaches zero, we then obtain K, in terms of ϵ_x:

$$K = \frac{-\partial^2 \epsilon_x}{\partial y^2} \tag{3.17}$$

More generally, if there exists the horizontal strain term ϵ_y, combining (3.15) and (3.17), a general form of local curvature is:

$$K = -\frac{\partial^2 \epsilon_y}{\partial x^2} + \frac{\partial^2 \gamma_{xy}}{\partial x\, \partial y} - \frac{\partial^2 \epsilon_x}{\partial y^2} \tag{3.18}$$

In the case of wind turbine towers, the Gaussian curvature of cylindrical shell is equal to zero; thus, the local curvature is equal to zero at any point on the shell; if buckling fails to occur, whether local buckling or overall buckling, then this can be expressed as:

$$\frac{\partial^2 \epsilon_y}{\partial x^2} - \frac{\partial^2 \gamma_{xy}}{\partial x\, \partial y} + \frac{\partial^2 \epsilon_x}{\partial y^2} = 0 \tag{3.19}$$

This equilibrium, the plane-strain compatibility condition, provides us with a criterion with which to measure whether buckling has happened or not. Additionally, this equilibrium is dynamic-available, although it based on classical concepts that could be integrated at any time point or during any time period. However, it needs very high levels of calculation resource. After shell buckling has happened, changes in the local Gaussian curvature can be written as:

$$\frac{\partial^2 \epsilon_y}{\partial x^2} - \frac{\partial^2 \gamma_{xy}}{\partial x\, \partial y} + \frac{\partial^2 \epsilon_x}{\partial y^2} = \Delta K_i \tag{3.20}$$

Figure 3.3 shows a portion of the cylindrical shell section,[1] embedded within a cylindrical coordinate system, and all acting loads on its surface and boundaries:

[1] This paragraph section has been published in Ma, Martinez-Vazquez and Baniotopoulos (2020). Yang Ma was the primary author, while Pedro Martinez-Vazquez and Charalampos Baniotopoulos contributed with reviewing, editing and supervision of the paper.

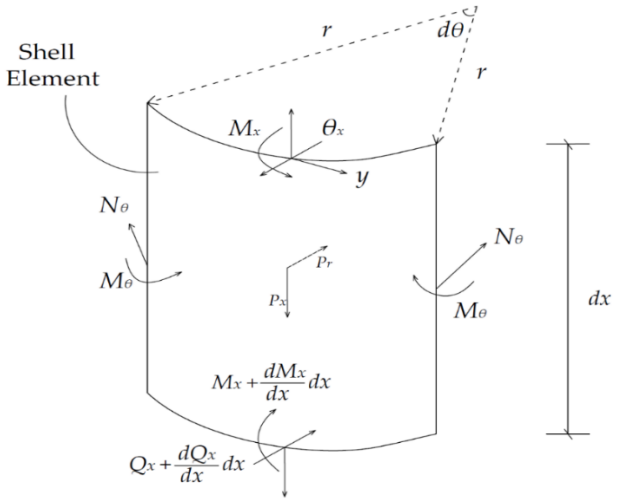


Figure 3.3. Loads on a shell element

The Cartesian coordinate system marked as x-y-z comprises x representing the direction along the axis of the shell section, and z the normal nature of the shell surface. This coordinate system is equivalent to the x-θ-r coordinate system. N_θ is the boundary of the primary compression/tension force of the element; M_θ is the moment generated according to the θ coordinate; Q is the force along the tube axis; P is the surface pressure; and r is the radii of the cylindrical shell.

In terms of the circumferential element displacement, as can be seen in Figure 3.4 ds is used to represent the original shell surface. Meanwhile, ds' is the displaced shell mid-surface, and df represents the displacement in z direction. In such terms, the distortion rate of the shell element is revealed as:

$$\frac{\partial\theta}{\partial s} = \frac{\partial\theta}{r\,\partial\theta} = \frac{1}{r} \tag{3.21}$$

$$\frac{\partial\theta'}{\partial s'} = \frac{d\theta + \left(\frac{\partial^2 f}{\partial s^2}\right) ds}{(r-f)d\theta} \tag{3.22}$$

$$x_\theta = \frac{\partial\theta'}{\partial s'} - \frac{1}{r} \approx \frac{1}{r^2}\left(f + \frac{\partial^2 f}{\partial\theta^2}\right) \tag{3.23}$$

$$x_{x\theta} r d\theta = -\left(\frac{\partial^2 f}{\partial x\,\partial\theta} + \frac{\partial v}{\partial x}\right) d\theta \tag{3.24}$$

In Equation (3.24), $x_{x\theta}$ represents the distortion rate of the cross-section of the shell's surface, and $rd\theta$ is the arc length of the selected shell element.

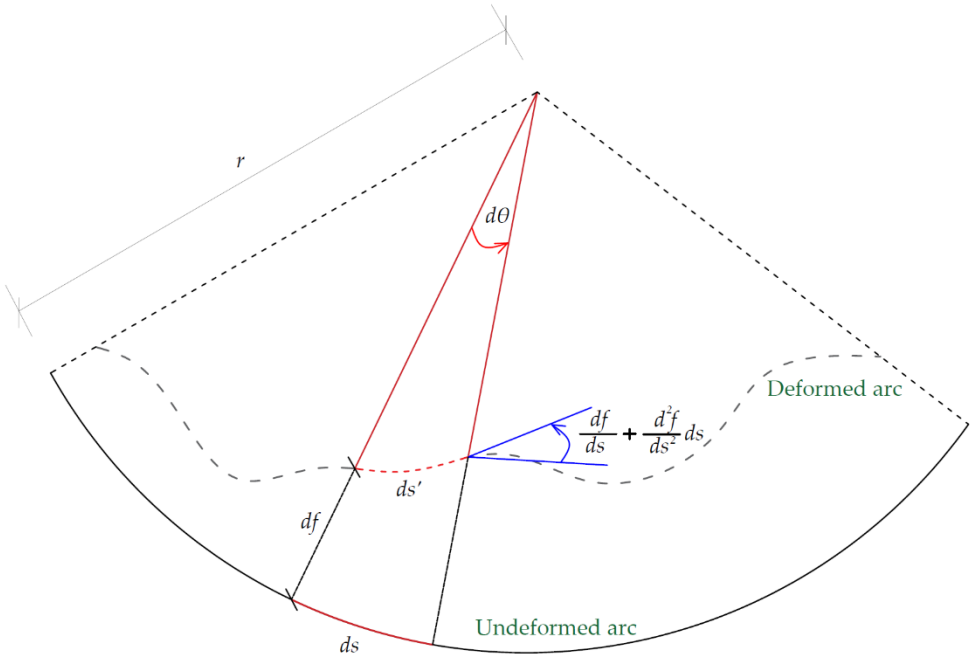


Figure 3.4. Assumed circumferential shell element deformation

On the assumption that the shell mid-surface is inextensible, shell-surface displacement shows variations in the x-axis, along the radial and normal-to-radial direction. Ignoring the mid-surface strain change, the first simultaneous function could thus be written as:

$$\begin{cases} \dfrac{\partial u}{\partial x} = 0 = \varepsilon_x \\ \dfrac{\partial v}{r\partial\theta} - \dfrac{f}{r} = 0 \\ \dfrac{1}{r}\dfrac{\partial u}{\partial\theta} + \dfrac{\partial v}{\partial x} = 0 = \gamma_{x\theta} \end{cases} \tag{3.25}$$

The local Gaussian curvature of the shell in Figure 3.3 can find extrinsic expression in terms of the principal radii of curvature R_1R_2 according to the principal directions X, Y, showing as (Hilbert and Cohn-Vossen, 1999):

$$K = \frac{1}{R_1 R_2} \tag{3.26}$$

The Cartesian coordinate interconnection, meanwhile, could be written as:

$$Z = (X^2/2R_1) + (Y^2/2R_2) \tag{3.27}$$

We use κ_1, κ_2 as the change of curvature in the principal directions X, Y, namely, 1, 2, at a certain local point; we then undertake a differential on Equation (3.26), the general formation of local curvature change ΔK_i being:

$$\Delta K_i = \frac{\kappa_1}{R_2} + \frac{\kappa_2}{R_1} = -\frac{\partial^2 \epsilon_y}{\partial x^2} + \frac{\partial^2 \gamma_{xy}}{\partial x\, \partial y} - \frac{\partial^2 \epsilon_x}{\partial y^2} \tag{3.28}$$

This equation forms the foundation of the membrane effect calculation, as well as the of the relationships between displacement and curvature changes (Calladine and Sanders, 1984, Teng and Rotter, 2006). We then use u, v, to represent the tiny displacement on the element. As shown in Figure 3.3, the strain and curvature expression on shell surface can be expressed as:

$$\begin{aligned}
\epsilon_x &= \frac{\partial u}{\partial x} \\
\epsilon_y &= \frac{\partial v}{\partial y} + \frac{\omega}{a} \\
\gamma_{xy} &= \frac{\partial v}{\partial x} + \frac{\partial u}{\partial y} \\
\kappa_x &= -\frac{\partial^2 \omega}{\partial x^2} \\
\kappa_y &= -\frac{\partial^2 \omega}{\partial y^2} - \frac{\omega}{a^2} \\
\kappa_{xy} &= -\frac{\partial^2 \omega}{\partial x\, \partial y} + \frac{1}{a}\frac{\partial v}{\partial x}
\end{aligned} \tag{3.29}$$

In the simultaneous equations, a represents the radius of the shell surface according to r. The reversed relation between the radial displacement ω and the curvature changes as follows:

$$\begin{aligned}
\omega(x) &= C_1 + C_2 x - \frac{kappa_x x^2}{2} \\
\omega(y) &= C_1 e^{-\frac{iy}{a}} + C_2 e^{\frac{iy}{a}} - a^2 kappa_y
\end{aligned} \tag{3.30}$$

Here, *kappa* represents Kappa curve (also known as Gutschoven's curve) with its curvature as (Lawrence, 2013):

$$\kappa(\theta) = \frac{8(3 - \sin^2\ \theta)\sin^4\ \theta}{a(\sin^2\ (2\theta) + 4)^{\frac{3}{2}}} \tag{3.31}$$

The alteration derived from Equation (3.29) can account for displacements if shell surface strains have obtained, as shown by Calladine and Sanders (1984):

$$\frac{1}{a}\frac{\partial^2 w}{\partial x^2} = \frac{\partial^2 \epsilon_y}{\partial x^2} - \frac{\partial^2 \gamma_{xy}}{\partial x\, \partial y} + \frac{\partial^2 \epsilon_x}{\partial y^2} \tag{3.32}$$

It is important to mention the difference and transformation between the cylindrical coordinate and the Cartesian coordinate in this research, to support subsequent analysis. Figure 3.5 shows a general shell element in the Cartesian coordinate system: a point P with coordinate (x, y, z) can be expressed via three parameters α, β, γ, based on three functions in the space:

$$x = f_1(\alpha, \beta, \gamma), y = f_2(\alpha, \beta, \gamma), z = f_3(\alpha, \beta, \gamma) \tag{3.33}$$

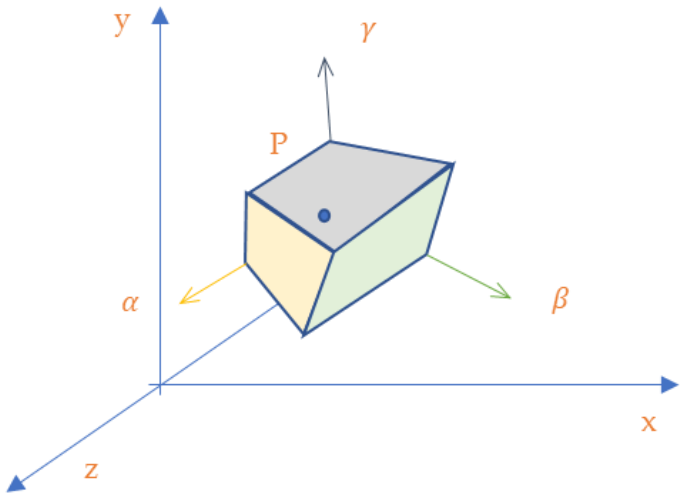


Figure 3.5. A random shell element in Cartesian coordinate system.

This gives us the total derivative on x, y, z:

$$\left.\begin{aligned} \mathrm{d}x &= \frac{\partial x}{\partial \alpha}\mathrm{d}\alpha + \frac{\partial x}{\partial \beta}\mathrm{d}\beta + \frac{\partial x}{\partial \gamma}\mathrm{d}\gamma \\ \mathrm{d}y &= \frac{\partial y}{\partial \alpha}\mathrm{d}\alpha + \frac{\partial y}{\partial \beta}\mathrm{d}\beta + \frac{\partial y}{\partial \gamma}\mathrm{d}\gamma \\ \mathrm{d}z &= \frac{\partial z}{\partial \alpha}\mathrm{d}\alpha + \frac{\partial z}{\partial \beta}\mathrm{d}\beta + \frac{\partial z}{\partial \gamma}\mathrm{d}\gamma \end{aligned}\right\} \tag{3.34}$$

The arc length along curve α is represented by $\mathrm{d}s_1 = \sqrt{\mathrm{d}x^2 + \mathrm{d}y^2 + \mathrm{d}z^2}$, then expressed via α, β, γ is $\mathrm{d}s_1 = \left[\left(\frac{\partial x}{\partial \alpha}\mathrm{d}\alpha\right)^2 + \left(\frac{\partial y}{\partial \alpha}\mathrm{d}\alpha\right)^2 + \left(\frac{\partial z}{\partial \alpha}\mathrm{d}\alpha\right)^2\right]^{1/2}$. The Lame parameters H were applied to representing the ratio between the increments along arc α and the increments of the Cartesian coordinates, fully expressed as:

$$\left.\begin{aligned} H_1 &= \left[\left(\frac{\partial x}{\partial \alpha}\right)^2 + \left(\frac{\partial y}{\partial \alpha}\right)^2 + \left(\frac{\partial z}{\partial \alpha}\right)^2\right]^{1/2} \\ H_2 &= \left[\left(\frac{\partial x}{\partial \beta}\right)^2 + \left(\frac{\partial y}{\partial \beta}\right)^2 + \left(\frac{\partial z}{\partial \beta}\right)^2\right]^{1/2} \\ H_3 &= \left[\left(\frac{\partial x}{\partial \gamma}\right)^2 + \left(\frac{\partial y}{\partial \gamma}\right)^2 + \left(\frac{\partial z}{\partial \gamma}\right)^2\right]^{1/2} \end{aligned}\right\} \tag{3.35}$$

Here, H_1, H_2, H_3 represent the Lame parameters along α, β, γ directions respectively.

Further, six simultaneous equations could be obtained, revealing relationships between H_1, H_2, H_3 and α, β, γ:

$$\left.\begin{aligned} \frac{1}{H_1^2}\frac{\partial H_2}{\partial \alpha}\frac{\partial H_3}{\partial \alpha} + \frac{\partial}{\partial \beta}\left(\frac{1}{H_2}\frac{\partial H_3}{\partial \beta}\right) + \frac{\partial}{\partial \gamma}\left(\frac{1}{H_3}\frac{\partial H_2}{\partial \gamma}\right) &= 0 \\ \frac{1}{H_2^2}\frac{\partial H_3}{\partial \beta}\frac{\partial H_1}{\partial \beta} + \frac{\partial}{\partial \gamma}\left(\frac{1}{H_3}\frac{\partial H_1}{\partial \gamma}\right) + \frac{\partial}{\partial \alpha}\left(\frac{1}{H_1}\frac{\partial H_3}{\partial \alpha}\right) &= 0 \\ \frac{1}{H_3^2}\frac{\partial H_1}{\partial \gamma}\frac{\partial H_2}{\partial \gamma} + \frac{\partial}{\partial \alpha}\left(\frac{1}{H_1}\frac{\partial H_2}{\partial \alpha}\right) + \frac{\partial}{\partial \beta}\left(\frac{1}{H_2}\frac{\partial H_1}{\partial \beta}\right) &= 0 \end{aligned}\right\} \tag{3.36}$$

and:

$$\left.\begin{aligned}
&\frac{\partial^2 H_1}{\partial\beta\,\partial\gamma}-\frac{1}{H_2}\frac{\partial H_1}{\partial\beta}\frac{\partial H_2}{\partial\gamma}-\frac{1}{H_3}\frac{\partial H_1}{\partial\gamma}\frac{\partial H_3}{\partial\beta}=0\\
&\frac{\partial^2 H_2}{\partial\gamma\,\partial\alpha}-\frac{1}{H_3}\frac{\partial H_2}{\partial\gamma}\frac{\partial H_3}{\partial\alpha}-\frac{1}{H_1}\frac{\partial H_2}{\partial\alpha}\frac{\partial H_1}{\partial\gamma}=0\\
&\frac{\partial^2 H_3}{\partial\alpha\,\partial\beta}-\frac{1}{H_1}\frac{\partial H_3}{\partial\alpha}\frac{\partial H_1}{\partial\beta}-\frac{1}{H_2}\frac{\partial H_3}{\partial\beta}\frac{\partial H_2}{\partial\alpha}=0
\end{aligned}\right\} \tag{3.37}$$

Equation (3.36) and (3.37) express the interconnections between six radius-of-curvature and three Lame parameters. Afterwards, the six components of strains can be obtained:

$$\left.\begin{aligned}
\varepsilon_1 &= \frac{1}{H_1}\frac{\partial u_1}{\partial\alpha}+\frac{1}{H_1H_2}\frac{\partial H_1}{\partial\beta}u_2+\frac{1}{H_1H_3}\frac{\partial H_1}{\partial\gamma}u_3\\
\varepsilon_{12} &= \frac{H_2}{H_1}\frac{\partial}{\partial\alpha}\left(\frac{u_2}{H_2}\right)+\frac{H_1}{H_2}\frac{\partial}{\partial\beta}\left(\frac{u_1}{H_1}\right)\\
\varepsilon_2 &= \frac{1}{H_2}\frac{\partial u_2}{\partial\beta}+\frac{1}{H_2H_3}\frac{\partial H_2}{\partial\gamma}u_3+\frac{1}{H_2H_1}\frac{\partial H_2}{\partial\alpha}u_1\\
\varepsilon_{23} &= \frac{H_3}{H_2}\frac{\partial}{\partial\beta}\left(\frac{u_3}{H_3}\right)+\frac{H_2}{H_3}\frac{\partial}{\partial\gamma}\left(\frac{u_2}{H_2}\right)\\
\varepsilon_3 &= \frac{1}{H_3}\frac{\partial u_3}{\partial\gamma}+\frac{1}{H_3H_1}\frac{\partial H_3}{\partial\alpha}u_1+\frac{1}{H_3H_2}\frac{\partial H_3}{\partial\beta}u_2\\
\varepsilon_{31} &= \frac{H_1}{H_3}\frac{\partial}{\partial\gamma}\left(\frac{u_1}{H_1}\right)+\frac{H_3}{H_1}\frac{\partial}{\partial\alpha}\left(\frac{u_3}{H_3}\right)
\end{aligned}\right\} \tag{3.38}$$

Here, the ε_{ij} represents shear strains and ε_i represents primary strains.

If the mid-surface maintains a certain distance to a regular point z or a plane, the stress–strain relation (based on Hook's Law) can be given as:

$$\left.\begin{aligned}
\sigma_\alpha &= \frac{E}{1-\nu^2}\left(\varepsilon_\alpha+\nu\varepsilon_\beta\right)\\
\sigma_\beta &= \frac{E}{1-\nu^2}\left(\varepsilon_\beta+\nu\varepsilon_a\right)\\
\tau_{\alpha\beta} &= \frac{E}{2(1+\nu)}\gamma_{a\beta}
\end{aligned}\right\} \tag{3.39}$$

Here, ν is Poisson's ratio, σ_α, σ_β representing the primary stress along the α,β axis, and $\tau_{\alpha\beta}$ is the shear stress. Equation (3.39) is a form of physical expression for a general shell element; this could be improved for particular usage. Novozhilov (1959) recommended a very simple form for the expansion of these long and complex

physical equations from the perspective of strain-energy concept; this will be discussed in later sections.

3.3 Stress and strain in axially compressed cylindrical shells

3.3.1 Basic relations for shells under axial compression

From Figure 3.3, we derive expressions for stress and strain in the cylindrical shells of a wind turbine tower. This then reveals the relationships between general forces, stresses, strains, and displacements on tube surface.[2]

The circumferential load N_θ and moment M_θ do not vary with coordinate θ, because the circumferential displacement equals zero in this adopted linear model. Furthermore, by letting u, v, and f be the displacements in x, y, and z directions respectively, one derives the following basic equilibrium equations (Calladine and Sanders, 1984, Eslami, 2017, Donnell, 1934):

$$\begin{cases} \dfrac{dN_x}{dx} dx \cdot rd\theta + P_x rd\theta dx = 0 \ (x - axis) \\ \dfrac{d\theta_x}{dx} dx \cdot rd\theta + N_\theta \tan\theta \, d\theta + P_r dx \cdot rd\theta = 0 \ (z - axis) \\ in \ which \ \tan d\theta \approx d\theta \\ \dfrac{dM_x}{dx} dx \cdot rd\theta - (Q_x rd\theta dx) = 0 \ (y - axis \ moment) \end{cases} \tag{3.40}$$

It follows that, by cancelling out similar items dx and $rd\theta$, Equation (3.40) becomes:

$$\begin{cases} \dfrac{dN_x}{dx} + P_x = 0 \\ \dfrac{d\theta}{dx} + \dfrac{1}{r} N_\theta - P_r = 0 \\ \dfrac{dM_x}{dx} - Q_x = 0 \end{cases} \tag{3.41}$$

[2] Some of the following paragraphs have been published in Ma, Martinez-Vazquez and Baniotopoulos (2020). Yang Ma was the primary author, while Pedro Martinez-Vazquez and Charalampos Baniotopoulos contributed with reviewing, editing and supervision of the paper.

$$N_x = \frac{Et}{1-\nu^2}\left(\frac{du}{dx} - \nu\frac{f}{r}\right) \tag{3.42}$$

Here, ν represents the Poisson ratio (assumed to be 0.3 for structural steel). Moreover, taking into consideration the stress–strain relationship as per Hook's law (according to Equation (3.39)) while letting ε represent the strain, the following equations develop:

$$N_\theta = \frac{Et}{1-\nu^2}(\varepsilon_\theta + \nu\varepsilon_x) = -\frac{Et}{1-\nu^2}\left(\frac{f}{r} - \frac{du}{dx}\right) \tag{3.43}$$

Here, we note that the relation between M_x and displacement f can map from a plane slab once curved to a cylindrical shell:

$$M_x = -D\frac{d^2f}{dx^2} \tag{3.44}$$

$$M_\theta = \nu M_x \tag{3.45}$$

$$D = \frac{Et^3}{12(1-\nu^2)} \tag{3.46}$$

D here is the stiffness of the slab-like shell.

To eliminate the term Q_x from Equation (3.41), however, we follow:

$$\frac{d^2}{dx^2}\left(D\frac{d^2f}{dx^2}\right) + \frac{Eh}{r}f - \nu N_x - P_r = 0 \tag{3.47}$$

Equation (3.47) can be simplified by letting $P_r = 0$, which seems sensible for a tower shell without radial pressure imposed on it:

$$D\frac{d^4f}{dx^4} + \frac{Eh}{r}f - \nu\frac{N_x}{r} = 0 \tag{3.48}$$

Equations (3.47) or (3.48) are basic differential equations for cylindrical shells, here representing a portion of the wind turbine tower, the solution to which is (Elaydi, 2005):

$$f = C_1e^{h_1x} + C_2e^{h_2x} + C_3e^{h_3x} + C_4e^{h_4x} \tag{3.49}$$

Here, the terms C_i are constants of the integration while h_i are roots to the following polynomial:

$$h^4 + 4\beta^4 = 0 \qquad \beta = \frac{Et}{4Dr^2} = \frac{3(1-v^2)}{r^2 t} \tag{3.50}$$

If the dimension of β is reciprocal to the length L, then we find:

$$h = \pm\beta(1 \pm i) \tag{3.51}$$

$$f = e^{-\beta x}\left(C_1 e^{i\beta x} + C_2 e^{-i\beta x}\right) + e^{\beta x}\left(C_3 e^{i\beta x} + C_4 e^{-i\beta x}\right) \tag{3.52}$$

$$f = e^{-\beta x}(C_1 \cos\beta x + C_2 \sin\beta x) + e^{\beta x}(C_3 \cos\beta x + C_4 \sin\beta x) + f(x) \tag{3.53}$$

Equation (3.53) defines f as the displacement field in direction z and stands as the general solution to Equation (3.47).

3.3.2 The eigenvalue calculation in linear buckling

Linear analysis for buckling problems in cylindrical shells under compression offers a basic step for further advanced analysis such as combined loading conditions, nonlinear buckling analysis, and imperfection issues (Timoshenko and Goodier, 2011). The methodology applied for the previous rod, the 'two-surface' concept, might usefully be applied to cylinders here. The assumption is that the planer x-y coordinate will now be expanded to a cylindrical angular coordinate, allowing $\theta = y/a$. The implementation of this 'two-surface' concept on the cylinder shell is to assume there exists an external pressure throughout the shell surface, and that this is equal to the lateral forces generated by the buckled shell. Thus we apply the aforementioned sinusoidal functions to represent the pressure in a similar form to Equation (3.13):

$$p = p_r \sin(\pi x/l)\sin(\pi y/b) \tag{3.54}$$

Here, p is the pressure generated on the shell surface; p_r as denoted in Figure 3.3, the applied pressure on the shell surface; and l and b the longitudinal and circumferential half wavelength on shells. If we accept the continuous cylindrical shell as having unchanged in-plane stresses—that is N_x, N_y, N_{xy} are constants throughout the shell

section—the localised additional pressure Δp_1 can be given by changes of local curvatures (Calladine and Sanders, 1984):

$$-\Delta p_1 = (-N_x)\kappa_x - 2N_{xy}\kappa_{xy} + \left(-N_y\right)\kappa_y \tag{3.55}$$

At the earlier pre-buckling stage, the wavenumber was high (Yamaki, 1985), thus we could omit the circumferential displacement happening on cylinders, and Equation (3.55) can be given as:

$$\Delta p_1 = (-N_x)\frac{\partial^2 \omega}{\partial x^2} - 2N_{xy}\frac{\partial^2 \omega}{\partial x\,\partial y} + \left(-N_y\right)\frac{\partial^2 \omega}{\partial y^2} \tag{3.56}$$

The lateral force's sum of bending surface and stretching surface equals zero, then, and the pressure generated by bending is:

$$\frac{\partial^2 M_x}{\partial x^2} + \frac{2\,\partial^2 M_{xy}}{\partial x\,\partial y} + \frac{\partial^2 M_y}{\partial y^2} = -p_{\mathrm{B}} \tag{3.57}$$

Moreover, $-\Delta p_1 + p_{\mathrm{B}} = 0$ stands for an axially compressed cylinder shell without any realistic applied lateral pressure. Based on the equations given above, the eigenvalues of buckling can be obtained in a linear elastic range, which provides a series of simple surface displacements for the later arc length method and initial geometrical imperfections. This series of eigenmode is shown as in Equation (3.13):

$$\omega = \omega_n \sin(\pi x/l)\sin(\pi y/b) \tag{3.58}$$

Here, the l and b should be integers and continuous, due to the real boundary conditions of the wind turbine tower shell: the edges of the tower shell will be regarded as rigid, and the circumferential wave should be continuous in a certain number of entire periods. A more general form of the displacement shape of the tower shell takes an asymmetric form, in which a specific shape is axisymmetric, and the normal pressure is in the form of (Calladine and Sanders, 1984):

$$p_n = w_n\left[\frac{Et}{a^2 l^4}\left(\frac{1}{l^2} + \frac{1}{b^2}\right)^{-2} + \frac{\pi^4 E t h^2}{12}\left(\frac{1}{l^2} + \frac{1}{b^2}\right)^2\right] \tag{3.59}$$

Here, $\frac{Et}{a^2l^4}\left(\frac{1}{l^2}+\frac{1}{b^2}\right)^{-2}$ represents the stretching part and $\frac{\pi^4 Eth^2}{12}\left(\frac{1}{l^2}+\frac{1}{b^2}\right)^2$ the bending part; Et is the in-plane stiffness, while t is the effective thickness of the shell.

Equation (3.59) reveals that the generated pressure in buckled shapes has a close relationship with the geometrical configurations of the cylindrical shell. This depends primarily on the radii of the shell, the effective shell thickness, and the wavenumbers, both in longitudinal and circumferential directions; the buckling behaviour of the cylindrical shell is determined by these parameters. Therefore, our analysis is now concentrated on buckling analysis based on different geometries of the tower shell, such as the tower thickness, its diameter, its section length, and its materials. In the last few decades, a great deal of buckling research has focused on these parameters (Kidane et al., 2003, Wullschleger, 2006, Vasilikis et al., 2016, Singer, 1967, Ma et al., 2020, Riks, 1997, Hutchinson, 1968, Singer et al., 2002, Tennyson, 1969, Edlund, 2007, Reese and Bert, 1974, Horton and Durham, 1963, Dimopoulos and Gantes, 2012, Yamki and Kodama, 1979). These conclusions also allow us to analyse the ratio between the stretching and bending parts, to establish a better understanding of the membrane effects in the shell-buckling process (although this represents a classical method in the linear stage).

When we combine Equation (3.58) and (3.59), an upgraded form of the assumed displacement is represented as:

$$\Delta \mathrm{p} = \omega_n \left[\frac{Et}{a^2l^4}\left(\frac{1}{l^2}+\frac{1}{b^2}\right)^{-2} + \pi^4 D\left(\frac{1}{l^2}+\frac{1}{b^2}\right)^2\right] \sin(\pi x/l)\sin(\pi y/b) \tag{3.60}$$

This expression also contains the stretching and bending parts in the righthand terms. If we let Equation (3.60) equal (3.56) in order to build a balance and allowing for no external pressure being added, then the eigenvalue becomes:

$$(-N_x) = \frac{Et}{\pi^2 a^2 l^2}\left(\frac{1}{l^2}+\frac{1}{b^2}\right)^{-2} + \pi^2 l^2 D\left(\frac{1}{l^2}+\frac{1}{b^2}\right)^2 \tag{3.61}$$

This is a well-known equation, and interestingly the term $\pi^2 l^2 D \left(\frac{1}{l^2}+\frac{1}{b^2}\right)^2$ is the buckling eigenvalue of a flat plate, as shown in Equation (3.14) by Calladine and Sanders (1984). Therefore, the first term on the right represents the stretching part provided by the cylindrical shell, and the extra buckling bearing capacity is due to the geometry of a cylinder. This equation also reveals the importance of the membrane part in terms of buckling resistance; that is, if the cylindrical geometry tends to a flattened plate, a certain percentage of its supporting capacity will be eliminated and the overall buckling load will reduce in line with the flattening, and the flattening will happen especially during the cylinder's bending moments.

3.4 Stress and strain in cylindrical shells under bending moment

The study of shell sections subjected to bending is essential for the analysis of a wind turbine tower under combined loading conditions. In extreme wind events, large thrust load applied on the rotor generates a considerable bending moment on the tower structures and the bending load will transmit to the tower bottom throughout the shell sections of the entire tower. According to the tower buckling case study in previous chapters, the bending effect will focus on the secondary bottom shell section of the wind turbine tower. The reason for this is that historical records and onsite inspections identify that the secondary bottom shell is involved in the highest percentage of recorded buckling failures, apparently due to large induced bending and compression, which is not always in line with predictions (CWIF, 2020a, Chou et al., 2013, Dimopoulos and Gantes, 2012, Hutchinson, 2016, Chen et al., 2016, Chen and Xu, 2016). Buckling-related failure is distinguished from other types of tower structural failure, such as bolt connection failure, flange failure (Alonso-Martinez et al., 2019), or blade-hitting damage, because it is more dependent on initial

imperfections or material non-homogeneity, which causes uneven stress flow across the secondary bottom shell[3].

In their earliest iterations, long tubular shells under bending loads were regarded as a rod. Brazier and Southwell (1927) first started investigating bending thin-walled cylindrical shells. They argued for a phenomenon called 'ovalisation', which means that when an initially straight cylinder is placed under bending loads, the cross-section of the cylinder will be ovalised: it tends to be flattened on both the compression side and tension side. This ovalisation will reduce the buckling resistance of the tube, as demonstrated by the Equation (3.61), and the flattening of the cross-section narrows the buckling load difference between a flat plate and a perfect cylinder. This ovalisation idea introduced a concept called extreme fibre, which could be observed around the area perpendicular to the bending plane, and the bending effect was originally calculated as a beam.

Seide and Weingarten (1959) applied the linear membrane theory on an elastic buckling tube and observed the bifurcation buckling behaviour. They argued that the bifurcation buckling load of a bending tube is slightly higher than the bifurcation buckling performance of an axially compressed tube, and they provided an expression of the ultimate stress on the extreme fibre as

$$\sigma_c^e = \frac{Et}{[3(1-\upsilon^2)]^{1/2}R} \tag{3.62}$$

The variants have the same meaning as in previous sections. Furthermore, the bifurcation buckling moment has its lower bound as

$$M_c^e = \frac{E\pi Rt^2}{[3(1-\nu^2)]^{1/2}} \tag{3.63}$$

[3] This paragraph has been published in Ma, Martinez-Vazquez and Baniotopoulos (2020). Yang Ma wrote the major parts, while Pedro Martinez-Vazquez and Charalampos Baniotopoulos contributed by reviewing, editing and supervising the paper.

On an elastic shell, which is infinitely long, Brazier and Southwell (1927) obtained an expression of the ultimate bending moment that a tubular shell could sustain, given by the following:

$$M_{\mu}^{e} = 0.5443 M_{c}^{e} \tag{3.64}$$

Meanwhile, the curvature could be expressed as

$$\kappa_{\mu}^{e} = 0.8165 \kappa_{c}^{e} \tag{3.65}$$

Here, the κ_{c}^{e} is the overall curvature based on Equation (3.63). The maximum deflection that happens when the buckling collapse occurs is $\frac{2}{9}R$, which is derived from equations above.

When looking particularly at the secondary bottom shell section on the wind turbine tower, under pure bending condition, the ovalisation of the cross-section could be depicted as in Figure 3.6 (Ma et al., 2020).

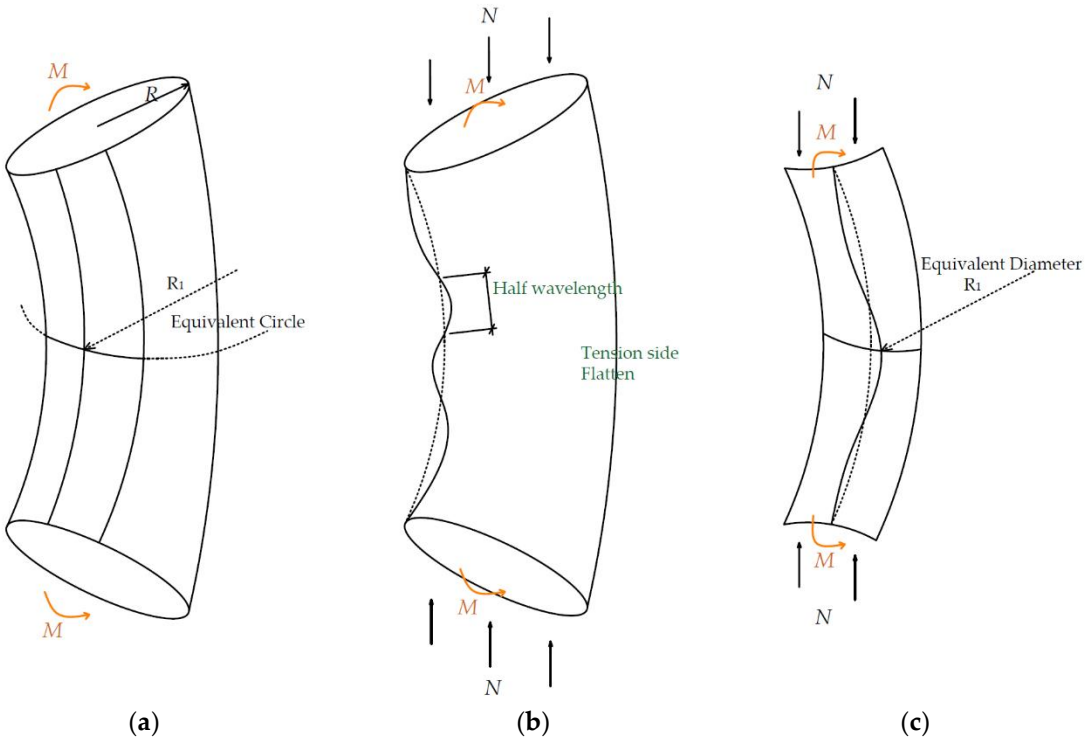


Figure 3.6. (**a**) Section ovalisation of a bending cylindrical shell; (**b**) the resulting effect of combined loads; and **(c)** the strip of a highly stressed shell segment (Ma et al., 2020).

Along the longitudinal direction of tubular shells, pure bending wrinkles the shell regions subject to the highest compression stress, as shown in Figure 3.6. The pure bending moment thus triggers prebuckling on the compressed wall while stretching the tension side, as in Figure 2.6a. The interaction between bending and axial stress is complex and has prompted ample study in the past (Donnell, 1934, Griffin, 1973, Kempner and Chen, 1972, Reese and Bert, 1974, Winterstetter and Schmidt, 2002, Wang and Sadowski, 2020). The present investigation thus intends to shed light on the nature of the collapse mechanism derived from lateral loading that affects wind turbine towers, through the mathematical formulations laid out in the following paragraphs[4].

The nonlinear moment-curvature of a section is given by:

$$M = EI(M)\frac{d^2u}{dx^2} \tag{3.66}$$

The terms $\frac{d^2u}{dx^2}$ represent the curvature of the shell section from Equation (3.63), which shows the limit of the moment derived equivalently as (Brazier and Southwell, 1927):

$$M_{lim} = 2\sqrt{2}\frac{ERt^2\pi}{9} \tag{3.67}$$

In line with the previous section, the bifurcation moment for perfectly cylindrical shells is revealed to be Equation (3.63) (Houliara and Karamanos, 2010). As the cross-section of the shell progresses into an oval shape, the buckling stress σ_c with respect to the local minor axis R_1 (after Hutchinson (1968)) is expressed as:

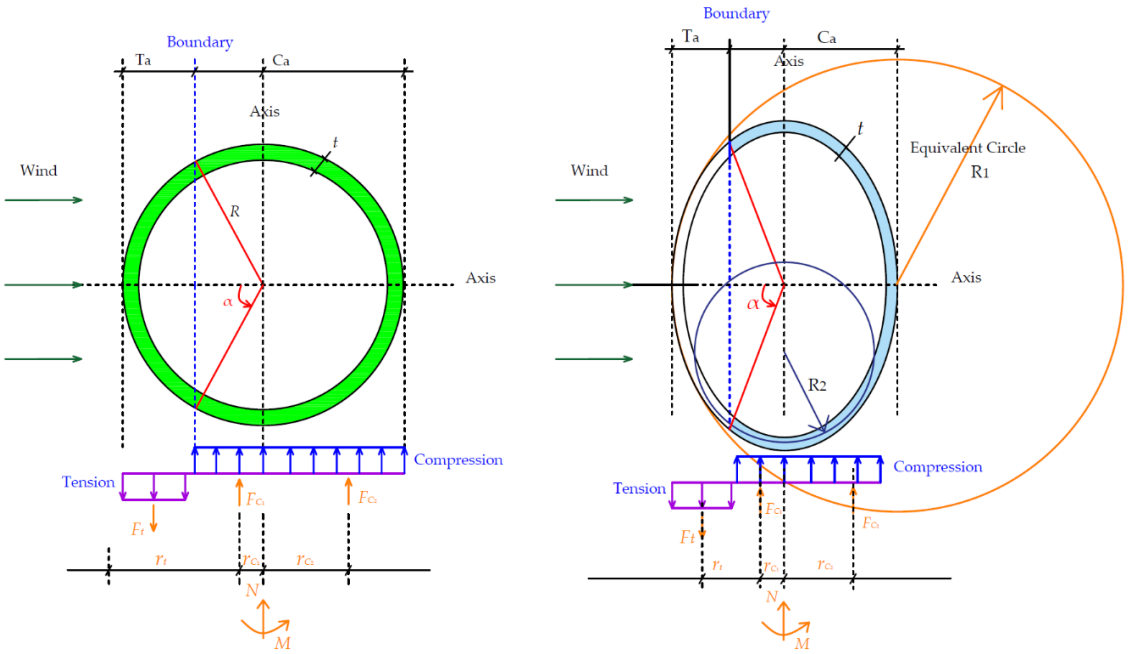
$$\sigma_c = \frac{1}{\sqrt{3(1-v^2)}}\left(\frac{Et}{R_1}\right) \tag{3.68}$$

[4] Some of these paragraphs have been published in Ma, Martinez-Vazquez and Baniotopoulos (2020). Yang Ma wrote the major parts, while Pedro Martinez-Vazquez and Charalampos Baniotopoulos contributed with reviewing, editing and supervising the paper.

On account of the local minor axis R_1, the very simple equilibriums for the ovalised cross-section could be calculated based on Figure 3.7 (a). As the ovalisation shown in Figure 3.7 (b) manifests, the control equations become (Ma et al., 2020):

$$\begin{aligned} N &= F_{C_1} + F_{C_2} - F_t = F_y(\mathrm{AreaC}_A - \mathrm{AreaT}_A) \\ &= F_y[2\pi R_2(\pi - 2\alpha)t + 2\alpha R_1 t - 2\alpha R_1 t] \\ &= F_y[2\pi R_2 t(\pi - 2\alpha)] \end{aligned} \tag{3.69}$$

$$\begin{aligned} M &= F_t(r_t + r_{C_1}) - F_{C_1} r_{C_1} + F_{C_2} r_{C_2} \\ &= F_y\{2\alpha R_1 t(r_t + r_{C_1}) - [R_2(\pi - \alpha)t(r_{C_1})] + (\pi r t \cdot r_{C_2})\} \end{aligned} \tag{3.70}$$



(**a**) (**b**)

Figure 3.7. Loading conditions of undeformed and ovalised shell cross-sections, (**a**) tubular shell cross-section without ovalisation and (**b**) ovalised tubular shell cross-section (Ma et al., 2020) [5].

We can take this study further based on Brazier's outcomes, by defining the circumferential stretching strain as (Gellin, 1980):

$$\eta = e + \frac{1}{2}e^2 + \frac{1}{2}\beta^2 \tag{3.71}$$

[5] This figure has been published in Ma, Martinez-Vazquez and Baniotopoulos (2020). Yang Ma wrote most of the work, while Pedro Martinez-Vazquez and Charalampos Baniotopoulos contributed by reviewing, editing and supervising the paper.

Here, e and β are ring displacement parameters on the cross-section, expressed as

$$e = \frac{\mathrm{d}v}{\mathrm{d}y} + \frac{\omega}{R}$$
$$\beta = \frac{v}{R} - \frac{\mathrm{d}\omega}{\mathrm{d}y} \tag{3.72}$$

The coordinate system is denoted according to Figure 3.3. The curvature in the cross-section plane could be expressed as Gellin (1980) suggested for plastic buckling analysis:

$$\epsilon_{xx} = E_{xx} + zK_{xx}; \epsilon_{yy} = E_{yy} + zK_{yy} \tag{3.73}$$

in which the K_{yy} represents bending strain in a circumferential direction as

$$K_{yy} = \frac{1}{\sqrt{1-\beta^2}} \frac{\mathrm{d}\beta}{\mathrm{d}y} \tag{3.74}$$

Furthermore, K_{xx} is the axial strain produced by bending.

Until this point, using linear elastic theories evolving into section ovalisation as a basis, we formulated a prebuckling system of linear equations to further study interactions induced by bending axials, and transient and postbuckling stages; we used non-classical energy methods and numerical simulations, which are discussed in the following chapters.

3.5 Stress and strain in cylindrical shells under combined compression and bending

In chapters 3.1–3.3, we concluded the classical buckling analysis on axially compressed cylinders, and on bent tubes in 3.4. In this section, we are going to investigate the stress–strain relations on a cylindrical shell, which are applied by combined compression load and bending moments.

It is worth noting here that the analysis and calculation of a tubular shell under combined load is much more easily obtained via energy methods rather than present

classical methods, owing to the complexity and limitations of the insensitive character of classical methods toward a time-history process such as buckling. However, basic study in the classical category will greatly inform the advanced analysis. Based on the centrally compressive force above, we should note that for wind turbine towers, the compressive load is no more symmetrical; with some eccentricity, the moment will combine with an axial load where the previous N_x (the overall axially compressive load) is variable instead of constant. This is shown in Figure 3.8, in which we assume a section of the shell has been applied with non-uniform compression loads.

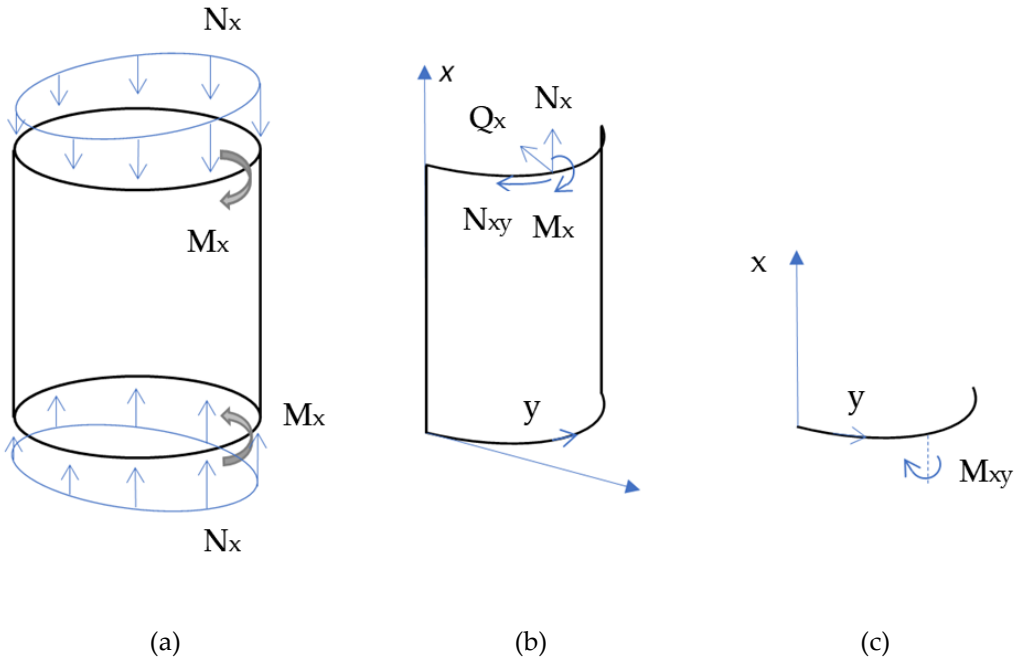


Figure 3.8. (a) Forces applied on a turbine tower shell tube; (b) four stress resultants that may be applied to the cylinder shell; (c) coordinates and twisting moment if considered.

Therefore, we update the axial load N_x and represent it by a periodic function as

$$N_x = -(N_0 + N_1 \cos\theta) \tag{3.75}$$

Here, the minimum N_0 is the minimum uniform compressive load and N_1 is the maximum. It is simple to conclude that the minimum compression load N_0 happens on the tensile side of bending, namely, on the side that is against the wind direction, which could be negative if the tension force generated by bending is higher than the gravity load generated by upper components along this fibre; however, N_1 is the

dominant load that triggers buckling and N_1 is generated along the 'extreme fibre' on the compression side.

N_1 determines the buckling criterion on the compression side, which comprises two parts: axial compression with eccentricity N_e, and axial compression by bending N_b. The former can be obtained if the configurations of the entire turbine tower are applied to determine the application point of upper gravity loads; the latter can be obtained based on Equation (3.69) (3.70), in which the ultimate factor of F_{C_2} is at the furthest point according to R_1. N_0 was omitted from this research, as buckling would not occur on the flattening side, whereas the magnitude of N_0 is essential for N_1 with the interconnection via Equation (3.75).

$$N_1 = N_e + N_b \tag{3.76}$$

In this equation, N_b equals $\alpha R_1 t$ and the α is a relatively slight radius of compression, represented by the width of the 'extreme fibre'. Here we introduce the axial compression geometry to demonstrate further combination, as shown in Figure 3.9.

Figure 3.9[6] represents a typical surface displacement, confirmed by periodic functions with a half-wavenumber equal to 7; based on this, the circumferential deflection becomes

$$f = -C_0 sin\frac{n\pi x}{L} \tag{3.77}$$

where C_0 is a constant and n equals the half-wavenumber along the shell length L. The radical strain of the unit mid-surface circumference can thus be expressed as:

$$\varepsilon_{xl} = -\frac{N}{Et}$$

$$\varepsilon_x E = \frac{E}{1-\nu^2}\left(\varepsilon_{x_2} + \nu\varepsilon_{\theta_2}\right)$$

$$\varepsilon_{x_2} + \nu\varepsilon_{\theta_2} = (1-\nu^2)\varepsilon_{x_l}$$

[6] Some of these paragraphs have been published in Ma, Martinez-Vazquez and Baniotopoulos (2020).

$$\varepsilon_{\theta_2} = -\nu\varepsilon_{x_l} + \frac{C_0}{r} sin\frac{n\pi x}{L}$$

$$\gamma_{xy} = x_y = x_{xy} = 0$$

$$x_x = C_0 \frac{n^2\pi^2}{L^2} sin\frac{\pi n x}{L} \tag{3.78}$$

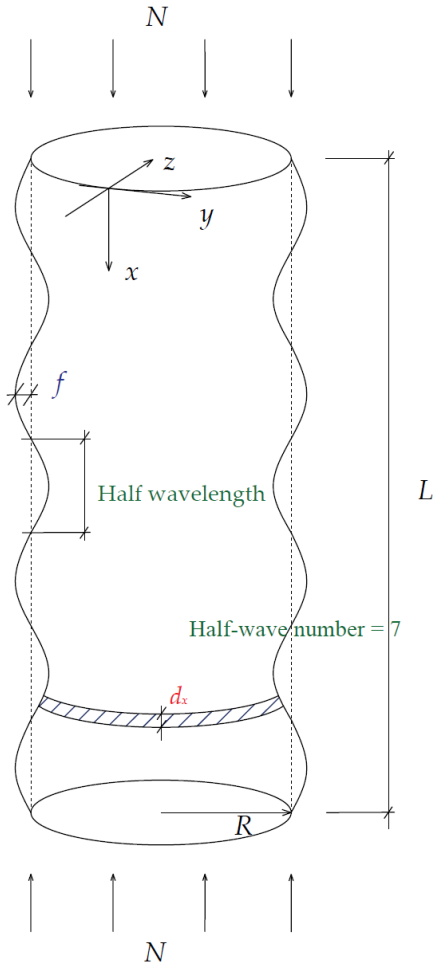


Figure 3.9. Assumed basic buckling shell deformation function under axial compressive load (Ma et al., 2020).

In the above equations, ε_{x_2} and ε_{θ_2} represent mid-surface axial strains after buckling.

The interaction between bending and axial compression is complex and not fully studied, and there is a gap in the research surrounding this area. The study of cylinder shell buckling under combined load is essential for designing wind turbine towers, and it will enable a better understanding of the resilience of turbine towers. In the following section, we create a hypothesis in the classical buckling category: the

prebuckling behaviour depends on a linear interaction between bending and compression, which determines the transient buckling and postbuckling process.

By combining Equation (3.71) and (3.78), we obtain the circumferential strain under combined loads:

$$\varepsilon_\theta = \left[-\nu\varepsilon_{x_l} + \frac{C_0}{r} sin\frac{n\pi x}{L}\right] + \varsigma[\left(\frac{\mathrm{d}v}{\mathrm{d}y} + \frac{\omega}{R}\right) + 0.5\left(\frac{\mathrm{d}v}{\mathrm{d}y} + \frac{\omega}{R}\right)^2 + 0.5(\frac{v}{R} - \frac{\mathrm{d}\omega}{\mathrm{d}y})^2] \quad (3.79)$$

ς represents the parameter based on load combination which could be determined via validation.

As Brazier suggested (Brazier and Southwell, 1927), the typical cross-section deformation is given by:

$$\omega = a\zeta\cos\ 2\theta \quad (3.80)$$

where parameter ζ is the measurement of the flattening of extreme fibre in dimensionless form. Then the circumferential displacement by bending is given by:

$$v = -\frac{1}{2}a\zeta\sin\ 2\theta \quad (3.81)$$

and the integration of this v along the full length of the circumference should equal to zero, as no mid-surface extension happens, based on the basic assumption in classical buckling analysis.

The buckling eigenvalue calculation could then be updated using the 'two-surface' theory. We linearly combined the Equation (3.80) and (3.77), and the updated circumferential displacement is:

$$f = -C_0 sin\frac{n\pi x}{L} + a\zeta\cos\ 2\theta \quad (3.82)$$

Additionally, this function should be periodic throughout the circumference, which could be automatically achieved due to the character of trigonometry functions. This function also formed a relation between shell length and radial displacement.

The Equation (3.56) can be rewritten as:

$$\Delta p_1 = (-N_1)\frac{\partial^2[-C_0 sin\frac{n\pi x}{L} + a\zeta\cos 2\theta]}{\partial x^2} - 2N_{xy}\frac{\partial^2[-C_0 sin\frac{n\pi x}{L} + a\zeta\cos 2\theta]}{\partial x\,\partial y} + \left(-N_y\right)\frac{\partial^2[-C_0 sin\frac{n\pi x}{L} + a\zeta\cos 2\theta]}{\partial y^2} \tag{3.83}$$

This is equal to:

$$\Delta p_1 = (-N_1)\frac{\partial^2[-C_0 sin\frac{n\pi x}{L}]}{\partial x^2} - 2N_{xy}\frac{\partial^2[-C_0 sin\frac{n\pi x}{L} + a\zeta\cos 2\theta]}{\partial x\,\partial y} + \left(-N_y\right)\frac{\partial^2[a\zeta\cos 2\theta]}{\partial y^2} \tag{3.84}$$

The circumferential displacement factor v contains the function of y implicitly.

Another 'surface'-generated pressure is given by Equation (3.57):

$$\frac{\partial^2[-D\frac{d^2(-C_0 sin\frac{n\pi x}{L} + a\zeta\cos 2\theta)}{dx^2}]}{\partial x^2} + \frac{\partial^2[-\upsilon D\frac{d^2(-C_0 sin\frac{n\pi x}{L} + a\zeta\cos 2\theta)}{dx^2}]}{\partial y^2} = -p_{\mathrm{B}} \tag{3.85}$$

We eliminated the term M_{xy} by ignoring the moment generated by torsion in this case. Then we allow $-\Delta p_1 + p_{\mathrm{B}} = 0$, and build a simultaneous equation together with Equation (3.48), which gives:

$$\frac{\partial^2\left[-D\dfrac{d^2(-C_0 sin\dfrac{n\pi x}{L}+a\zeta\cos 2\theta)}{dx^2}\right]}{\partial x^2}$$
$$+\frac{\partial^2\left[-\upsilon D\dfrac{d^2(-C_0 sin\dfrac{n\pi x}{L}+a\zeta\cos 2\theta)}{dx^2}\right]}{\partial y^2}$$
$$+(-N_1)\frac{\partial^2[-C_0 sin\frac{n\pi x}{L}]}{\partial x^2}-2N_{xy}\frac{\partial^2[-C_0 sin\frac{n\pi x}{L}+a\zeta\cos 2\theta]}{\partial x\,\partial y} \quad (3.86)$$
$$+\left(-N_y\right)\frac{\partial^2[a\zeta\cos 2\theta]}{\partial y^2}=0$$

$$D\frac{d^4[-C_0 sin\frac{n\pi x}{L}]}{dx^4}+\frac{Eh}{r}[-C_0 sin\frac{n\pi x}{L}+a\zeta\cos 2\theta]-\nu\frac{N_1}{r}=0$$

For this equation, we have an extra coordinate transition from angular to Cartesian, considering the dimensionless flattening parameter:

$$y=\omega\sin\,\theta+v\cos\,\theta \quad (3.87)$$

By substituting Equation (3.80) and (3.81), this is rewritten as

$$y=\frac{1}{4}a\zeta(-3\sin\,\theta+\sin\,3\theta)=-a\zeta\sin^3\,\theta \quad (3.88)$$

It is possible to express the curvature change by the parameter; substituted above into Equation (3.29) as the κ_y item, the circumferential curvature change is given by:

$$\kappa_y=-\left(\frac{1}{a^2}\right)\left(\omega+\frac{d^2\omega}{d\theta^2}\right)=\left(\frac{3\zeta}{a}\right)\cos\,2\theta \quad (3.89)$$

This expression provides the basis for later energy calculations, which will be discussed in Chapter 4.

3.6 Geometry imperfections in buckling calculation

As discussed in Chapter 2.3.4, geometry imperfections on cylindrical shells show high sensitivity to overall buckling behaviour and resistance. In the calculation procedure, imperfection must be considered, including the shape and magnitude on a perfect tubular shell. Many experimental results have been conducted even before the Peterson et al. (1968) regression equation, as shown in Figure 3.10 (Harris et al., 1957).

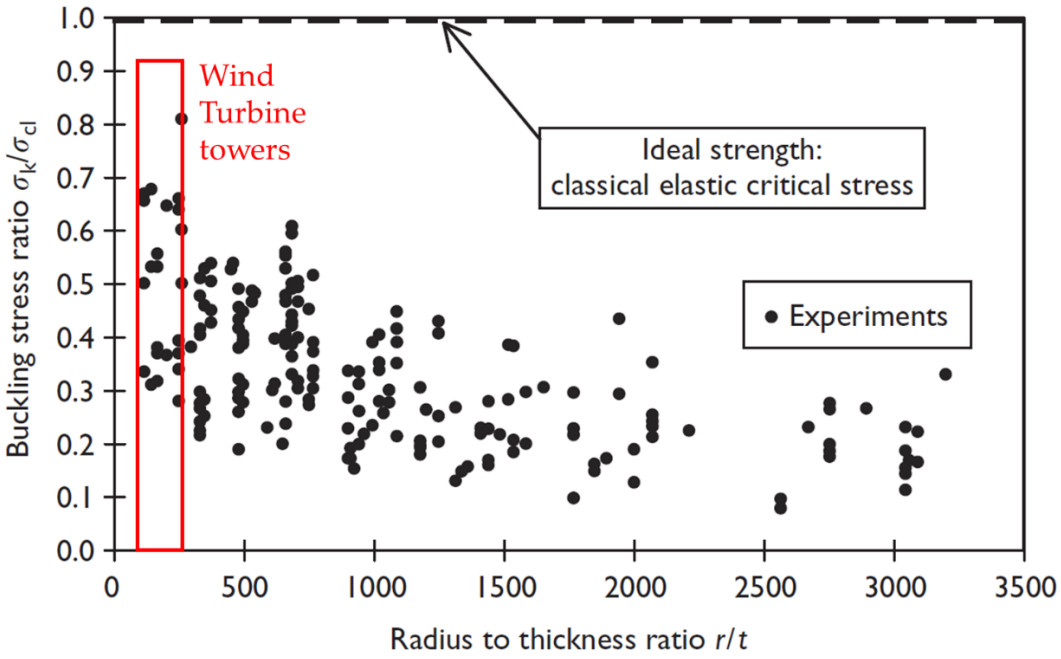


Figure 3.10. Experimental results of axially compressed cylindrical shells (after Harris et al. (1957) by Teng and Rotter (2006)).

Normally, the r/t ratio for wind turbine towers falls into the zone denoted by the red rectangle, which is highly scattered and based on experimental outcomes. A variety of research has attributed this scattering to imperfection sensitivity due to various imperfection configurations (Kao and Perrone, 1971, Hutchinson, 1968, Hornung and Saal, 2002, Donnell and Wan, 1950, Schneider, 1996, Yamki and Kodama, 1979). Yamaki (1984) carried out a series of elastic stability studies on various lengths of cylinders under compression. The postbuckling behaviour expressed via load-axial shortening has been reproduced by Teng and Rotter (2006), as shown in Figure 3.11.

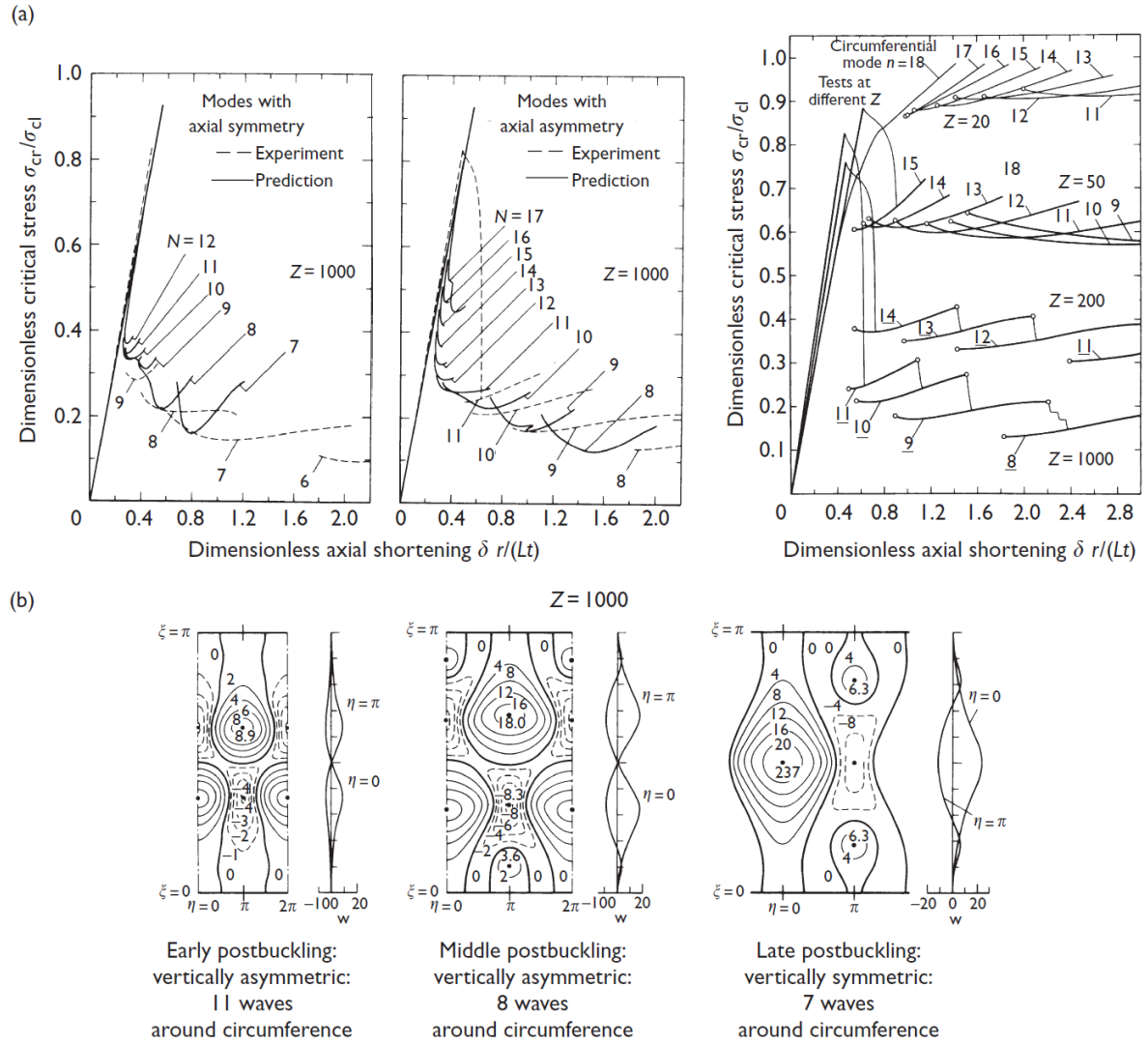


Figure 3.11. (a) Load-end shortening curves; (b) postbuckling modes in different buckling progressions. Axial compression applied to cylinder shells, reproduced by Teng and Rotter (2006), based on the data from Yamaki (1984).

Based on Figure 3.11, Yamaki (1984) claimed the shorter cylinders showed less sensitivity to imperfection due to more stable postbuckling behaviours than that of the longer cylinders. To demonstrate this, the parameter Z is assigned by Batdorf (Batdorf and Sines, 1980, Nemeth, 1994), based on the half-wavelength l, as

$$Z = \sqrt{(1-v^2)}\frac{L^2}{Rt} \simeq 5.70\left(\frac{L}{l}\right)^2 \tag{3.90}$$

in which the half-wavelength is related to Rt. Determined by the bending in prebuckling stage, here the l is given by:

$$l = \frac{\pi}{[3(1-v^2)]^{1/4}}\sqrt{Rt} \simeq 2.44\sqrt{Rt} \tag{3.91}$$

In addition, Yamaki (1984) noticed the importance of supporting boundary conditions that affect the postbuckling behaviour, as well as the length of cylindrical shells.

The ratio $\frac{L}{l}$ is essential for the value of Z, which is the dominant of buckling behaviour. The half-wavelength is obtainable based on the prebuckling shape assumption, as shown in the trigonometry functions mentioned in previous chapters. If the trigonometry function describes displacements on the shell surface in one direction, such as the longitudinal direction of a shell section, the visible picture of the shell surface is illustrated in Figure 28.

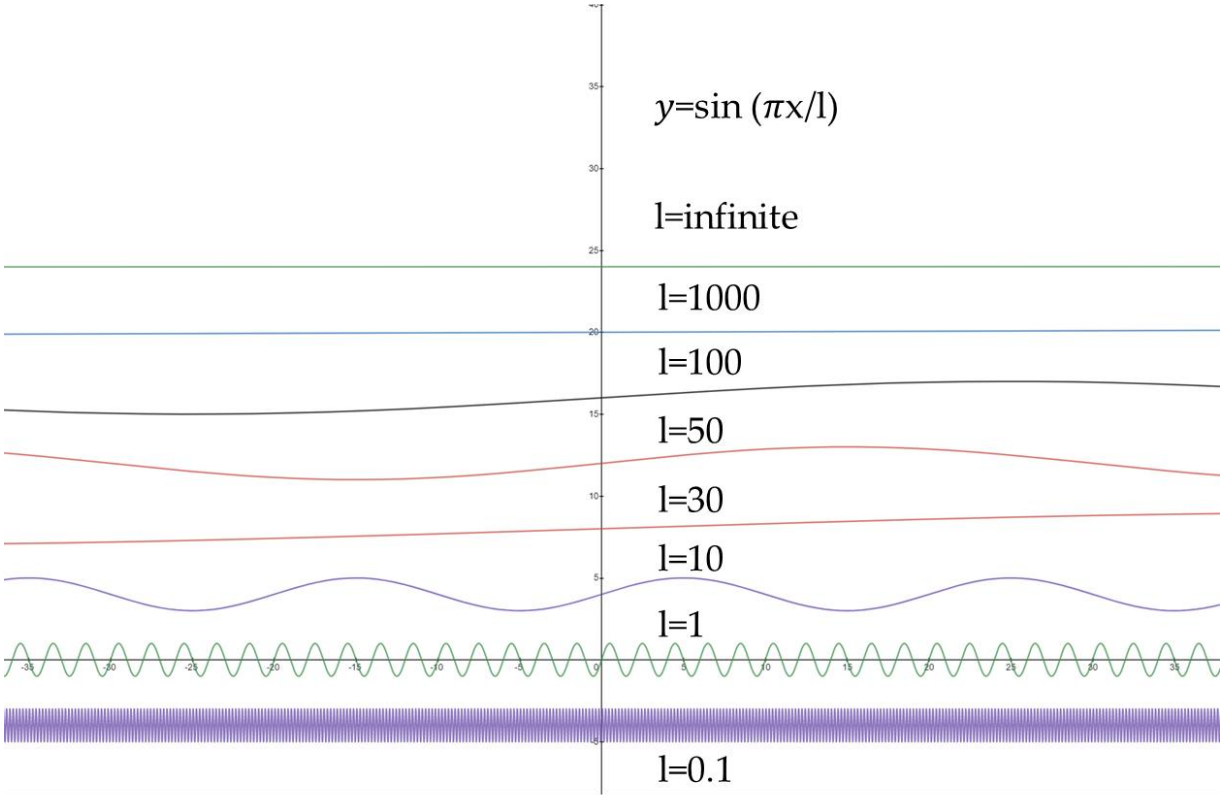


Figure 3.12. An illustration of displacements on a shell surface in the prebuckling stage, based on the assumption by sinusoidal functions.

We can easily observe that when the half-wavelength tends towards infinite, namely, the half-wavenumber tends to a minimum; the surface displacement is limited, which indicates that the shell geometry is perfect. In line with a lower value of Z, the

postbuckling path has more variations, which leads to similar conclusions to those from axial compression studies. On the other hand, if the half-wavenumber is extremely high, which means minimum half-wavelength, the postbuckling paths reveal more stale routes. However, we should notice that the deviation is very large in medium values of half-wavelength, within which bracket the wind turbine tower falls – thus, highly imperfect sensitivity occurs.

On account of the imperfect shape, the asymmetric type of buckling on a wind turbine tower inevitably occurs due to the equation we deduced in the last section, owing to the asymmetric behaviours between the compression side and the tension side; the compression side can be described well by periodic functions while the tension side is flattening. Koiter (1945) also noted that the axisymmetric imperfection can be ignored in buckling analysis, but the eigenvalues based on a perfect shell could be combined in FEM analysis, and the result would show in an asymmetric form (Riks, 1997).

In the case of the amplitude of geometry imperfections, various studies have made conclusive summaries: the amplitude sees monotonically increasing relations with the increase of buckling load reduction, as depicted in Figure 3.13.

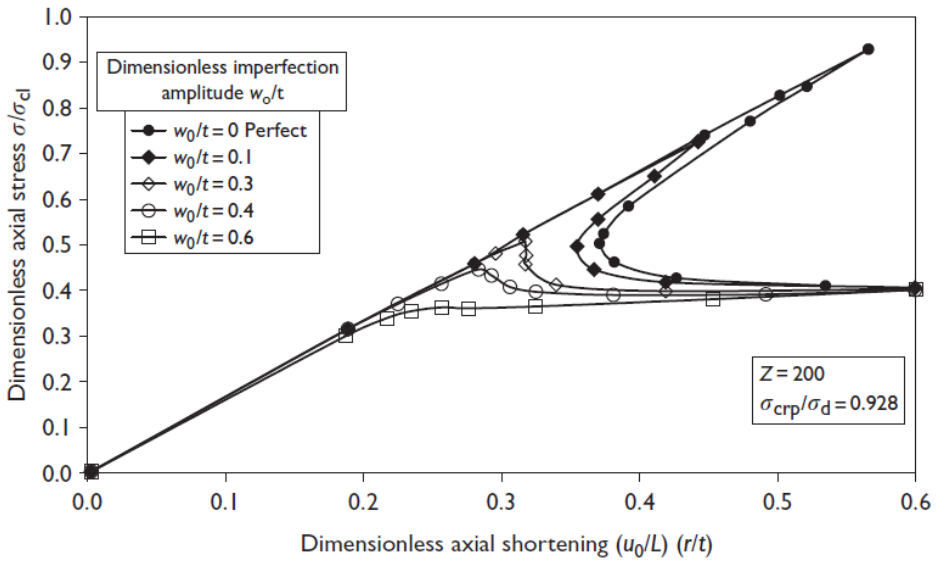


Figure 3.13. The relationship between different imperfection amplitudes and bifurcation points in axially compressive cylinders (reproduced by Teng and Rotter (2006) based on data produced by Yamaki (1984)).

Figure 3.13 displays the reduction of axial stress resistance when the dimensionless imperfection amplitude increases. When the depth of imperfection is 60% of the shell thickness, the bifurcation buckling behaviour is no longer obvious. Fortunately, this large magnitude of imperfection is rarely found on wind turbine towers, as deep dents or high bulges are easy to find in installation steps or during maintenance procedures, but lower imperfection amplitudes show similar bifurcation buckling behaviour compared to perfect shells. We must establish the exact difference between them, since it is not acceptable to ignore imperfection sensitivity in buckling analysis in combined loading conditions (Wang and Sadowski, 2020, Schneider, 1996).

The geometry imperfection of wind turbine towers should also consider the tower shell manufacturing tolerances by codes. Table 3.1 lists four examples of shell geometrical imperfection tolerance by selected design codes.

Codes	**Imperfection tolerance**
DnV (1995)	$\boldsymbol{w_0 = \frac{0.05 l_r}{1+\frac{l_r}{r}}}$, $\boldsymbol{l_r = 4\sqrt{rt}}$
ECCS (1998)	$\boldsymbol{w_0 = 0.01 l_r}$, $\boldsymbol{l_r = 4\sqrt{rt}}$
API (1998)	$\boldsymbol{w_0 = 0.01 l_r}$, $\boldsymbol{l_r = 4\sqrt{rt}}$
EC3 (2007) and EC9 (2006)	$\boldsymbol{w_0 = U_{rmax} l_{g\theta,x}}$, $\boldsymbol{l_{g\theta,circumferential} = 2.3(l^2 rt)^{0.25}}$ or $\boldsymbol{l_{g\theta,axial\ compression} = 4\sqrt{rt}}$

Table 3.1. Shell geometrical tolerance in selected codes.

For example, by applying the design code DnV (1995) on the 6000 mm diametre 30 mm wall thickness shell, the allowable $w_0 = 42.85$ mm while in the code ECCS (1998), the allowable $w_0 = 12$ mm. The imperfection ratio $w_0/t = 0.4$ in ECCS (1998) shows the maximum local dimple that could be tolerated in factory manufacturing. Additionally, it is explained in EN 1993-1-6 (2007) that when the imperfection

amplitude is less than 10% from the perfect shape, the verification should be done particularly due to the small imperfection ratio does not yield a lower value for the $r_{R,GMNIA}$ ratio.

By considering the well-developed manufacturing performance for modern wind turbine towers, the minimum 10% amplitude for the first linear modal is reasonable for this research and the following two modal shapes are practical to be introduced as well. Therefore, the geometry imperfection in this research was selected as a combination of eigenvalues after they have been multiplied by amplitude parameters. The amplitude w_0/t was selected as 0.1 for the first eigenvalue, 0.05 for the second eigenvalue, and 0.025 for the third eigenvalue. This combination is effective and practical for wind turbine towers, especially in the worst case scenario of a wind power plant regularly operating during extreme wind events (Ma et al., 2020). Afterwards, a sinusoidal shape function f_0 can be applied to the perfect shell based on the eigenvalue calculation, given by:

$$f_0 = 0.1 \sin\left(\frac{\pi x}{l_1}\right) \sin\left(\frac{\pi y}{b_1}\right) + 0.05 \sin\left(\frac{\pi x}{l_2}\right) \sin\left(\frac{\pi y}{b_2}\right) + 0.025 \sin\left(\frac{\pi x}{l_3}\right) \sin\left(\frac{\pi y}{b_3}\right) \quad (3.92)$$

in which, the l_1, b_1 is derived from the first eigenvalue, calculated by Equation (3.61), and l_2, b_2, l_3 and b_3 are derived from the second and third eigenvalues, respectively.

The following steps are the same as previous methods without imperfections.

3.7 Concluding remarks

In this chapter, the classical buckling theories have been implemented in the cylindrical shells. After discussing the geometries and curvatures of cylindrical shells, the equilibrium equations of a local Gaussian curvature are achieved. Then, the general curvature expressions of both circumferential and longitudinal have been discussed, and the local and overall surface displacement functions are obtained both in Cartesian coordinate and cylindrical coordinate. The stress–strain and surface displacement equilibriums have been conducted in axially compressive load

condition and then extended to pure bending load condition and combined load condition.

The geometry imperfection issue in cylindrical shell buckling has been investigated in the latter part of this chapter, which includes the reviews and comparisons on both imperfection shapes and magnitudes. The selection of geometric imperfection in this research has been decided as asymmetric shape, magnitude parameters at the combination of 0.1 of wall thickness for the first eigenvalue of linear buckling perturbation, 0.05 for the second eigenvalue, and 0.025 for the third eigenvalue.

4 NON-CLASSICAL BUCKLING ANALYSIS AND ENERGY METHODS

4.1 Equations of shell structures

It is possible to determine all of the eigenvalues of a buckling shell via classical buckling analysis concepts; that is, we can substitute various sets of possible wavenumbers or wavelengths into Equations (3.13) and (3.61), and the full range of eigenvalues can be obtained from scattered calculations. However, a large number of possible values for l and b will result in numerous batches of calculation jobs, and the judgement of the validation of parameters l and b should be made according to boundary conditions under specific loadings. The achievement of establishing all eigenvalues poses a tough question for the analysis of earlier studies, as the calculation resources, especially computers, were below the abundant level for scientific calculations. Only typical results had been reached by researchers by means of analytical approaches and entry-level numerical methods (Koiter, 1963, Koiter, 1945, Donnell and Wan, 1950, Donnell, 1934, Riks, 1997, Riks, 1979).

There are high-order partial differential equations in classical buckling analysis, such as the well-known Donnell equation, shown here as Equation (3.48). It was, however, impossible for all analytical solutions to be available until now, when we have well-developed numerical methods to achieve the numerical solutions to a level of accuracy which is precise enough for use in engineering. The modern scientific calculation is proficient at matrix manipulation, integral iteration, and approximation based on finite increments. Fortunately, the outcomes of energy methods are suitable for data processing in modern computers (Elaydi, 2005, Butcher and Goodwin, 2008). Ames

(2014) introduced and summarised a full range of typical numerical methods for partial differential equations, of which the finite element method in notable for its merit in solving equations, including parabolic equations, elliptic equations and hyperbolic equations.

Another advantage of applying energy methods to wind turbine tower buckling analysis is the efficiency of tracking paths of bifurcation buckling. The multiple stable postbuckling paths after the bifurcation point posed great difficulty to classical analyses, as the load–displacement relations changed dramatically and were discontinuous. Energy methods create additional conditions for the buckling path analysis, as the external work could be expressed by load–displacement multiplications and the internal work could be described by stress–strain multiplications. Variational methods allow us to obtain exact transient results at any specific point in the conservative system.

The analysis and interpretation of buckling stability based on energy methods therefore underpins the analysis of real wind turbine towers[7]. We note during that process that, based on the potential energy theory, energy is insensitive to the evolution path, and thus the stability equation is derived from the total potential energy equilibrium, as depicted in Figure 4.1. In this chart, the origin point represents the state of the unloaded (hence undeformed) shell section. The following point is the initial stage field, as an extreme to the vector $\overrightarrow{r_0}$. That state occurs past the application of gravity load and initial residual stress. Then, the basic stage field appears to describe the state under design loading, including upper structures installed during regular working periods. When external loads exceed the basic stage field, a trajectory following the vector $\overrightarrow{b_+}$ identifies the final stage. With this in mind, the final stage accommodates arbitrary displacement or input energy components $\overrightarrow{r_0}$, $\vec{b}$, and $\overrightarrow{b_+}$ and perhaps other interval components. Each field, therefore, represents a set of possible

[7] Some of the following paragraphs have been published in Ma, Martinez-Vazquez and Baniotopoulos (2020).

stable points at a given stage, and stage evolution happens only when additional energy components exceed partial stability energy ranges.

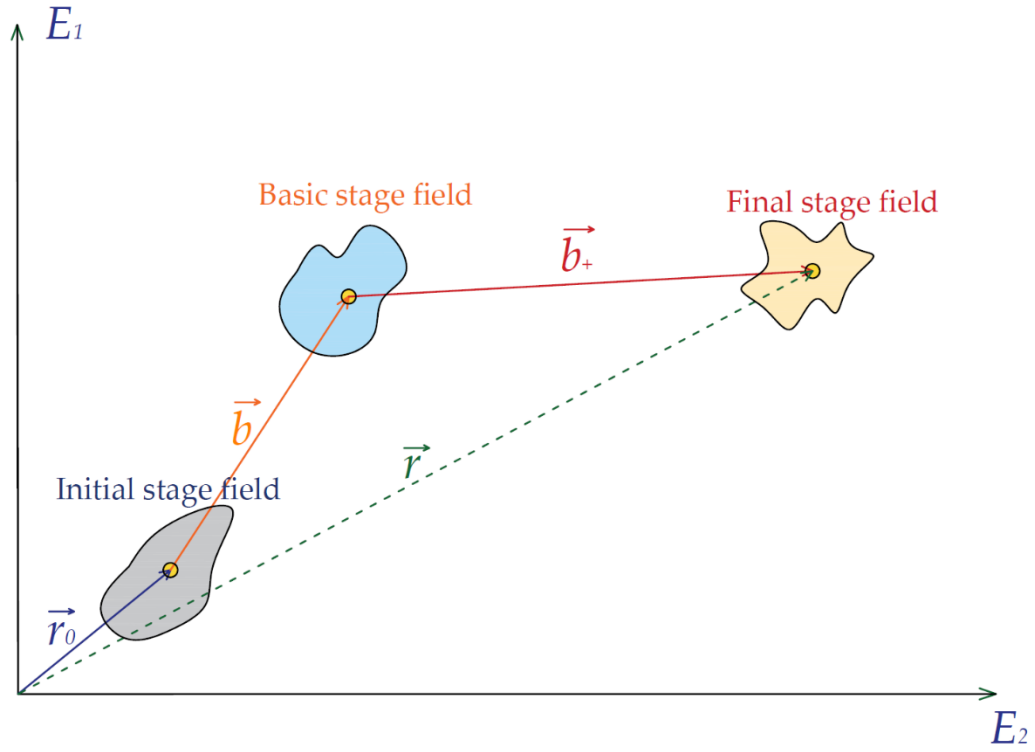


Figure 4.1. Energy state fields of stability analysis (Ma et al., 2020).

For instance, one of the possible additional energy paths to the final stage field from the origin could be described by Equation (4.1), in which each vector possesses multiple set elements:

$$\vec{r} = \overrightarrow{r_0} + \vec{b} + \overrightarrow{b_+} \tag{4.1}$$

In the static analysis, the kinetic energy component cancels this out; hence, the overall energy relates to the potential energy. In the arbitrary energy stage of a shell structure, the total potential energy $\prod$ can be divided into internal energy and external energy:

$$\Pi = \Pi_{internal} + \Pi_{external} = \Pi_i + \Pi_e \tag{4.2}$$

Here, $\Pi_{internal}$ represents the total potential energy stored by the shell elements, and the $\Pi_{external}$ represents the energy input from external load or environmental factors. Various possible energy paths have been applied in the above equations, and when

$\delta\prod = 0$, the neutral equilibrium state of the transition is realised. When this principle is translated to the eigenvalue problem involving the stiffness, geometries, and displacement matrices, in both its linear and nonlinear part, a typical simplified quadratic eigenvalue problem of the form unveils (Eslami, 2018, Hilburger, 2008):

$$K_T V = K_e + \lambda^*\left(K_{gl} + K_{vl}\right) + \lambda^{*2}\left(K_{gn} + K_{vn}\right)V = 0$$

$$\left(K_e + \lambda^* K_{gl}\right)V = 0 \tag{3.4}$$

In Equations (4.4), K_e represents the matrix of initial elastic stiffness, K_{gl} represents the matrix of initial linear geometries, K_{vl} represents the respective matrix of linear displacements, K_{gn} represents the initial geometrical stiffness matrix in quadratic form, K_{vn} represents the initial displacement matrix in the quadratic form, and V represents the nodal displacements of the selected element in the form of a vector. Equation (4.4) approximates the classical eigenvalue problem by ignoring the shell initial displacement, but can be updated based on the previous linear eigenvalue problems (see Equation (3.61)). Incremental methods could solve the numerical problem through incremental load steps, the equilibrium of which is checked iteratively. The solution of Equation (4.4) also relates to the critical load factor λ_{cr} depicted in Figure 2.12: λ^* is the eigenvalue solution of Equations (4.4), and is equal to λ_{cr} when it gets to its minimum value; this factor could in turn establish a relationship with a membrane and bending components (λ_m and λ_b, respectively), as follows:

$$\lambda_{cr} = \lambda_b + m \times \lambda_m \tag{4.4}$$

The membrane part λ_m is strongly linked to the total shell load bearing capacity, as shown in Figure 2.12. It is worth highlighting that, in that figure, the upper and lower load bounds delimit realistic buckling performances as an extension of linear-elastic bending strength and as part of the membrane effects developed by cylindrical shells. We thus derive the bending strain energy and membrane stretching strain energy in the following sections.

For a general shell element, considering the aforementioned Figure 3.5, we could carry out the expressions for basic parameters in the Cartesian coordinate system, as shown in the differential shell element in Figure 4.2.

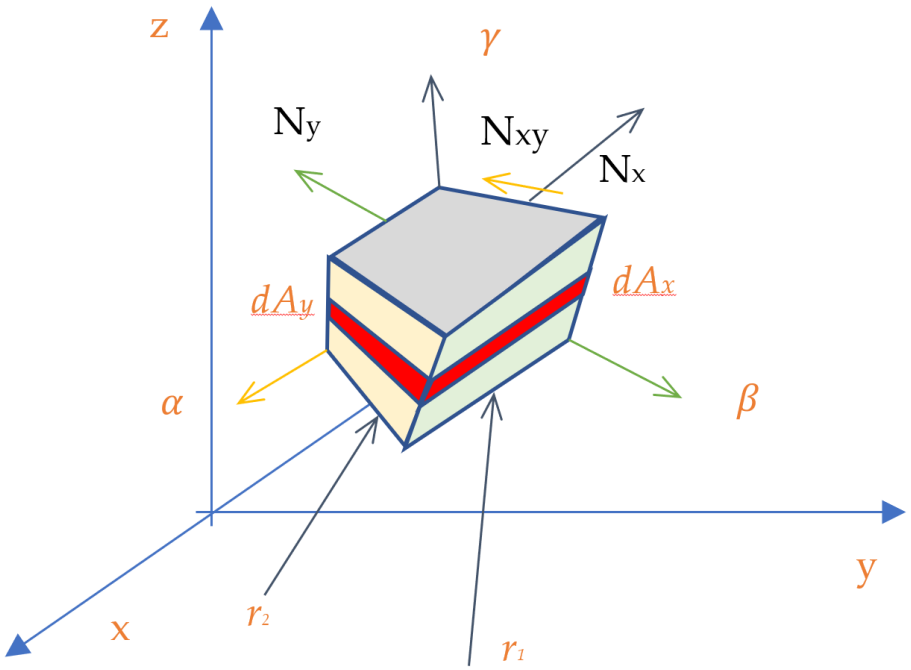


Figure 4.2. A differential element of a general shell section.

The area element could be written as

$$dA_x = \alpha dxdz = A\left(1+\frac{z}{r_1}\right)dxdz$$
$$dA_y = \beta dydz = B\left(1+\frac{z}{r_2}\right)dydz \tag{4.6}$$

where r_1 and r_2 are the radius of the shell mid-surface on two perpendicular planes, and for the turbine tower shell, $1/r_2$ is equal to zero, while for a plate, $1/r_2 = 1/r_1 = 0$.

Then, the integral is completed according to the thickness of the shell element and the full group of stress relations is given as follows (Langhaar, 2016):

$$
\begin{aligned}
N_x &= \frac{1}{B}\int_{-h/2}^{h/2} \beta\sigma_x dz = \int_{-h/2}^{h/2} \sigma_x \left(1+\frac{z}{r_2}\right) dz \\
N_y &= \frac{1}{A}\int_{-h/2}^{h/2} \alpha\sigma_y dz = \int_{-h/2}^{h/2} \sigma_y \left(1+\frac{z}{r_1}\right) dz \\
N_{xy} &= \frac{1}{B}\int_{-h/2}^{h/2} \beta\tau_{xy} dz = \int_{-h/2}^{h/2} \tau_{xy} \left(1+\frac{z}{r_2}\right) dz \\
N_{yx} &= \frac{1}{A}\int_{-h/2}^{h/2} \alpha\tau_{xy} dz = \int_{-h/2}^{h/2} \tau_{xy} \left(1+\frac{z}{r_1}\right) dz \\
Q_x &= \frac{1}{B}\int_{-h/2}^{h/2} \beta\tau_{xz} dz = \int_{-h/2}^{h/2} \tau_{xz} \left(1+\frac{z}{r_2}\right) dz \\
Q_y &= \frac{1}{A}\int_{-h/2}^{h/2} \alpha\tau_{yz} dz = \int_{-h/2}^{h/2} \tau_{yz} \left(1+\frac{z}{r_1}\right) dz \\
M_x &= \frac{1}{B}\int_{-h/2}^{h/2} \beta z\sigma_x dz \doteq \int_{-h/2}^{h/2} z \left(1+\frac{z}{r_2}\right) \sigma_x dz \\
M_y &= \frac{1}{A}\int_{-h/2}^{h/2} \alpha z\sigma_y dz = \int_{-h/2}^{h/2} z \left(1+\frac{z}{r_1}\right) \sigma_y dz \\
M_{xy} &= \frac{1}{B}\int_{-h/2}^{h/2} \beta z\tau_{xy} dz = \int_{-h/2}^{h/2} z \left(1+\frac{z}{r_2}\right) \tau_{xy} dz \\
M_{yx} &= \frac{1}{A}\int_{-h/2}^{h/2} \alpha z\tau_{xy} dz = \int_{-h/2}^{h/2} z \left(1+\frac{z}{r_1}\right) \tau_{xy} dz
\end{aligned}
\tag{4.7}
$$

It should be noted that the A, B in the above equations represent the Lame coefficients of the general shell, the H_1 and H_2, which are obtained by Equation (3.35).

Here we introduce the equations Langhaar (2016) derived for calculating elasticity; we remove the tensor calculus and rewrite the Equation (3.29) according to Lame coefficients:

$$
\begin{aligned}
\epsilon_x &= \frac{1}{\alpha}\left[u_x + \frac{\alpha_y v}{\beta} + \frac{\alpha_z w}{\gamma} + \frac{1}{2\alpha}\left(u_x + \frac{\alpha_y v}{\beta} + \frac{\alpha_z w}{\gamma}\right)^2 \right.\\
&\left. + \frac{1}{2\alpha}\left(v_x - \frac{\alpha_y u}{\beta}\right)^2 + \frac{1}{2\alpha}\left(w_x - \frac{\alpha_z u}{\gamma}\right)^2\right]\\
\epsilon_y &= \frac{1}{\beta}\left[v_y + \frac{\beta_z w}{\gamma} + \frac{\beta_x u}{\alpha} + \frac{1}{2\beta}\left(v_y + \frac{\beta_z w}{\gamma} + \frac{\beta_x u}{\alpha}\right)^2 \right.\\
&\left. + \frac{1}{2\beta}\left(w_y - \frac{\beta_z v}{\gamma}\right)^2 + \frac{1}{2\beta}\left(u_y - \frac{\beta_x v}{\alpha}\right)^2\right]\\
\epsilon_z &= \frac{1}{\gamma}\left[w_z + \frac{\gamma_x u}{\alpha} + \frac{\gamma_y v}{\beta} + \frac{1}{2\gamma}\left(w_z + \frac{\gamma_x u}{\alpha} + \frac{\gamma_y v}{\beta}\right)^2 \right.\\
&\left. + \frac{1}{2\gamma}\left(u_z - \frac{\gamma_x w}{\alpha}\right)^2 + \frac{1}{2\gamma}\left(v_z - \frac{\gamma_y w}{\beta}\right)^2\right]
\end{aligned}
\tag{4.8}
$$

$$
\begin{aligned}
\gamma_{yz} &= \frac{v_z}{\gamma} + \frac{w_y}{\beta} - \frac{\gamma_y w}{\beta\gamma} - \frac{\beta_z v}{\beta_\gamma} + \frac{1}{\beta\gamma}\left(v_y + \frac{\beta_z w}{\gamma} + \frac{\beta_x u}{\alpha}\right)\left(v_z - \frac{\gamma_y w}{\beta}\right)\\
&+ \frac{1}{\beta\gamma}\left(w_y - \frac{\beta_z v}{\gamma}\right)\left(w_z + \frac{\gamma_y v}{\beta} + \frac{\gamma_x u}{\alpha}\right) + \frac{1}{\beta\gamma}\left(u_y - \frac{\beta_x v}{\alpha}\right)\left(u_z - \frac{\gamma_x w}{\alpha}\right)\\
\gamma_{zx} &= \frac{w_x}{\alpha} + \frac{u_z}{\gamma} - \frac{\alpha_z u}{\gamma\alpha} - \frac{\gamma_x w}{\gamma\alpha} + \frac{1}{\gamma x}\left(w_z + \frac{\gamma_x u}{\alpha} + \frac{\gamma_y v}{\beta}\right)\left(w_x - \frac{\alpha_z u}{\gamma}\right)\\
&+ \frac{1}{\gamma\alpha}\left(u_z - \frac{\gamma_x w}{\alpha}\right)\left(u_x + \frac{\alpha_z w}{\gamma} + \frac{\alpha_y v}{\beta}\right) + \frac{1}{\gamma\alpha}\left(v_z - \frac{\gamma_y w}{\beta}\right)\left(v_x - \frac{\alpha_y u}{\beta}\right)\\
\gamma_{xy} &= \frac{u_y}{\beta} + \frac{v_x}{\alpha} - \frac{\beta_x v}{\alpha\beta} - \frac{\alpha_y u}{\alpha\beta} + \frac{1}{\alpha\beta}\left(u_x + \frac{\alpha_y v}{\beta} + \frac{\alpha_z w}{\gamma}\right)\left(u_y - \frac{\beta_x v}{\alpha}\right)\\
&+ \frac{1}{\alpha\beta}\left(v_x - \frac{\alpha_y u}{\beta}\right)\left(v_y + \frac{\beta_x u}{\alpha} + \frac{\beta_z w}{\gamma}\right) + \frac{1}{\alpha\beta}\left(w_x - \frac{\alpha_z u}{\gamma}\right)\left(w_y - \frac{\beta_z v}{\gamma}\right)
\end{aligned}
\tag{4.9}
$$

Equation (4.8) (4.9) contains numerous terms but in some situations, the quadratic terms can be omitted, such as for wind turbine towers. This general form can be updated for the cylindrical shell analysis by letting $x = r, y = \theta, z = z$, namely, $\alpha = \beta = \gamma = 1$.

We substitute $\gamma = 1$, and rewrite Equation (4.8) (4.9) as:

$$
\begin{aligned}
\epsilon_x &= \frac{1}{\alpha}\left(u_x + \frac{\alpha_y v}{\beta} + \alpha_z \omega\right) + \frac{\omega_x^2}{2A^2} \\
\epsilon_y &= \frac{1}{\beta}\left(\frac{\beta_x u}{\alpha} + v_y + \beta_z \omega\right) + \frac{\omega_y^2}{2B^2} \\
\gamma_{yz} &= \frac{\omega_y}{\beta} + v_z - \frac{\beta_z v}{\beta} \\
\gamma_{zx} &= u_x + \frac{\omega_x}{\alpha} - \frac{\alpha_z u}{\alpha} \\
\gamma_{xy} &= \frac{u_y}{\beta} + \frac{v_x}{\alpha} - \frac{\beta_x v}{\alpha\beta} - \frac{\alpha_y u}{\alpha\beta} + \frac{\omega_x \omega_y}{AB}
\end{aligned}
\tag{4.10}
$$

The general form of differential equilibriums given by Langhaar (2016) is as follows:

$$
\begin{aligned}
&\frac{\partial}{\partial x}\beta\gamma\sigma_x + \frac{\partial}{\partial y}\gamma\alpha\tau_{xy} + \frac{\partial}{\partial z}\alpha\beta\tau_{xz} + \gamma\alpha_y\tau_{xy} \\
&\qquad +\beta\alpha_z\tau_{xz} - \gamma\beta_x\sigma_y - \beta\gamma_x\sigma_z + \rho\alpha\beta\gamma F_x = 0 \\
&\frac{\partial}{\partial x}\beta\gamma\tau_{yx} + \frac{\partial}{\partial y}\gamma\alpha\sigma_y + \frac{\partial}{\partial z}\alpha\beta\tau_{yz} + \alpha\beta_z\tau_{yz} \\
&\qquad +\gamma\beta_x\tau_{yx} - \alpha\gamma_y\sigma_z - \gamma\alpha_y\sigma_x + \rho\alpha\beta\gamma F_y = 0 \\
&\frac{\partial}{\partial x}\beta\gamma\tau_{zx} + \frac{\partial}{\partial y}\gamma\alpha\tau_{zy} + \frac{\partial}{\partial z}\alpha\beta\sigma_z + \beta\gamma_x\tau_{zx} \\
&\qquad +\alpha\gamma_y\tau_{zy} - \beta\alpha_z\sigma_x - \alpha\beta_z\sigma_y + \rho\alpha\beta\gamma F_z = 0
\end{aligned}
\tag{4.11}
$$

This equation provides the basic general form for the static analysis as well as for pseudo-static analysis. If inertia force is substituted here, dynamic analysis is also available to a certain extent. The localised curvature and overall curvature can be introduced here to express surface moments according to Equation (3.26)–(3.31), which is rewritten as:

$$
\begin{aligned}
M_x &= D\left(\kappa_x + v\kappa_y\right) \\
M_y &= D\left(\kappa_y + v\kappa_x\right) \\
M_{xy} &= M_{yx} = \frac{1}{2}D(1-v)\kappa_{xy}
\end{aligned}
\tag{4.12}
$$

The differential equation written in the form of Lame coefficients is (Langhaar, 2016):

$$
\begin{aligned}
&\frac{\partial}{\partial x}(BN_x)+\frac{\partial}{\partial y}(AN_{yx})+N_{xy}\frac{\partial A}{\partial y}-N_y\frac{\partial B}{\partial x}+\frac{ABQ_x}{r_1}+ABP_x=0\\
&\frac{\partial}{\partial x}(BN_{xy})+\frac{\partial}{\partial y}(AN_y)+N_{yx}\frac{\partial B}{\partial x}-N_x\frac{\partial A}{\partial y}+\frac{ABQ_y}{r_2}+ABP_y=0\\
&\frac{\partial}{\partial x}(BQ_x)+\frac{\partial}{\partial y}(AQ_y)-\frac{AB}{r_1}N_x-\frac{AB}{r_2}N_y+ABP_z=0\\
&\frac{\partial}{\partial x}(BM_x)+\frac{\partial}{\partial y}(AM_{yx})+M_{xy}\frac{\partial A}{\partial y}-M_y\frac{\partial B}{\partial x}-ABQ_x+ABR_y=0\\
&\frac{\partial}{\partial x}(BM_{xy})+\frac{\partial}{\partial y}(AM_y)+M_{yx}\frac{\partial B}{\partial x}-M_x\frac{\partial A}{\partial y}-ABQ_y-ABR_x=0
\end{aligned}
\tag{4.13}
$$

Equation (4.13) comprises the complete general equilibriums for a random shell element, while in our cylindrical shell analysis, we can neglect the curvature change due to torsion and shear; for combined loading conditions, however, the curvature change owing to bending should not be ignored.

4.2 Strain energies on cylindrical shells

When considering energy methods, it is evident that the external work will be dissipated by internal works which contain two parts: the bending strain energy, and the stretching strain energy – namely, the membrane strain. We substitute Equation (4.12) into Equation (4.13), based on the basic view that strain energy on the shell element in Figure 4.2 can be approximated by Langhaar (2016):

$$
U=\iint ABdxdy\int_{-h/2}^{h/2}U_0dz \tag{4.14}
$$

When proposing this equation, he mentioned the term U_0 as the strain energy density.

The general expressions for membrane strain energy and bending strain energy are written as:

$$
\begin{aligned}
U_m&=\frac{G}{1-\nu}\iint\left[\epsilon_x^2+\epsilon_y^2+2\nu\epsilon_x\epsilon_y+\frac{1}{2}(1-\nu)\epsilon_{xy}^2\right]hABdxdy\\
U_b&=\frac{G}{12(1-\nu)}\iint\left[\kappa_x^2+\kappa_y^2+2\nu\kappa_x\kappa_y+\frac{1}{2}(1-\nu)\kappa_{xy}^2\right]h^3ABdxdy
\end{aligned}
\tag{4.15}
$$

in which $\epsilon_x, \epsilon_y, \kappa_x, \kappa_y$ are the exact values at the local point (x, y), strain magnitudes and Gaussian curvatures, respectively.

Since the shell is cylindrical, we apply the cylindrical coordinate system to previous equations, and thus we have: A=1 and B=a, the shell radius; $1/r_1 = 0$ according to Equation (4.6) and $r_2 = a$; the terms Q_x are ignored as the tangential forces from wind load have been omitted. The Equation (3.40) – (3.46) can be rewritten here as:

$$\frac{\partial N_x}{\partial x} + \frac{1}{a}\frac{\partial N_{x\theta}}{\partial \theta} = 0, \qquad \frac{\partial N_{x\theta}}{\partial x} + \frac{1}{a}\frac{\partial N_\theta}{\partial \theta} = 0 \tag{4.16}$$

The $N_{x\theta}$ and $N_{\theta x}$ here can be regarded the same. Following this, we have:

$$N_x = \frac{\partial^2 F}{\partial \theta^2}, N_\theta = a^2\frac{\partial^2 F}{\partial x^2}, N_{x\theta} = -a\frac{\partial^2 F}{\partial x\,\partial \theta} \tag{4.17}$$

The Airy stress function, denoted by F, has been introduced in Equation (4.17), and is generally expressed as:

$$\sigma_x = \frac{\partial^2 \varphi}{\partial y^2}; \qquad \sigma_y = \frac{\partial^2 \varphi}{\partial x^2}; \qquad \sigma_{xy} = -\frac{\partial^2 \varphi}{\partial x\,\partial y} - \left(f_x y + f_y x\right) \tag{4.18}$$

Here, f_x and f_y are body forces in their respective directions; φ represents the stress function and also provides the basis for Föppl-von Kármán equations for plate in large deflections (Föppl, 1910).

The total potential energy from Equation (4.15) is written as:

$$\begin{aligned} V = a\iint \Bigg\{ & \frac{Gh}{1-\nu}\Bigg[\left(\bar{u}_x + \frac{1}{2}\omega_x^2\right)^2 + \left(\frac{\bar{v}_\theta + \omega}{a} + \frac{\omega_\theta^2}{2a^2}\right)^2 \\ & + 2v\left(\bar{u}_x + \frac{1}{2}\omega_x^2\right)\left(\frac{\bar{v}_\theta + \omega}{a} + \frac{\omega_\theta^2}{2a^2}\right) + \frac{1}{2}(1-v)\left(\bar{v}_x + \frac{\bar{u}_\theta}{a} + \frac{\omega_a \omega_\theta}{a}\right)^2\Bigg] \\ & + \frac{Gh^3}{12(1-v)}\left[\omega_{xx}^2 + \frac{\omega_{\theta\theta}^2}{a^4} + 2v\omega_{xx}\frac{\omega_{\theta\theta}}{a^2} + 2(1-v)\frac{\omega_{x\theta}^2}{a^2}\right]\Bigg\} dx d\theta \end{aligned} \tag{4.19}$$

Here, $\bar{u}_x, \bar{v}_\theta$ are the values of the coordinate on the mid-surface of the shell.

Furthermore, the Euler function mentioned in Equation (3.48) is rewritten in this form:

$$D\left(w_{xxxx}+\frac{2}{a^2}w_{xx\theta\theta}+\frac{1}{a^4}w_{\theta\theta\theta\theta}\right)+\frac{N_\theta}{a}$$
$$=p+N_x w_{xx}+\frac{2}{a}N_{x\theta}w_{x\theta}+\frac{1}{a^2}N_\theta w_{\theta\theta} \tag{4.20}$$

Here, $D=\frac{Eh^3}{12(1-v^2)}$ is the same as in previous functions. Equation (4.20), originally deduced by Donnell (1934), considers moments on shell surfaces, and we see that the terms $N_{x\theta}, w_{x\theta}, w_{\theta\theta}, w_{xx}$ are nonlinear and N_x, N_θ, $N_{x\theta}$ are all derived from nonlinear calculations. This demonstrates the superiority of this technique over classical buckling analysis, as this non-classical method takes the nonlinearity into consideration.

We can simplify the general equations above into a Cartesian coordinate system for a cylinder: based on the basic assumption of the plane slab without the strain components ε_z, γ_{xz}, and γ_{yz}, the accumulated energy of slab U_s results in[8],

$$U_s=\frac{1}{2}\int_v\left(\sigma_x\varepsilon_x+\sigma_y\varepsilon_y+\tau_{xy}\gamma_{xy}\right)dxdydz \tag{4.21}$$

where,

$$\sigma_x=-\frac{Ez}{1-v^2}\left(\frac{\partial^2 f}{\partial x^2}+v\frac{\partial^2 f}{\partial y^2}\right),\qquad \varepsilon_x=-z\frac{\partial^2 f}{\partial x^2}$$
$$\sigma_y=-\frac{Ez}{1-v^2}\left(\frac{\partial^2 f}{\partial y^2}+v\frac{\partial^2 f}{\partial x^2}\right),\qquad \varepsilon_y=-z\frac{\partial^2 f}{\partial y^2} \tag{4.22}$$
$$\tau_{xy}=-\frac{Ez}{1+v^2}\left(\frac{\partial^2 f}{\partial x\,\partial y}\right),\qquad \gamma_{xy}=-2z\left(\frac{\partial^2 f}{\partial x\,\partial y}\right)$$

If the slab thickness is maintained constantly without thickness variation, the integration of the energy equation shows no variation with z. Considering Equation (3.44) and introducing the curvature items to the equation to describe cylindrical shells, the following equation is yielded:

[8] Some of the following paragraphs have been published in Ma, Martinez-Vazquez and Baniotopoulos (2020).

$$U = \frac{D}{2}\iint_A \left\{(\nabla^2 f)^2 - 2(1-\nu)\left[\frac{\partial^2 f}{\partial x^2}\frac{\partial^2 f}{\partial y^2} - \left(\frac{\partial^2 f}{\partial x \partial y}\right)^2\right]\right\} dxdy$$

$$= \frac{1}{2}\iint_A \left\{M_x \frac{\partial^2 f}{\partial x^2} + 2M_{xy}\frac{\partial^2 f}{\partial x \partial y} + M_x \frac{\partial^2 f}{\partial y^2}\right\} dxdy \tag{4.23}$$

$$= \frac{1}{2}\iint_A D\{(K_x + K_y)^2 - 2(1-\nu)[K_x K_y - {K_{xy}}^2]\} dxdy$$

In Equation (4.23), A represents the shell surface area. Furthermore, by letting curvature components K_x, K_y, and K_{xy} be curvature variations represented by as x_x, x_y, and x_{xy}, we could express the bending strain energy as:

$$U_b = \frac{D}{2}\iint_A \left\{\left(x_x + x_y\right)^2 - 2(1-\nu)\left[x_x x_y - x_{xy}^2\right]\right\} dxdy \tag{4.24}$$

The in-plane strain energy is due to the membrane effect. The mid-surface stretching then becomes:

$$U_m = \frac{1}{2}\iint_A \left\{N_x \varepsilon_{x0} + N_y \varepsilon_{y0} + N_{xy}\gamma_{xy0}\right\} dxdy$$

$$= \frac{Et}{2(1-\nu^2)}\iint_A \left\{\left(\varepsilon_{x\theta} + \varepsilon_{y\theta}\right)^2 - 2(1-\nu)\left[\varepsilon_{x\theta}\varepsilon_{y\theta} - \frac{1}{4}\gamma_{xy\theta}^2\right]\right\} dxdy \tag{4.25}$$

All of the shell surface displacement functions could be expressed accurately with trigonometric functions embedded in relatively simple algorithms, as discussed above. The nodal displacement function of the tower shell was assumed approximately by the sum of two items as:

$$u = u_1 + u_2,\ v = v_1 + v_2,\ f = f_1 + f_2 \tag{4.26}$$

In this way, each displacement component is described as:

$$\begin{cases} u_1 = 0 \\ u_2 = -r\sum_{n=1}^{\infty}\frac{1}{n}(b_n \sin n\theta + d_n \cos\theta) \\ v_1 = r\sum_{n=1}^{\infty}(a_n \cos n\theta - c_n \sin\theta) \\ v_2 = r\sum_{n=1}^{\infty}(b_n \cos n\theta - d_n \sin\theta) \\ f_1 = -r\sum_{n=1}^{\infty} n(a_n \sin n\theta + c_n \cos\theta) \\ f_2 = -r\sum_{n=1}^{\infty} n(b_n \sin n\theta + d_n \cos\theta) \end{cases} \quad (4.27)$$

In equation (4.27), we improved the simpler equations that examined either one sinusoidal function, such as Equation (3.8), or multiplicated sinusoidal functions, such as Equation (3.58), and created this form of sinusoidal function plus cosine function via parameters. The shell strain energy stays at a minimum under the hypothesis of inextensible shell performance. The bending strain energy U_{b1}, under the condition $\frac{\partial^2 f}{\partial x^2} = x_x = 0$, therefore follows:

$$U_{b1} = \frac{D}{2}\iint_A \{{x_\theta}^2 + 2(1-\nu)x_{x\theta}^2\} r d\theta dx \quad (4.28)$$

Equation (4.28) is distinct from Equation (4.24). The former provides the integration in polar coordinates and is split from stretching strain energies. Moreover, by substituting Equation (3.25) into Equation (4.28), and combining this process with displacement functions (4.26), we are able to quantify the basic total strain energy of the unstretched shell section (the first element that is obliterated) as follows (Calladine and Sanders, 1984):

$$U = \pi DL \sum_{n=2}^{\infty} \frac{(n^2-1)^2}{r^3} \Big\{ r^2 n^2 [a_n^2 + (\mathrm{c}_n)^2] + \frac{1}{3} L^2 n^2 [b_n^2 + (\mathrm{d}_n)^2] + 2(1-\nu) r^2 [b_n^2 + (\mathrm{d}_n)^2] \Big\} \tag{4.29}$$

where, a_n, b_n, c_n, and d_n are constants that depend on loading conditions. Once defined, these lead to trigonometric functions that express initially assumed displacements. For example, when n = 1,

$$\begin{cases} v_1 = r(a_1 \cos\theta - c_1 \sin\theta) \\ f_1 = r(a_1 \sin\theta - a_1 \cos\theta) \end{cases} \tag{4.30}$$

The relationship between virtual work and applied axial load N is therefore (let $n = l$ in previous sections):

$$\delta_w = 2\pi N \left[v \int_0^L C_0 \sin \frac{l\pi x}{L} dx + \frac{r}{2} \int_0^L \left(C_0 \frac{l^2\pi^2}{L^2} \sin \frac{l\pi x}{L} \right)^2 dx \right] \tag{4.31}$$

To sum up the virtual works δ_{U_m} (membrane strain energy) and δ_{U_b} (bending strain energy), the equation above progresses to:

$$\begin{aligned} \delta_U &= \delta_{U_m} + \delta_{U_b} \\ &= -2Ev\pi t\varepsilon_{x_l} \int_0^L C_0 \sin \frac{l\pi x}{L} dx + \frac{\pi^2 C_0^2 EtL}{2r} + C_0 \frac{2\pi^4 aLD\pi l^4}{2L^4} \end{aligned} \tag{4.32}$$

when $\delta_w = \delta_U$.

Finally, by considering Equations (4.31) and (4.32) while letting $C_0 \neq 0$, one identifies the following approximation to the critical load N_{cr}:

$$\left(\frac{\pi EtL}{2\gamma} + \frac{\pi^2 \gamma l^4 D}{2L^3} - \frac{\pi^3 r l^2 N}{2L} \right) C_0^2 = 0 \tag{4.33}$$

$$N_{cr} = D \left(\frac{l^2\pi^2}{L^2} + \frac{EL^2 t}{Dr^2 l^2 \pi^2} \right) \tag{4.34}$$

This equation indicates a very simple approach via energy methods for the critical buckling load, in a longitudinal direction under axial compressive loads. The bending effects are applied through the energy method in the following section.

4.3 Combined bending moment and axial load on cylindrical shells using energy methods

The classical bending calculations have been derived in section 3.4 and 3.5. In this section, the improved combined loading calculation will be derived by means of energy methods, based on the connection via curvature change and wavelengths.

The circumferential stretching strain was generated on the shell surface under pure bending moments, which can be rewritten by substituting Equation (3.72) to Equation (3.71):

$$\eta = \left(\frac{\mathrm{d}v}{\mathrm{d}y} + \frac{\omega}{R}\right) + \frac{1}{2}\left(\frac{\mathrm{d}v}{\mathrm{d}y} + \frac{\omega}{R}\right)^2 + \frac{1}{2}\left(\frac{v}{R} - \frac{\mathrm{d}\omega}{\mathrm{d}y}\right)^2 \tag{4.35}$$

At the same time, the longitudinal stretching strain can be given by (Gellin, 1980):

$$E_{xx} = -\kappa h \tag{4.36}$$

It is supposed that the extreme fibre happened at the point when y=0, according to Figure 3.7 (b), and the deviation h on the Cartesian coordinate can be expressed as

$$h = (R + w)\cos\left(y/R\right) - v\sin\left(y/R\right) \tag{4.37}$$

If we assume that in the prebuckling and transient buckling stages, there is no extension of the mid-surface of the shell in the circumferential direction, the circumferential stretching strain should be equal to zero, and thus the derivative on Equation (4.35) should be written as:

$$\delta\eta = [1 + \left(\frac{\mathrm{d}v}{\mathrm{d}y} + \frac{\omega}{R}\right)]\delta(\frac{\mathrm{d}v}{\mathrm{d}y} + \frac{\omega}{R}) + (\frac{v}{R} - \frac{\mathrm{d}\omega}{\mathrm{d}y})\delta(\frac{v}{R} - \frac{\mathrm{d}\omega}{\mathrm{d}y}) = 0 \tag{4.38}$$

If a small rotation happened on the cylinder, following the suggestion of Brazier and Southwell (1927),

$$\sin\ \phi = \phi \tag{4.39}$$

and the circumferential bending strain is

$$K_{yy} = \frac{1}{\sqrt{1-\phi^2}}\frac{\mathrm{d}\phi}{\mathrm{d}y} \tag{4.40}$$

If the nonlinear terms are maintained, primary strains in both directions are:

$$\epsilon_{xx} = E_{xx} + zK_{xx}; \qquad \epsilon_{yy} = E_{yy} + zK_{yy} \tag{4.41}$$

The relationship between stress–strain has been suggested by Ramberg and Osgood (1943): they gave their names to the so-called 'Ramberg-Osgood' stress–strain curve, denoted by:

$$\epsilon = \sigma + \mathbb{K}\left(\frac{S_1}{E}\right)^{n-1}\sigma^n \tag{4.42}$$

This has been characterised by Gellin (1980):

$$\epsilon = \frac{\sigma}{E}\left[1 + \frac{3}{7}\left|\frac{\sigma}{\sigma_Y}\right|^{n-1}\right] \tag{4.43}$$

σ_Y here is the effective yielding stress. However, Gellin argued that the solutions do not need to be obtained by increment methods based on deformation theory, which were limited due to the scant calculation resources available in the 1980s. We are now able to achieve the full range of solutions using increment methods, such as the arc-length method for variation equations on energy expressions.

The constitution relations could be applied in this research to the expressions of strain energy for an ovalised cylinder. We can refer to the two dimensional constitutive relations (Gellin, 1980):

$$\boldsymbol{\epsilon_{xx}} = \frac{1}{E_s}\left(\sigma_{\boldsymbol{x}} - \nu_s\sigma_{yy}\right); \qquad \boldsymbol{\epsilon_{yy}} = \frac{1}{E_s}\left(\sigma_{yy} - \nu_s\sigma_{\boldsymbol{x}}\right) \tag{4.44}$$

Here, E_s is secant modulus calculated by Equation (4.43). The subsequent variational step applied to the internal work for a finite element is (Gellin, 1980):

$$\delta U = \int_0^{2\pi R}\int_{-\hbar/2}^{\hbar/2}\left(\sigma_{xx}\delta\epsilon_{xx} + \sigma_{yy}\delta\epsilon_{yy}\right)\mathrm{d}z\mathrm{d}y \tag{4.45}$$

Equation (4.41) can be substituted here, and Equation (4.45) rewritten as:

$$\delta U = \int_0^{2\pi R}\left(M_{xx}\delta K_{xx} + M_{yy}\delta K_{yy} + N_{xx}\delta E_{xx} + N_{yy}\delta E_{yy}\right)\mathrm{d}y \tag{4.46}$$

It is worth noting that the terms M_{xx}, M_{yy}, N_{xx}, N_{yy} are combinations of bending and axial compressing loads, although (Gellin, 1980) and Brazier and Southwell (1927) argued that the items M_{yy} and N_{xx} should be neglected due to their infinitesimal values in pure bending.

The updated curvature expressions and displacement functions will be introduced here. According to Equation (4.27), the u, v, f deformation functions in terms of angular coordinate θ could be extended and discretised following the suggestion by Brush et al. (1975) on a general ring analysis:

$$\begin{aligned}
f(\theta) &= a_0 + a_1\sin\,\theta + \sum_{n=2,4,6,\ldots} a_n\cos\,n\theta + \sum_{n=3,5,7,\ldots} a_n\sin\,n\theta \\
v(\theta) &= -a_1\sin\,\theta + \sum_{n=2,4,6,\ldots} b_n\sin\,n\theta + \sum_{n=3,5,7,\ldots} b_n\cos\,n\theta \\
u(\theta) &= \sum_{n=2,4,6,\ldots} c_n\cos\,n\theta + \sum_{n=3,5,7,\ldots} c_n\sin\,n\theta \\
\gamma(\theta) &= \gamma_0 + \gamma_1\sin\,\theta + \sum_{n=2,4,6,\ldots} \gamma_n\cos\,n\theta + \sum_{n=3,5,7,\ldots} \gamma_n\sin\,n\theta
\end{aligned} \tag{4.47}$$

In comparison to Equation (4.27), the fourth equation $\gamma(\theta)$ refers to distortion that occurred on the cylindrical shells. The parameters a_n, b_n determined by in-plane displacement happened on the tubular cross-section and c_n, γ_n refer to that on the out-of-plane part. The transitions of coordinate values can refer to Equation (3.82).

Several researchers have studied the interactions between the ovalisation and moment on a bending tube, connected by the effective measurement: curvature. Most of these studies were conducted based on experimental observations. In the 1920s, Brazier and Southwell (1927) addressed the moment–curvature relation as

$$M = \pi\kappa\left[1 - \frac{3}{2}\kappa^2\right] \tag{4.48}$$

based on the normalised ovalisation–curvature relation as

$$\zeta = \kappa^2 \tag{4.49}$$

ζ represents the normalised ovalisation of the bent tube. This is a very simple method of general calculation for initially straight cylinders and the outcome has been revised by Reissner (1959), who uses the ovalisation–curvature relation, indicated by:

$$\zeta = \frac{\kappa\lambda}{\lambda^2} + \kappa^2 \tag{4.50}$$

Here $\lambda = \frac{Rt}{r^2\sqrt{1-\nu^2}}$ is a parameter to describe the geometry of a cylinder, and the moment–curvature relationship is renewed as follows:

$$M = \pi\kappa\left[1 - \frac{3}{4\lambda^2}(1+\kappa\lambda)(1+2\kappa\lambda)\right] \tag{4.51}$$

Reissner (1959) result was enhanced in the 1980s by Boyle (1981), who addressed a more accurate and detailed moment–curvature relation based on the same ovalisation–curvature relation as Equation (4.50), indicated by:

$$M = \frac{\pi\kappa}{(1-\nu^2)} + \left[1 - \frac{3}{4\lambda^2}\frac{(1+\kappa\lambda)(1+2\kappa\lambda)}{(1-\nu^2) + \frac{5(1+\kappa\lambda)^2}{6\lambda^2}}\right] \tag{4.52}$$

The equations provided above show a path for studying the interactions between Brazier's effect and the bending resistance of a cylindrical shell section, and also emphasise the importance of curvature as a geometrical parameter; additionally, a

dimensionless form of geometry and forces is a practical method for parametric studies.

Before now based on energy methods, it has been extremely troublesome to calculate a section of wind turbine tower under combined loading conditions, simply as by combining previous equations. The total internal strain energy equals the sum of strain energy due to axial compression and strain energy generated by bending, which is represented as:

$$\begin{aligned} \delta U &= \delta U(axial\ compression) + \delta U(bending) \\ &= \delta[U_b + U_m](axial\ compression) + \delta U[U_b + U_m](bending) \end{aligned} \tag{4.53}$$

The two parts share the same curvature expression and mid-surface deformation function; this forms the continuation conditions for a cylindrical shell section as a conservative system.

4.4 Concluding remarks

This chapter applied the non-classical buckling theories and energy concepts to the shell buckling analysis of wind turbine tower section. The nonlinearity of displacement has been introduced, and the energy function has been applied by assuming that the tower section was a conservative system, then allowing for the external work to be equal to the sum of internal strain energies. A system of expressions for general elementary stress and strain were derived based on element analysis. Utilising the variational algorithms in energy methods, the relation between shell surface displacement functions and internal–external stress–strain items were obtained. The equilibriums under the energy category implicitly contained the curvature parameters, and the assumed form of the displacement function in Chapter 3 was updated to an alternative form.

5 NUMERICAL SIMULATIONS

5.1 Finite element method

5.1.1 The concept of finite element method

Finite element method (FEM) is a widely used method for numerical simulations in engineering fields, as well as for some specific mathematical areas. The basic concept of FEM in engineering is to subdivide a real structure into a finite number of elements which are connected continuously; in other words, a structure has been discretised into a countable number of tiny geometries, which are also called 'mesh'. The matrix theory provided the basis for the effective calculation of FEM, especially in the case of computers' solving processes, and fundamentally, a long series of partial differential equations can be solved using a particular numerical method. FEM saw its popularity increase along with the development of computer science, especially after the 1970s, and it has recently become a solid approach that is narrowing gaps between theoretical research and engineering practice.

Variational formulation characterises FEM, and we chose this as an effective solving algorithm after optimising it for structural discretisation; the post-processing steps will also be applied, such as visualisation or data outputs. FEM can give solutions for any mechanical problem if the model has been created correctly and the solving algorithm determined effectively; what should be considered is the economic calculation time and the issues of convergence, especially in the computational fluid dynamics (CFD).

5.1.2 The original wind turbine structure

The first step is to determine the simulation objectives for FEM analysis in this research. As we discussed in previous chapters, the secondary bottom tower section is the part most vulnerable to buckling failure, and this section has been chosen as the basic model in this research. The bottom section of the wind turbine tower is effectively stiffened by both ring stiffeners and longitudinal stiffeners, and door-opening reinforcement. For the secondary bottom section, especially for a cylindrical shell structure under combined loads, a pure shell section is the best choice for a buckling mechanism investigation due to the large variation of stiffening configurations that can influence the buckling behaviour comprehensively. This is preferable for obtaining a fundamental understanding of the complex buckling paths and the results of pure shell structure are the lower bound for wind turbine tower design.

The tower shell contains numerous geometry configurations which may be designed specifically for certain wind farms or general models for normal wind resource areas. In the category of tower geometry, the buckling behaviour of a pure cylindrical shell section depends on the diameter, wall thickness, and cylinder length – we apply the ratios between these geometry configurations to parametrically analyse the buckling process, in line with previous research. Therefore, the length–radius ratio (L/R) and the radius–wall thickness ratio (R/t) have been chosen for the non-dimensional analysis. It is widely believed that the specific magnitude of shell geometry has no relation to the buckling behaviour, whereas shells with different sizes but with the same L/R and R/t ratios reveal the same buckling responses (Ma et al., 2020, Hutchinson, 1968, Von Karman and Tsien, 1939, Teng and Rotter, 2006, Donnell, 1934, Seide and Weingarten, 1959, BATTERMAN, 1965, Gellin, 1980, Edlund, 1974).

A prototype of a wind turbine tower has been chosen for the FEM modelling, in the hope of narrowing the gap between theoretical outcomes and engineering practice.

The modern cylindrical steel tower for wind energy harvesting contains numerous prototypes and general models. We selected a typical prototype of a wind turbine tower, the NREL 5 MW baseline wind turbine (Jonkman et al., 2009), for FEM modelling settings. The general information about the tower is listed below:

Category:	**Values**
Height:	87.600 m
Elevation at base:	0 m
Elevation at top:	87.600 m
Average mass distribution:	3,976 kg/m
Total mass:	348.338 t
Modulus of elasticity:	210.000 GPa
Shear modulus:	80.769 GPa
Poisson's ratio:	0.300
Density:	8,500 kg/m^3
Yield stress:	355.000 MPa
For bottom cross-section,	
Euler buckling load:	1,589.720 MN (162,106 t)
Euler buckling stress:	1.208 GPa
Slenderness:	41
Axial capacity:	467.045 MN (47,625 t)
Relative slenderness:	0.542
Top diameter (outer):	3.870 m
Base diameter (outer):	6.000 m
Top thickness:	25 mm
Base thickness:	35 mm

Table 5.1 Basic information on the NREL 5 MW tower.

For the secondary bottom section of the NREL 5 MW tower, the basic information is listed in Table 5.2:

Category:	Values
Height:	8.76 m
Elevation at base:	8.76 m
Elevation at top:	17.52 m
Thickness:	34 mm
Average mass distribution:	3,976 kg/m
Total mass:	52.700 t (5,281 kg/m)
Diameter:	5.822 m
Area (outer):	26.626 m2
Cross-section area:	0.621 m2
EI, 1st axis:	546.469 GNm2

Table 5.2 Basic information about the NREL 5 MW tower, secondary bottom section.

Based on the tower section information above, we infer that the shell models are as follows: the fixed diameter is 6.0m; there are various thicknesses that step up in 3 mm increments, from 24 mm thickness to 36 mm thickness; shell lengths are 9.0 m, 12.0 m, 15.0 m and 20.0 m. This set of geometry configurations could generally cover a popular range of L/R ratio and R/t ratios for modern cylindrical steel towers, following the model geometry in FEM analysis listed in Table 5.3:

No.	Diameter D	Length L	Thickness t	L/R	R/t
1	6000	20,000	24	6.66	125
2	6000	15,000	24	5	125
3	6000	12,000	24	4	125
4	6000	9000	24	3	125
5	6000	20,000	27	6.66	111.11
6	6000	15,000	27	5	111.11
7	6000	12,000	27	4	111.11
8	6000	9000	27	3	111.11
9	6000	20,000	30	6.66	100
10	6000	15,000	30	5	100
11	6000	12,000	30	4	100
12	6000	9000	30	3	100
13	6000	20,000	33	6.66	90.91
14	6000	15,000	33	5	90.91
15	6000	12,000	33	4	90.91
16	6000	9000	33	3	90.91

17	6000	20,000	36	6.66	83.33
18	6000	15,000	36	5	83.33
19	6000	12,000	36	4	83.33
20	6000	9000	36	3	83.33

Table 5.3. Model geometry size in the FEM analysis.

5.1.3 Shell elements

Shell elements are nominated, as the wind turbine tower thickness is small compared to its diameter and length; consequently, the primary stresses in the thickness direction are ignored. The typical shell elements have been depicted in Figure 5.1 (Abaqus, 2014). The reasonable choices for wind turbine towers' shell elements fall between the S4R and C3D8R elements. After comparing these two element structures, it is clear that S4R shell element is time-efficient and accurate for the shell buckling analysis in this case (Ma et al., 2020).

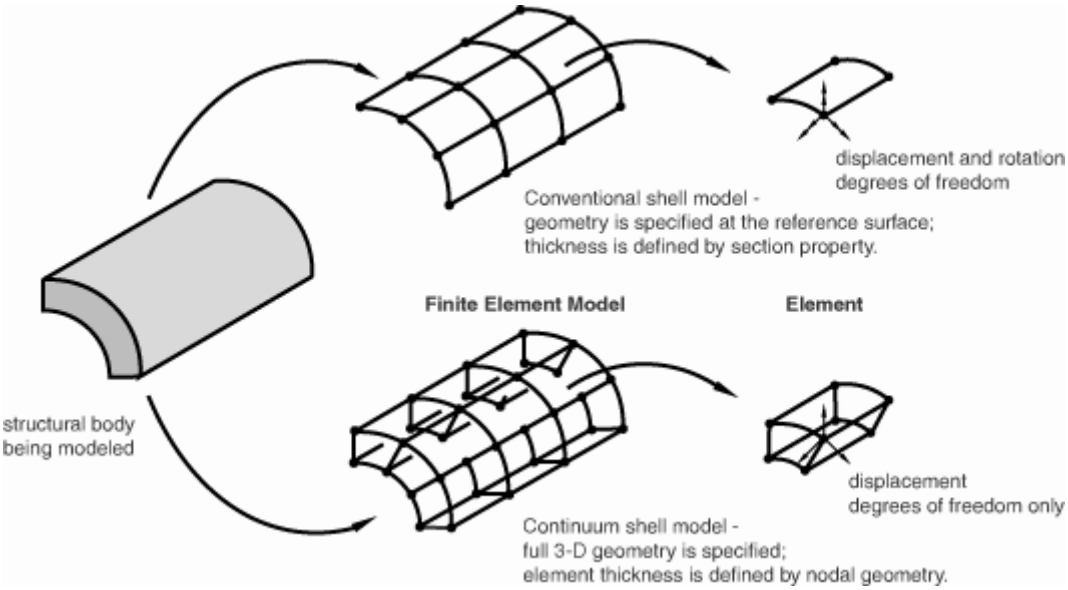


Figure 5.1. The illustration of conventional versus continuum shell elements by Abaqus (2014).

The S4R element is named as ' 4-node reduced integration element' in Abaqus (2019); this is a kind of shell element which considers the conventional stress and displacement applied to shell elements, with nodes by each of the 4 corners, calculated via reduced integrations (which are optional). An illustration of the S4R element is shown in Figure 5.2.

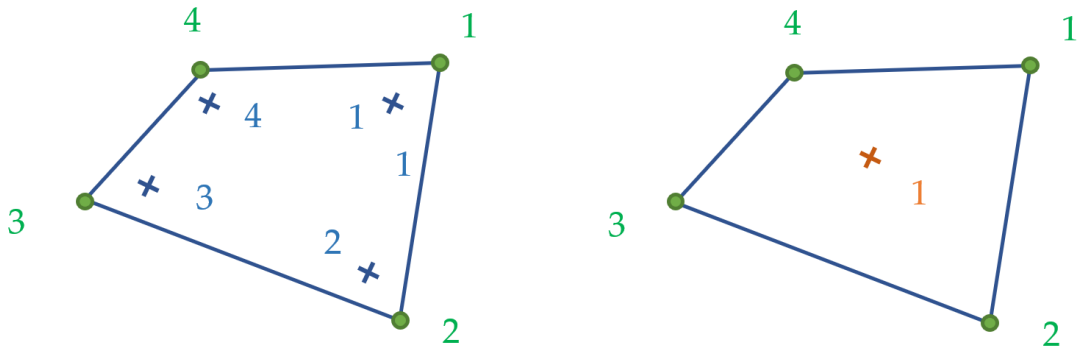


Figure 5.2. The 4-node element and the S4R element.

Furthermore, the R/t ratios of our models are in the range of 83.33–125, which has a large ratio between the thickness in the normal direction, and the magnitude in both directions on the shell surface; this will result in an accuracy problem and convergence issues if applied to the continuum solid elements such as the C3DBR element.

5.1.4 Eigenvalue buckling prediction, geometry imperfections and the Riks method

In ABAQUS/Standard, the analysis steps contain a simple function for estimating the buckling load by eigenvalue extraction, based on the linear prebuckling calculation and response (Abaqus, 2014). The prediction step is to apply the static perturbation loads to the model and by increments add the applied load until the buckling occurs, while recording a series of buckling eigenvalues respectively to each of the eigenmodes. This linear buckling prediction in the linear category provides essential data for our later nonlinear buckling analysis (both the transient buckling analysis and postbuckling analysis). The equations solved in the eigenvalue buckling steps given by (Abaqus, 2014) are:

$$\int_{VB} \mathbf{P}:\frac{\partial \bar{\mathbf{v}}}{\partial \mathbf{X}} dV^B = \int_{S^B} \mathbf{p}\cdot\bar{\mathbf{v}} dS^B + \int_{V^B} \mathbf{b}\cdot\bar{\mathbf{v}} dV^B \tag{5.1}$$

Here, $\bar{\mathbf{v}}$ is an arbitrary virtual velocity field, P is the load on the structure boundary, labelled as S^B, b is the unit-volume body force, V^B is the element volume, and X

represents the coordinate of a mass point in the space. This prediction method is conceptually similar to the previous derived eigenvalue calculation but particularly designed for computer calculation by matrix programming.

The eigenvalue buckling prediction will carry out the designated number of sequences of eigenvalues and the linear ultimate buckling load. The first few eigenmodes could be extracted as initial displacement geometry, if applied to a perfect shell; the initial geometry imperfections are applied. The modal shapes for a perfect cylinder are asymmetric, except for the first modal; therefore, we need to use a combination of the first few modals. The geometric imperfections introduced in our modelling were reflected in modal shape imperfections, calculated with a linear buckling analysis for axial compression scenarios[9]. As shown in Figure 5.3, the first compression modal was approximately symmetric with respect to the z-axis, while the second and third modal were asymmetric. The initial loading condition of the wind turbine tower shell was assumed to be purely compressive, and therefore without eccentricity generated by the lateral motion of the upper segment of the structure, including nacelle and blades, during static load. The first three compressive modal shapes reproduced complex initial imperfections at rates of 10% for the first modal, 5% for the second modal, and 2.5% for the third modal. This enabled us to determine the lower buckling bound effectively, which depicts a typical compression modal combination, as represented in Figure 5.3.

[9] Some of the following paragraphs have been published in Ma, Martinez-Vazquez and Baniotopoulos (2020).

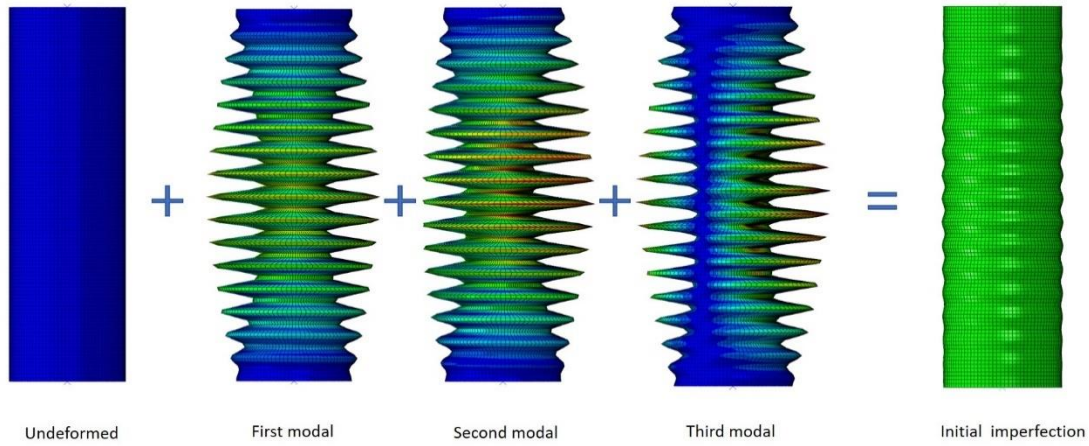


Figure 5.3. Modal imperfection shape combination of the cylindrical shell; the result is shown in a scale factor of 100 (Ma et al., 2020).

On account of the impact of amplitudes of imperfection in FEM, we referred to the results summarised by Teng and Rotter (2006) who collected four buckling stress–imperfection amplitude relations, in the axisymmetric imperfections shown in Figure 5.4.

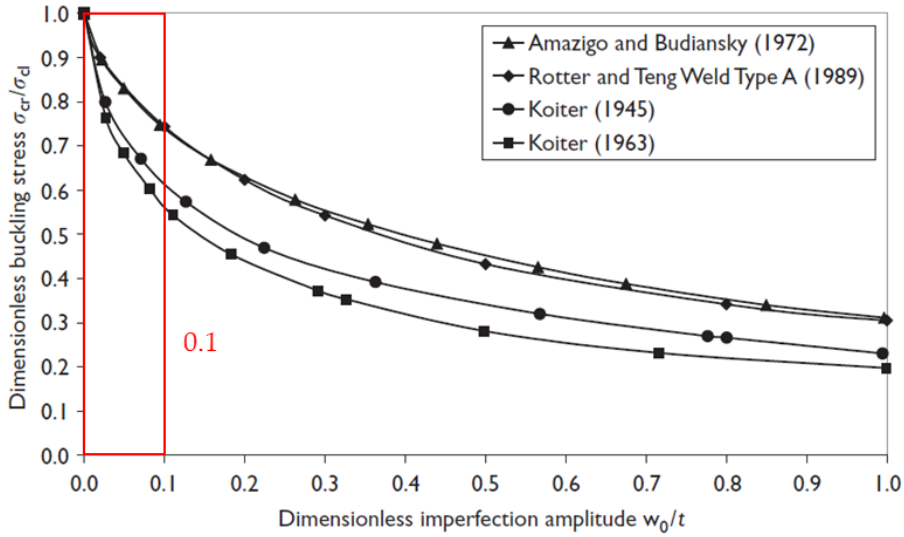


Figure 5.4. Relationship between buckling stress reduction and amplitude of axisymmetric imperfections. (Reproduced by Teng and Rotter (2006)).

We could observe that for the axisymmetric imperfection, the buckling stress drops dramatically half of the entire asymptote amount in the first 10 % of the imperfection amplitude followed by another half in the next 90 % w_0/t. As the imperfection is rarely

large in the wind turbine industry, and according to the geometrical imperfection tolerance by design codes discussed in the Chapter 3.6 and the onsite maintenance operations, 0.1 of the first axisymmetric eigenmode in the dimension of shell thickness for initial geometry imperfection is relatively appropriate and practical in this case.

When considering the asymmetric imperfection, such as the second modal shape and third modal shape, we referred to the review by Teng and Rotter (2006) about the non-symmetric buckling to the imperfect shells, as shown in Figure 5.5. It is noticeable that as the imperfection amplitude grows larger, the circumferential buckling mode decreases, which means the size of the buckled area increases. The imperfection amplitude in the range of -0.05 to 0.05 already reveals noticeable variations; therefore, we selected 5% for the second modal shape and 2.5% for the third modal shape (Ma et al., 2020). In total, this setting introduces a superposition imperfection at 17.5 % according to the dimension of shell wall thickness and this figure falls into the range between the minimum 10 % by EN 1993-1-6 (2007) and the maximum tolerance 40 %. These insensitive modal shapes after the third eigenvalue are neglected in this FEM analysis.

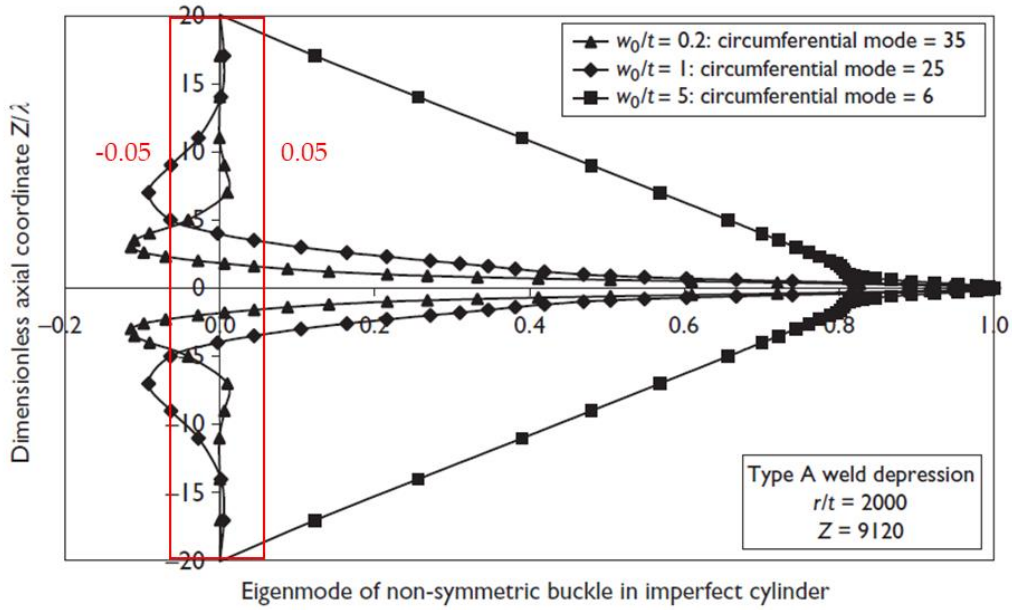


Figure 5.5. The relation of imperfect amplitudes to the critical buckling modes.

The Riks method (Riks, 1997, Riks, 1979, Riks et al., 1996), a kind of arc-length method applied as a function in ABAQUS, is a finite element equation-solving approach. Riks (1979) first enhanced the arc-length method for a specific snapping behaviour in the buckling paths. The Riks method works for displacement control and force control in ABAQUS, by suggesting a parameter called the load proportionality factor (LPF). In basic tower design steps, linear eigenvalue calculation is sometimes sufficient for engineering purposes, but is unable to reveal the postbuckling buckling behaviour which we were aiming for. The Riks method is suitable for tracking postbuckling paths via a static analysis procedure, which reduces the calculation load for a dynamic analysis, although the buckling procedure is a dynamic behaviour. The jumping and snapping phenomenon in the postbuckling stage is a form of ill-conditioned question for structural analysis and it is unreliable in the places where classical static analysis cannot validate the results. As shown in Figure 5.6, a random postbuckling path for a wind turbine cylinder, we can observe the snap-through and snap-back actions along the path.

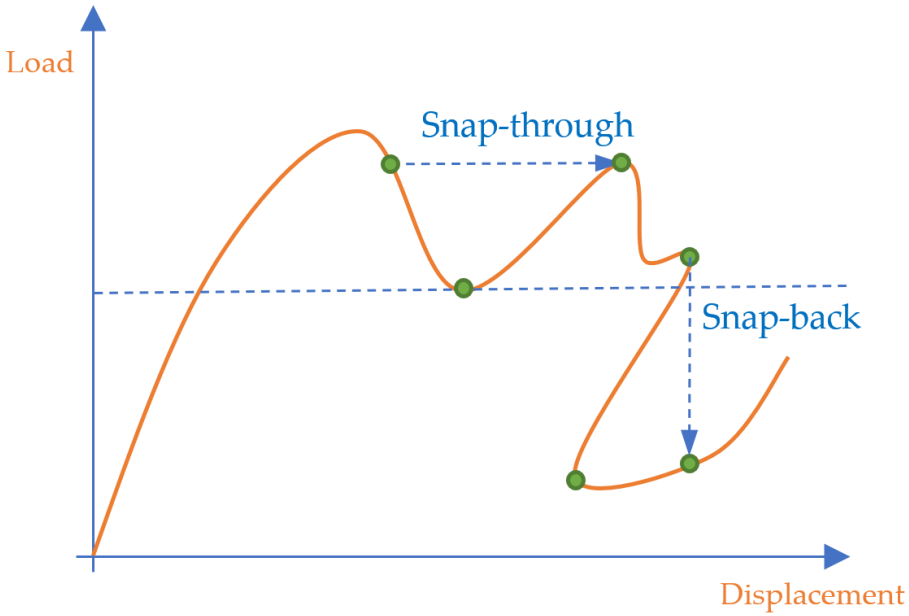


Figure 5.6. The snap-through and snap-back phenomenon in the postbuckling stage for a cylinder.

We could observe that when snap-through happens along the postbuckling path, the route is controlled by the load when the load is unchanged; when snap-back happens,

however, it is under the control of displacement. The Riks method, applying both controls in the full analysis process, allows us to obtain the full buckling path before we terminate the numerical simulation, using steps limitation or displacement limitation.

The arc-length iteration steps are illustrated in Figure 5.7. The iterations in ABAQUS depend on the length of the radius of the circle for the obtaining of next interaction point, which will become the centre of the future circle for the next iteration step. The arc-length is R in Figure 5.7, Δx_i represents the increment of displacement and Δy_i represents the increment of loads or forces. Therefore, the arc-length method is a step-by-step procedure with strict convergence judgements. The Riks increments implemented in ABAQUS would thus approach the failure state until the fixed 1000 steps are completed, otherwise the job is aborted to prevent a lack of convergence.

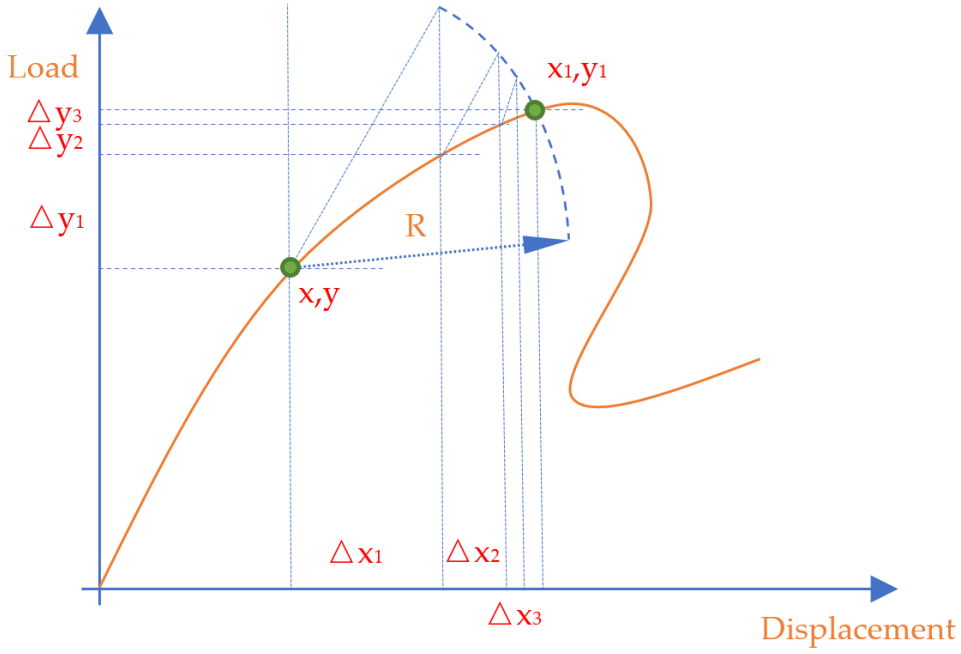


Figure 5.7. The arc-length iteration in the postbuckling path for a cylinder.

5.2 Applied external loads on shell section

The combined applied loads on wind turbine towers should be calculated and validated although the Riks method, which can track the full procedure of the shell buckling to an extent that may never occur in a tower section. The numerical simulation of external wind loads will provide essential information for the load settings of buckling analysis in ABAQUS. The NREL 5WM wind turbine was created and set in a special FEM software, ASHES. The third element was selected for data output, as it is located in the secondary bottom section of the wind turbine tower. Based on the model of tower and wind grid in Figure 5.8, the precise NREL 5 MW wind turbine was created based on the configurations listed in Table 5.1 and Table 5.2, and constructed with length of the NREL 5 MW blades set at 61.5 m. The simulation time period was set as 30s, and the following data were considered: (a) the maximum normal stress, which provides the reference for stress yielding judgement; (b) the moment time-history curve, which provides the reference for bending load apply in ABAQUS; (c) maximum shear force, which is a reference for the thrust load apply in ABAQUS; (d) strain energy, which is a rough measurement according to the results in ABAQUS; (e) deformed length, which is equal to the end-shortening of the shell section. The targeted wind speed was over 11.235 m/s for 5.0 MW rated power, with the required RPM at 12.1. The wind speed was set at 12 m/s, 30 m/s and an extreme rate of 70 m/s; under the latter wind speed, the wind turbine tower collapses overwhelmingly. The respective curves under 12 m/s wind are illustrated in Figure 5.9.

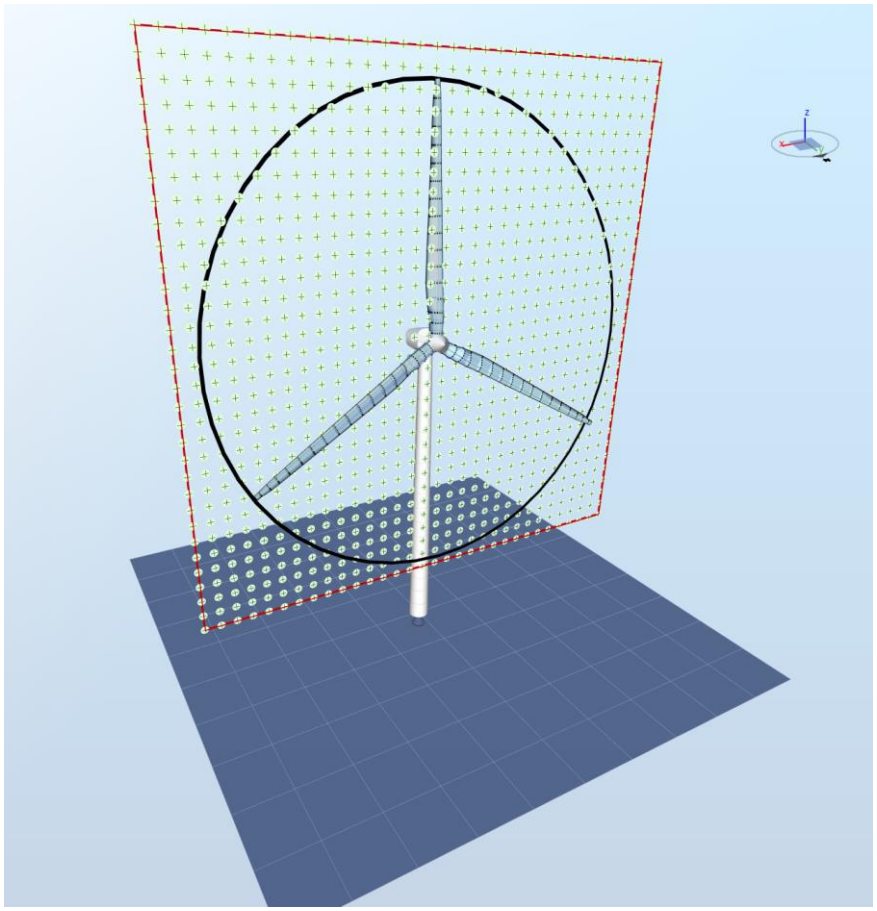
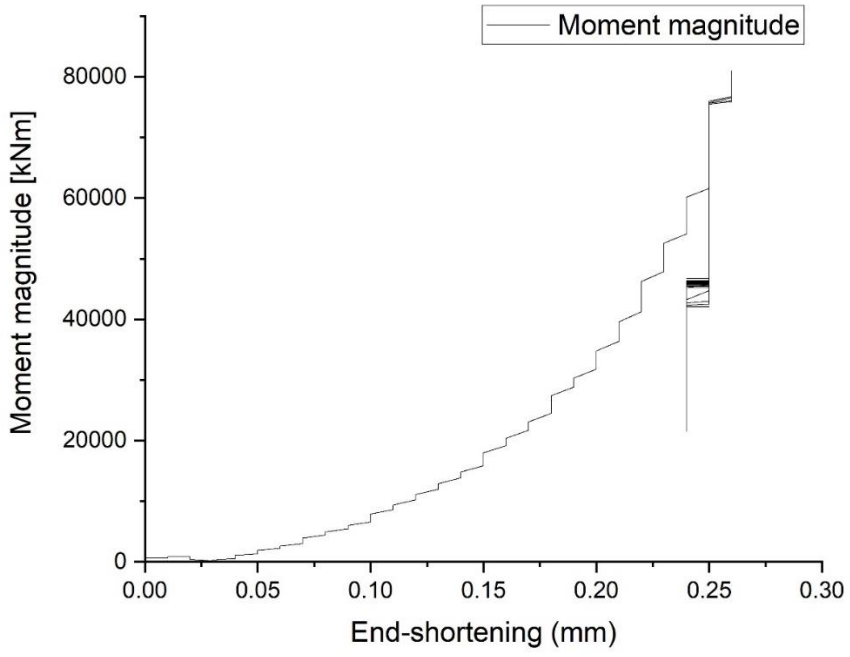


Figure 5.8. The model of the NREL 5 MW wind turbine and wind grid in ASHES.



(a)

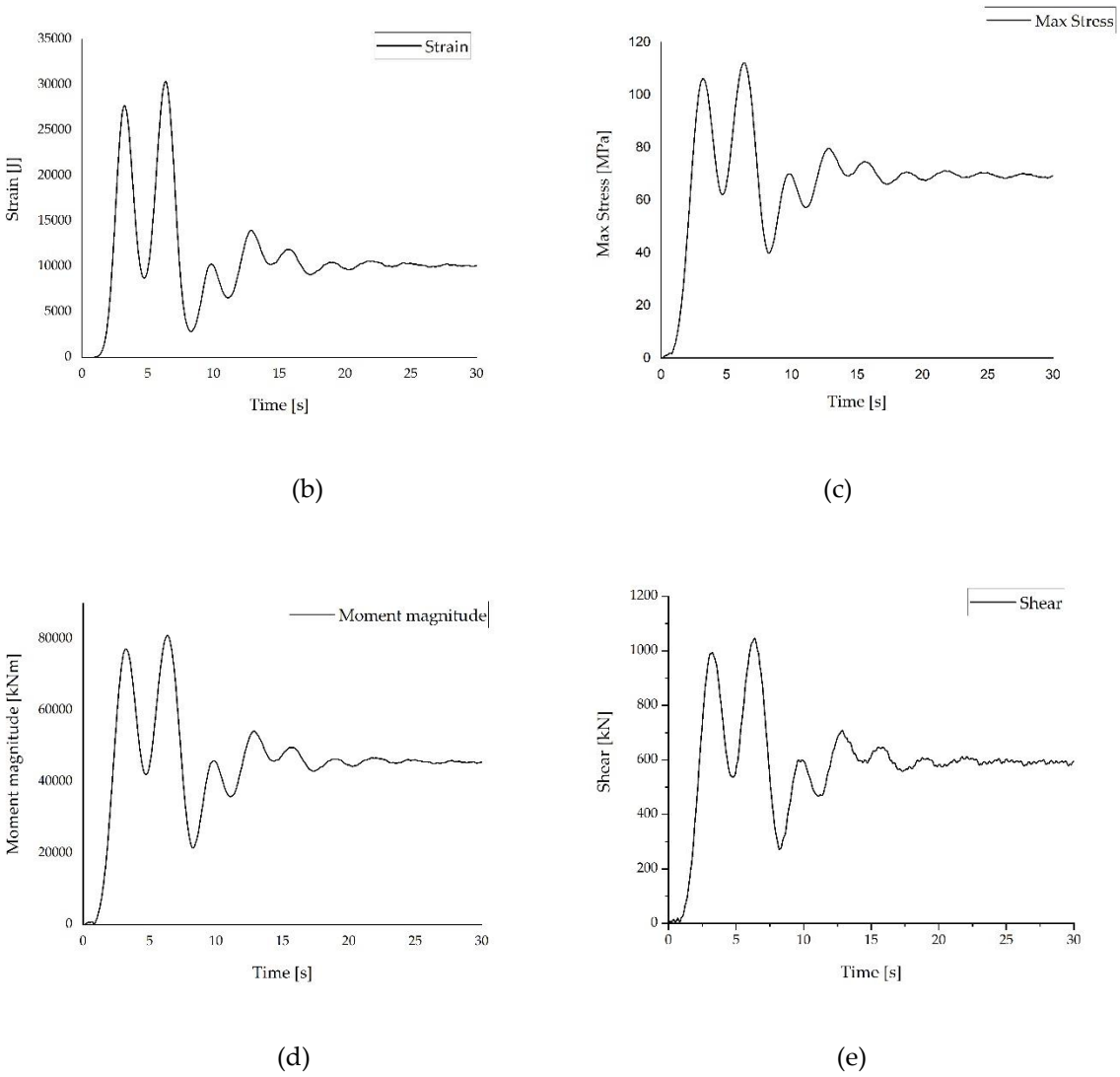
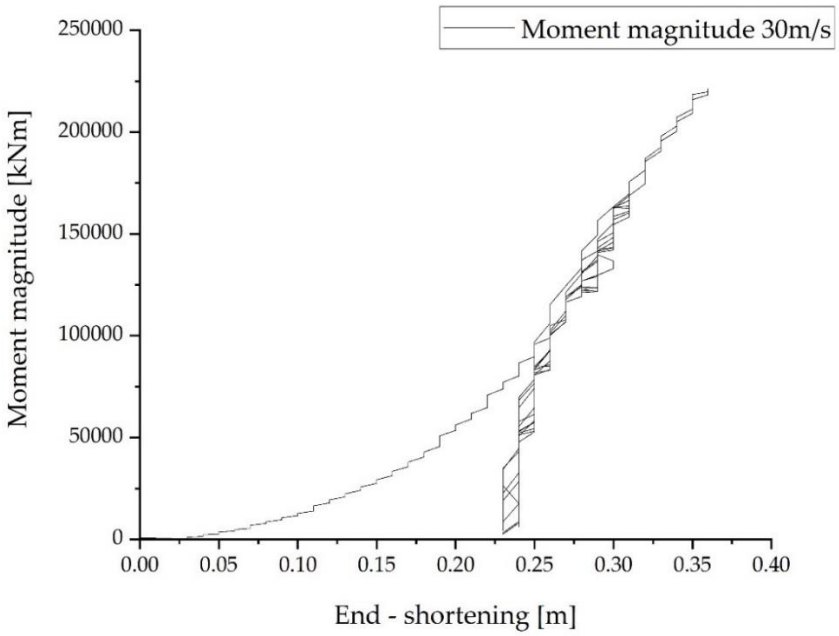


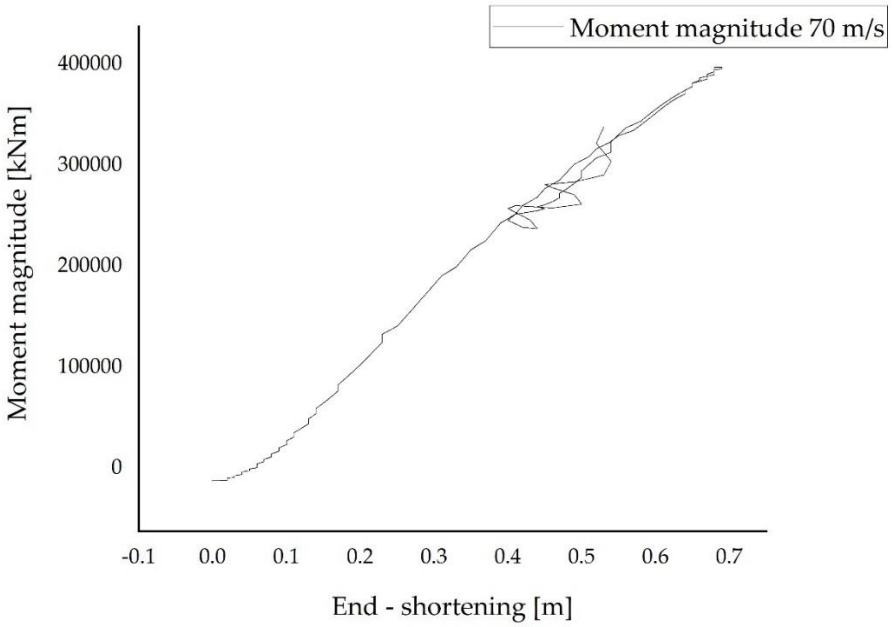
Figure 5.9. Results of NREL 5 MW wind turbine under 12 m/s wind. (a) Moment magnitude – end shortening curve. (b) Strain energy curve. (c) Maximum normal stress. (d) Moment magnitude. (e) Shear stress.

The end-shortening was the length deviation calculated by using the elongation data, divided by the initial length of the element as 4.86667 m. The vibration behaviour can be observed in Figure 5.9 (a) according to the moment generated by dynamic wind load from stationary, and other parameters portray similar dynamic responses according to wind speed change from 0 m/s to a steady 12 m/s. The overlapped 'bold lines' in Figure 5.9 (a) represents the amount of end shortening varies in a small range under a relatively steady moment magnitude. This phenomenon in line with the other

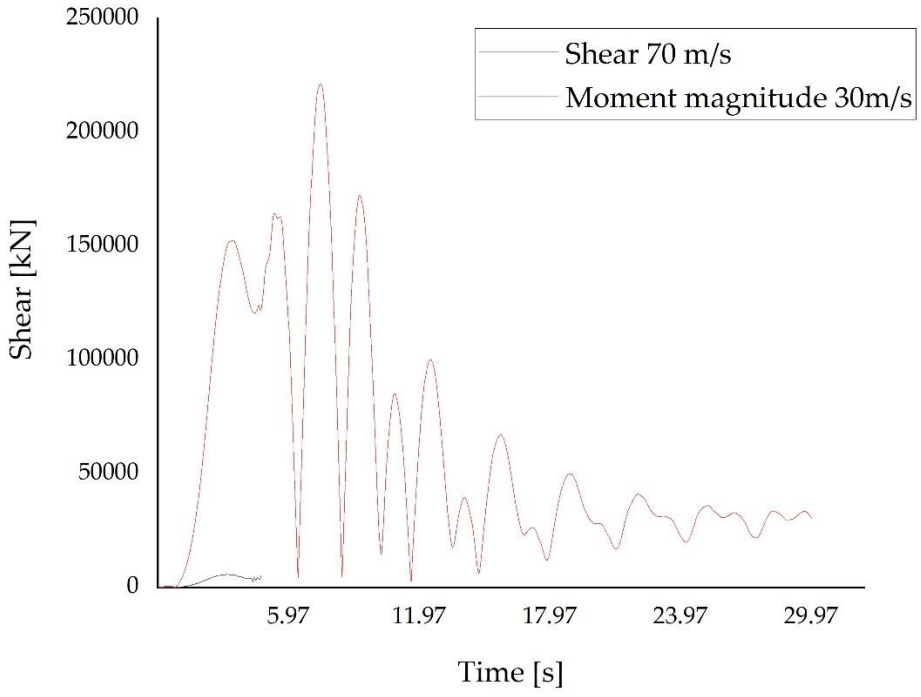
parameters shown in Figure 5.9 (b), (c), (d), (e) that each curve observed less fluctuating after 20 second which reveals the entire tower is under a regular operating condition in the 12m/s dynamic wind loads. The responses generated by 30 m/s and 70 m/s are shown in Figure 5.10. It is clear that: the tower experienced more severe vibrations in 30 m/s winds represented by a wider end-shortening variation range than that in 12 m/s winds; the collapse of the wind turbine tower happened about 5 seconds after 70 m/s wind was applied, as the curve was then impossible to track. The load-end-shortening curve reduces dramatically under extreme wind via the snap-back path shown in Figure 5.10 (b), with negligible structural resilience observed. The magnitudes of the respective parameters provide references for the following pure shell element FEM analysis in ABAQUS.



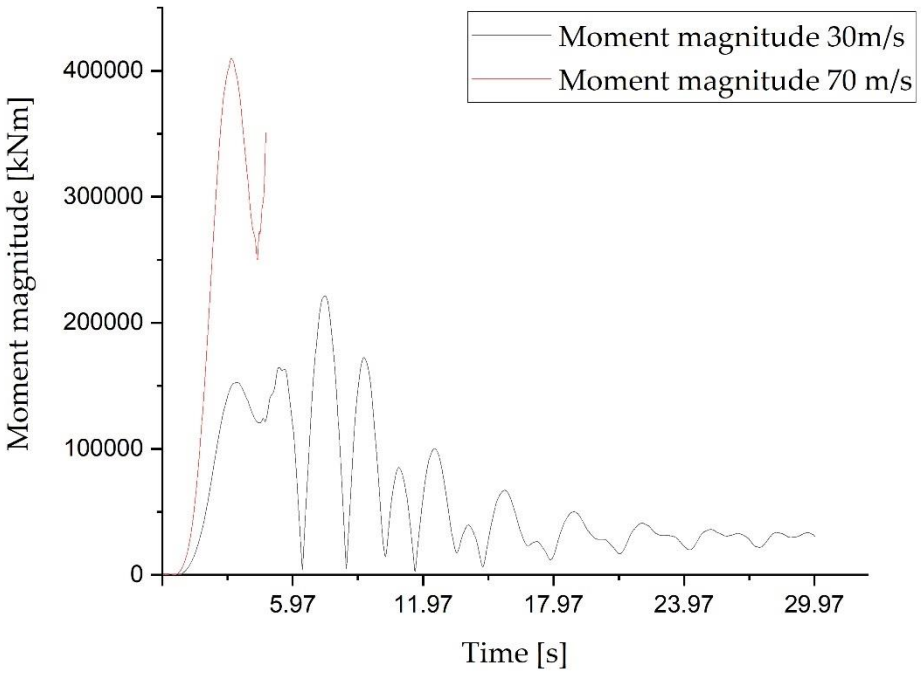
(a)


Moment magnitude 70 m/s
Moment magnitude [kNm]
400000
300000
200000
100000
0
-0.1
0.0
0.1
0.2
0.3
0.4
0.5
0.6
0.7
End - shortening [m]

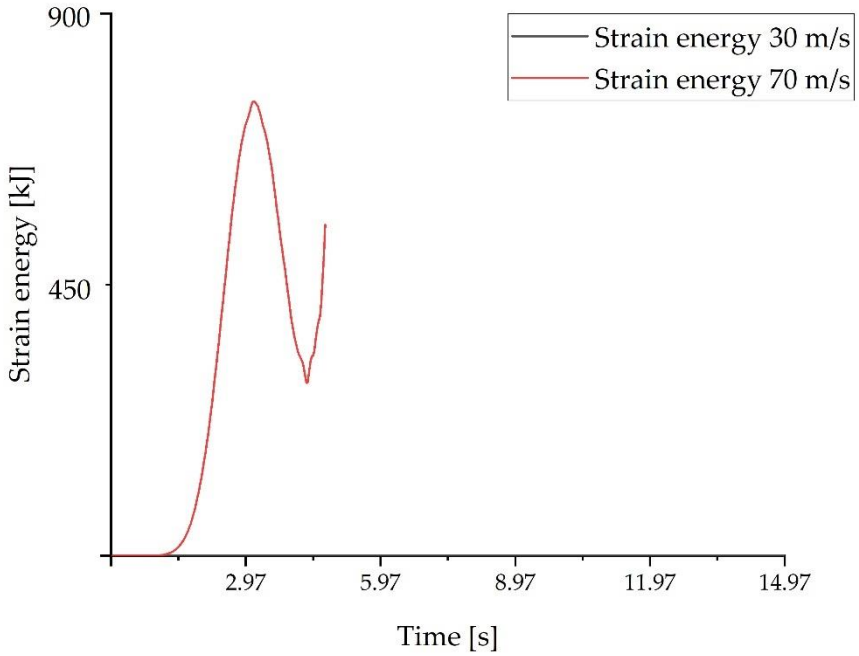
(b)


Shear 70 m/s
Moment magnitude 30m/s
Shear [kN]
250000
200000
150000
100000
50000
0
5.97
11.97
17.97
23.97
29.97
Time [s]

(c)


Moment magnitude 30m/s
Moment magnitude 70 m/s
Moment magnitude [kNm]
400000
300000
200000
100000
0
5.97
11.97
17.97
23.97
29.97
Time [s]

(d)


Strain energy 30 m/s
Strain energy 70 m/s
Strain energy [kJ]
900
450
2.97
5.97
8.97
11.97
14.97
Time [s]

(e)

Figure 5.10. Results of the NREL 5 MW wind turbine under 30 m/s and 70 m/s wind. (a) Moment magnitude – end shortening curve in 30 m/s wind. (b) Moment magnitude – end shortening curve in 70 m/s wind. (c) Shear stresses in 30 m/s and 70 m/s winds. (d) Moment magnitudes in 30 m/s and 70 m/s winds. (e) Strain energy curves; the magnitude of the 70 m/s curve is far above the 30 m/s curve, which is very close to the axis due to the unit of vertical coordinate is kJ.

5.3 Concluding remarks

This chapter discusses the numerical simulation methods and settings for finite element analysis. The selection of NREL 5MW baseline wind turbine for FEM modelling geometry and material settings has been discussed and a set of 20 typical models have been listed. Followed by the shell element selection, eigenvalue predictions and superposition geometry imperfection implementations in FEM.

The discussion of the choice of Riks method as the calculation algorithm in ABAQUS has been conducted. In the latter part of this Chapter, for the verifications and providing references for ABAQUS steps with specific values, the selected NREL prototype of wind turbine tower model has been simulated in dynamic processes by the software ASHES.

6 NUMERICAL RESULTS

6.1 Modelling details

A series of finite element models were developed and expanded in this study, based on some models published in previous works by Ma et al. (2020)[10]. After examining the tower geometry and solving algorithms discussed in Chapter 5, four different shell lengths and five different tube thicknesses were developed, in all cases intended for a tower of 6 m diameter, fixed at the base. Tube segments were 9 m, 12 m, 15 m, and 20 m in length with a thickness of 24 mm, 27 mm, 30 mm, 33 mm and 36 mm, respectively. These specifications enable the parameterisation of wind turbine towers with length–radius (L/R) and radius–thickness (R/t) ratios. Typically, R/t varied from 83.33 to 125, as shown in Table 5.3. L/R ratios, on the other hand, varied between 3 and 6.66.

Our study considered three loading conditions: axial compression (with and without imperfections), pure bending, and axial–bending interactions. The above parameterisation was derived in 100 tower shell prototypes, amongst which 20 were designed as linear buckling models and 80 were specific loading configuration models, in accordance with their respective eigenvalue analysis. The boundary conditions used for axial compression analysis consisted of a fixed bottom edge and were free to displace and rotate the top edge. For pure bending, we restricted any horizontal displacement of the bottom edge and rotation along the x and y-axis, again leaving the top edge free to displace and rotate. The combined loading scenario replicates the boundary conditions set for pure bending. In the modelling, the shapes of the tube

[10] Some of the following paragraphs have been published in Ma, Martinez-Vazquez and Baniotopoulos (2020).

ends did not deform after tie constraints were assigned along the circumferences, relative to a reference point around the geometrical centre of the shell, which simulated the connection flange and ring stiffening inside the wind turbine tower; this, in turn, prevented ovalisation from taking place at both ends. The finite element method software ABAQUS was therefore calibrated for this study by choosing S4R element types (Abaqus, 2014), whose four nodes reduce the integration of the shell element linearly using the Riks method (Abaqus, 2014, Riks, 1979), including linear buckling, eigenvalue processing and iterations for numerical stability. The maximum number of increments of static Riks analysis was set at 1000, which was considered adequate to approach the collapsed state of the tower shell, and fixes the cease for increments, which is particularly efficient when running models containing various structural configurations. The minimum arc-length increment was 10^{-8} to accurately define the performance in the neighbourhood of bifurcation or snap-through points. The fixed diameter of multiple models guarantee insensitivity to circumferential wavelength according to element numbers, while the longitudinal element performance shows less inference on the simulation results. The number of the thickness integration point was 7 and the element size of all models was set as 200 mm × 200 mm with the curvature control at a maximum of 0.1, which provided additional postbuckling accuracy (see the meshing example shown in Figure 6.1). The optimum mesh size is of the same size as the models are of same diameter and shape, and the results of mesh sensitivity test on 20 m length shell with 27 mm wall thickness shown in Table 6.1. From Table 6.1, it is noticeable that after the mesh size smaller than 200mm the stress values will not change apparently whereas the number of elements and nodes surge exponentially together with the CPU time and RAM occupation which unable the workstation to carry the parallel calculation even for handful of jobs in ABAQUS. Hence, for the optimum balance point between performance and calculation resource, the mesh selection of 200mm × 200 mm is decided in this simulation analysis for meshing each cylindrical shell models. The elastoplastic parameterisation of material and stress–strain information both map experimental

data linked to S355 steel. This data constructed an 11-point curve characterised by a Poisson ratio of 0.3.

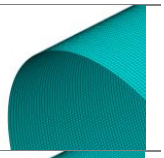
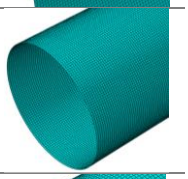
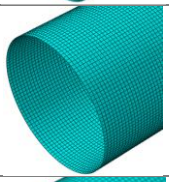
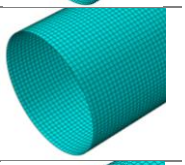
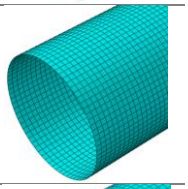
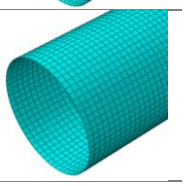
Mesh size (mm)	Von Mises Stress (MPa)	Max Principal Stress (MPa)	Arc Length (500th step)	Number of Elements	Number of Nodes	Meshing examples
50	437.35	502.53	0.042801	150,800	151,177	
100	437.34	502.44	0.042924	37,412	37,600	
150	437.31	502.27	0.043121	16,758	16,884	
200	437.02	502.01	0.043751	9,306	9,400	
250	434.72	498.77	0.045035	5,925	6,000	
300	428.10	486.95	0.157736	4,158	4,221	

Table 6.1. Mesh sensitivity analysis results.

The geometric imperfections introduced in our modelling were reflected in modal shape imperfections, calculated with a linear buckling analysis for axial compression scenarios. The first compression modal was approximately symmetric along the z-axis, while the second and third modals were asymmetric. The initial loading condition of the wind turbine tower shell was assumed to be purely compressive and, therefore, without eccentricity generated from the lateral motion of the upper segment of the structure during static load, including the nacelle and blades. The first three

compressive modal shapes then reproduced complex initial imperfections at rates of 10% for the first modal, 5% for the second modal, and 2.5% for the third modal, as discussed in Chapter 3 and 5. It is important to note that the eigenmodes output by linear buckling analysis should be scaled due to the modals are non-scaled, without any relations to the real geometry settings for models. We are in a mm unit system hence we add a line of code in ABAQUS as:

```
**-----------------------------------------
*IMPERFECTION, FILE=YOUR_FILENAME, STEP=1
1,1
**-----------------------------------------
```

This enabled us to define the initial geometrical imperfections based on ratios to wall thickness, and to determine the lower buckling bound effectively, which depicts a typical compression modal combination. The imperfection shape combination was implemented in ABAQUS via keyword editing in GUI, as depicted in Figure 6.2.

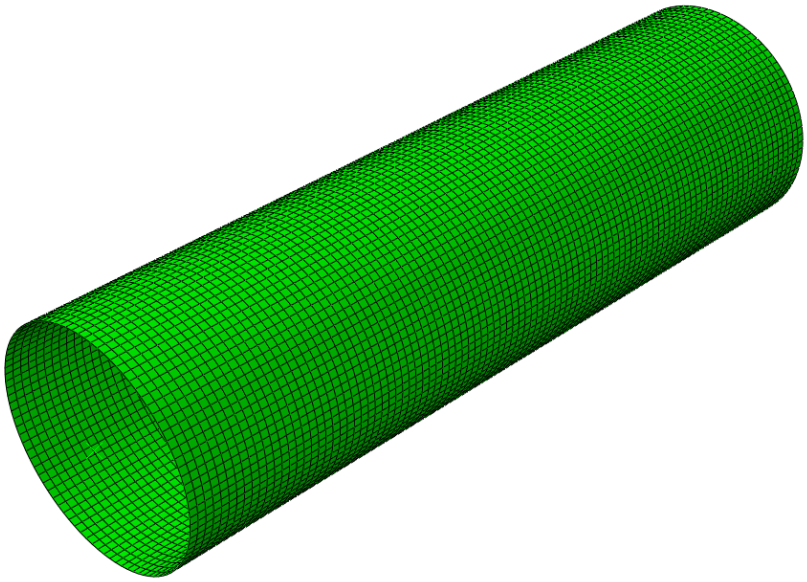


Figure 6.1. An example of meshing for 20.0 m shell section.

```
** ----------------------------------------------------------------
**
** STEP: Step-1
**
*IMPERFECTION,FILE=Job-11-12000 Non-linear-36mm,STEP=1
1,0.1
2,0.05
3,0.025
*Step, name=Step-1, nlgeom=YES, inc=1000
*Static, riks
1e-05, 0.001, 1e-08, 1., ,
**
** LOADS
**
```

Figure 6.2. Imperfection implement in ABAQUS via keyword editor, based on linear buckling modal calculations.

The amount of axial compressive load applied at the upper reference point during the Riks algorithm was decided based on the previous linear buckling analysis for each model, and the amount of bending moment was assigned at relatively large scales to exceed the plastic range of material stress, as predicted by Equation (3.70). We applied the compression load as eccentric compression according to Equation (3.75), as

$$N_x = -(N_0 + N_1 \cos\theta)$$

which was applied in ABAQUS by means of 'Create expression filed'. The Riks increments implemented in ABAQUS would thus approach the failure state until the fixed 1000 steps were completed; otherwise, the job would be aborted to prevent a lack of convergence. The magnitude of applied axial load and thrust load referred to the data output in ASHES as well.

6.2 Buckling eigenmodes in linear analysis

The first step is to obtain the first three eigenmodes of linear buckling for each model listed in Table 5.3. It is predicted that the first modal is axisymmetric while the following two modals are asymmetric. Examples of the first three modals of the shell section, which are 20 m in length and 30 mm in thickness, are depicted in Figure 6.3. By combining the first three modals with coefficients, the intended asymmetric initial geometry imperfections for each cylinder have been achieved, as the asymmetric

imperfection mode has a lower bound than the axisymmetric mode (Koiter, 1945, Koiter, 1970, Teng and Rotter, 2006). The first modal shape represented in the visualisation of ABAQUS is a function of surface displacement along the longitudinal direction, with deviations from the original perfectly straight shell surface.

A section of the displacement curve, 35% of the length to the left end, has been selected for curve fitting. The feathering by surface deviations is shown in Figure 6.4. (a). The displacement function has been curve fitted, as shown in Figure 6.4. (b). The best curve fitting results were carried out in MATLAB by Fourier functions of eight terms. The Fourier functions' forms are as follows:

$$f(x) = \frac{a_0}{2} + \sum_{n=1}^{\infty} [a_n \cos(nx) + b_n \sin(nx)] \tag{6.1}$$

This is a more general but also more complex equation for eigenvalue calculation than that shown in Chapter 3 and 4: it is a fitted function in the form of the sum of sinusoidal function, which can transform to sinusoidal function plus cosine function by parameters, as expressed by Equation (3.82). The sum of the sinusoidal function curve fitting and the function results are shown in Figure 6.5.

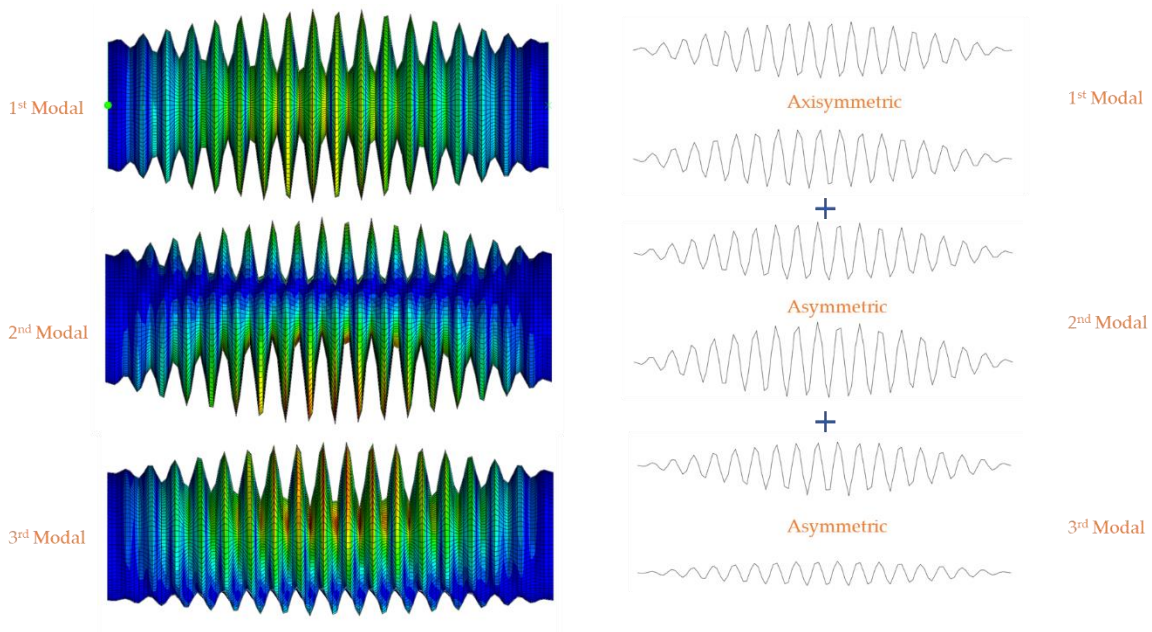
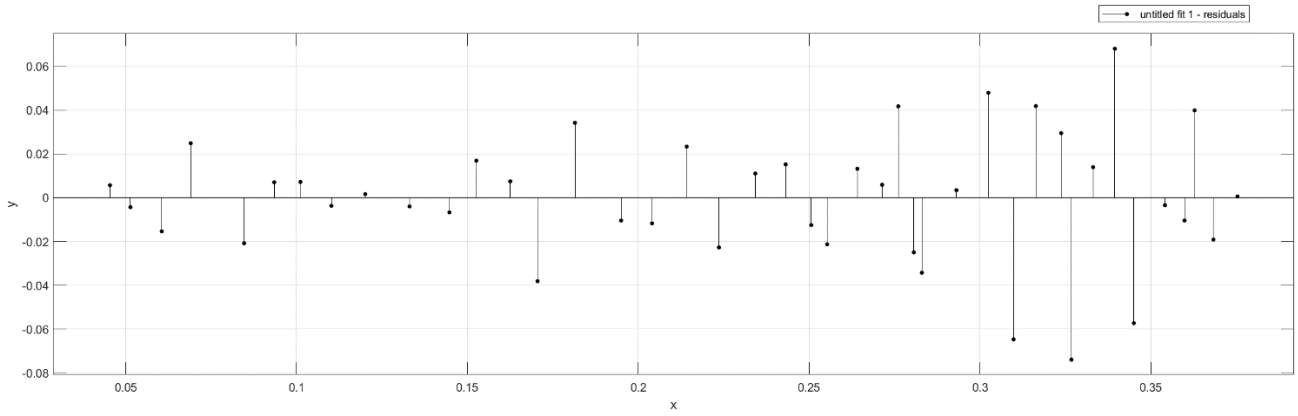
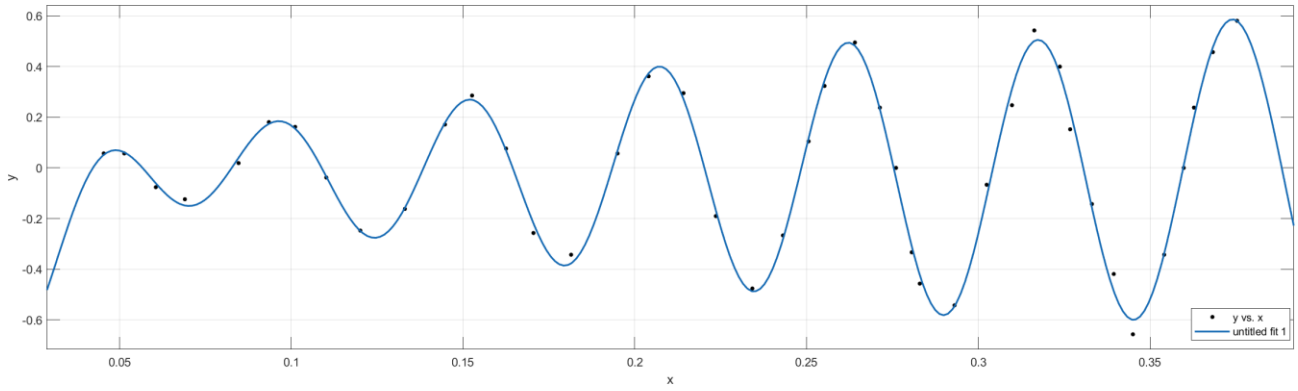


Figure 6.3. An illustration of the first three modals of the 20 m shell section at 30 mm thickness. The combination of modal shapes resulted in the asymmetric geometry imperfection.



(**a**)



(**b**)

Figure 6.4. (**a**) The feathering of deviations of surface displacement according to the initial perfect surface, ready for curve fittings. (**b**) The curve fitting example by Fourier function with eight terms.

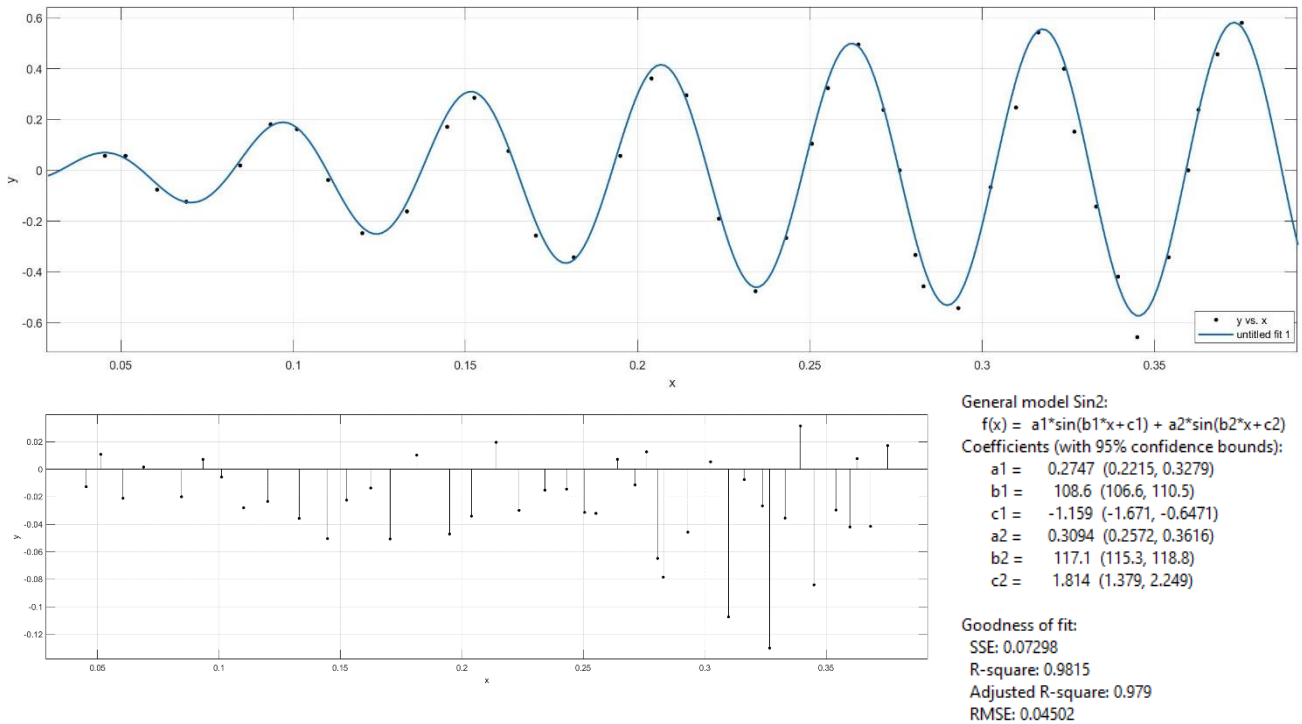


Figure 6.5. The curve fitting example by the sum of sinusoidal functions with two terms. The displacement function f(x) shares the convertible form with Equation (3.82); coefficients ai, bi were shown by the right side.

By substituting the coefficients depicted in Figure 6.5 to the equation systems based on Equation (3.86), we have the linear buckling load validation results as shown in Figure 6.6. The simulation results fitted well with the theoretical results on different thickness cylinders, with reasonable fluctuations. The discrepancy between theoretical and FEM results in terms of both magnitude and shape is attributed to the initial shape function in respective calculations. On accounts of the curve shape, when we introduce the curve-fitted sinusoidal functions of the left 35% length by FEM to the theoretical simulations, the phase diversities of sinusoidal function leaded to the sine and inverted sine curves which resulted in the switch to respective wall thicknesses. We reproduce the Equation (3.82) here $f = -C_0 sin\frac{n\pi x}{L} + a\zeta \cos 2\theta$ which could be rewritten in similar format as the curve fitting model in Figure 6.5, as $f = -C_0 sin\frac{n\pi x}{L} + a\zeta(1 - sin^2\theta)$. This initial shape function has a phase difference to the implemented curve fitting function $f(x) = 0.2747 \sin(108.6\text{x} - 1.159) + 0.3094 \sin(117.1x + 1.814)$. Meanwhile, the substituted initial shape function brought magnitude variances to the theoretical results by the discrepancies between ideal initial imperfect function and the curve fitting function. One of the practical and efficient solving methods for a four-order partial differential equation system is the Garlerkin Method which rewrites the function in the form of linearly independent polynomials and hence the weak form is obtainable however the test function should be known and designed particularly. We applied both the Fourier series expansion and sinusoidal expansions for the partial differential equations and the result depends highly on the initial trigonometric functions describing the geometry imperfections. Therefore, the magnitude of buckling load factors varied reasonably from 39.13% to 7.32% of the gap reducing along with the wall thickness increasing but shown stable convergence tendency. The approximated shape function has a higher effect on shells with smaller wall thickness other than the imperfect insensitivity of shell structures

with thicker shell surface. The theoretical results are found in MATLAB with the core code presented in Appendix A. Besides, the trail solving approach by finite-difference method (FDM) has been discussed and presented in Appendix B, however we notice the computational complexity, accuracy errors, and boundary condition requirements of FDM shown less advantages than FEM in this question.

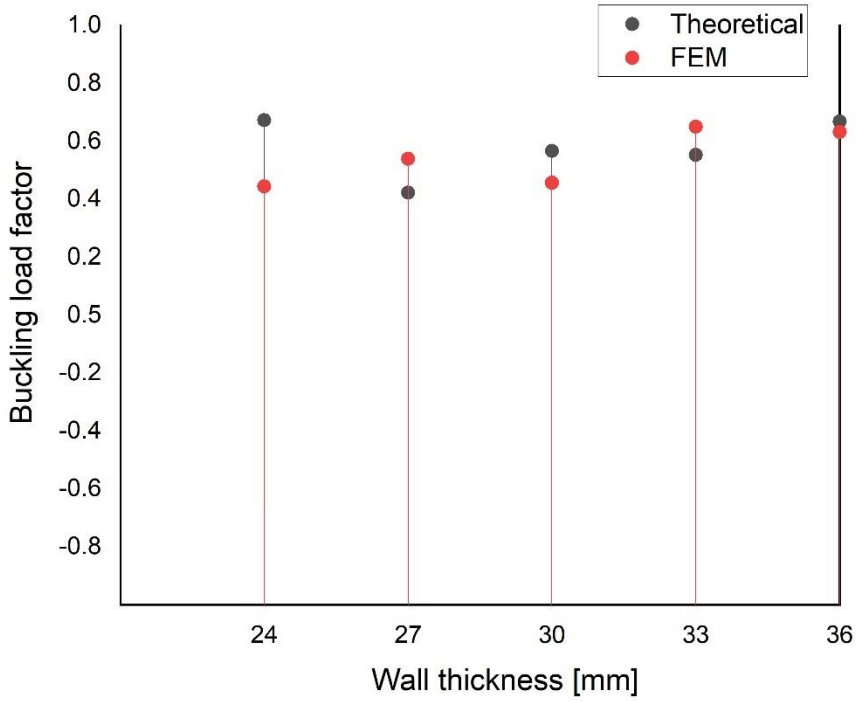


Figure 6.6. Linear buckling load in ABAQUS vs. buckling load using linear theory, in accordance with cylinders of various wall thickness.

6.3 Buckling under axial compressions

6.3.1 Validation of axial compression buckling analysis

Twenty models for each turbine tower configuration have been created and tested under axially compressive loads. The compression load was set as one concentrated load at the reference point on each end, similar to the linear buckling setting shown in

Figure 6.7. Updated eccentric compression loads were also applied to the shell edge, followed by equation (3.75) in terms of N_1, with the ultimate compressive load on the extreme fibre. We validated the compression buckling results in comparison with the well-known knockdown factor put forward by Peterson et al. (1968) based on a large experimental database. The simulation results of the R/t ratio at 83.34, 111.11, and 125 have been published in previous research, as shown in Figure 6.7[11]. This proved that the basic settings of the buckling analysis agreed with experimental evidence into imperfect shell performance for similar R/t ratios. The net deviations obtained seemed acceptable, as our simulation results lay above the experimental regression curve shown in the figure, as expected.

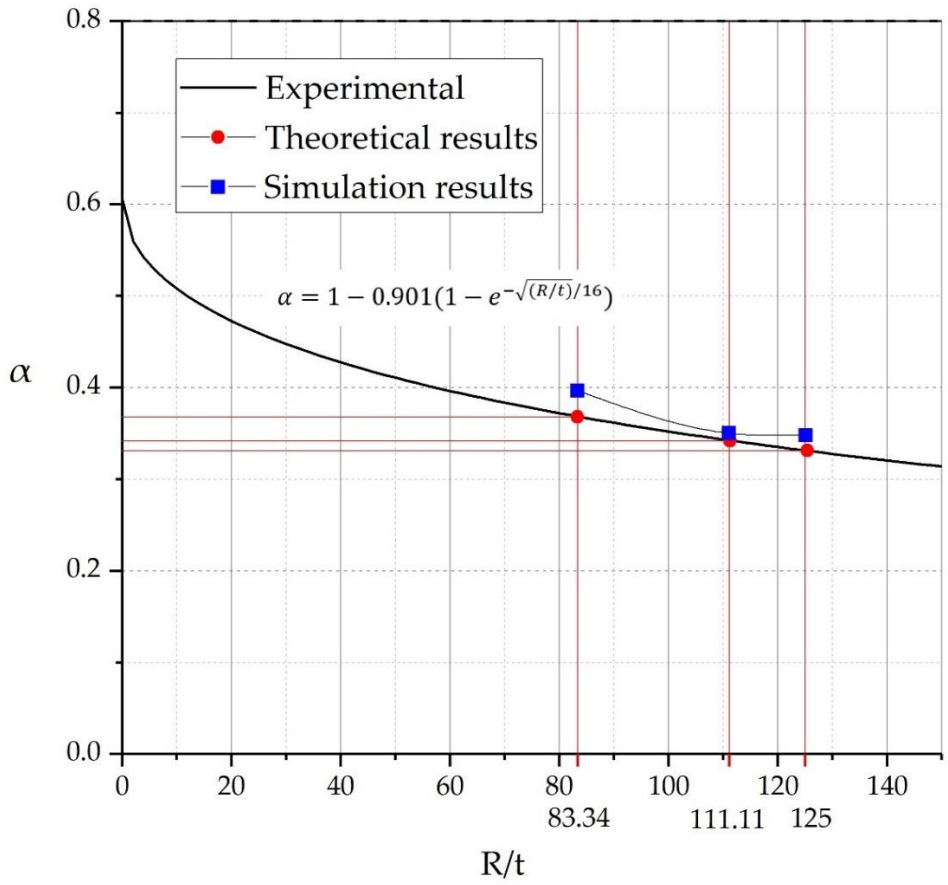


Figure 6.7. Imperfect shell knockdown factor of simulation results, compared to experimental results conducted by Peterson et al. (1968), over a selected range of R/t from 0 to 150 (Ma et al., 2020).

[11] Some of the following paragraphs have been published in Ma, Martinez-Vazquez and Baniotopoulos (2020).

6.3.2 Buckling behaviour according to different shell lengths

The buckling behaviour of different lengths has been compared equivalently using models with different L/R ratios in this study. We compared the longest 20 m shell section with the shortest 9 m models under axial compression on perfect shells. Figure 6.8 depicts the surface deformation and stress distribution for the 9 m shell, while Figure 6.9 shows the same scenario for the 20 m shell.

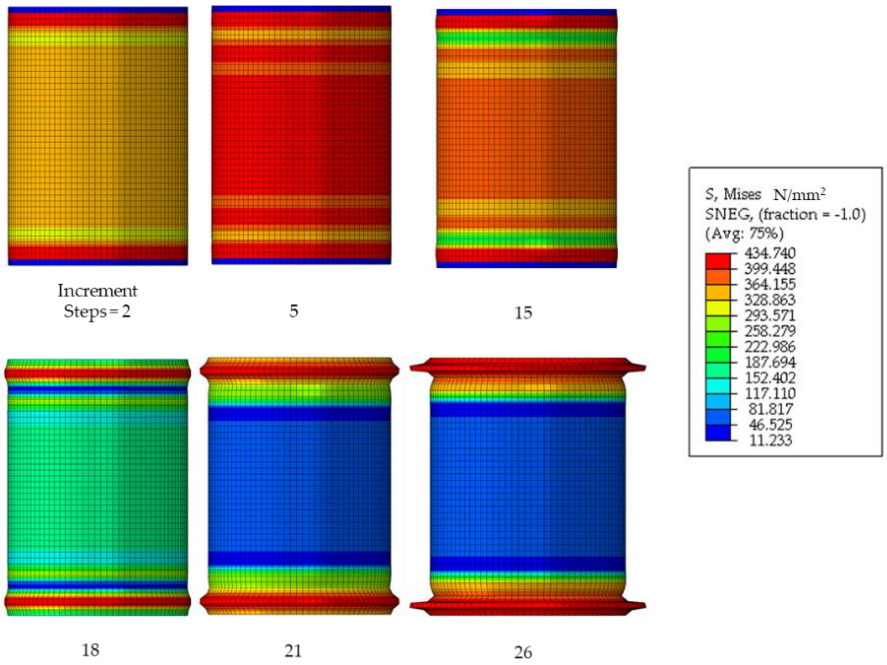


Figure 6.8. Shell (9 m at 24 mm) surface deformation and stress distribution under axial compressive load (Ma et al., 2020).

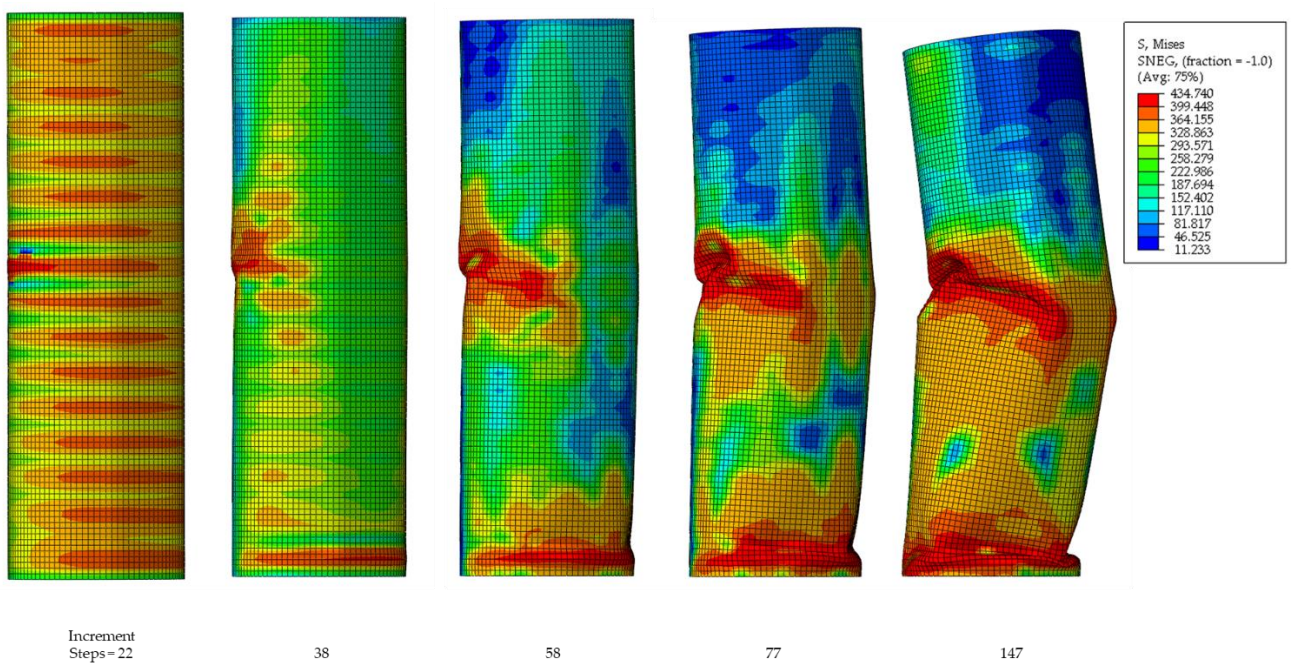


Figure 6.9. Shell (20 m at 24 mm) surface deformation and stress distribution under axial compressive load.

Figure 6.8 shows the stress and deformation associated with axial compression and illustrates how the axial compression led to symmetric buckling at both the top and bottom of the shell, with buckle bulges developing 800 mm from the edge, which we understood as a characteristic failure mode of cylindrical metal shells (Benedettini, 1999, Edlund, 2007). In practice, we could expect such features to appear on short water tanks and silos that are shaped like an 'elephant foot'; however, these could have different R/t ratios with respect to the shell section studied here (Teng, 1996, Sadowski and Rotter, 2011, Kim and Kim, 2002, Hornung and Saal, 2002) which will be discussed later.

When comparing Figure 6.8 to Figure 6.9, the differences emerged. The buckling types are generally varied, as the 9 m shell tends towards the 'elephant foot'-shaped buckling at each end, while the 20 m shell has a buckle point around the mid-length by one side, which is asymmetric. As the buckling process develops, and as the increment steps forward, the secondary buckling area emerges near the shell bottom. This is mainly because the asymmetric buckling results in longitudinal axis bent, leading to increased compression on the opposite side (the right side in Figure 6.9).

The circumferential wavelength has less influence on the axial compression buckling, especially for longer cylinders (Yamki and Kodama, 1979); therefore, the longitudinal curvature change was focused on buckling path investigation. According to Equation (4.34), in the right-hand second term we have:

$$\frac{EL^2t}{Dr^2l^2\pi^2} \tag{6.2}$$

We can observe that the magnitude of the term (6.2) depends on t/r^2 and t/l^2, indicating that r and l are at the same order. The first term in Equation (4.34) is:

$$\frac{l^2\pi^2}{L^2} \tag{6.3}$$

This strongly determines the overall buckling load according to the wavelength in longitudinal direction l. We removed the longitudinal wavenumber change along the extreme fibre on the compression side, which is connected to local curvature, as shown in Figure 6.10. The local curvature changed dramatically with the increase of the compression load: the wavenumber dropped intensively in the early steps and maintained a long interval until the entire shell collapsed. In the meantime, circumferential curvature change has been recorded as shown in Figure 6.11.

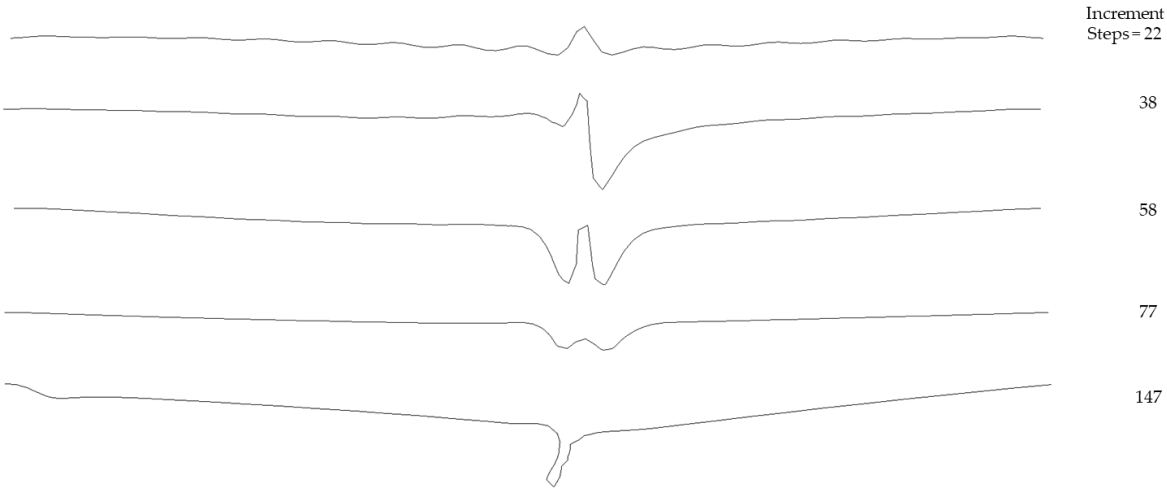


Figure 6.10. Shell (20 m at 24 mm) extreme fibre wavenumber change under axial compressive load.

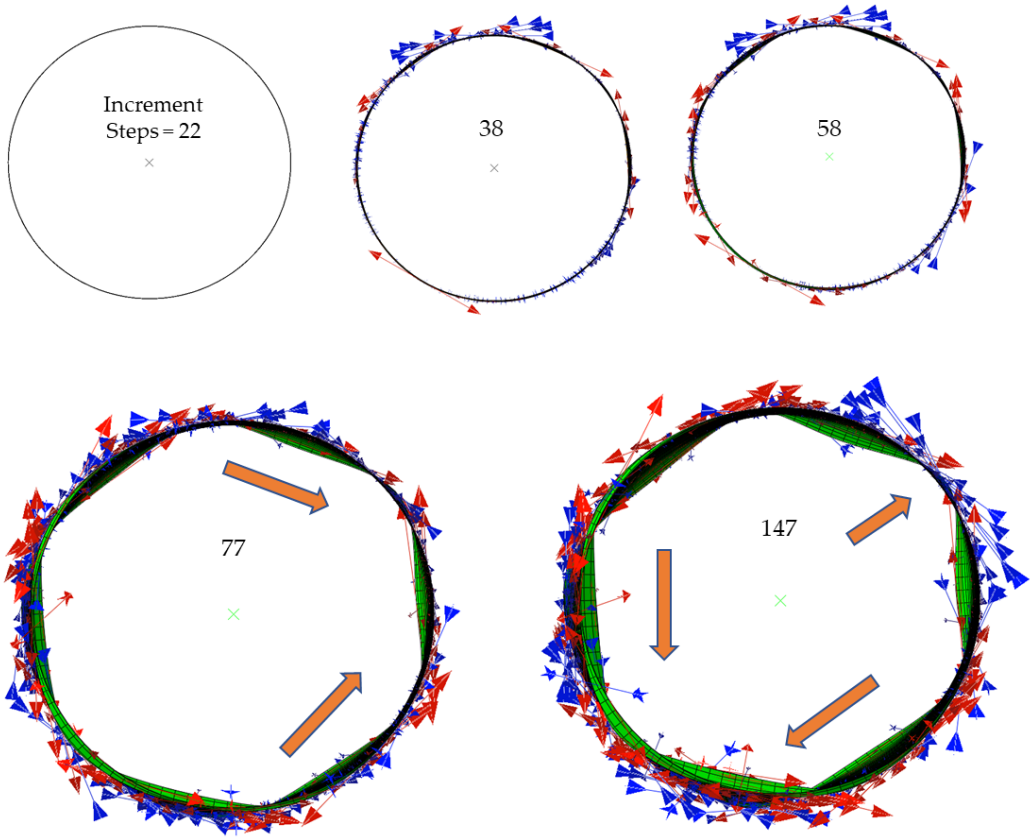


Figure 6.11. Shell (20 m at 24 mm) circumferential fibre curvature change under axial compressive load.

In Figure 6.11, the blue arrow indicates inward displacement changes and the red arrow represents outward displacement changes on the shell surface. The peak value of displacement function, i.e., the highest deviation point, showed periodic character and circumferential flow marked by thick arrows, which are expressed precisely in buckling Equation (3.82), according to the angular coordinate change of θ. For the

shorter 9 m cylinder, despite the axisymmetric buckling mode shown in Figure 6.8, the circumferential curvature change remains less flowing, as shown in Figure 6.12. The curvature change process tended towards an even distribution, after a few steps flowed radically in the initial stage, and eventually led to the 'elephant foot' type of bulge buckling near both ends.

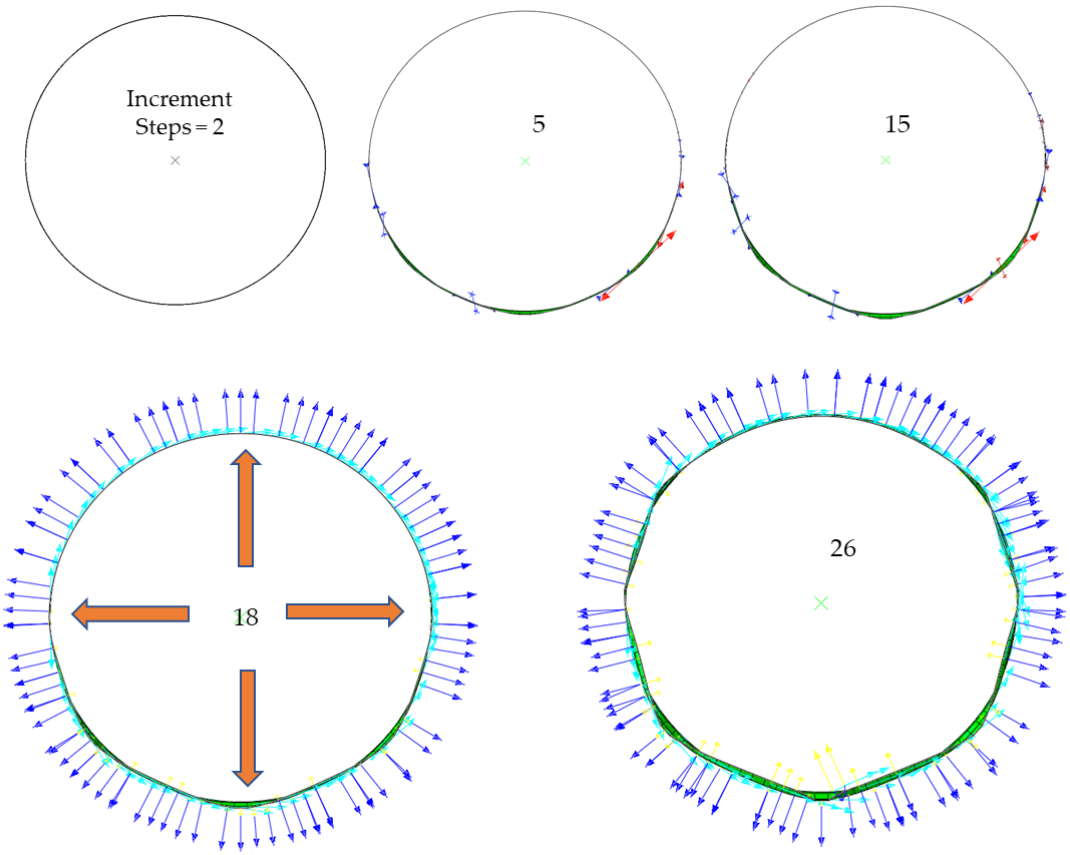


Figure 6.12. Shell (20 m at 24 mm) circumferential fibre curvature change under axial compressive load.

Figure 6.13 shows the applied load–end shortening relations of both length shell sections (9 m at 24 mm and 20 m at 24 mm). The curves indicate that the longer shell has better bifurcation buckling resilience followed by larger displacement flow, while the shorter shell has a very limited higher compression bearing capacity, but the buckling path is obviously 'sharp', representing worse postbuckling progression ductility. The balance between elastic bearing capacity and postbuckling behaviour is a meaningful consideration that designers should take, and the equivalent pure shell length can be affected largely by the configurations of stiffening rings.

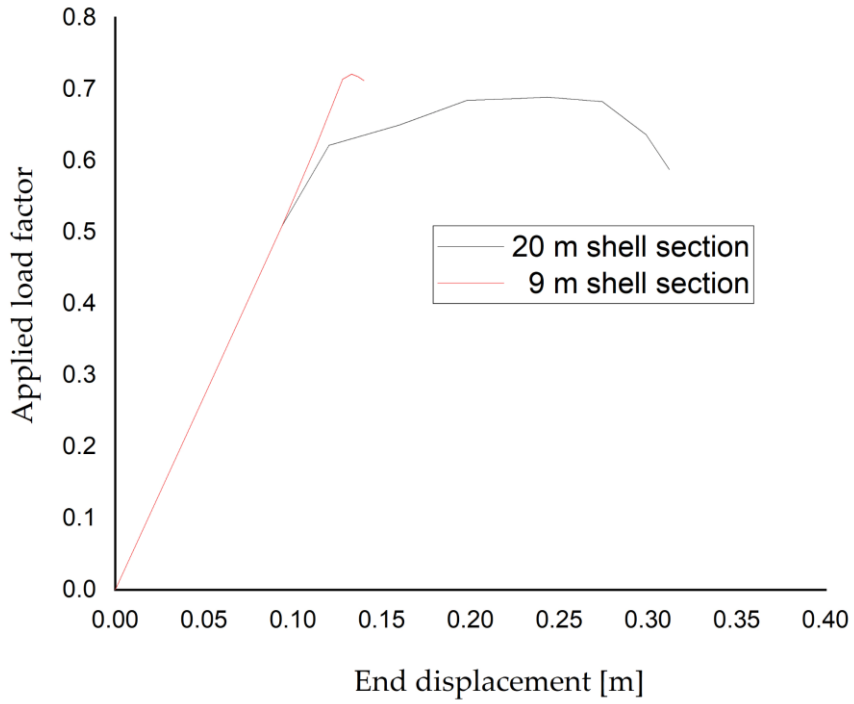


Figure 6.13. Shell (20 m and 9 m at 24 mm) axial load–end shortening curves under axial compressive load.

6.3.3 Buckling behaviour according to different shell thicknesses

The FEM results show less buckling resistance in correspondence to the R/t ratio than that of the L/R ratio, in line with the conclusion derived by Yamki and Kodama (1979). This phenomenon can be analysed based on the equations deduced in Chapters 3 and 4. In the linear stage, according to Donnell's Equation (3.48), the medium term on the left-hand side, $\frac{Eh}{R}f$ (here h represents the wall thickness t) reveals a linear contribution to the overall magnitude based on the surface displacement function f. The deformation of the surface is small, which reduces the effort of the coefficient t/R.

The R/t ratio has been enhanced in energy methods, in the general shell element form as seen in Equation (4.7); axial compression load is an integral throughout the shell thickness and the Lame coefficient B is considered to the ratio $\frac{z}{r_2}$, which explicitly contains the influence of R/t. Here, z relates to shell thickness, and r_2 is the radius of mid-surface of the local element.

The buckling behaviour of the same shell length with a different R/t ratio has been compared between the 20 m at 24 mm shell and 20 m at 36 mm shells. The stress distributions and deformed shapes of the 20 m at 36 mm shell are shown in Figure 6.14. The increment steps were selected, as the same LPF applied to the shell as to the 24 mm thickness shell. The comparison between Figure 6.14 and Figure 6.9 reveals fairly similar buckling behaviour for different wall thicknesses. The R/t ratio to axially compressed loading scenario has a limited effect on the buckling and postbuckling behaviours.

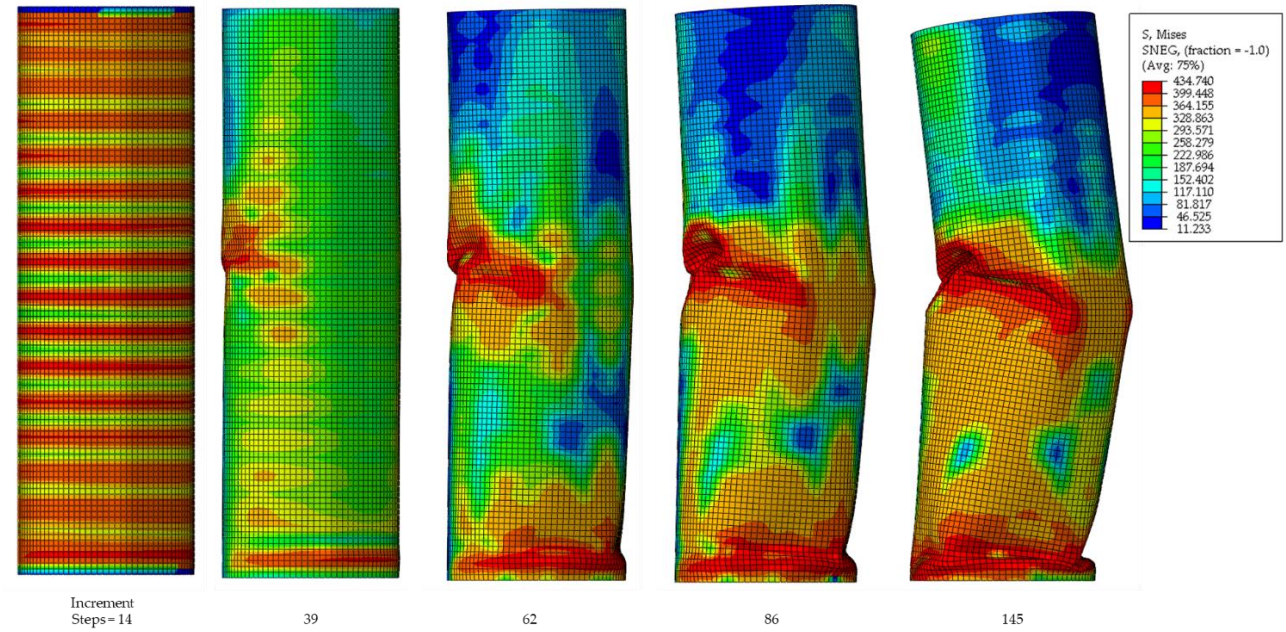


Figure 6.14. Shell (20 m at 36 mm) surface deformation and stress distribution under axial compressive load.

6.4 Pure bending buckling analysis

6.4.1 Bending behaviour for different shell lengths

The main concern about pure bending in a wind turbine tower shell is the observation of curvature change, both longitudinal and circumferential. The curvature change in the longitudinal direction would ideally be concentrated near the mid-span (Dimopoulos and Gantes, 2012, Tafreshi, 2008), while the circumferential curvature change would illustrate Brazier's effect, ovalisation (Brazier and Southwell, 1927). The

shell length effects in the buckling category will be discussed in this section. Shell models with different lengths have been chosen: 20 m at 30 mm (L/R = 6.66) and 9 m at 30 mm (L/R = 3). The surface deformations and stress distributions are shown in Figure 6.15 and Figure 6.16.

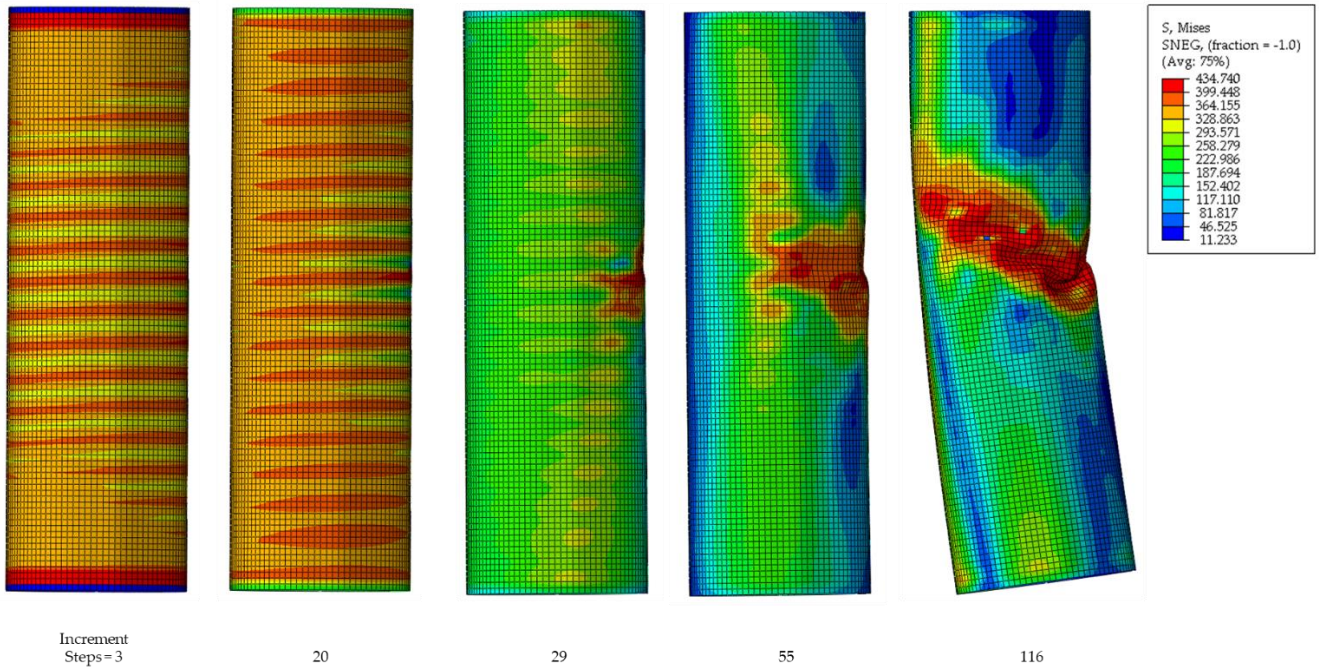


Figure 6.15. Shell (20 m at 30 mm) surface deformation and stress distribution under the pure bending moment.

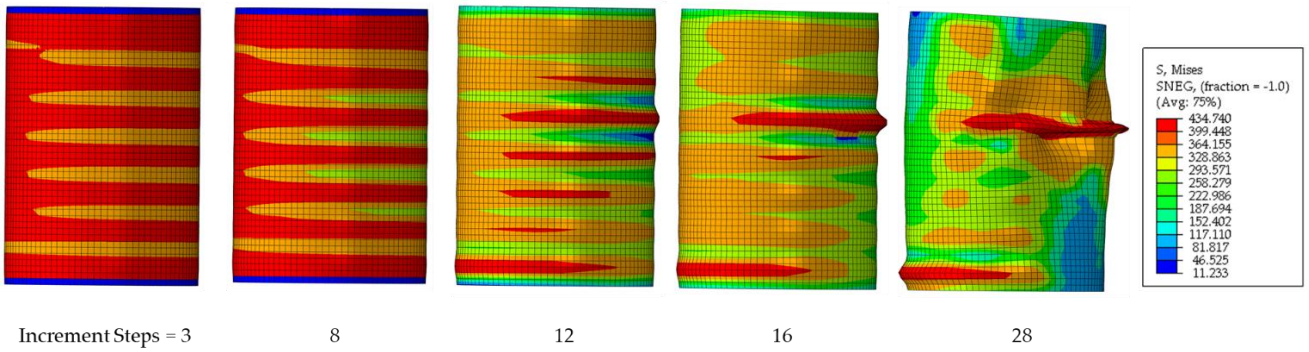


Figure 6.16. Shell (9 m at 30 mm) surface deformation and stress distribution under the pure bending moment.

It is noticeable that both lengths of shells reveal similar buckling behaviour. The buckle points happen near the mid-span on the compression side of the shell. The longitudinal buckle points are generally located at the mid-span due to the boundary conditions of the shell; moreover, the 9 m shell model is observed as more dependent

on the supporting boundary conditions, as the secondary buckle point emerged on the bottom of tension side. The bottom buckle point in Figure 6.16 has also been affected due to stress arrangement along the shell surface, as it has less length for stress and strain distribution. In the early stage of the prebuckling process, wave-like displacements are observed along the shell length but concentrated rapidly to the mid-span area as a beam member. The cut-out view of the extreme fibre on the compression side on the 20 m shell model has been illustrated in Figure 6.17.

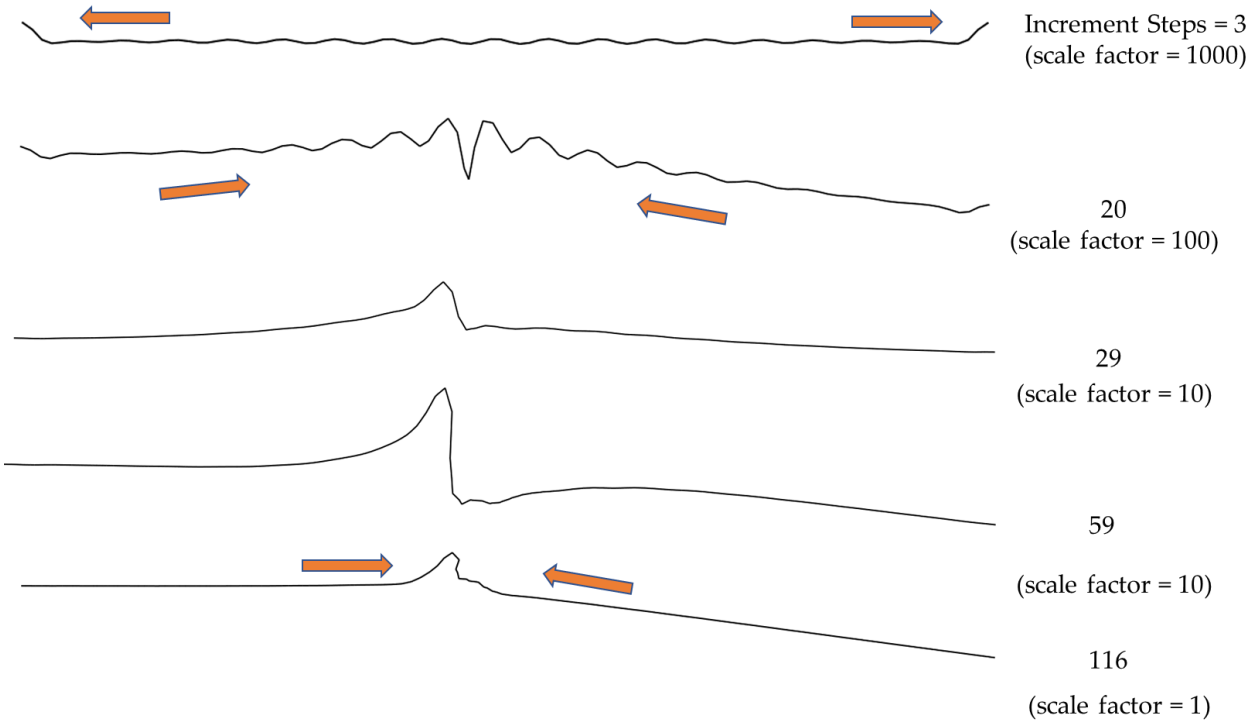
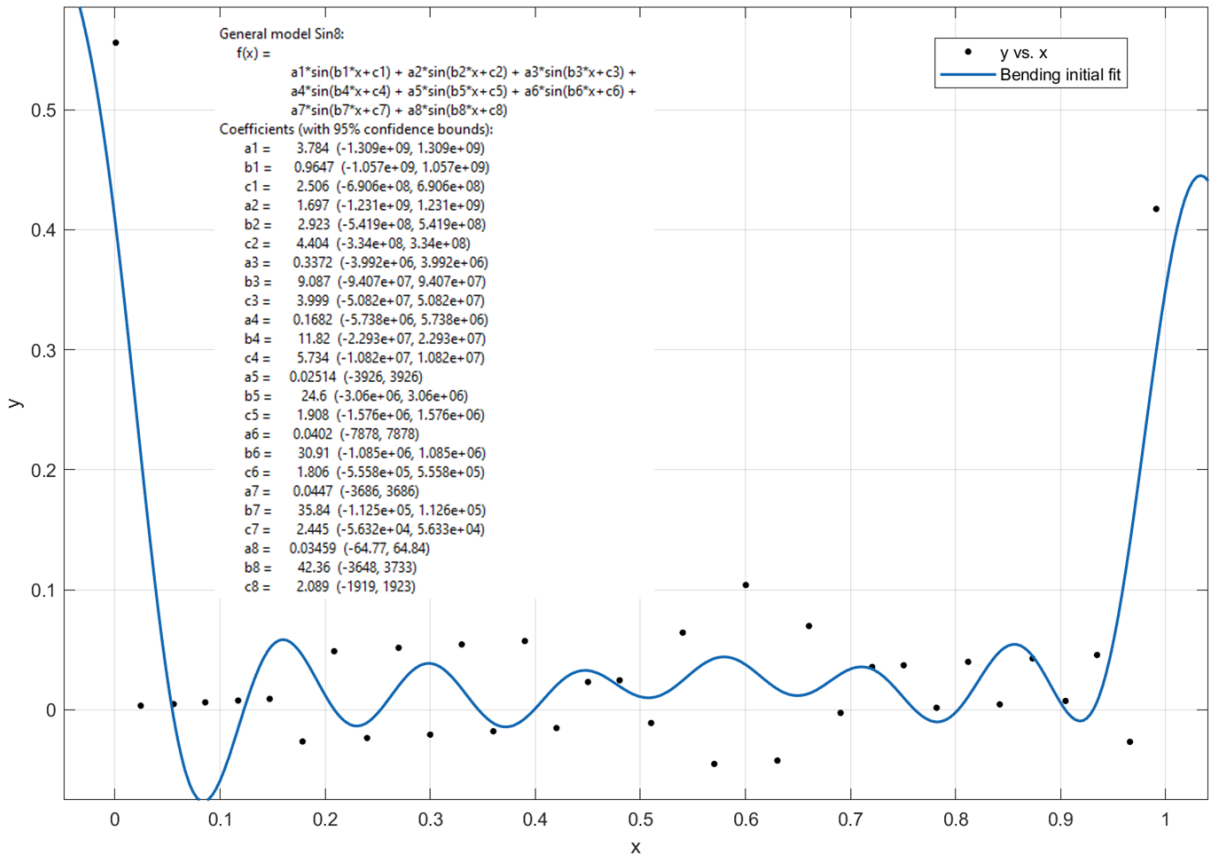
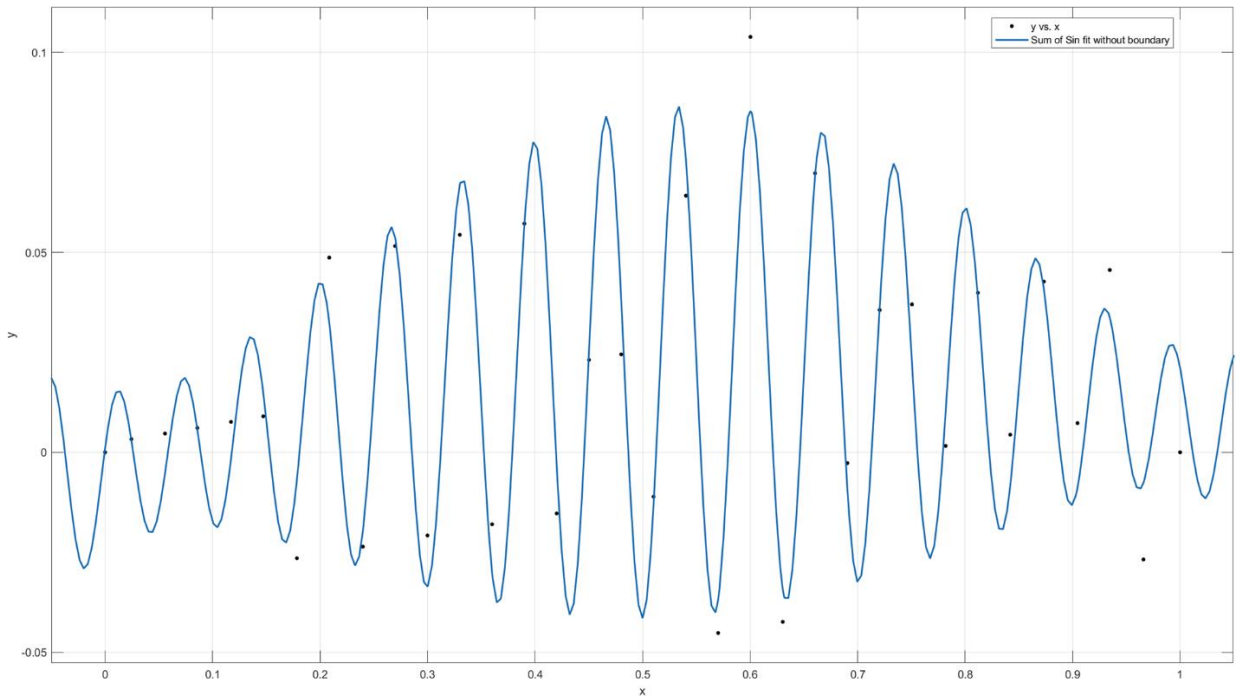


Figure 6.17. Shell (20 m at 30 mm) extreme fibre wavenumber change under bending.

At the third increment step, the initial shell surface displacement shape was wave-like. We selected it out and did a curve-fitting manipulation using MATLAB, with the form of the sum of sinusoidal functions shown in Figure 6.18. (a) in Figure 6.18 has considered the large deviation points (deviated over 0.4 and 0.5) at both ends of the shell while (b) ignored the displacement integral points on boundary conditions.



(a)



(b)

Figure 6.18. The curve fitting example by the sum of sinusoidal functions with (a) eight terms and (b) three terms. **(a)** Contains two points on boundaries while **(b)** omitted boundary conditions observed a

better fit with less coefficient terms. The displacement function f(x) shares the convertible form as Equation (3.82), coefficients were shown as well.

The displacement function cannot validated by fewer than six parameters if the edge points considered, owing to the large deviation that occurred near the supporting ends of the shell. The bending–buckling performance relies more on the boundary conditions than the axial compression conditions. The significance of boundary conditions should be dealt with either complex displacement function or extra discussions on boundary condition issues. We substituted this displacement function into the Equation system by the former approach in Chapter 4 and the longitudinal buckling load was in keeping with the theoretical results.

In terms of the circumferential curvature change, the ovalisation was observed by cutting out the extreme fibre on the plane perpendicular to the longitudinal shell axis, as shown in Figure 6.19. We increased the scale factor to 100 at steps 16 and 21 to exaggerate the circumferential displacements. At step 16, the ovalisation emerged horizontally but it is a mixed elliptical function with multiple parameters; this proved that the simple ovalisation function may not be precise enough for the transient buckling stage, which sees an extremely rapid local curvature change, as predicted by the increment steps 18 and 26. The inward dents are worse than the bulge-like outward displacement, as discussed in a range of research, and this phenomenon was observed in the postbuckling process: after increment step 26, the wavenumber was maintained and failure was concentrated at the inward dents without any bifurcation paths observed.

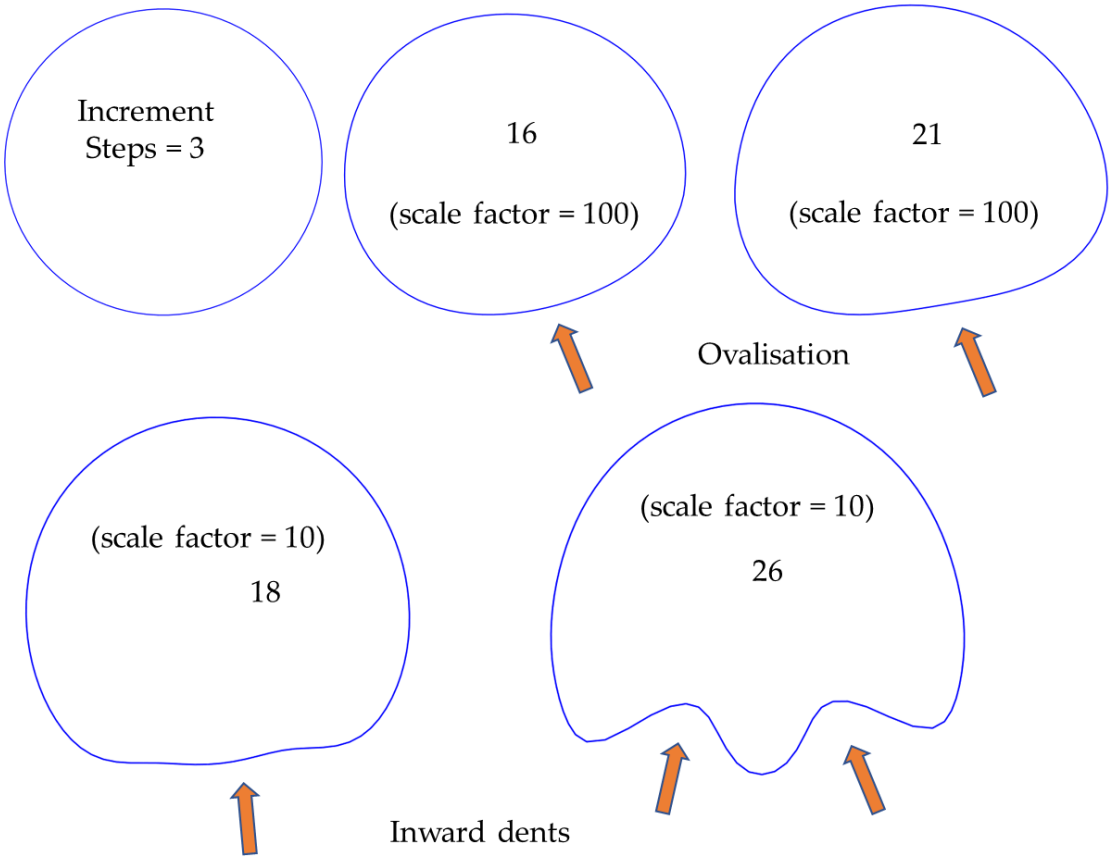


Figure 6.19. The cut-out view of the circumferential curvature change on 20 m at 30 mm shell under a bending moment.

The L/t ratio has fewer effects on the buckling load, based on the comparison between 20 m and 9 m shells of same wall thickness. The L/t ratio has limited influence on the buckle point location, but the position of buckle area depends highly on the supporting boundary conditions of shells.

6.4.2 Bending behaviour for different shell thicknesses

Shell models with equivalent lengths in different thicknesses were selected in this section for the analysis of the effects on R/t ratio. The buckling behaviour showed similarity generally but with certain differences in detail. The 20 m at 24 mm shell model was selected for comparison with the 20 m at 30 mm shell in the last section. The typical buckling process of the 20 m at 24 mm model is shown in Figure 6.20.

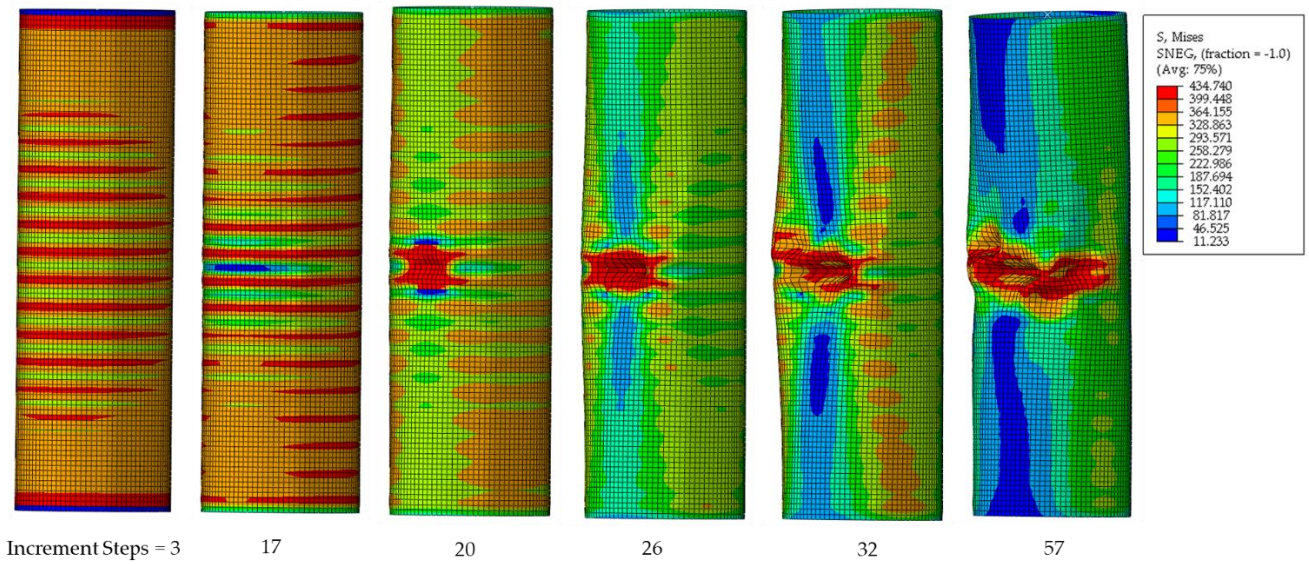


Figure 6.20. Shell (20 m at 24 mm) surface deformation and stress distribution under the pure bending moment.

Notably, a similar type of buckling occurred on the shell of 24 mm: the buckle point emerged in the mid-span area, with a higher concentration character than that of 30 mm shell; the stress concentration led to one buckle point with a bigger adjacent area than the shell shown in Figure 6.15; the one buckle point sustained a longer period, and the wavenumber progressions occurred in the late postbuckling stage, both circumferential and longitudinal; after the failure occurred, less shell area was affected than in the thicker tube.

The thin-walled shell buckling under bending showed less wavenumber evolution, with a highly condensed buckle point emerging at the mid-span surface; this is due to the lower in-plane bending resistance capacity of thinner shells. The thicker shell showed better strain energy dissipation capacities. The loss of membrane effect in the buckled area resulted in the concentration of stress in this region, owing to the large and rapid local curvature change on the shell surface. To investigate the circumferential curvature change, the cross-section cut-out view is shown in Figure 6.21.

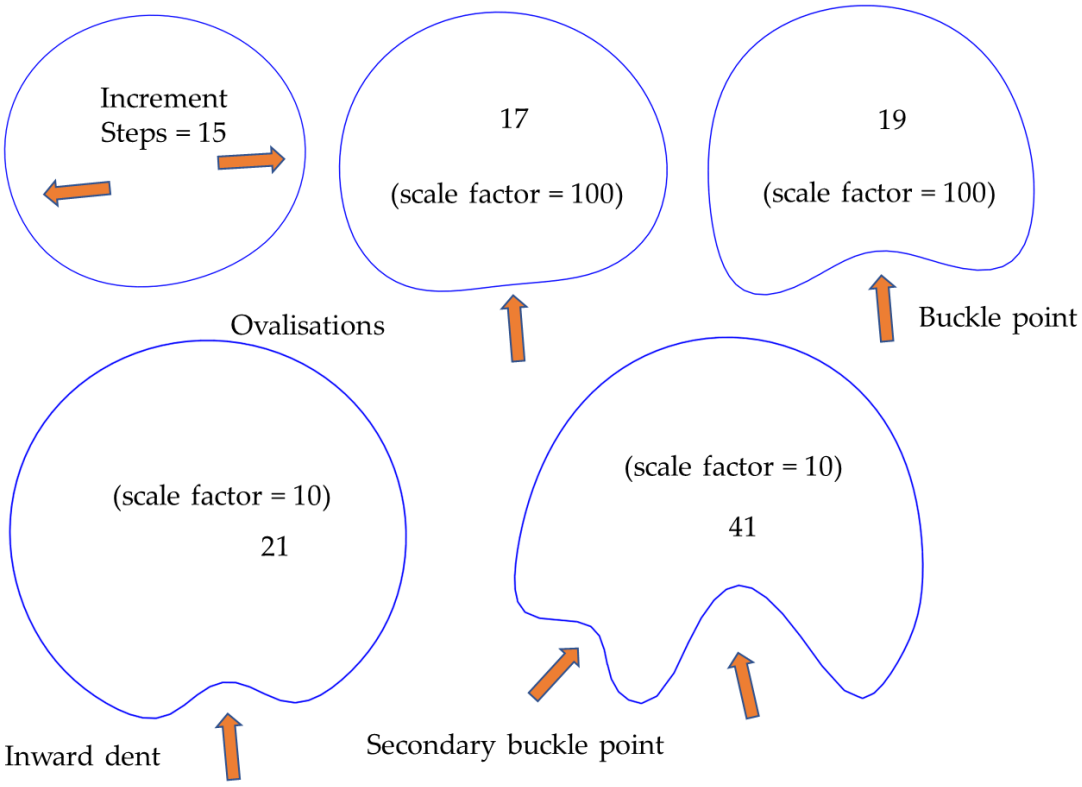


Figure 6.21. The cut-out view of circumferential curvature change on the 20 m at 24 mm shell under a bending moment.

According to Figure 6.21, the ovalisation was observed in the prebuckling stage at increment steps 15 and 17. However, at increment step 19, the flattened region on the compression side in previous steps abruptly buckled, and the flattened plate-like shell section experienced a single inward dent. This asymmetric buckling mode allowed more strain energy to drain to this area and after comprehensive evolution, the secondary buckle point emerged mainly due to the membrane effect loss in its adjacent area. This result reveals, other than the sensitivity of L/R ratio under axial compression, the R/t ratio has significant effects on bending buckling sensitivity.

6.5 Buckling analysis under combined loading conditions[12]

6.5.1. The typical buckling induced failure under combined loading conditions

For combined loading, we selected our model of 20 m long with 24 mm wall thickness (R/t = 125, L/R = 6.67) for validation. Figure 6.22 illustrates the structural performance that we observed. The sequence shown depicts a characteristic progression of failure. That simulation resulted from progressing increment steps of combined loading, which revealed the longitudinal half-wavenumber emerging between steps 12 and 18; this is aligned with the prebuckling displacement that is implicit in Equation (3.77), characterised by the features proper of periodic trigonometry functions. At increment step 16, the flattening effect resulted in mid-length stress concentrations and the original longitudinal wavelength remained unchanged until incremental step 25. Then, the inward single buckle dent developed instantly within the time frame by steps 20–25, while buckling started increasing more actively from increment 38. Furthermore, the circumferential half-wave number developed between steps 25 and 135, gradually evolving from one single buckle point to eight inward dents (two other dents were on the side viewpoint at step 135). The number of buckle point developments stopped in the postbuckling stage, when the shell section underwent large displacements, which triggered a rapid decrease in the load factor; the displacement and rotation at the top simultaneously increased. Past this point, the wind turbine tower could not provide regular service requirements. The compressive side circumferential half-wave number in the range 6–8 is commonly observed in real historical collapse cases, as reported by onsite photos (CWIF, 2020b, Chen et al., 2016, Chen and Xu, 2016, Donnell, 1934). The lateral side view shown for step 200 shows the flattening of the shell surface on the tension side and the expansion of buckling across

[12] Some of the following paragraphs have been published in Ma, Martinez-Vazquez and Baniotopoulos (2020).

the cylindrical shell. This modelling thus enabled us to accurately devise serviceability and strength limit states (Hau, 2013, EN1993, 2007, DNV, 2013).

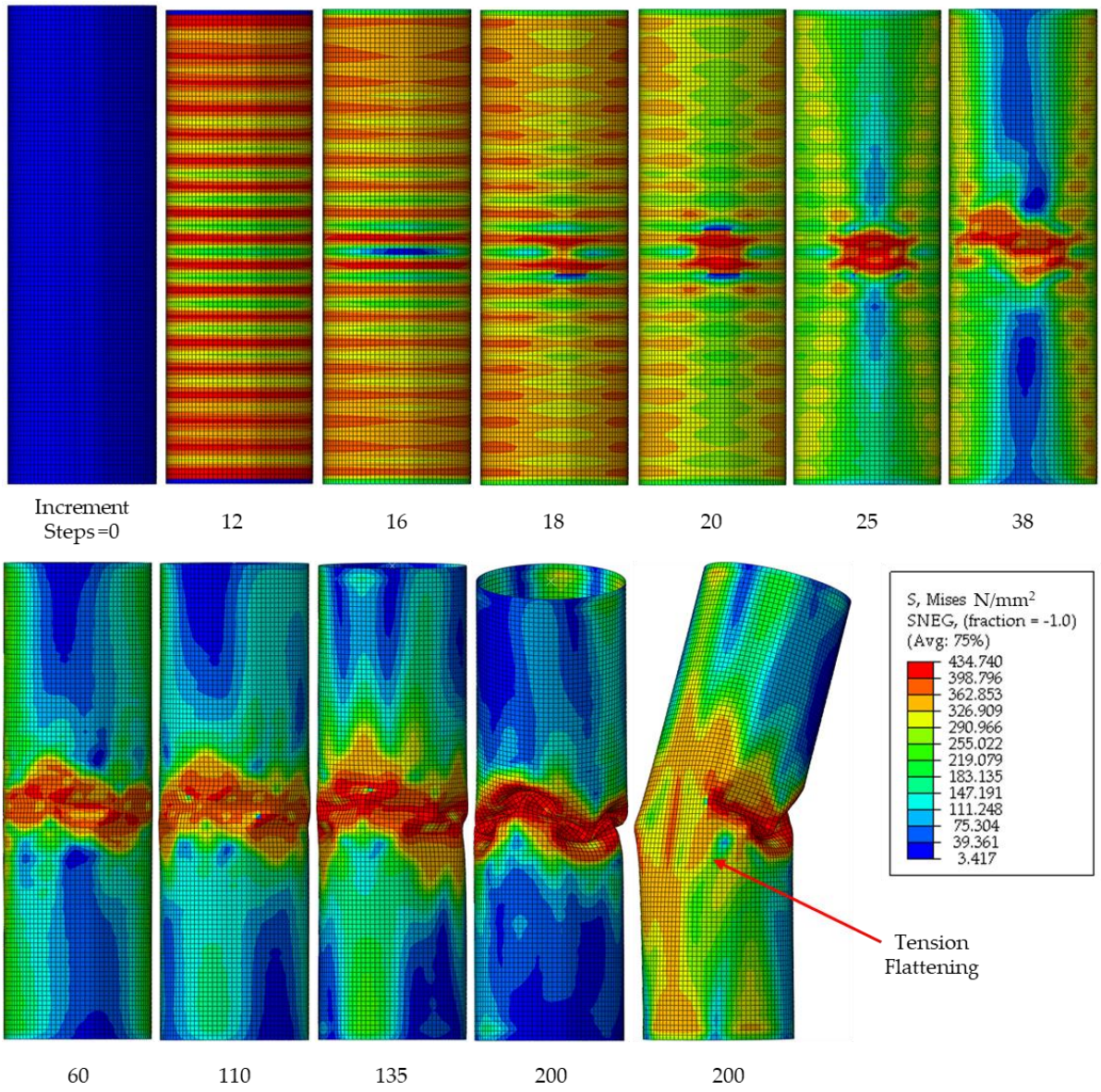


Figure 6.22. Shell (20 m at 24 mm) stress distributions and deformations on the compressive side of the cylindrical shell in 11 increment steps, and the view of tension side showing a flattening effect (Ma et al., 2020).

6.5.2 Buckling progression under different loading conditions

Figure 6.23 shows the deformed tower tube (20 m at 24 mm) when subject to uniform compression; Figure 6.24, a cut-out view of Figure 6.20, shows the equivalent surface deformation paths under pure bending, while Figure 6.25 reproduces these for combined effects in the critical compression region. Figure 6.23 shows a longitudinal

wave near the mid-length of the tubular shell, which derives from initial imperfections (eigenvalue results determined the highest gradient in the mid-length areas). In that figure, it can be observed how the section curvature increased under pure bending, with the loading increasing incrementally as discussed in 6.3.2, and the longitudinal concentration located near the mid-span. At step 39, we counted 4 half-waves, while the number decreased to 3 at step 121, 1 at step 168, and rose back to 3 at step 187. The system became unstable past step 232. Buckling theory describes these changes as the dissipation and rearrangement of strain energy on the shell surface, both through stretching λ_m and bending λ_b (see Figure 2.12). Under uniform compression, buckling also appeared at the fixed edge of the bottom tube segment, partially stimulated by the imposed motion constraints. Figure 6.24 shows asymmetric bending taking place at high incremental steps, also as a result of initial imperfections, which reveals that the failure mode was highly sensitive to such imperfections, as confirmed by experimental research (Benedettini, 1999, Winterstetter and Schmidt, 2002, Peterson et al., 1968, Castro et al., 2013a, Wagner et al., 2017). This was captured during our interpretation of buckling equilibrium paths, discussed above.

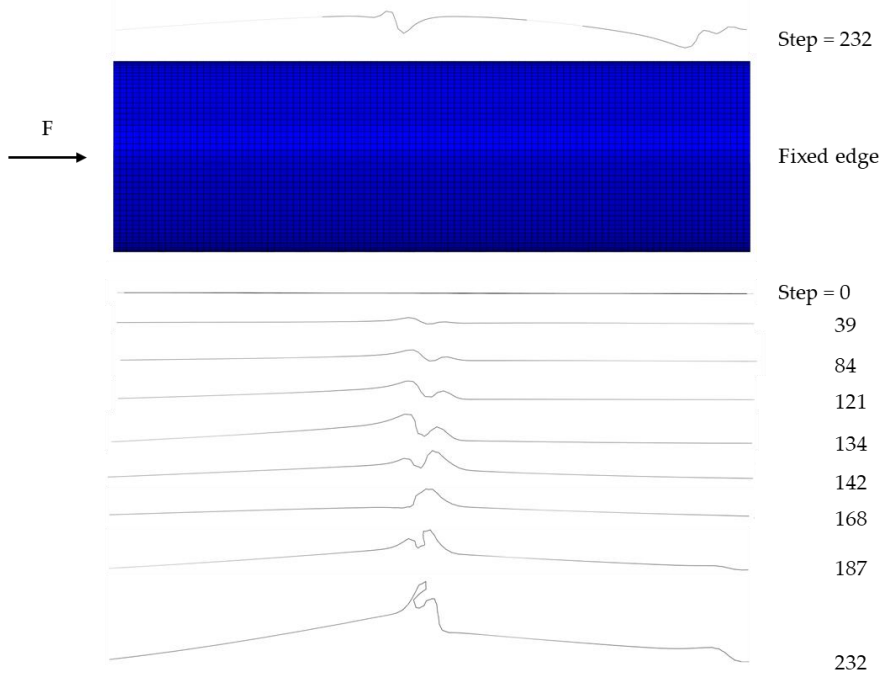


Figure 6.23. Shell (20 m at 24 mm) longitudinal surface displacement under axial compressive load, (scale factor = 5).

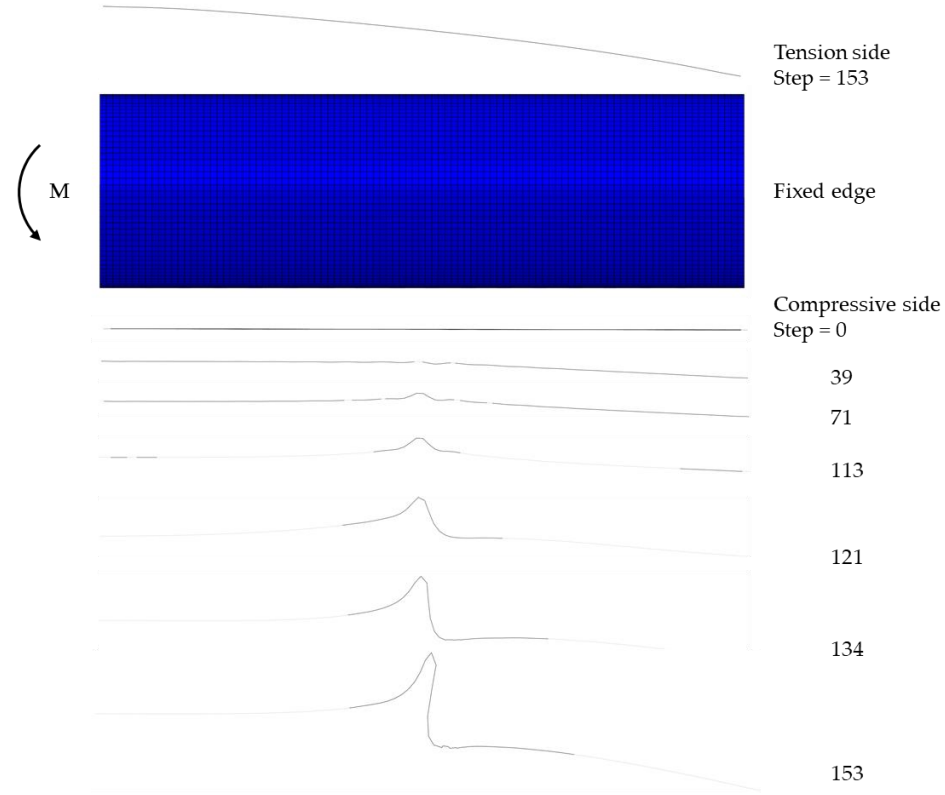


Figure 6.24. Shell (20 m at 24 mm) longitudinal surface displacement under the bending moment (scale factor = 5).

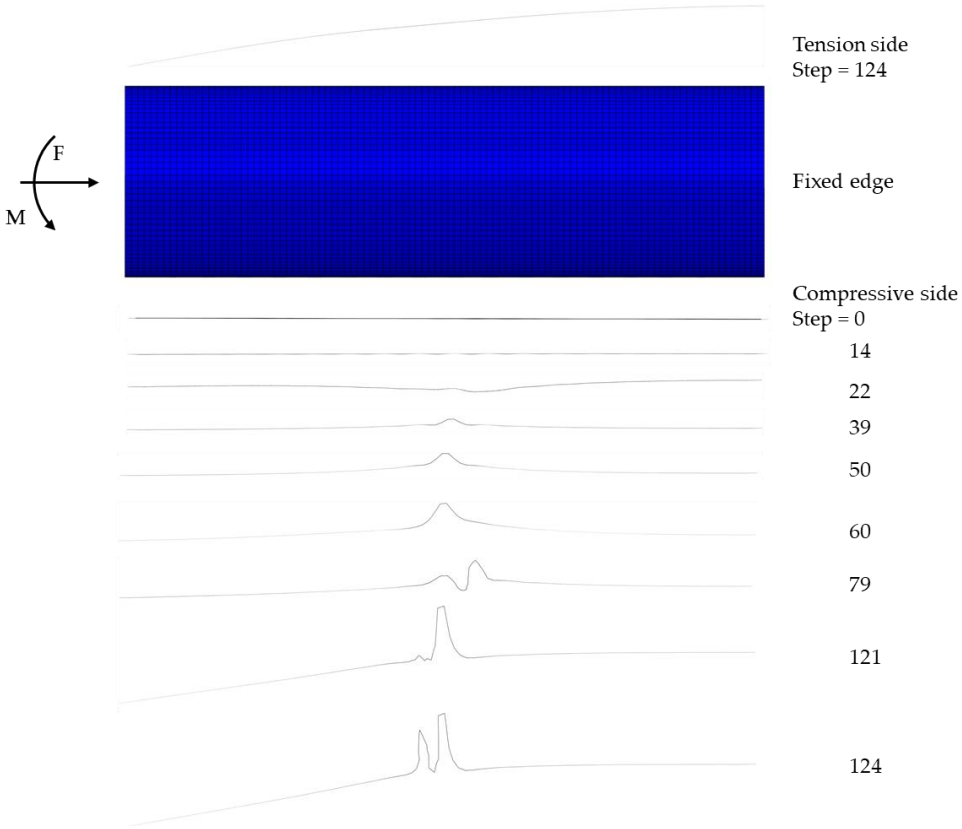


Figure 6.25. Shell (20 m at 24 mm) longitudinal surface displacement under combined loading, (scale factor = 5).

The results obtained for the pure bending load in section 6.3 are in line with previous modelling outcomes (Karamanos, 2002, Sadowski and Rotter, 2013, Guarracino et al., 2009), which predict that initial waving develops at the mid-span, followed by the flattening of both compressive and tension sides, to induce the cross-sectional ovalisation illustrated in Figures 3.7 and 3.8. The deformation patterns observed at steps 39 and 71 justified the use of a simple trigonometry function in Equation (3.77) to simulate longitudinal periodic displacement. Figure 6.24 also suggests that the curvature at the mid-span unchained the buckling collapse, framed between steps 71 and 153; as expected, the tension side remained flat during that process.

The performance of the shell under combined loading naturally reproduces compression and bending effects. Longitudinal wave shapes resemble those seen for axial compression, i.e., they contain a long extension of prebuckling surface displacement due to the initial imperfections and joint loading. The bending moment partially flattened the compression side and then increased half-waves along the length of the segment (Calladine and Sanders, 1984). Buckling emerged at step 39, with a large dent and two adjacent bulges. Buckling in the longitudinal direction thus developed rapidly as the shell membrane effect vanished. In the corresponding numerical process, the factor of λ_m was eliminated to define the lower bound of bearing capacity, which fuelled the shell's progression to the postbuckling branch. In summary, the combined loading condition accelerated the evolution of buckling via mid-length stress concentration, initiated by pure bending and magnified by compressive effects, as shown in Figure 6.22.

6.5.3. Buckling development for different shell lengths

The previous results were enhanced with a series of shell models. These included a segment of 24 m length with 24 mm thickness (Figure 6.9), which enabled the comparison of shell length effects (L/R ratio)—note that the above results related to a 24 m-long shell with L/R = 6.67, hence the R/t ratio remained equal to 125 (Figure 6.9).

Figure 6.26 shows the progression of stress and deformation through 10 characteristic configurations. It is noticeable that the area affected by buckling differed for the long and short tubes. The failure of the short tube was located near the bottom, as opposed to the mid-length, as seen in the long segment. The distribution of the first visible waves varied less in the short segment, as predicted by Equation (3.77) where the assumed displacement function has a denominator of length L. The stress concentration observed at step 6 developed near the base, which (as before) relates to constraints imposed at the boundary. These represent the flange-to-flange connection of adjacent segments or the stiffening rings that induce sudden stiffness changes. Three half-waves appeared at step 16, which caused stress redistribution, local flattening, and curving, thus inducing geometrical changes in the adjacent shell elements.

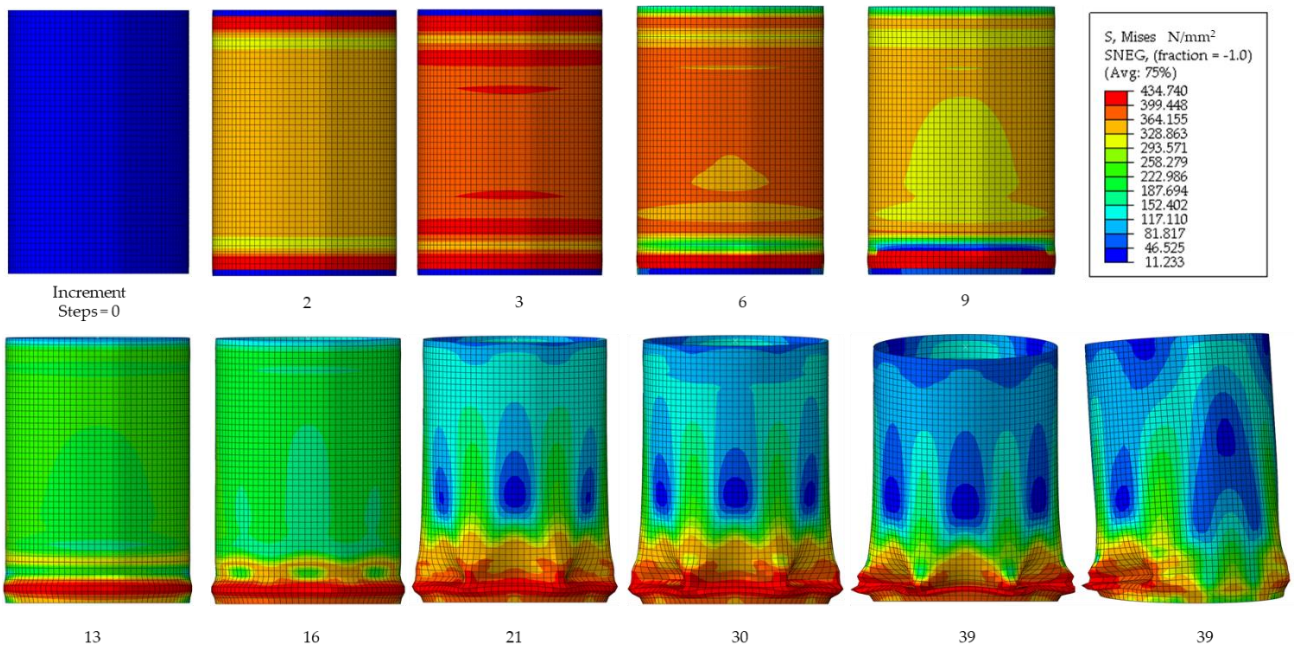


Figure 6.26. Shell (9 m at 24 mm) stress distributions and deformations on the compressive side of the cylindrical shell in 10 increment steps, and the view of the tension side showing a flattening effect.

Compared to Figure 6.20, Figure 6.27 describes pure bending effects. Here we can see how stress concentration took place at step 31, pinpointed at both edges; this followed initial periodic waves and flattening combined through the tube length. It thus seems

that the shorter shells are more susceptible to boundary conditions, as opposed to the assumed initial displacement or geometrical imperfections. When we put Figure 6.9 and Figure 6.20 together with Figure 6.26 and 6.27, the combination tendency of the axial compression and the pure bending is noticeable, but also the buckle point under combined loadings was concentrated at the bottom, mainly due to the complicated interactions between boundary conditions and bending effects.

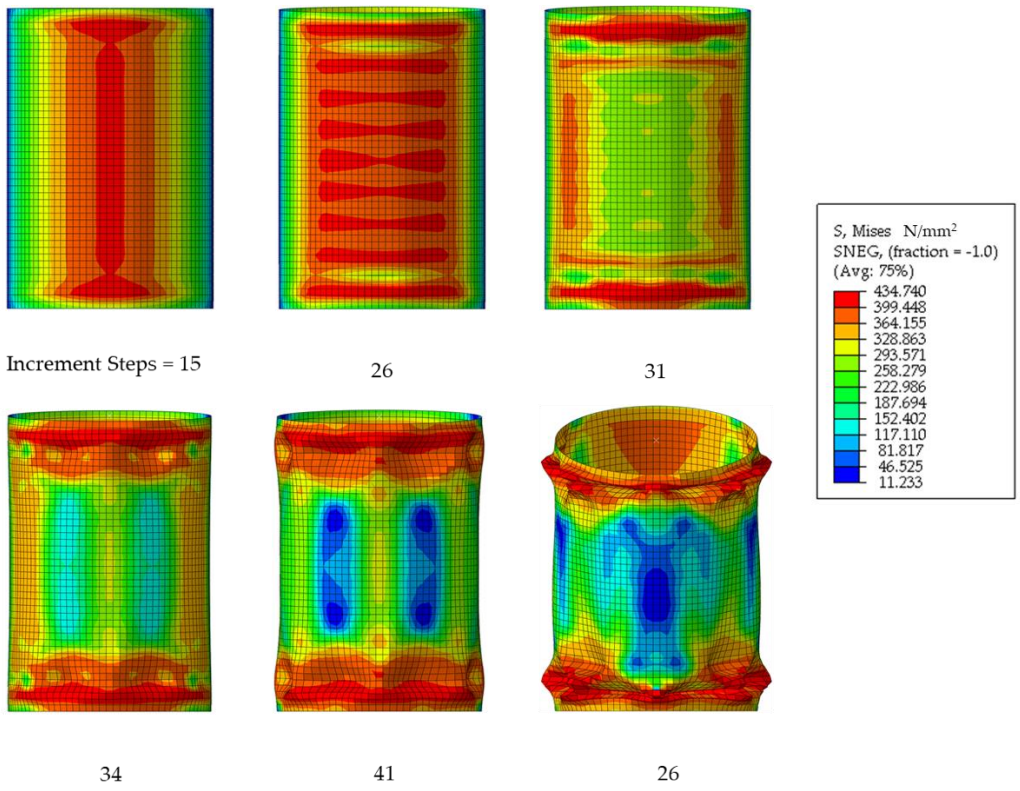


Figure 6.27. Shell (9 m at 24 mm) surface deformation and stress distribution under the pure bending moment.

6.5.4. Buckling behaviour analysis considering energy – curvature relations

We apply the energy perspective for further investigations, as illustrated in Figures 6.28 and 6.29. This allowed us to track the dissipation of strain energy and the change of curvature in two different shell lengths. In these figures, the vertical axis measures the strain energy magnitude in relation to the normalised longitudinal dimension, through a sequence of incremental steps. The normalised longitudinal dimension and

circumferential dimension were calculated based on the full length and circumference of the shell, in a range from 0 to 1.

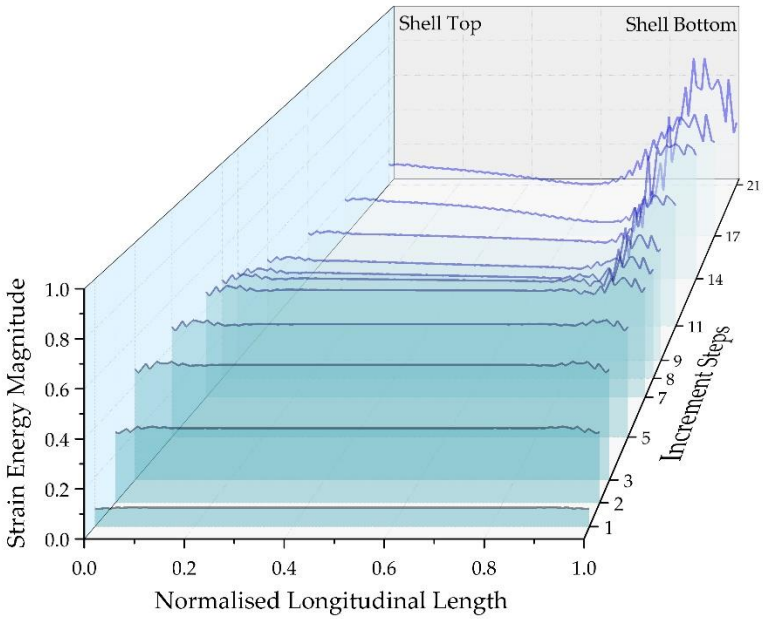


Figure 6.28. Shell (9 m at 24 mm) strain energy magnitudes along the normalised longitudinal length at typical increment steps, under combined loads.

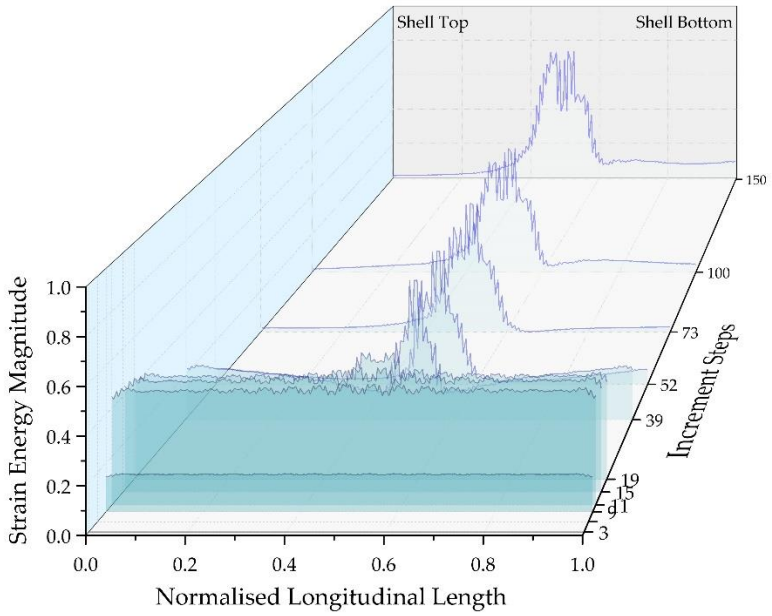


Figure 6.29. Shell (20 m at 24 mm) strain energy magnitudes along the normalised longitudinal length at typical increment steps, under combined loads.

In the early stages of the incremental load process, both the 9 m and 20 m shells were characterised by evenly distributed strain energy, with tiny periodic patterns along

the length as the result of initial wavenumbers in the prebuckling stage. At that point, the strain–stress relationship was linear and in accordance with Hook's Law. It is rational to represent the displacement function by trigonometry functions at this stage. As the load increased, two different strain energy redistribution patterns were revealed on each shell: the 9 m shell experienced decreased strain energy in the upper and mid-length and an accumulation of energy at the bottom end. In contrast, the 24 m shell experienced an increase in strain energy at its middle length, followed by a large decrease at both edges. This phenomenon, in line with the highly influential R/t ratio under the bending moment that reveals the dominant role that the bending moment plays, started in the prebuckling stage and lasted until the collapsed postbuckling stage.

Figure 6.30 addresses the evolution of strain energy distribution associated with the pure bending for the 9 m long shell – the 'elephant foot' buckling shape. In this case, bending, i.e., ovalisation, is a less important contributor to buckling than boundary conditions; in contrast, ovalisation seemingly defines strain and stress distribution and expansion in longer shells, as shown in Figure 6.31.

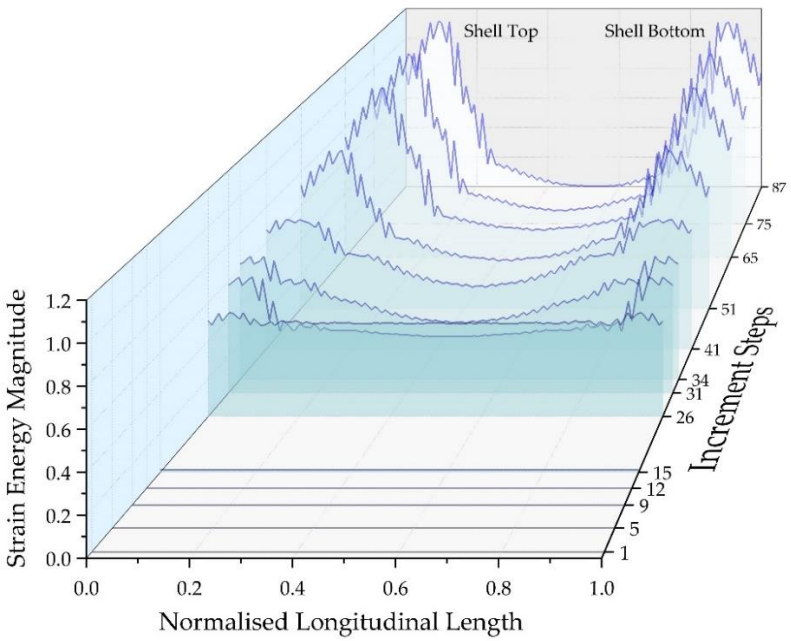


Figure 6.30. Shell (9 m at 24 mm) strain energy magnitudes along the normalised longitudinal length in typical increment steps, under the pure bending moment.

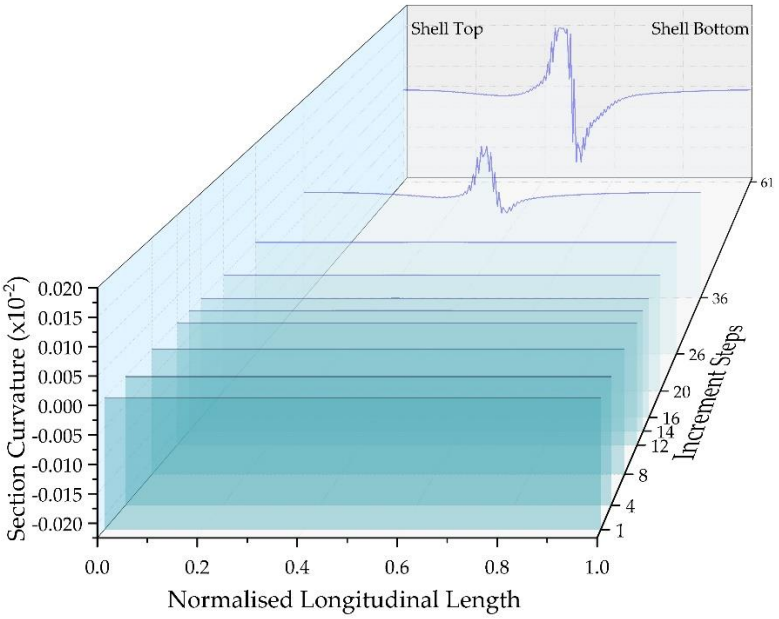


Figure 6.31. Shell (20 m at 24 mm) section curvature along the normalised longitudinal length in typical increment steps, under the pure bending moment.

Furthermore, Figure 6.31 shows the curvature of the 20 m shell under pure bending, according to Figures 6.11 and 6.12, which precedes local buckling. In this case, the curvature fluctuated throughout the length of the tube while becoming pronounced at the middle span, which resembles the performance of a solid beam (Calladine and Sanders, 1984, Langhaar, 2016, Timoshenko et al., 1951). Figure 6.32 enhances the curvature observed on a lower scale in Figure 6.31. Notably, the curvatures at steps 4, 8, and 12 were suitably described by periodic trigonometry functions, with such configurations subsequently changing rapidly as the section underwent buckling (see also Figure 6.34). The longitudinal section curvature of the combined loading scenario was similar to the one observed for pure bending ones. This can be appreciated by scrutinising Figures 6.31–6.33. Figure 6.33 (b) is a zoomed-in illustration of the first five increments shown in Figure 6.33 (a). The section curvature coordinate is zoomed in by 104 times, which allows us to observe the very strict periodic sinusoidal function at increment steps 3 and 8. It is reasonable to set fewer coefficients for trigonometry functions and curvature expressions but this may result in reduced accuracy in the

later buckling stage, when curvature and deformation are progressing intensively. This also explains the shortboard of the linear buckling analysis with simple displacement function forms, whereas a complex shape function increases the calculation burden exponentially.

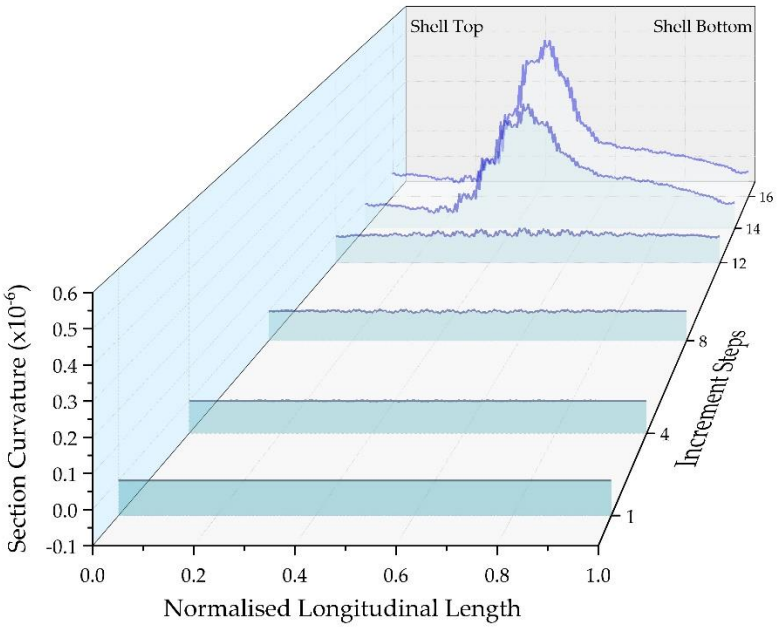
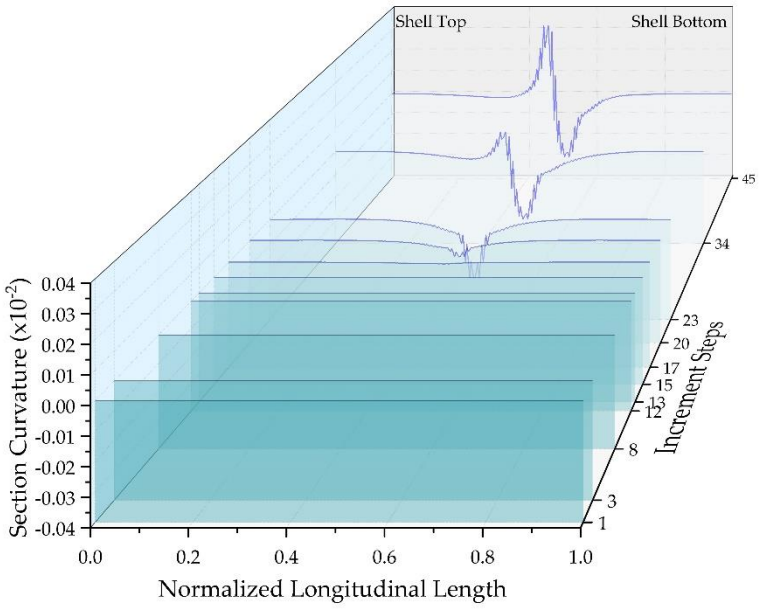
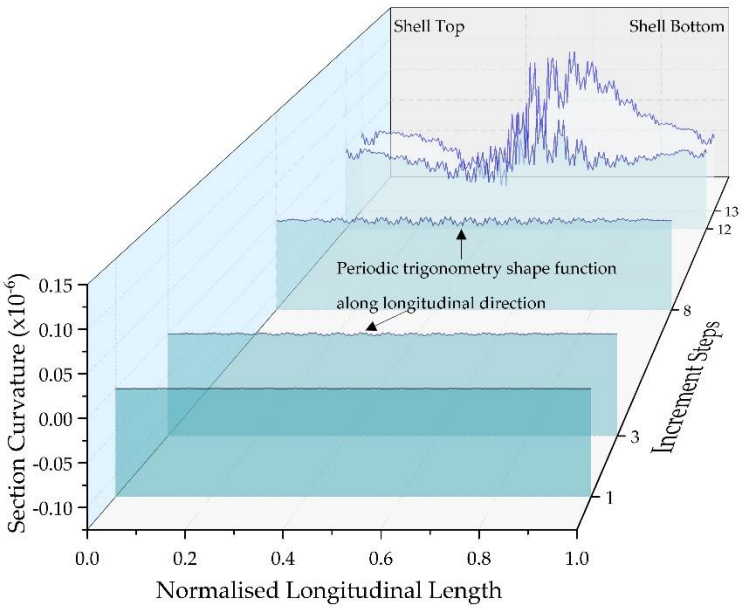


Figure 6.32. Partially enlarged shell (20 m at 24 mm) section curvature along the normalised longitudinal length at early increment steps, under the pure bending moment.



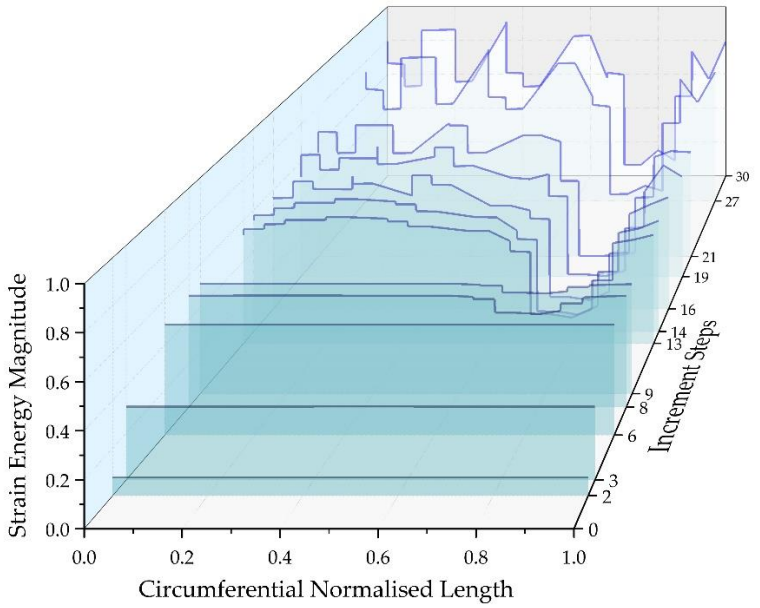
(**a**)



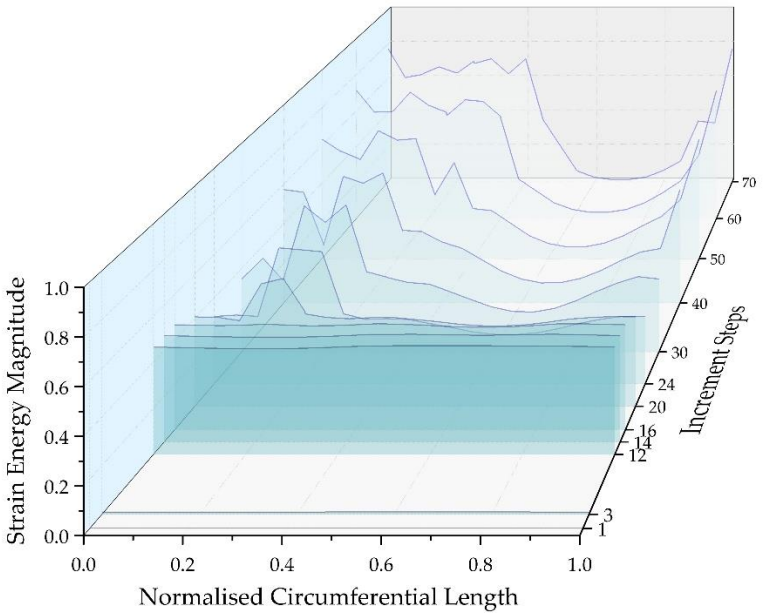
(**b**)

Figure 6.33. Shell (20 m at 24 mm) section curvature along the normalised longitudinal length under combined loads, (**a**) at typical increment steps and (**b**) partially enlarged at early increment steps.

On the other hand, the circumferential strain energy and evolution are shown in Figure 6.34. The transition from smooth to highly asymmetric curves seen along the length of the shell is replicated along the circumference; however, the distribution of strain varied radically between the short and long tubes. In general, the strain distribution seems step-like for the short tube segment (Figure 3.8a), while for the long segment, these appear to be concentrated at specific points (peaks). The strain energy distribution indicates that the area and the thickness of shell surface play dominant roles in deciding energy dissipation behaviour: the larger the area, and the greater the thickness, the better the strain energy dissipation paths may occur, with better ductility and resilience in the structure.



(**a**)



(**b**)

Figure 6.34. Shell strain energy magnitude along the normalised longitudinal length under combined loads, at typical increment steps: (**a**) 9 m at 24 mm shell and (**b**) 24 m at 24 mm shell.

6.5.6. Buckling development for different shell thickness

Further to the examination of the evolution of stress and deformations for varying shell lengths under combined load, we present here the results collected for varying shell thicknesses. The models for comparison include the 9 m-long segments analysed above, with thicknesses of 36 mm (R/t = 83.33) and 24 mm (R/t = 125). These correspond to a L/R ratio of 3. Figure 6.35 shows the deformation and surface stress distributions via 10 characteristic configurations in relation to combined loading. The features shown in Figure 6.35 contrast with those shown in Figure 6.26 for the 24 mm shell. The 36 mm-thick shell shows less dependency on boundary conditions, arguably due to the lower rate of variation in stiffness between the inner sections and edges. Stress augmentation became visible at steps 20–24, as a half-ring bulging emerged, leading to further circumferential wavenumbers. The circumferential wavenumber passed from 1 to 5, then to 9, which contrasted with the more gradual evolution seen in the 24 mm-thick shell.

According to these results, the lower R/t ratio provided better energy expansion for shell structures in buckling, which manifested at early load stages. The higher the wavenumber during the prebuckling state, the better the energy dissipation, and the greater the similarity to pure bending buckling (buckling was triggered at the middle length of the member). Based on Equations (4.29), (4.24) (4.25), and (3.70), the shell thickness was proved to be a controlling factor for higher energy storage capacity, which in turn allowed multiple buckling equilibrium paths; the developed mathematical framework provided a foundation for this (Bardi and Kyriakides, 2006). The mechanism seen in this investigation is consistent with those seen elsewhere (Bardi and Kyriakides, 2006, Calladine and Sanders, 1984, Hutchinson, 1965, Hutchinson, 2016, Winterstetter and Schmidt, 2002, Yamaki, 1984, Yamaki et al., 1975).

The buckling types in FEM analysis under combined loading simulated the typical wind turbine tower collapse phase well. As we could see in Figure 6.36, the buckling

types of the fractured wind turbine towers were similar to the numerical simulation results we carried out in combined loading scenarios. The analysis also validated that the on-site buckling wavenumber of wind turbine towers are in the range of 1 to 9 and usually between 3 and 6.

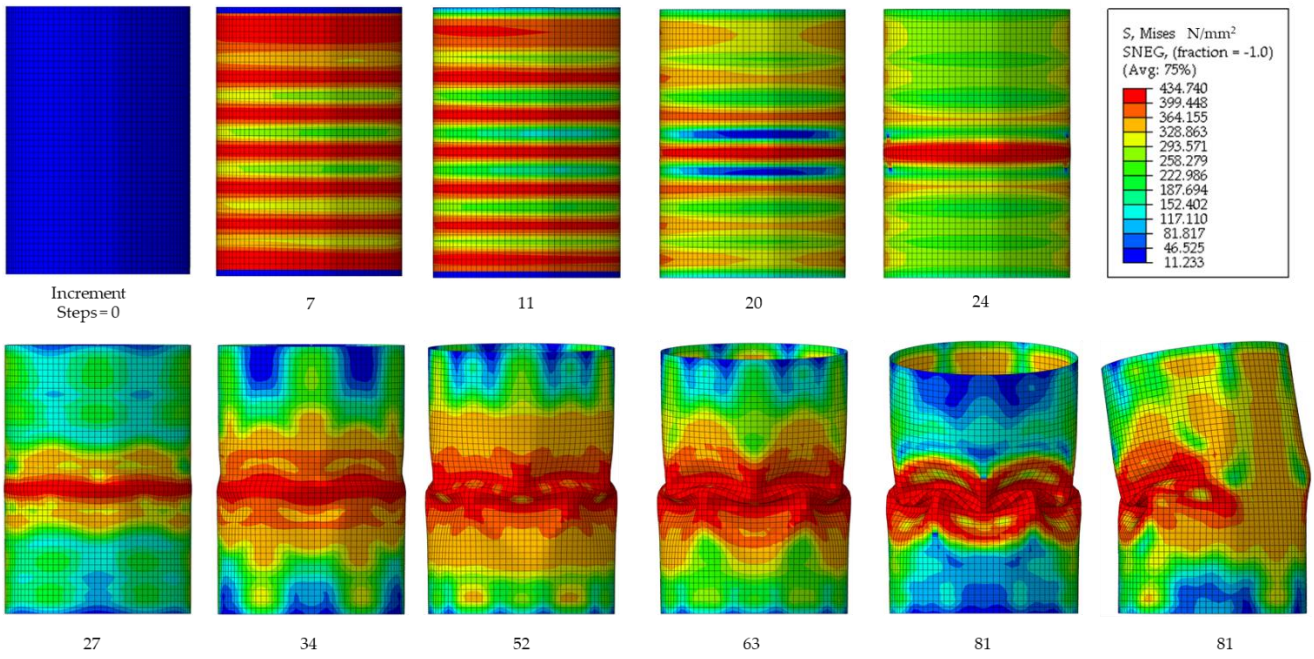


Figure 6.35. Shell (9 m at 36 mm) stress distributions and deformations on the compressive side of the cylindrical shell in 10 incremental steps, and a view of the tension side showing a flattening effect.

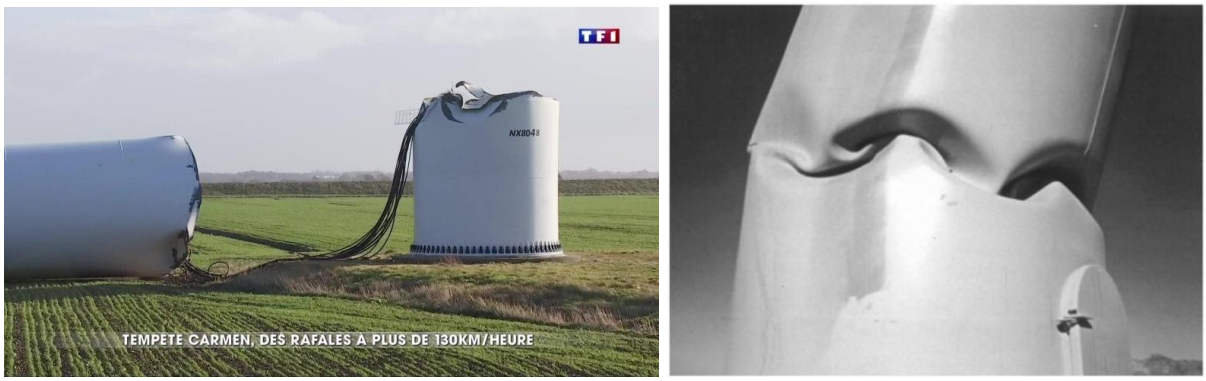


Figure 6.36. The buckling types observed in collapsed wind turbine towers on-site. The wavenumbers can be identified as 3 and 4 (CWIF, 2020b).

6.5.7. Bending – compression ratios and imperfections

In order to investigate the interactions between the magnitude of bending moments and axial compression, a simple parametric study was carried out in this research. 20

m shell models with five wall thicknesses have been selected for this discussion. The combined load has been applied in various combinations as batch jobs in ABAQUS. The ultimate bending moment refers to the result simulated in ASHES, and the ultimate compression load is derived from the linear buckling analysis. The ratio of bending vs. compression has been calculated non-dimensionally, with the magnitude increasing in step increments of 0.05 from 0 to 1.5. The buckling load factor refers to the ideal theoretical result, which has been used in the knockdown factor study (Peterson et al., 1968). The best-fit curves of shells with different wall thicknesses have been drawn in Figure 6.37.

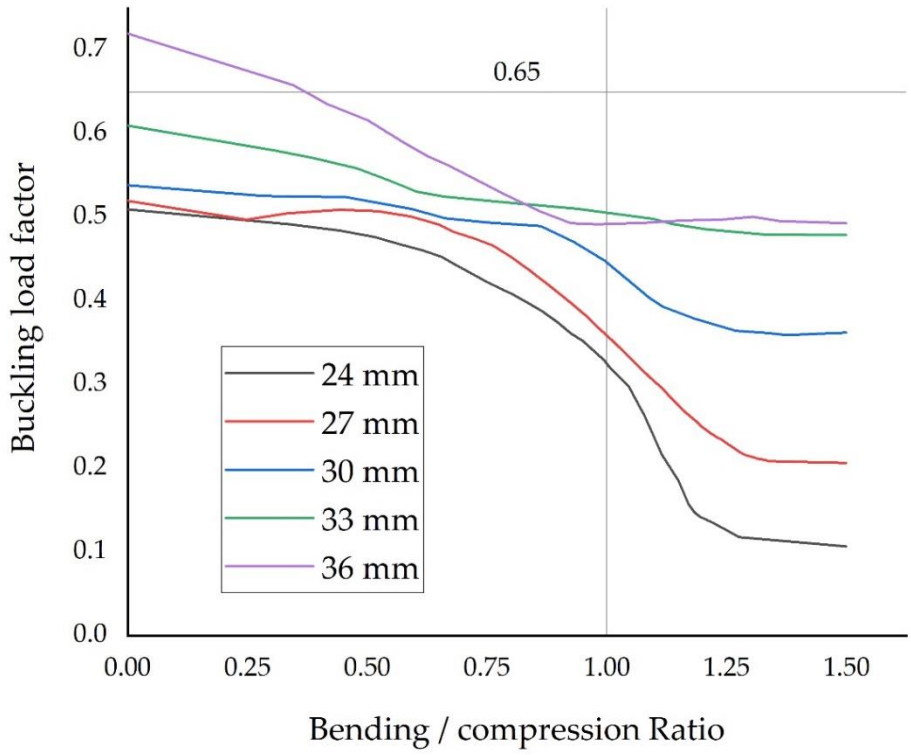


Figure 6.37. The curves of the bending/compression ratio to buckling load factor for shell structure, under combined loading conditions with different wall thickness.

The reference value for axial compression by knockdown factor is 0.65 (Peterson et al., 1968) (marked in Figure 6.37), and we can see that only the 36 mm shell exceeded the lower bound under axial compression as we added the unfavourable initial geometry imperfections to the shells. The thinnest 24 mm shell sees a rapid drop along with the

increase of the bending moment, revealing the significant influence made by bending effects. The 27 mm and 30 mm shells exhibited a similar trend under intense bending moments, with a mild decrease. Shells with thicker walls displayed better performance against the increased bending moment, owing to the better energy dissipation routes and stronger constitution relations between longitudinal and circumferential curvatures.

Combined axial compression and bending at a certain combined ratio reduced the critical buckling load of a cylindrical steel shell. This appeared in Figures 6.38 and 6.39 shown belowat the bending / compression ratio equals to 1. On the other hand, a load factor corresponding to a 24 mm thickness shell peaked for the 15 m-long model, other than the 9 m or 20 m, which revealed an optimum solution for that L/R factor interval; noting that, the maximum load factor was 0.312 for the 20 m shell model, far less than the experimental recommended knock-down factor of 0.65, for the ideal theoretical buckling load λ_{cr} (Peterson et al., 1968).

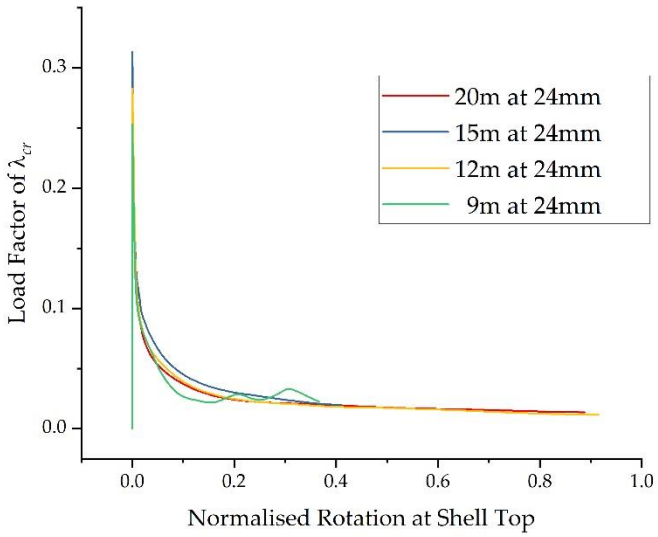


Figure 6.38. Load–rotation curves of 4 shell models of 24 mm thickness in different lengths.

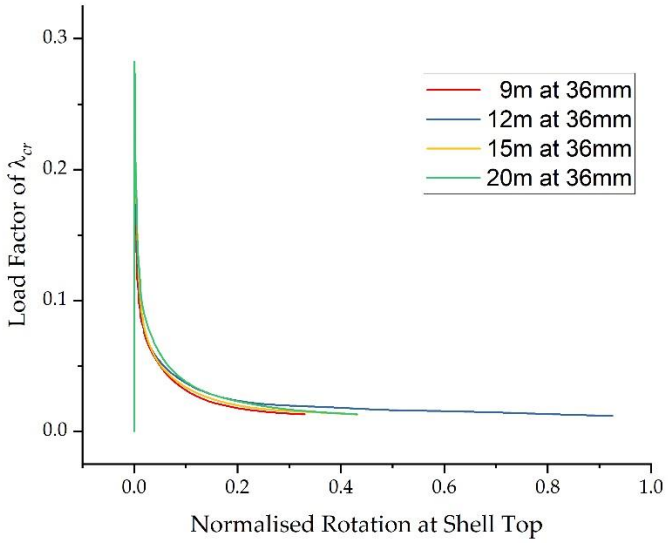


Figure 6.39. Load–rotation curves of 4 shell models of 36 mm thickness in different lengths.

The imperfection sensitivity observed under combined loading conditions as well, with similar buckling behaviour to axial compression scenarios. A 20 m shell model without initial geometric imperfection was created and analysed, comparing to the result with imperfection, illustrated in Figuire 6.40.

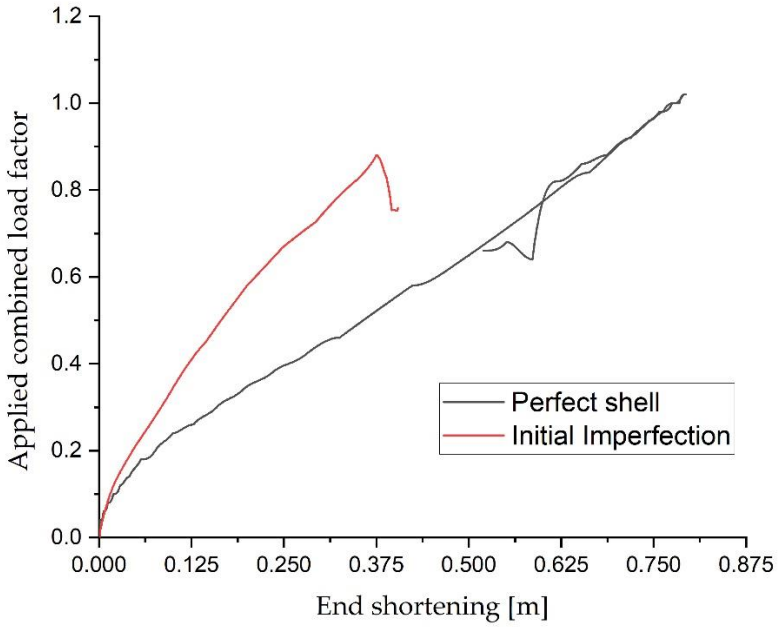


Figure 6.40. Load–end shortening curves of 20 m 24 mm shells with and without initial geometry imperfection.

In Figure 6.40, the load – end shortening curve of perfect shell is 'sharper' than that with initial geometry imperfections, whereas perfect shell has a higher buckling load resistance. The buckling path of imperfect shell evolved faster due to the imperfection leads to a rapid concentrate of stress to the weak area where sees an intense curvature change, furthermore, the bending moment accelerates this concentration. The aerodynamic results by ASHES in extreme combined load conditions shown the calamitous outcomes either, as shown in Figure 5.9 and 5.10.

The buckling analysis under combined load considering initial imperfection provides us the most unfavourable conditions for a wind turbine tower in extreme wind events, and this concept of analysis should be regarded as the lower bound for wind turbine design, either by means of energy methods or detailed numerical simulations.

6.6 Concluding remarks

This Chapter presents the full list of typical results of buckling analysis in ABAQUS and discusses the intended outcomes. The FEM results have been compared to theoretical analysis and ASHES solutions mentioned in Chapter 5. 20 different shell models were implemented with initial imperfections embedded using the FEM via the Riks method for tracking buckling paths. The results show that buckling evolution paths are significantly affected by bending parts, which leads to section ovalisation that in turn changes the internal strain energy dissipation routine and section curvature. The cylinder's geometrical parameters, the length–radius ratio (L/R) and radius–thickness ratio (R/t), also show strong influences on buckling behaviours, seemingly linked to a noticeable reduction in the shell buckling bearing capacity during the combined loading scenarios.

7 CONCLUSIONS AND RECOMENDATIONS

This thesis has conducted a series of buckling analyses for the modern wind turbine tower, using various approaches which highlighted the energy methods. The modern technique of harvesting wind energy with wind turbines has been developed over four decades, and the methods for advanced structure analysis, especially buckling analysis, have evolved over three centuries. However, there is a gap in the research between the theoretical outcomes and the state-of-the-art practical engineering activities. To better understand the mechanism of wind turbine tower collapse, a simple buckling analysis founded on classical theory and energy methods was carried out; after that, a set of numerical models was analysed by numerical simulations such as the finite element method and mathematical software.

The buckling analysis presented here is a vast topic, containing numerous theories and concepts about how best to operate the analysis for wind turbines, and a historical case study of wind turbine tower collapse has been laid out. Following the conclusions drawn from the case study, this thesis pinpointed the objectives and methodology for buckling analysis: thin-walled steel cylindrical shell structures under combined loading conditions, with designated initial geometric imperfections on the shells, to produce the full buckling process for the understanding of the mechanisms. Thereafter, the main conclusions that can be drawn are listed as follows:

1. The most common reasons for wind turbine tower collapses were identified in the updated historical case study. It emerged that these were unexpected extreme wind load levels, combined with human errors such as poor quality control, faulty construction, erroneous operation and improper maintenance. The extreme wind

events accounted for 42% of all failures resulting in tower collapse, and were, therefore, the reason for 9.2% of all accidents. A certain percentage of the cases of collapse could not be attributed to a single factor, as the combination of the reasons laid out above largely contributes to miscellaneous tower collapse. Nevertheless, extreme wind is still identified as the most common major cause, and hence wind load must be taken into account when analysing shell structure buckling.

2. Furthermore, in the structural engineering category, buckling types have been concluded based on the case study. It is difficult to arrive at any single conclusion concerning all tower buckling incidences; however, a range of typical buckling modes can be observed and examined from the on-site investigation and analysis. To our knowledge, this type of wind turbine tower collapse demonstrated a phenomenon in which the wavenumber in the circumferential direction was between 1 and 9, and usually in the range from 3 to 6; meanwhile, the longitudinal wavenumber had a narrower variation, between 1 and 4. This final buckling type inspired and confirmed the judgement factor in the following research – the parameters determining buckling behaviour can be assumed in practical ranges.

3. The buckling analysis strategy proved effective and rational for wind turbine tower structures. The final research objective is to analyse the full buckling path on a cylindrical steel shell structure with geometric imperfections, under a combination of axial compression and bending moment. To achieve this target, the buckling analysis has been divided into the following steps: classical buckling analysis for perfect shells under compressive load, perfect shells under pure bending, perfect shells under combined load, imperfect geometry applied to the perfect shells, and upgraded calculation equations. The flowchart of non-classical buckling analysis followed the same line of logic.

4. In the classical buckling analysis section, the basic equations were derived from the simple two-surface theory for flat rectangular plates. After considering the geometry difference between the plate and cylindrical shells, the geometry and

curvature study has been conducted by selecting an element of the turbine tower shell. The expressions for curvature change and shell surface displacement have been derived in both the longitudinal and circumferential directions. The general formation of local curvature change has been achieved and has been expressed in both general and elementary forms. The stress–strain relations have also been derived for the buckling analysis using Lame parameters in components.

5. The governing equations for cylindrical shells under axial compression have been studied and promoted. Based on the well-known Donnell equation, the simplified differential equation has been obtained, in relation to the interactions between external force, shell geometry and the surface displacement function. We assumed and discussed different forms of displacement functions for the expression of shell surface deformation, and the characteristics were validated in the numerical simulation sections. The eigenvalue equations in the linear buckling stage were obtained under axial compression, which illustrates the relation of linear buckling load to shell geometries, especially in the R/t and L/t ratios.

The governing equations for perfect shells have been obtained under the bending moment. An equation system has been created by comparing the experimental results and theoretical solutions. The Brazier's effect has been introduced; however, much simpler cross-sectional moment equilibriums have been derived, with the ovalisation parameters introduced explicitly in the equations.

6. Stress–strain expressions and the governing functions of surface displacement were deduced under combined loading conditions. The interaction between the axial compression and the bending moment was established through the consistent displacement functions. The extreme fibre was regarded as the calculation objective, as the buckling happened primarily along the extreme fibre. For the longitudinal mid-surface deformation, the governing equation equals the sum of the compression and bending effects; more specifically, it comprises compression results in wave-like deformations, and bending results in warping and flattening

deformations. The governing equation for the circumferential mid-surface deformation also contains these two parts; nevertheless, the bending part results in ovalised deformation in this direction. Despite the limitations, this governing equation provided a linear form of comprehensive deformation description and demonstrated the strong effect of the combination of axial compression and bending moment. Equilibrium consistency has the extra requirements of the continuum conditions for the longitudinal and circumferential deformation in perpendicular directions. This result appears consistent with the numerical simulation results.

7. The imperfection has been discussed and derived for buckling calculations. The imperfection was shown to play an essential role in cylindrical shell buckling problems, which widened the gap between ideal theoretical calculations and experimental results. In the buckling equilibriums, imperfection has been introduced by adjusting the initial surface displacement function. The simple trigonometry functions laid out in previous chapters could be upgraded to multiple term sinusoidal functions or the Fourier function for a better description of the initially imperfect shell section.

8. The energy methods for buckling issues have been discussed in Chapter 4. The procedure insensitivity of energy methods provides us with a more convenient way to track the buckling path, particularly for the transient buckling stage and postbuckling stage. We established the energy function by assuming that the tower section was a conservative system, and then allowing for the external work to be equal to the sum of internal strain energies. A series of expressions for general elementary stress and strain were derived based on element analysis. Utilising the variational algorithms in energy methods, the relation between displacement functions and internal–external stress–strain items were obtained. The equilibriums under the energy category implicitly contained the curvature parameters, and the assumed form of the displacement function was updated. By analysing the expressions

parametrically, the close connection between strain energies and curvatures was inferred, and the buckling mode jumping conditions were fulfilled.

9. We used numerical methods to simulate 100 models in the FEM software ABAQUS and ASHES. The models were created based on the NREL 5 MW wind turbine prototype by selecting the secondary bottom section of the tower for nonlinear buckling analysis. The tower sections were set at a fixed 6 m diameter with lengths of 9–20 m and shell thicknesses of 24–36 mm, in order to replicate all the typical modern wind turbine tower configurations, with R/t at 83.33–125 and L/R at 3–6.66. The aerodynamic results were simulated by ASHES, applying steady winds of 12 m/s, 30 m/s and 70 m/s, and these results provided the respective parameters for the ABAQUS shell element FEM analysis. The end shortening–load curve depicted the tower's resilience to various wind speeds and showed a narrower postbuckling path in extreme wind events.

10. The linear buckling analysis was performed in ABAQUS for load prediction in the following nonlinear analysis, and for the asymmetric shape data in the following imperfection implementation. The first three linear buckling modals were obtained for each model, and the curve-fitting result carried out in MATLAB revealed a high level of consistency. The linear buckling result validated the eigenvalue calculations presented in the preceding theory section.

11. The Riks method was applied to FEM models to analyse the nonlinear buckling of cylindrical shells. Three loading scenarios were simulated for each model: axial compression, pure bending, and combined loadings. In the axial compression analysis, the effects of the L/R ratio were compared between 9 m and 20 m shell models with 24 mm shell thickness. The results showed the buckling behaviour of shorter cylinders was more dependent on boundary conditions, with an 'elephant foot' bulge appearing near both ends, while longer shells have a larger area for strain energy dissipation, and so buckle points tended to be located in the mid-span area. Changing the R/t ratio had a limited effect on the buckling and postbuckling behaviours: similar

buckling types were presented, and the compression had occurred between the 20 m at 24 mm shell and 20 m at 36 mm shell.

12. The pure bending buckling numerical analysis indicated a significant effect on shell surface curvature change. The bending behaviour for different shell lengths illustrated the marked influence of boundary conditions on a shorter cylinder, while the longitudinal curvature change is similar in different shell lengths. The comparison was carried out between the 20 m at 30 mm shell and 9 m at 30 mm shell. The displacement function in the early prebuckling stage has been curve-fitted in MATLAB; it proved the high dependency on supporting conditions, and a trigonometric displacement function with a higher number of coefficients should be applied for the sake of result accuracy. The buckling sensitivity of shells in bending is highly affected by the R/t ratio, as the wall thickness plays a significant role in the buckle point emerging and the number of buckle points that appear.

13. The buckling analysis under combined loading revealed several highlighted mechanisms. The ovalisation effect underpinned the buckling derived from bending and axial interactions. This implies a flattening of the compression segment longitudinally, and a tapering of the local curvature circumferentially. The contribution of the bending effect to buckling under combined load should be consciously noted. The buckling point tended to appear at the mid-length of the shell section; however, the postbuckling scenarios were less redundant than the axial compression ones, which reaffirms previous statements that the buckle point under bending generally tends to emerge in the mid-span area on the compressive side, while under compression it has multiple possible locations across the shell surface. It is worth noting that few models predicted bifurcation branching and mode jumping. Under the combined load, a lower L/R ratio proved to be heavily dependent on boundary conditions, whereas a higher L/R showed patterns that resemble those observed under pure bending buckling. This could be due to a larger shell surface area enabling a redistribution of energy that fuels buckling mechanisms. This behaviour in

combined conditions incorporates the respective behaviour of shells under compression and bending.

14. The result analysis has been carried out from the perspective of energy concentration/dissipation, focusing on the relationship between strain energies and curvatures. Examining the energy elements revealed that a lower R/t ratio, namely thicker walls, boosted energy dissipation and expansion, which in turn enhanced surface deformation rates, and therefore buckling equilibrium paths. Strain energy appeared strongly dependent on local curvature – a property that feeds into linear functions that describe local bending and membrane strain. Furthermore, the arc length method (Riks method) fit any buckling analysis of shell structures, as it determined the realistic solution for instability problems, particularly when those derived from initial geometrical imperfections. A simple study of examples of the bending–compression ratio revealed the severance effect of the bending moment and the reduction of buckling performance upon the axially compressed cylinders.

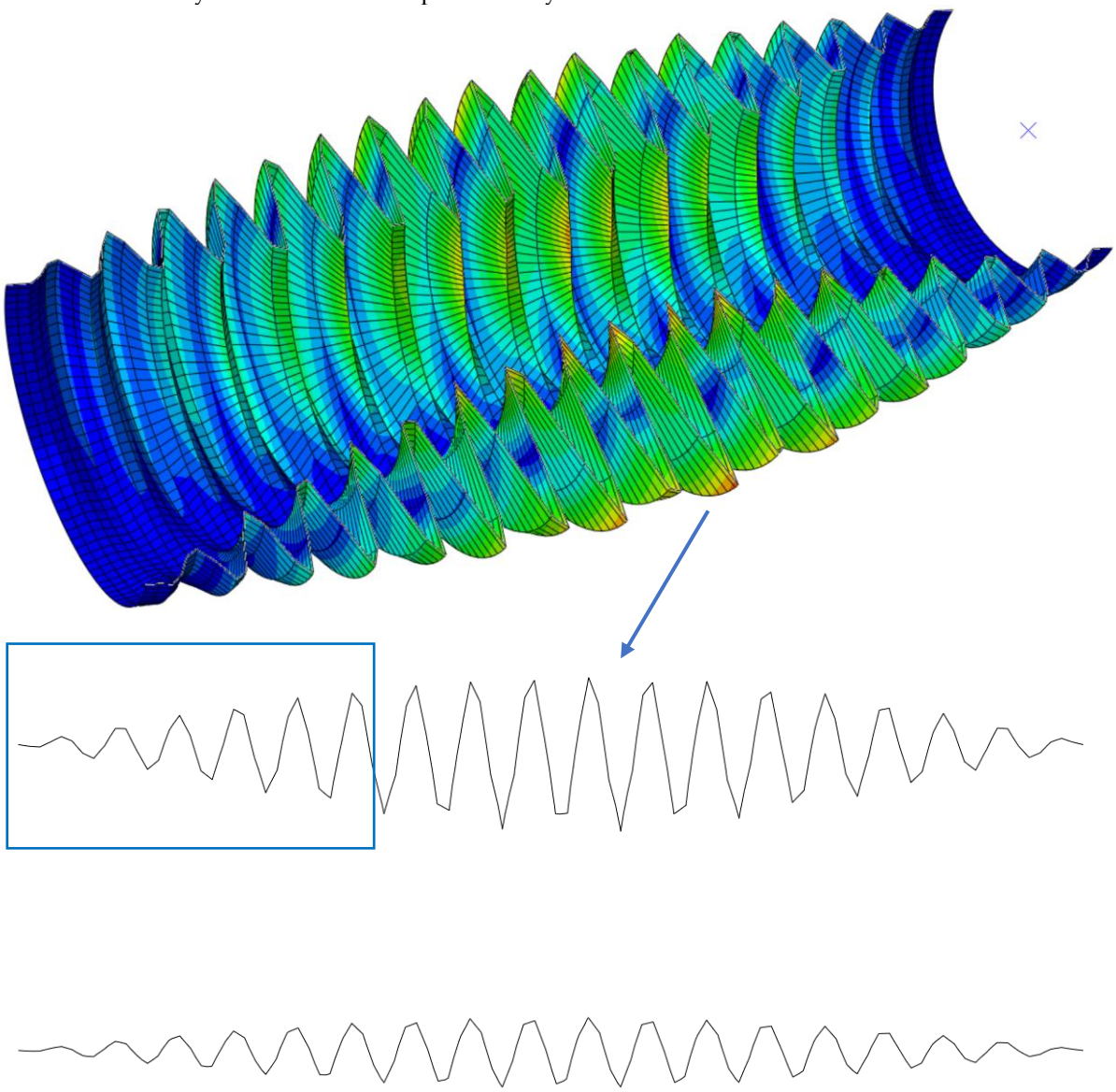
Although the efforts listed above have made a tiny impact on the study of buckling analysis for wind turbine towers, there are still research gaps to fill, especially in light of the increasing demand for energy, and the requirement for higher turbine towers with superior resistance to external loads and resilience against unfavourable conditions. Classical buckling theory had not been significantly developed for a few decades and, as such, as many higher-ordered partial differential equations are unable to obtain the analytical solutions. These differential equations themselves, as well as other mathematical expressions, are a mirror reflecting the real world, which contains numerous uncertainties, variations and hidden truths. By employing numerical methods and modern calculation resources, we could practically approach some meaningful solutions via shortcuts but are still with noticeable variances and far from revealing all the hidden truths about this issue – buckling.

APPENDIX A

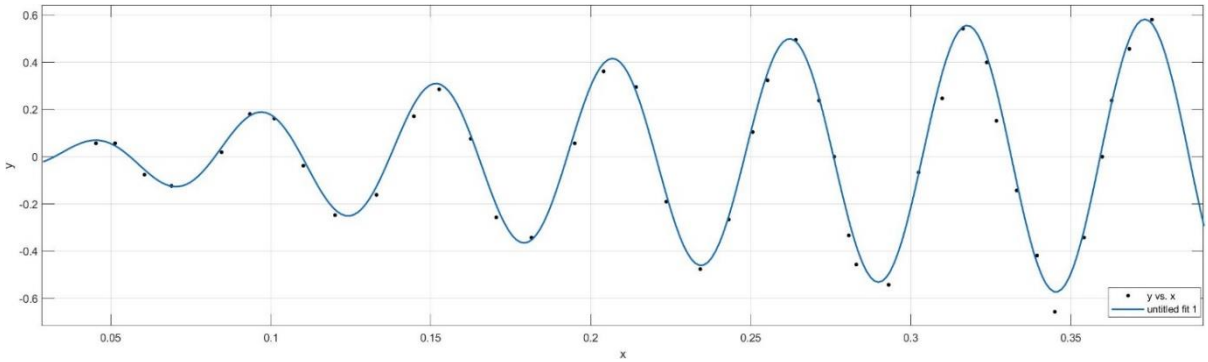
MATLAB code relating to Section 6.2

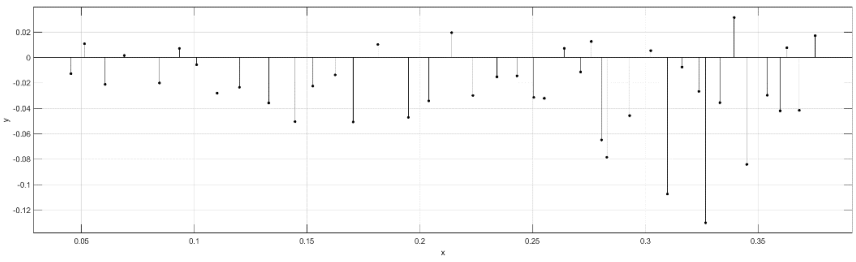
The buckling load validation of equations in MATLAB

After we run the simulations in ABAQUS of the first three modals of the 20 m shell section at 30 mm thickness, the combination of modal shapes resulted in the asymmetric geometry imperfection.
The cut-view of asymmetric modal shapes of the cylinder shell has been obtained shown below:



A section of the upper surface displacements, 35% of the length to the left end, has been selected for curve fitting in MATLAB via Curve Fitting Toolbox 3.5. The sum of the sinusoidal function curve fitting and the function results are shown in follow figure:





General model Sin2:
f(x) = a1*sin(b1*x+c1) + a2*sin(b2*x+c2)
Coefficients (with 95% confidence bounds):
a1 = 0.2747 (0.2215, 0.3279)
b1 = 108.6 (106.6, 110.5)
c1 = -1.159 (-1.671, -0.6471)
a2 = 0.3094 (0.2572, 0.3616)
b2 = 117.1 (115.3, 118.8)
c2 = 1.814 (1.379, 2.249)

Goodness of fit:
SSE: 0.07298
R-square: 0.9815
Adjusted R-square: 0.979
RMSE: 0.04502

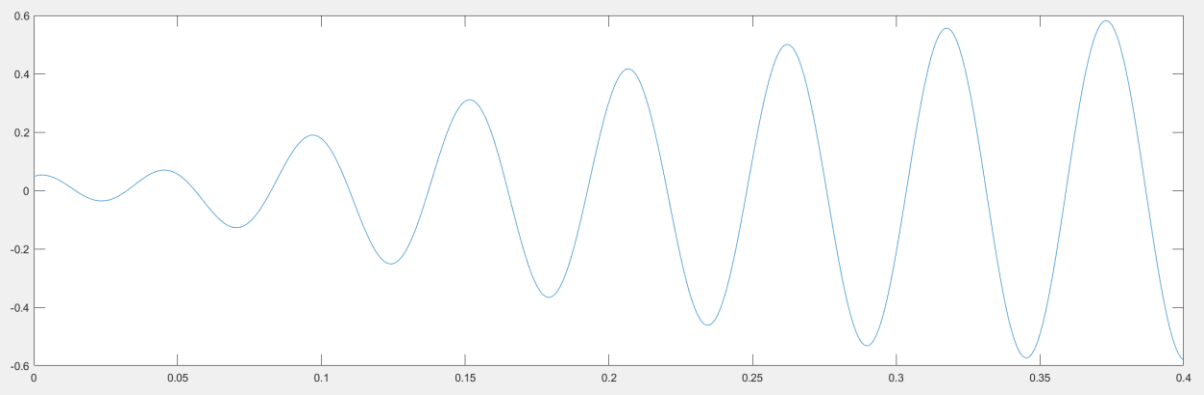
The initial surface function obtained as:

$$f(x) = 0.2747\sin(108.6x - 1.159) + 0.3094\sin(117.1x + 1.814)$$

Then in MATLAB:

```
function Appendix A %implement the curve-fitting sinusoidal functions
clc; clear;
%input variables
a1=0.2747;
b1=108.6;
c1=-1.159;
a2=0.3094;
b2=117.1;
c2=1.814;
x=0:0.001:0.4;
fx=a1*sin(b1*x+c1)+a2*sin(b2*x+c2);
plot(x,fx)
end
```

Plotted as:



Then in MATLAB:

```
syms t x v E f r u x D Eo Ex Pr Qx;
```

```
dsolve('DNx+Px=0','DO+NO/r-Pr=0','DMx-Qx=0','x');% basic differential simultaneous equations
Nx=E*t/(1-v^2)*(diff(u,'x',1)-v*f/r);%Eq. 3.42
%NO=E*t/(1-v^2)*(Eo+v*Ex);% Eq. 3.43
NO=-E*t/(1-v^2)*(f/r-diff(u,'x',1));% Eq. 3.43
Mx=-D*diff(f,'x',2);% Eq. 3.44
MO=v*Mx;% Eq. 3.45
D=E*t^3/(1-v^2)/12;% Eq. 3.46
y1=D*diff(f,'x',2);
dsolve('D2y1+E*h*f/r-v*Nx-Pr=0','x');% Eq. 3.47
f1=C1*exp(h1*x)+C2*exp(h2*x)+C3*exp(h3*x)+C4*exp(h4*x);% Eq. 3.49
%B1=E*t/(4*D*r^2);
B=3*(1-v^2)/(r^2*t);
h1=B*(1+1i);
h2=B*(1-1i);
h3=-B*(1+1i);
h4=-B*(1-1i);
f2=exp(-B*x)*(C1*exp(1i*B*x)+C2*exp(-1i*B*x))+exp(B*x)*(C3*exp(1i*B*x)+C4*exp(-1i*B*x));
f=exp(-B*x)*(C1*cos(B*x)+C2*sin(B*x))+exp(B*x)*(C3*cos(B*x)+C4*sin(B*x))+fx;%standard solutions
pB=-(diff(Mx,'x',2)+2*diff(diff(Mxy,'x',1),'y',1)+diff(My,'y',2));% Eq. 3.57
Detp=wn*(E*t/(a^2*l^4)*(1/(l^2)+1/(b^2))^(-2)+pi^4*D*(1/(l^2)+1/(b^2))^2)*sin(pi*x/l)*sin(pi*y/b);
Nx=-(E*t/(pi^2*a^2*l^2)*(1/(l^2)+1/(b^2))^(-2)+pi^2*l^2*D*(1/(l^2)+1/(b^2))^2);
N=Fy*(2*pi*R2*(pi-2*a)*t+2*a*R1*t-2*a*r1*t);
M=Fy*(2*a*R1*t*(rt+rc1)-(R2*(pi-a)*t*(rc1))+(pi*r*t*rc2));
Nx=-(N0+N1*cos(O));
Exl=-N/(E*t);
Ex=(Ex2+v*EO2)/(1-v^2);
Ex2=(1-v^2)*Exl-v*EO2;
EO2=-v*Exl+C0/r*sin(n*pi*x/L);
rxy=0;xy=0;xxy=0;
xx=Co*n^2*pi^2*sin(n*pi*x/L)/(L^2);% Eq. 3.78
EO=(-v*Exl+Co/r*sin(n*pi*x/L))+s*((diff(v,'y',1)+w/R)+
0.5*(diff(v,'y',1)+w/R)^2+0.5*(v/R-diff(w,'y',1)^2));%Eq. 3.79
a1=0.2747;
b1=108.6;
c1=-1.159;
a2=0.3094;
b2=117.1;
c2=1.814;
x=0:0.001:0.4;
f=a1*sin(b1*x+c1)+a2*sin(b2*x+c2); %instead of the original f=-Co*sin(n*pi*x/L)+a*s*cos(2*O) in Eq. 3.82
Detp1=(-N1)*diff(f,'x',2)-2*Nxy*diff(diff(f,'x',1),'y',1)+(-Ny)*diff(f,'y',2);% Eq. 3.83
pB=-(diff(-D*diff(f,'x',2),'x',2)+diff(-v*D*diff(f,'x',2),'y',2));% Eq. 3.85
pB=(-N1)*diff(f,'x',2)-2*Nxy*diff(diff(f,'x',1),'y',1)+(-Ny)*diff(f1,'y',2);% Eq. 3.86
N1=r/v*(D*diff(f,'x',4)+E*h/r*f);%N1 represents the buckling loads under the condition of applying curve fitting
results to previous equations
```

By substituting the geometry parameters of the 20 m length at 30 mm wall thickness shell, and adjusting the amplitude of sinusoidal functions to the magnitude according to wall thickness, it is hence to obtain the nondimensional buckling load factor with imperfection is:

$$\lambda = \frac{6.28 \times 10^8}{9.09 \times 10^8} = 0.6913$$

Meanwhile, the buckling load factor of FEM result is $\lambda = 0.6407$ sees a difference at $\frac{0.6913-0.6407}{0.6913} \times 100\% = 7.32\%$.

APPENDIX B

MATLAB code relating to Section 6.2

The solving approach by finite-difference method in MATLAB

```
%clear
%using simple English spellings for respective Greek notations in equations
L=1;R=1;h=0.02;P=1;E=1e6;%cylindrical shell geometries, as nondimensional
%L is shell length, R is radius, h is the wall thickness
%keep L equals 1 and other two factors defined by L/R L/t ratios
v=0.3;%Poison's ratio
x=0:0.05:L;y=0:0.05:pi*R;%discrete step length, could be tested and adjusted
N=length(y);dt=0.01;%divide the elements along longitudinal and circumferential directions
xi=pi*x/L;eta=pi*y/(pi*R);%nondimensional notations for convenient calculations
w0=meshgrid(xi,eta);f0=meshgrid(xi,eta);%meshing
c=1/12*(1-v^2);alpha=L^2/(pi^2*R*h);beta=L*N/(pi*R);%notations for convenience
Pcl=2*pi*E*h^2/(3*(1-v^2));sigma=P/Pcl;%buckling load factor
%then the Finite Difference Method applied to basic 4-order Donnell PDEs
%the PDE form written as D∇^4W − R^−1F,xx − F,yyW,xx + 2F,xyW,xy − −F,xxW,yy = 0 (Yamaki, 1976)
for i=1:4
   w(:,:,i)=w0*0;f(:,:,i)=w0*0; %the initial value set as 0
end
for i=5:1000%the FDM discretizing the function on grid, this discretizing could be adjusted for accuracy and
processor time
   w1=w(:,:,i-1);f1=f(:,:,i-1);
   f(:,:,i)=(-alpha*diff2d(w1,[-1:1],1,2,1)+beta^2*(diff2d(diff2d(w1,[-1:1],1,1,1),[-1:1],2,1,1).^2-...
      diff2d(w1,[-1:1],1,2,1).*diff2d(w1,[-1:1],2,2,1)))*dt^4-f(:,:,i-4)+4*f(:,:,i-3)-6*f(:,:,i-2)+4*f(:,:,i-1);
   w(:,:,i)=(alpha*diff2d(f1,[-1:1],1,2,1)+beta^2*(diff2d(f1,[-1:1],2,2,1).*diff2d(w1,[-1:1],1,2,1)-...
      2*diff2d(diff2d(f1,[-1:1],1,1,1),[-1:1],2,1,1).*diff2d(diff2d(w1,[-1:1],1,1,1),[-1:1],2,1,1)+...
      diff2d(f1,[-1:1],1,2,1).*diff2d(w1,[-1:1],2,2,1)))/c*dt^4-w(:,:,i-4)+4*w(:,:,i-3)-6*w(:,:,i-2)+4*w(:,:,i-1);
end

%as the subscript of each variant in MATLAB defines from 1, the following
%variant names have been defined as a series started from 1, which contains
%differences to equations in the dissertation
m=10;n=11;  %m and n of orthogonal functions
np=10;nq=11;  %the value of p and q varies from 0 to a finite number, using np, nq to define the maximums
p=1:np;q=1:nq;
a=sym('a', [m,n]); %a is the parametric matrix which intended to obtain
f=fun(a);  %fun is a designed test function
F=f./(p.^2+q.^2*beta^2).^2;F(1,1)=0;
px=-alpha/(sqrt(3*(1-v^2))*beta^2)*sigma;
py=v*beta^2*px+sum(p.^2.*F(p,1));  %arbitrary constants determined by boundary conditions and
nondimensional notations
%parameters calculation
Cq=cos(h*q*beta*pi);
Sq=sin(h*q*beta*pi);Qq=q.^2*beta^2*((3-v)^2*Sq.^2-(1+v)^2*q.^2*beta^2*pi^2);%arbitrary constants
Aq=1./Qq*sum((p.^2-v*q.^2*beta^2)*F(p,q)*((3-v)*(1-v)/(1+v)*Sq.^2-(1+v)*q.^2*beta^2*pi^2-...
   2*(-1).^p*(1+v).*q*beta*pi));%arbitrary constants
```

```
Bq=1./Qq*sum((p.^2-v*q.^2*beta^2)*F(p,q)*Sq*((3-v)*Sq+(-1).^p*(1+v).*q*beta*pi));%arbitrary constants
Hq=-1./Qq*sum((p.^2-v*q.^2*beta^2)*F(p,q)*(Cq-(-1).^p)*((3-v)*Sq+(-1).^p*(1+v).*q*beta*pi));%arbitrary
constants
Gq=(1-v)*Hq/(1+v);%arbitrary constants
delta=eye(length(p));
a_=a;%arbitrary constants

%eq is the function fulfilled by a
J=(p.^2-v*q.^2*beta^2)./(p.^2+q.^2*beta^2).^2;
K(1:2:end,:)=(Cq-1)./((1+v).*q.*beta*pi.*((3-v).*Sq-(1+v).*q.*beta*pi));
K(2:2:end,:)=(Cq+1)./((1+v).*q.*beta*pi.*((3-v).*Sq+(1+v).*q.*beta*pi));
K(:,1)=0;
for r=1:m %the discretizing factor of m and n could be tested and trail-and-error for an optimum option
   for s=1:n
      phi_s(:,:,r,s)=(r*q-s*p).^2.*((1+delta(q,s))*(a_(p-r-1,abs(q-s))-a_(p-r+1,abs(q-s)))+...
         (a_(p+r-1,q+s)-a_(p+r+1,q+s)))+(r*q+s*p).^2.*((1+delta(q,s))*(a_(p+r-1,abs(q-s))-...
         a_(p+r+1,abs(q-s)))+(a_(p-r-1,q+s)-a_(p-r-1,q+s)));
   end
end
phi=phi_s(:,:,r-1,:)-phi_s(:,:,r+1,:);
pai_s=((m-p)*n-m*q).^2.*J(m-p,q)+((m+p)*n-m*q).^2.*J(m+p,q);
pai=pai_s(p-1,:,m-1,:)+pai_s(p+1,:,m+1,:)-pai_s(p-1,:,m+1,:)-pai_s(p+1,:,m-1,:);
for r=1:m
   for s=1:n
eq(r,s)=[(1+delta(s,1)*(c*((r-1)^2+s^2*beta^2)^2+beta^2*px*((r-1)^2+v*s^2*beta^2))*a(r,s)-a_(r-2,s)+...
   (1+delta(s,1))*(c*((r+1)^2+s^2*beta^2)^2+beta^2*px*((r+1)^2+v*s^2*beta^2))*a(r,s)-a(r+2,s)+...
   sum(sum(F(p,q)*(alpha*(1+delta(s,1))*((r-1)^2*delta(p,r-1)-(r+1)^2*delta(p,r+1))*delta(q,s)-...
   4*alpha*p^2*delta(q,1)*delta(r,l)*delta(s,1)+4*alpha*delta(q,s)*(p.^2-v*s^2*beta^2)*K(p,s)*(1+(-
1).^(p+r+1))*...
   ((r-1)^2*J(r-1,s)-(r+1)^2*J(r-1,s))+p^2*s^2*beta^2*delta(q,1)*(2*a(r,s)-a_(r-2,s)-a(r+2,s))+...
   1/4*beta^2*phi(p,q,r,s)-(p.^2-v*q.^2*beta^2)*beta^2*K(p,q)*sum(1+(-
1)^(m+p+r))*((1+delta(q,s))*a(m,abs(q-s))*...
   pai(r,q,m,q-s)+a(m,q+s)*pai(r,q,m,q+s))))))-4*v*alpha*beta^2*px*delta(r,1)*delta(s,1)];
   end %equations after integration and for brevity
end
a=matlabFunction(eq,'Vars',{a});
f=fun(a);
F=f./(p.^2+q.^2*beta^2).^2;F(1,1)=0;

%function fun (f) calculated via following equation after the value of a obtained
f=0.5*px*eta.^2+0.5*py*xi.^2+sum((Aq*cos(h*q*beta.*xi)+Bq*q*beta*xi*sin(h*q*beta.*xi)+Gq*sin(h*beta*x
i)+ Hq*q*beta*xi*cos(h*q*beta.*xi))*cos(q*eta))+sum(sum(F(p,q).*cos(p.*xi).*cos(q.*eta)));

%solution visualizations, loads vs. surface displacements
subplot(2,2,1);mesh(x,y,reshape(w(:,:,500),Nx,Nx));xlabel('y');ylabel('x');zlabel('w');
subplot(2,2,2);mesh(x,y,reshape(w(:,:,1000),Nx,Nx));xlabel('y');ylabel('x');zlabel('w');
subplot(2,2,3);mesh(x,y,reshape(f(:,:,500),Nx,Nx));xlabel('y');ylabel('x');zlabel('f');
subplot(2,2,4);mesh(x,y,reshape(f(:,:,1000),Nx,Nx));xlabel('y');ylabel('x');zlabel('f');

function du = diff2d(u,formwork,direction,order,bondary)
%this function used for the difference calculation of the matrix along the x direction
%u is the differencing vector, formwork is the templet of differentiation,
%direction is the difference direction (default as 1-horizontal,
%order is the diff order default is 1
%boundary default as 0, when set as 1, we use one-sided difference to
%calculate the boundary (we adopt the same number of nodes as formwork)
%the returning value is the similar vector as u
```

```
if nargin==2
   direction=1;order=1;bondary=0;
elseif nargin==4
   bondary=0;
end
if direction==2
   u=u.';
end
coeff_u=coeff(formwork,order);
m=formwork(1);n=formwork(end);
%applying templet difference on irregular boundary points
leng=length(formwork);du=u.*0;
for i=1:leng
   du(:,1-m:end-n)=du(:,1-m:end-n)+coeff_u(i).*u(:,1-m+formwork(i):end-n+formwork(i));
end
%applying one-sided difference to regular boundary points
if bondary==1
   %left boundary
   formwork_left=formwork-m;coeff_left=coeff(formwork_left,order);
   for i=1:leng
      du(:,1:-m)=du(:,1:-m)+coeff_left(i).*u(:,1+formwork_left(i):-m+formwork_left(i));
   end
   %right boundary
   formwork_right=formwork-n;coeff_right=coeff(formwork_right,order);
   for i=1:leng
      du(:,end-n+1:end)=du(:,end-n+1:end)+coeff_right(i).*u(:,end-
n+1+formwork_right(i):end+formwork_right(i));
   end
end
if direction==2
du=du.';
end
end
function x = coeff(node,order)
%this function defined for the calculation of difference parameters at given nodes
%node is the positional vector of node point according to the calculating point, e.g. [-2,-1,0]
%order is the order of the derivative intended to solve (e.g. default is 1)
if nargin==1
   order=1;
end
m=length(node);
factor=ones(m,1); pownode=ones(m,1);  b=zeros(m,1); b(order+1)=1; A=zeros(m,m);
for i=2:m
   factor(i)=(i-1)*factor(i-1);
end
for i=1:m
   a=node(i);
   for j=2:m
      pownode(j)=a*pownode(j-1);
   end
   A(:,i)=pownode./factor;
end
[L,U]=lu(A); x=U\(L\b);
end
```

REFERENCES

Abaqus (2019). Abaqus software. 6.14 ed. Palo Alto, CA, USA: ABAQUS Inc.

Abaqus, V. (2014). 6.14 Documentation, Dassault Systemes Simulia Corporation.

Akbarov, S. D. (2012). Stability loss and Buckling delamination, Springer, Berlin, Heidelberg. ISBN 978-3-642-30289-3, doi: https://doi.org/10.1007/978-3-642-30290-9

Alfutov, N. a. E. (2013). Stability of elastic structures, Springer Science & Business Media, Berlin, Heidelberg. ISBN 978-3-540-65700-2, doi: https://doi.org/10.1007/978-3-540-49098-2.

Aliabadi, M. H., Falzon, B. G. & Scientific, W. (2008). Buckling and Post Buckling Structures: Experimental, Analytical and Numerical Studies, Imperial College Press.

Almroth, B. (1965). Influence of Edge Conditions on the Stability of Axially Compressed Cylindrical Shells. AIAA Journal, 4**,** 40.

Almroth, B. J. (1963). Postbuckling behavior of axially compressed circular cylinders. AIAA Journal, 1**,** 630-633.

Alonso-Martinez, M., Adam, J. M., Alvarez-Rabanal, F. P. & Del Coz Díaz, J. J. (2019). Wind turbine tower collapse due to flange failure: FEM and DOE analyses. Engineering Failure Analysis, 104**,** 932-949.

Ames, W. F. (2014). Numerical methods for partial differential equations, Academic Press.

Andrianov, I. V., Awrejcewicz, J. & Manevitch, L. I. (2013). Asymptotical mechanics of thin-walled structures, Springer Science & Business Media.

API 2000. (1998). Venting Atmospheric & Low-Pressure Storage Tanks, Nonrefrigerated & Refrigerated; 5th Edition.

Arabian-Hoseynabadi, H., Oraee, H. & Tavner, P. J. (2010). Failure Modes and Effects Analysis (FMEA) for wind turbines. International Journal of Electrical Power & Energy Systems, 32**,** 817-824.

Arani, A. G., Golabi, S., Loghman, A. & Daneshi, H. (2007). Investigating elastic stability of cylindrical shell with an elastic core under axial compression by energy method. Journal of Mechanical Science Technology, 21**,** 983-996.

Arbocz (1974). The effect of initial imperfections on shell stability. 205-245.

Arbocz, J. & Babcock Jr, C. D. (1969). The effect of general imperfections on the buckling of cylindrical shells.

Arbocz, J. & Starnes Jr, J. H. (2002). Future directions and challenges in shell stability analysis. Thin-walled structures. 40**,** 729-754.

Arbocz, J. J. S. (1992). The effect of initial imperfections on shell stability: An updated review. 94**,** 14692.

Bäckstrand, J. & Hurtig, A. (2017). Final report RO 2017: 01. Stockholm, Sweden: Statens Haverikommission.

Bardi, F. C. & Kyriakides, S. (2006). Plastic buckling of circular tubes under axial compression—part I: Experiments. International Journal of Mechanical Sciences, 48, 830-841.

Bas, J., Carriveau, R., Cheng, S. & Newson, T. (2012).Strain response of a wind turbine tower as a function of nacelle orientation. BIONATURE 2012, The Third International Conference on Bioenvironment, Biodiversity and Renewable Energies, 12-18.

Batdorf, S. & Sines, G. (1980). Combining data for improved Weibull parameter estimation. Journal of the American Ceramic Society, 63, 214-218.

Batterman, S. C. (1965). Plastic buckling of axially compressed cylindrical shells. 3, 316-325.

Benedettini, F. (1999). Buckling Experiments: Experimental Methods in Buckling of Thin–Walled Structures Vol. 1: Basic Concepts, Columns, Beams and Plates J. Singer, J. Arbocz and T. Weller John Wiley & Sons, Chichester. Meccanica, 34, 66-67.

Berry, P., Rotter, J. & Bridge, R. (2000). Compression tests on cylinders with circumferential weld depressions. Journal of engineering mechanics, 126, 405-413.

Boyle, J. (1981). The finite bending of curved pipes. International Journal of Solids Structures, 17, 515-529.

Brazier, L. G. & Southwell, R. V. (1927). On the flexure of thin cylindrical shells and other "thin" sections. 116, 104-114.

Brush, D. O., Almroth, B. O. & Hutchinson, J. (1975). Buckling of bars, plates, and shells.

Burton, T., Sharpe, D., Jenkins, N. & Bossanyi, E. (2001). Wind energy handbook, Wiley Online Library.

Bushnell, D. (1981). Buckling of shells-pitfall for designers. AIAA journal. 19, 1183-1226.

Butcher, J. C. & Goodwin, N. (2008). Numerical methods for ordinary differential equations, Wiley Online Library.

Calladine, C. (1995). Understanding imperfection-sensitivity in the buckling of thin-walled shells. 23, 215-235.

Calladine, C. & Sanders, J. (1984). Theory of Shell Structures. Journal of Applied Mechanics-transactions of The Asme - J Appl Mech, 51.

Capecchi, D. (2012). History of virtual work laws: a history of mechanics prospective, Springer Science & Business Media.

Carlstedt, N.-E. (2004). Driftuppföljning av vindkraftverk: årsrapport 2003, Energimyndigheten.

Castro, S. G., Zimmermann, R., Arbelo, M. A. & Degenhardt, R. (2013). Exploring the constancy of the global buckling load after a critical geometric imperfection

level in thin-walled cylindrical shells for less conservative knock-down factors. Thin-Walled Structures. 72, 76-87.
Chan, T. M., Gardner, L., Law, K. H. (2010). Structural design of elliptical hollow sections: a review. Proceedings of the Institution of Civil Engineers-Structures Buildings. 163, 391-402.
Chen, X., Li, C. & Tang, J. (2016). Structural integrity of wind turbines impacted by tropical cyclones: A case study from China. Journal of Physics: Conference Series, IOP Publishing, 042003.
Chen, X., Li, C. & Xu, J. (2015). Failure investigation on a coastal wind farm damaged by super typhoon: A forensic engineering study. Journal of Wind Engineering and Industrial Aerodynamics, 147, 132-142.
Chen, X. & Xu, J. Z. (2016). Structural failure analysis of wind turbines impacted by super typhoon Usagi. Engineering Failure Analysis, 60, 391-404.
Chou, J.-S., Chiu, C.-K., Huang, I. K. & Chi, K.-N. (2013). Failure analysis of wind turbine blade under critical wind loads. Engineering Failure Analysis, 27, 99-118.
Chou, J.-S. & Tu, W. (2011). Failure analysis and risk management of a collapsed large wind turbine tower. 18, 295-313.
Cwif (2020a). Summary of Wind Turbine Accident data to 30 June 2020. CWIF
Cwif. (2020b). Summary of Wind Turbine Accident data to 30 September 2020 [Online]. Available:http://www.caithnesswindfarms.co.uk/AccidentStatistics.htm [Accessed 16/10 2020].
De Paor, C., Kelliher, D., Cronin, K., Wright, W. & Mcsweeney, S. (2012). Prediction of vacuum-induced buckling pressures of thin-walled cylinders. Thin-walled structures. 55, 1-10.
Degenhardt, R., Kling, A., Zimmermann, R., Odermann, F. & De Araújo, F. (2012). Dealing with imperfection sensitivity of composite structures prone to buckling. Advances in computational stability analysis. book edited by Safa Bozkurt Coskun, ISBN 978-953-51-0673-9.
Dimopoulos, C. A. & Gantes, C. J. (2012). Experimental investigation of buckling of wind turbine tower cylindrical shells with opening and stiffening under bending. Thin-Walled Structures, 54, 140-155.
DnV. (1995). Buckling strength analysis. Det Norske Veritas AS, pp. 1–44.
DnV. (2013). Design of offshore wind turbine structures. Standard DNV-OSJ101, Det Norske Veritas AS.
Donnell, L. H. (1934). A new theory for the buckling of thin cylinders under axial compression and bending. Transactions of The American Society of Mechanical Engineers, AER-56-12, 795-806.
Donnell, L. H. & Wan, C. C. (1950). Effects of imperfections on buckling of thin cylinders and columns under axial compression. Journal of Applied Mechanics, 73-83.

ECCS. (1998). Enhancement of ECCS design recommendations and development of Eurocode 3 parts related to shells buckling. Buckling of Shells 5th Ed Brussels: European Convention for Constructional Steelwork,

Edlund, B. (1974). Thin-walled cylindrical shells under axial compression: prebuckling, buckling, and postbuckling behaviour: Monte Carlo simulation of the scatter in load carrying capacity, Chalmers University of Technology.

Edlund, B. (1977).Buckling of axially compressed thin-walled cylindrical shells with asymmetric imperfections. Preliminary Report, Second International Colloquium on the Stability of Steel Structures, Massonnet C, Maquoi R (eds). Liège, Belgium, 579-588.

Edlund, B. (2002). Buckling of axially compressed thin-walled cylindrical shells with asymmetric imperfections: theory andexperiment. In: IVANYI, M. (ed.) Stability and Ductility of Steel Structures. Budapest.

Edlund, B. (2007). Buckling of metallic shells: Buckling and postbuckling behaviour of isotropic shells, especially cylinders. Structural Control and Health Monitoring, 14**,** 693-713.

Elaydi, S. (2005). An Introduction to Difference Equations. Springer, New York, US. ISBN 978-1-4419-2001-0, doi: https://doi.org/10.1007/0-387-27602-5.

Elishakoff, I. (2000). Uncertain buckling: its past, present and future. International Journal of Solids Structures. 37, 6869-6889.

En1993-1-6 (2003). Eurocode 3, Part 1.6: Strength and Stability of Shell Structures. Brussels, 89/106/EEC - Construction products.

En1993 (2007). Eurocode 3: Design of Steel Structures-Part 1-6: Strength and Stability of Shell Structures. CEN Brussels.

Encyclopaedia Britannica. (2009). Buckling [Online]. Available: https://www.britan--nica.com/science/buckling [Accessed 17/05 2020].

Eslami, M. R. (2017). Buckling and Postbuckling of Beams, Plates, and Shells, Springer International Publishing.

Esslinger, M. & Geier, B. (1977). Some remarks on the elastic buckling of isotropic cylinders. In: C, M. & R, M. (eds.) Final Report, Second International Colloquium on the Stability of Steel Structures. Lie`ge, Belgium.

Eurocode 9. (2006). Eurocode 9 - Design of aluminium structures - Part 1-5: Shell structures. European comitee for standardization, Brussels, Belgium.

Fallah, A. & Aghdam, M. (2011). Nonlinear free vibration and post-buckling analysis of functionally graded beams on nonlinear elastic foundation. European Journal of Mechanics-A/Solids. 30, 571-583.

Fitch & James, R. (1968). The buckling and post-buckling behavior of spherical caps under concentrated load. 4**,** 421-446.

Flügge, W. (2013). Stresses in shells, Springer Science & Business Media.

Fok, S. L. (2002). Analysis of the buckling of long cylindrical shells embedded in an elastic medium using the energy method. The Journal of Strain Analysis for Engineering Design, 37**,** 375-383.

Föppl, A. (1910). Vorlesungen über technische Mechanik, BG Teubner.

Forrestal, M. J. & Herrmann, G. (1965). Buckling of a long cylindrical shell surrounded by an elastic medium. International Journal of Solids and Structures, 1**,** 297-309.

Ge-Renewableenergy. (2020). Haliade-X 12 MW offshore wind turbine platform [Online]. Available: https://www.ge.com/renewableenergy/wind-energy/offshore-wind/haliade-x-offshore-turbine [Accessed 23/10 2020].

Gellin, S. (1980). The plastic buckling of long cylindrical shells under pure bending. International Journal of Solids and Structures, 16**,** 397-407.

Gintautas, T. & Sørensen, J. (2014). Integrated system reliability analysis. Denmark: Department of Civil Engineering Aalborg University, Denmark.

Golding, E. W. & Harris, R. (1976). The generation of electricity by wind power, E. & FN Spon London. Spon's Electrical-Engineering Series, doi: https://doi.org/10.1002/qj.49708235431

Griffin, D. (1973). Inelastic and creep buckling of circular cylinder due to axial compression, bending, and twisting. Westinghouse Electric Corp., Pittsburgh, Pa.(USA). Advanced Reactors Div.

Guarracino, F., Walker, A. & Giordano, A. (2009). Effects of boundary conditions on testing of pipes and finite element modelling. International Journal of Pressure Vessels and Piping - Int J Pressure Vessels Piping, 86**,** 196-206.

Gwec. (2020a). Global Wind Report 2019 [Online]. Available: https://gwec.net/global-wind-report-2019/ [Accessed 15/08 2020].

Gwec. (2020b). Wind power industry to install 71.3 GW in 2020, showing resilience during COVID-19 crisis [Online]. Available: https://gwec.net/gwec-wind-power-industry-to-install-71-3-gw-in-2020-showing-resilience-during-covid-19-crisis/ [Accessed 06/11 2020].

Hamilton, S. W. R. (1834). On a general method in dynamics, Richard Taylor.

Hamilton, W. R. (1835). Second essay on a general method in dynamics. Philosophical Transactions of the Royal Society of London, 125**,** 95-144.

Hao, P., Wang, B., Tian, K., Du, K. & Zhang, X. (2015). Influence of imperfection distributions for cylindrical stiffened shells with weld lands. Thin-Walled Structures, 93**,** 177-187.

Harris, L. A., Suer, H. S., Skene, W. T. & Benjamin, R. J. (1957). The stability of thin-walled unstiffened circular cylinders under axial compression including the effects of internal pressure. Journal of the Aeronautical Sciences, 24**,** 587-596.

Hau, E. (2013). Wind turbines: fundamentals, technologies, application, economics, Springer Science & Business Media.

Hilbert, D. & Cohn-Vossen, S. (1999). Geometry and the Imagination, Chelsea Publishing (American Mathematical Society). ISBN-13 : 978-0821819982.

Hilburger, M., Waas, A. & Starnes Jr, J. (1997). Modeling the dynamic response and establishing post-buckling/post snap-thru equilibrium of discrete structures via a transient analysis.

Hilburger, M. W. (2008). The development of shell buckling design criteria based on initial imperfection signatures. Buckling and Postbuckling Structures: Experimental, Analytical and Numerical Studies. World Scientific.

Homer, H., (2015). The odyssey. Xist Publishing.
Hornung, U. & Saal, H. (2002). Buckling loads of tank shells with imperfections. International Journal of Non-Linear Mechanics, 37, 605-621.
Horton, W. & Durham, S. (1963). The Effect of Restricting Buckle Depth in Circular Cylindrical Shells Repeatedly Compressed to the Buckling Limit. Stanford univ calif.
Houliara, S. & Karamanos, S. A. (2010). Buckling of Thin-Walled Long Steel Cylinders Subjected to Bending. Journal of Pressure Vessel Technology, 133.
Hu, H.-T., Yang, C.-H. & Lin, F.-M. (2006). Buckling analyses of composite laminate skew plates with material nonlinearity. Composites Part B: Engineering. 37, 26-36.
Hu, Y., Baniotopoulos, C. & Yang, J. (2014). Effect of internal stiffening rings and wall thickness on the structural response of steel wind turbine towers. Engineering Structures, 81, 148-161.
Huang, H. & Han, Q. (2009). Nonlinear elastic buckling and postbuckling of axially compressed functionally graded cylindrical shells. International Journal of Mechanical Sciences, 51, 500-507.
Huang, N.-C. (1964). Unsymmetrical buckling of thin shallow spherical shells.
Hutchinson, J. (2016). Buckling of spherical shells revisited. Proceedings of the Royal Society A: Mathematical, Physical and Engineering Science, 472, 20160577.
Hutchinson, J. W. (1965). Axial Buckling of Pressurized Imperfect Cylindrical Shells. AIAA Journal, 3, 1461-1466.
Hutchinson, J. W. (1968). Buckling and Initial Postbuckling Behavior of Oval Cylindrical Shells Under Axial Compression. Journal of Applied Mechanics, 35, 66-72.
Hutchinson, J. W. & Thompson, J. M. T. (2017). Nonlinear buckling behaviour of spherical shells: barriers and symmetry-breaking dimples. Philosophical Transactions of the Royal Society A: Mathematical, Physical Engineering Sciences 375, 20160154.
IEC International Electrotechnical Commission, G. (2005). Iec 61400-3: Wind turbines–part 1: Design requirements. 64.
Ishihara, T., Yamaguchi, A., Takahara, K., Mekaru, T. & Matsuura, S. (2005). An analysis of damaged wind turbines by Typhoon Maemi in 2003. Proceedings of the 6th Asia-Pacific Conference on Wind Engineering. Seoul, Republic of Korea2005, 1413-28.
Ismail, M. S., Ifayefunmi, O., Fadzullah, S. H. S. M. & Johar, M. (2020). Buckling of imperfect cone-cylinder transition subjected to external pressure. International Journal of Pressure Vessels and Piping, 187, 104173.
Jiang, D., Landis, C. M. & Kyriakides, S. (2016). Effects of tension/compression asymmetry on the buckling and recovery of NiTi tubes under axial compression. International Journal of Solids and Structures, 100-101, 41-53.
Johnson, H. (2019). Earthquake Loading Effects On The Buckling Of Liquid Filled Cylindrical Storage Tanks.

Jonkman, J., Butterfield, S., Musial, W. & Scott, G. (2009). Definition of a 5-MW reference wind turbine for offshore system development. National Renewable Energy Lab.(NREL), Golden, CO (United States).

Juan, A., Moran, J., Guerra, M., Couto, A., Ayuga, F. & Aguado, P. (2006). Establishing stress state of cylindrical metal silos using finite element method: Comparison with ENV 1993. Thin-walled structures. 44, 1192-1200.

Kao, R. & Perrone, N. (1971). Asymmetric Buckling of Spherical Caps With Asymmetrical Imperfections. Journal of Applied Mechanics, 38**,** 172-178.

Karam, G. N. & Gibson, L. J. (1995). Elastic buckling of cylindrical shells with elastic cores—II. Experiments. International Journal of Solids and Structures, 32**,** 1285-1306.

Karamanos, S. (2002). Bending instabilities of elastic tubes. International Journal of Solids and Structures, 39**,** 2059-2085.

Kempner, J. & Chen, Y.-N. (1972). Buckling and Initial Postbuckling of Oval Cylindrical Shells under Combined Axial Compression and Bending. Transactions of the New York Academy of Sciences, 36**,** 58.

Khamlichi, A., Bezzazi, M. & Limam, A. (2004). Buckling of elastic cylindrical shells considering the effect of localized axisymmetric imperfections. Thin-Walled Structures, 42**,** 1035-1047.

Kidane, S., Li, G., Helms, J., Pang, S.-S. & Woldesenbet, E. (2003). Buckling load analysis of grid stiffened composite cylinders. Composites Part B: Engineering, 34**,** 1-9.

Kim, S.-E. & Kim, C.-S. (2002). Buckling strength of the cylindrical shell and tank subjected to axially compressive loads. Thin-Walled Structures, 40**,** 329-353.

Koiter, W. (1970). The Stability of Elastic Equilibrium. Thesis Delft, F10**,** 325.

Koiter, W. J. P., Kon. Ned. Ak. Wet., (1963). The effect of axisymmetric imperfections on the buckling of cylindrical shells under axial compression. 66**,** 265-279.

Koiter, W. J. T. (1945). On the stability of elastic equilibrium (in Dutch).

Koiter, W. T. (1967). On the stability of elastic equilibrium, National Aeronautics and Space Administration.

König, F. (1976). Windenergie in praktischer Nutzung, Pfriemer.

Kroplin, B., Dinkier, D. (1986). Dynamic versus static buckling analysis of thin walled shell structures. Finite element methods for plate shell structures. 2, 229-251.

Kröplin, B., Dinkler, D., Hillmann. (1985).An energy perturbation applied to nonlinear structural analysis. Computer Methods in Applied Mechanics Engineering, 52**,** 885-897.

Kumar, P. & Srinivasa, C. J. (2020). On buckling and free vibration studies of sandwich plates and cylindrical shells: A review. Journal of Thermoplastic Composite Materials. 33, 673-724.

Lagaros, N. D. & Karlaftis, M. G. (2016). Life-cycle cost structural design optimization of steel wind towers. Computers & Structures, 174**,** 122-132.

Lancaster, E., Calladine, C. & Palmer, S. (2000). Paradoxical buckling behaviour of a thin cylindrical shell under axial compression. International Journal of Mechanical Sciences, 42**,** 843-865.

Langhaar, H. L. (2016). Energy Methods in Applied Mechanics, Dover Publications.

Lavassas, I., Nikolaidis, G., Zervas, P., Efthimiou, E., Doudoumis, I. & Baniotopoulos, C. (2003). Analysis and design of the prototype of a steel 1-MW wind turbine tower. Engineering structures. 25, 1097-1106.

Lawrence, J. D. 2013. A catalog of special plane curves, Courier Corporation.

Lee, K.-S. & Bang, H.-J. (2012). A study on the prediction of lateral buckling load for wind turbine tower structures. International Journal of Precision Engineering and Manufacturing, 13**,** 1829-1836.

Lee, L. H. N. (1962). Inelastic Buckling of Initially Imperfect Cylindrical Shells Subject to Axial Compression. 29, 87-95.

Li, Z.-Q., Chen, S.-J., Ma, H. & Feng, T. (2013). Design defect of wind turbine operating in typhoon activity zone. Engineering Failure Analysis. 27, 165-172.

Ma, L., Wang, T. (2003). Nonlinear bending and post-buckling of a functionally graded circular plate under mechanical and thermal loadings. International Journal of Solids Structures. 40, 3311-3330.

Ma, Y., Martinez-Vazquez, P. & Baniotopoulos, C. (2019). Wind turbine tower collapse cases: a historical overview. Proceedings of the Institution of Civil Engineers - Structures and Buildings, 172**,** 547-555.

Ma, Y., Martinez-Vazquez, P. & Baniotopoulos, C. (2020). Buckling Analysis for Wind Turbine Tower Design: Thrust Load versus Compression Load Based on Energy Method. Energies. 13**,** 5302.

Mandal, P. & Calladine, C. (2000). Buckling of thin cylindrical shells under axial compression. International Journal of Solids Structures 37**,** 4509-4525.

Manuello, A. (2020). Multi-body rope approach for grid shells: Form-finding and imperfection sensitivity. Engineering Structures, 221**,** 111029.

Manwell, J., Mcgowan, J. & Rogers, A. (2006). Wind Energy Explained: Theory, Design and Application, Second Edition.

Martins, A. D. & Silvestre, N. (2020). Modal analysis and imperfection sensitivity of the post-buckling behaviour of cylindrical steel panels under in-plane bending. Engineering Structures, 207**,** 110-127.

Matos, H., Kishore, S., Salazar, C. & Shukla, A. (2020). Buckling, Vibration, and Energy Solutions for Underwater Composite Cylinders. Composite Structures. 112-282.

Mittelstedt, C. J. a. M. R. (2020). Buckling and Post-Buckling of Thin-Walled Composite Laminated Beams—A Review of Engineering Analysis Methods. 72.

Nationalpost. (2016). 'Rare' collapse of 80-metre wind turbine in Cape Breton believed to be a Canadian first [Online]. Available: https://nationalpost.com/news/canada/rare-collapse-of-80-metre-wind-turbine-in-cape-breton-believed-to-be-a-canadian-first [Accessed 17/05 2020].

Nemeth, M. (1994). Nondimensional parameters and equations for buckling of anisotropic shallow shells. Journal of Applied Mechanics, 61**,** 664-669.

Novozhilov, V. V. (1959). The theory of thin shells, P. Noordhoff.
Nuta, E., Christopoulos, C. & Packer, J. (2011). Methodology for seismic risk assessment for tubular steel wind turbine towers: application to Canadian seismic environment. Canadian Journal of Civil Engineering. 38, 293-304.
Pearson, C. E. (1956). General theory of elastic stability. Quarterly of Applied Mathematics. 14, 133-144.
Pei, P. E. I. (2017). Collapse of wind turbine under investigation [Online]. Tulsa, USA. Available: http://www.powerengineeringint.com/articles/2017/01/collapse-of-wind-turbine-under-investigation.html [Accessed 11/09 2019].
Peterson, J., Seide, P. & Weingarten, V. (1968). Buckling of thin-walled circular cylinders. NASA Sp, 8007.
Pinna, R. & Ronalds, B. F. (2004). Buckling and collapse of cylinders with one end open and one end simply supported with varying axial restraint. International Journal of mechanical sciences, 46, 541-559.
Pircher, M., Berry, P., Ding, X. & Bridge, R. Q. (2001). The shape of circumferential weld-induced imperfections in thin-walled steel silos and tanks. Thin-Walled Structures 39, 999-1014.
Putnam, P. C. (1974). Power From The Wind, Van Nostrand Reinhold.
Ramberg, W. & Osgood, W. R. (1943). Description of stress-strain curves by three parameters.
Reese, C. & Bert, C. (1974). Buckling of Orthotropic Sandwich Cylinders Under Axial Compression and Bending. Journal of Aircraft - J aircraft, 11, 207-212.
Reinke, T., Sadowski, A. J., Ummenhofer, T. & Rotter. (2014). Large scale bending tests of spiral welded steel tubes. Eurosteel.
Reissner, E. (1959). On finite bending of pressurized tubes. Applied Mech, Series E26, 386-392.
Riks, E. (1979). An incremental approach to the solution of snapping and buckling problems. International Journal of Solids and Structures, 15, 529-551.
Riks, E., Rankin, C. C., Brogan, F. (1996). On the solution of mode jumping phenomena in thin-walled shell structures. Computer methods in applied mechanics engineering. 136, 59-92.
Riks, E. (1997). Buckling analysis of elastic structures: a computational approach. Advances in Applied Mechanics. 34, 1-76.
Riso, D. (2008). Final report on investigation of a catastrophic turbine failures, February 22 and 23, 2008. December.
Robert Gasch, J. T. (2012). Wind power plants : fundamentals, design, construction and operation. 2nd ed. Berlin,London: Springer.
Rossi, A., Nicoletti, R. S., De Souza, A. S. C. & Martins, C. H. (2020). Lateral distortional buckling in steel-concrete composite beams: A review. Structures, Elsevier, 1299-1312.
Rotter, J. (2005). The practical design of shell structures exploiting different methods of analysis. 71-86.

Rotter, J. M. & Teng, J.-G. (1989). Elastic stability of cylindrical shells with weld depressions. Journal of Structural Engineering. 115, 1244-1263.

Rotter, J. M. J. T.-W. S. (1998). Shell structures: the new European standard and current research needs. 31, 3-23.

Rudd, M. T., Hilburger, M. W., Lovejoy, A. E., Lindell, M. C., Gardner, N. W. & Schultz, M. R. (2018). Buckling response of a large-scale, seamless, orthogrid-stiffened metallic cylinder. AIAA/ASCE/AHS/ASC Structures, Structural Dynamics, and Materials Conference, 2018. 19-87.

Sadowski, A. & Rotter, J. (2011). Buckling of very slender metal silos under eccentric discharge. Engineering Structures - Eng Struct, 33, 1187-1194.

Sadowski, A. & Rotter, J. (2013). Solid or shell finite elements to model thick cylindrical tubes and shells under global bending. International Journal of Mechanical Sciences, 74.

Schmidt, H. J. J. O. C. S. R. (2000). Stability of steel shell structures: General Report. 55, 159-181.

Schneider, M. H. (1996). Investigation of the stability of imperfect cylinders using structural models. Engineering Structures, 18, 792-800.

Schneider, W. (2006). Stimulating equivalent geometric imperfections for the numerical buckling strength verification of axially compressed cylindrical steel shells. Computational Mechanics 37, 530-536.

Schneider, W. & Thiele, R. J. B. (1999). Beurteilung von Versagenszuständen mittels quasistatischer Analyse. 74, 485-494.

Schneider, W., Timmel, I. & Höhn, K. (2005). The conception of quasi-collapse-affine imperfections: A new approach to unfavourable imperfections of thin-walled shell structures. Thin-Walled Structures, 43, 1202-1224.

Seide, P. & Weingarten, V. I. (1959). On the buckling of circular cylindrical shells under pure bending. Trw space technology labs los angeles calif.

Seide, P., Weingarten, V. I. & Morgan, E. J. (1960).The Development of Design Criteria For Elastic Stability of Thin Shell Structures.

Shakouri, M., Spagnoli, A. & Kouchakzadeh, M. A. (2014). Re-interpreting simultaneous buckling modes of axially compressed isotropic conical shells. Thin-Walled Structures, 84, 360-368.

Singer, J. (1967). The Influence of Stiffener Geometry and Spacing on the Buckling of Axially Compressed Cylindrical and Conical Shells. Technion-Israel inst of tech haifa dept of areonautical engineering.

Singer, J., Arbocz, J. & Weller, T. (2002). Buckling experiments, Second Edittion.

Sofiyev, A. J. C. S. (2019). Review of research on the vibration and buckling of the FGM conical shells. 211, 301-317.

Tafreshi, A. (2008). Instability of delaminated composite cylindrical shells under combined axial compression and bending. Composite Structures, 82, 422-433.

Teng, J. G. (1996). Buckling of Thin Shells: Recent Advances and Trends. Applied Mechanics Reviews, 49.

Teng, J. G. & Rotter, J. M. (2006). Buckling of Thin Metal Shells, CRC Press.

Tennyson, R. (1969). Buckling modes of circular cylindrical shells under axial compression. 7, 1481-1487.
Thestructuralengineer.Info. (2020). Wind turbines destroyed in Evia, Greece [Online]. Available:https://www.thestructuralengineer.info/news/wind-turbines-destroyed-in-evia-greece [Accessed 13/05 2020].
Thompson, J. J. T. a. Q. (1962). The elastic instability of a complete spherical shell. 13, 189-201.
Thompson, J. M. T. & Hunt, G. W. (1973). A General Theory of Elastic Stability, J. Wiley.
Timoshenko, S., Goodier, J. N. & Goodier, J. N. 1951. Theory of Elasticity, McGraw-Hill.
Timoshenko, S. P. & Goodier, J. (2011). Theory of elasticity.
Tomás, A., Tovar, J. P. J. C. & Structures (2012). The influence of initial geometric imperfections on the buckling load of single and double curvature concrete shells. 96, 34-45.
Tovstik, P. E., Smirnov, A. L., Frise, P. R. & Shir Guran, A. (2001). Asymptotic methods in the buckling theory of elastic shells, World Scientific.
Tulczyjew, W. M. (1977).The legendre transformation. Annales de l'IHP Physique théorique, 101-114.
Van Es, S. H., Gresnigt, A. M., Vasilikis, D. & Karamanos, S. a. (2016). Ultimate bending capacity of spiral-welded steel tubes–Part I: Experiments. Thin-Walled Structures. 102, 286-304.
Vasilikis, D., Karamanos, S. A., Van Es, S. H. J. & Gresnigt, A. M. (2016). Ultimate bending capacity of spiral-welded steel tubes – Part II: Predictions. Thin-Walled Structures, 102, 305-319.
Veritas, N. (2002). Guidelines for design of wind turbines, Det Norske Veritas: Wind Energy Department, Ris ̧ National Laboratory.
Von Karman, T., Dunn, L. G. & Tsien, H.-S. (1940). The influence of curvature on the buckling characteristics of structures. Journal of the Aeronautical Sciences. 7, 276-289.
Von Karman, T. & Tsien, H.-S. (1941). The Buckling of Thin Cylindrical Shells Under Axial Compression. Journal of the Aeronautical Sciences, 8, 303-312.
Von Karman, T. & Tsien. (1939).The buckling of spherical shells by external pressure. Journal of the Aeronautical Sciences, 7, 43-50.
Wagner, R., Hühne, C., Niemann, S. & Khakimova, R. (2017). Robust design criterion for axially loaded cylindrical shells - Simulation and Validation. Thin-Walled Structures, 115, 154-162.
Wang, B., Zhu, S., Hao, P., Bi, X., Du, K., Chen, B., Ma, X. & Chao, Y. J. (2018). Buckling of quasi-perfect cylindrical shell under axial compression: A combined experimental and numerical investigation. International Journal of Solids and Structures, 130-131, 232-247.
Wang, J. & Sadowski, A. J. (2020). Elastic Imperfect Cylindrical Shells of Varying Length under Combined Axial Compression and Bending. 146, 04020014.

Weingarten, V. I., Morgan, E. J. & Seide, P. (1965). Elastic stability of thin-walled cylindrical and conical shells under axial compression. AIAA Journal, 3, 500-505.

Windeurope. (2020). Wind energy and economic recovery in Europe [Online]. Available: https://windeurope.org/data-and-analysis/product/wind-energy-and-economic-recovery-in-europe/ [Accessed 25/10 2020].

Windpower. (2020). Clash of the titans -- top 5 biggest onshore turbines [Online]. Available: https://www.windpowermonthly.com/article/1592000/clash-titans-top-5-biggest-onshore-turbines [Accessed 15/08 2020].

Winterstetter, T. A. & Schmidt, H. (2002). Stability of circular cylindrical steel shells under combined loading. Thin-Walled Structures, 40, 893-910.

Wu, J., Zhu, J., Dong, Y. & Zhang, Q. (2020). Nonlinear stability analysis of steel cooling towers considering imperfection sensitivity. Thin-Walled Structures, 146, 106448.

Wullschleger, L. (2006). Numerical investigation of the buckling behaviour of axially compressed circular cylinders having parametric initial dimple imperfections. ETH Zurich.

Wunderlich, W. & Albertin. (2002). Buckling behaviour of imperfect spherical shells. International Journal of Non-Linear Mechanics. 37, 589-604.

Yamaki, N. (1976). Experiments on the postbuckling behavior of circular cylindrical shells under torsion. Buckling of structures. Springer.

Yamaki, N., and S. Kodama. (1976) Postbuckling behavior of circular cylindrical shells under compression. International Journal of Non-Linear Mechanics. 11, 99-111.

Yamaki, N. (1984). Elastic stability of circular cylindrical shells, Elsevier.

Yamaki, N. (1985). Elastic Stability of Circular Cylindrical Shell. Journal of Applied Mechanics, 52.

Yamaki, N., Otomo, K. & Matsuda, K. (1975). Experiments on the postbuckling behavior of circular cylindrical shells under compression. Experimental Mechanics, 15, 23-28.

Yamki, N. & Kodama, S. (1979). Perturbation Analyses for the Postbuckling and Imperfection Sensitivity of Circular Cylindrical Shells under Torsion. In Theory of Shells (Proceedings of 3rd IUTAM Symposium on Shell Theory), ed. W. T. Koiter and G. K. Mikhailov, 635-667.

Zhu, E., Mandal, P. & Calladine, C. (2002). Buckling of thin cylindrical shells: an attempt to resolve a paradox. International Journal of Mechanical Sciences 44, 1583-1601.